

HETEROATOM CONTAINING POROUS CARBON MATERIALS FOR ELECTROCHEMICAL ENERGY STORAGE APPLICATIONS

Thesis submitted
in partial fulfillment for the degree of
Doctor of Philosophy

By
RESHMA C.



Department of Chemistry
Indian Institute of Space Science and Technology
Thiruvananthapuram-695547

April 2019

To my beloved Father, Mother and Brother

CERTIFICATE

This is to certify that the thesis entitled “**Heteroatom Containing Porous Carbon Materials for Electrochemical Energy Storage Applications**” submitted by **Reshma C.** to the Indian Institute of Space Science and Technology Thiruvananthapuram, in partial fulfilment for the award of the degree of **Doctor of Philosophy** is a *bona fide* record of research work carried out by her under my supervision. The contents of this thesis, in full or in parts, have not been submitted to any other Institution or University for the award of any degree or diploma.

Dr. J. Mary Gladis
Supervisor
Associate Professor
Department of Chemistry

Thiruvananthapuram

Counter signature of the HOD with seal

April 2019

DECLARATION

I declare that this thesis entitled “**Heteroatom Containing Porous Carbon Materials for Electrochemical Energy Storage Applications**” submitted in partial fulfilment of the degree of **Doctor of Philosophy** is a record of original work carried out by me under the supervision of Dr. J. Mary Gladis, and has not formed the basis for the award of any other degree or diploma, in this or any other Institution or University. In keeping with the ethical practice of reporting scientific information, due acknowledgments have been made wherever the finding of others have been cited.

Reshma C.

SC13D004

Thiruvananthapuram

April 2019

ACKNOWLEDGEMENTS

Completion of this doctoral dissertation would not have been possible without the support of several people who have helped and encouraged during my study at Indian Institute of Space Science and Technology.

Firstly and foremost I would like to express my deepest gratitude to my research supervisor, Dr. J. Mary Gladis, Associate Professor, Department of Chemistry for giving me an opportunity to work under her supervision, constant support, valuable guidance and consistent encouragement. I have been extremely lucky to have a supervisor who cared so much about my work and responded to my questions and queries so promptly.

I take this opportunity to thank Dr. K. S. Das Gupta, former Director of IIST and Dr. V. K. Dadhwal, present Director, IIST for providing research facilities during the tenure of my work. I would also like to thank Professor Kuruvilla Joseph, Dean, Student Activities, and Dr. Nirmala Rachael James, HOD, Department of Chemistry for their constant support. My heartfelt thanks to the IIST for the financial support.

I would like to thank the doctoral committee members Dr. C. Gouri, Dr. Ranga Rao, Dr. Smitha Juhari, Dr. K. Y. Sandhya, Dr. Chakravarthy for their constructive criticisms and valuable comments during my Ph.D. journey. I express my sincere thanks to Dr. Arul Manual Stephan, CSIR-CECRI for providing the facilities to do the electrochemical characterization. I also thank all faculty members of the Department of Chemistry for their constant support.

I am deeply indebted to all my colleagues and staffs of the Department of Chemistry, without them the thesis would not have come to a successful completion. I also offer my sincere thanks especially to Haritha H, Varanya J, Sreekala K and Athul Mohanan for their kind support. I am extremely grateful to M. Raja and Shruthi Suriya

Kumar to carry out the research so smoothly. I deeply acknowledge my senior colleagues Dr. Raneesh Konnola, Dr. Mohammed Mukthar Ali, Dr. Kavitha M. K., Dr. Sujith Vijayan, Dr. Rakesh R, Dr. Lavanya J, Dr. Remya mol T, Dr. Narasimman R, Dr. Sarah Titus, Dr. Sarika P.R, Dr. Jalaja K, for their strong motivation in the initial phase of my research.

I cannot forget the valuable presence of my friend Aswathi R and she always helped me whenever I need the support, which I cannot forget in my life. I express my sincere thanks to Dr. Veena V. S during the IIST days, I enjoyed the time that I spent with her. I also acknowledge my colleagues Dr. Manjunatha Ganiga, Devi Renuka K, Meegle S Mathew, Neema P. M, Praveen Wilson, Yogesh Choudhary, Sanu Xavier, Saisree S, Arya Nair J S, BDS Deeraj, Varsha M V, Ann Mary Tomy, Dr. Roymon Joseph, Dr. Linsha V and Sona Xavier. I appreciate staff members, Jayasree L, Dileep, Jayasree Dinesh, Rehana, Loveson Albert, Bindu P C, Remya T, Sreekumaran Nair, Thushara Bindu and Muralidharan Nair for helping me in every possible way. I thank Anisha U, Reshmi S, Randeep N C, Shiju S.S, Swetha Day, Aswathy M and all other IIST friends for their support.

I deeply acknowledge CSIR-CECRI, Kerala University, IIT Madras, STIC CUSAT, Amrita Cochin and PSG Coimbatore for the characterization studies.

I am truly grateful to my mother, father and brother for their affection, encouragement, and inspiration during my research tenancy. They always helped me to explore my potential and pursue my dreams. I would like to extend my sincere gratitude to each and every one who has rendered their help directly or indirectly during this research. I am extremely thankful to the God Almighty for all the blessings showered upon me.

(Reshma C.)

ABSTRACT

Over the past two decades, there has been an intense focus on the electrochemical energy storage devices viz. batteries and supercapacitors (SCs). Lithium-sulphur batteries (LSBs) received more attention in the energy storage sector owing to their high theoretical capacity of 1675 mA h g^{-1} and high theoretical energy density. In this doctoral work carbon with different morphology is successfully prepared and was used for the fabrication of electrodes in the SCs and LSB cathodes. The activated carbon is prepared by ZnCl_2 activation followed by carbonization. Its electrochemical evaluation was carried out by using CV, GCD and EIS studies. Detailed investigations on the prepared electrode materials for LSB and SC applications were carried out and the descriptions of the results were presented in seven chapters.

In the first chapter, a general introduction on LSBs and SCs including its principle, limitations and state of art of the present scenario are mentioned. More emphasis is given to aspects which are currently focused on the thesis.

In the second chapter, Multiwalled carbon nanotube/sulphur/polyindole (MWCNT/S/PIN) nanocomposite was developed as cathode material for LSBs to alleviate capacity decay. It was synthesized by chemical precipitation of sulphur onto functionalized MWCNT followed by in-situ polymerization of indole. MWCNT/S/PIN nanocomposite exhibited 1490 mA h g^{-1} as initial specific capacity and enhanced cycling stability compared to the binary nanocomposite (MWCNT/S). The MWCNT/S/PIN composite cathode displayed 1043 mA h g^{-1} after 100 cycles at a 0.1C rate with 70% capacity retention. The better electrochemical performance of ternary nanocomposite cathode material was attributed to the synergistic effect of functionalized MWCNT and polyindole which provides improved conductivity and effective fencing of intermediate polysulphides (PSs).

In the third chapter, heteroatom doped microporous carbon (HMC) materials were prepared from 4, 4'-diamino-diphenyl sulphone (DDS) by pyrolyzing at $950 \text{ }^\circ\text{C}$ in a single step without activation. The structural changes with the variation of carbonisation time were investigated. The heteroatom doped porous carbon-sulphur (HMCS) composite is used as LSB positive electrode material. A comparative study was performed using materials prepared at the carbonisation time 1 & 2 h. The porous carbon matrix was used as a conductive host along with N, O functionalities to restrain the polysulphide diffusion into the electrolytes during the discharge process. HMC-2S exhibits better performance than the HMC-1S due to its higher surface area and pore volume, it can accommodate the volume changes of sulphur inside the carbon matrix than the HMC-1S during the cycling process. In addition, solid-state symmetric supercapacitor was fabricated using HMC with KOH and Na_2SO_4 gel electrolytes. The symmetric supercapacitor using Na_2SO_4 gel electrolyte gives a maximum energy

density of 35 W h kg^{-1} at a power of 529 W kg^{-1} and 91.07% capacity retention is obtained at 5000 cycles at a current density of 0.6 A g^{-1} .

To improve the performance of the LSBs further, inherently doped iron oxide nanoparticles and N, O heteroatom doped high surface area hierarchically porous carbon tubes (HPC) were prepared from vetiver roots in the fourth chapter. To analyse the impact of structural, morphological and energy storage capacities of HPC materials were prepared at the pyrolysis temperature varying from $600 \text{ }^\circ\text{C}$ to $900 \text{ }^\circ\text{C}$ was carried out. HPC with the high surface area ($1879 \text{ m}^2 \text{ g}^{-1}$) and pore volume ($0.91 \text{ cm}^3 \text{ g}^{-1}$) were obtained at $800 \text{ }^\circ\text{C}$. This material was investigated in detail for SC and LSB electrodes. The symmetric supercapacitor delivered 67.8 W h kg^{-1} at a power of 749 W kg^{-1} and exhibits 88% capacity retention after 10,000 cycles at a current density of 0.5 A g^{-1} . In addition, the HPC- $800 \text{ }^\circ\text{C}$ was used to incorporate sulphur (HPCS) and supported as cathode material for lithium-sulphur batteries. The HPCS exhibited an initial discharge capacity of 1584 mA h g^{-1} and reversible capacity of 1069 mA h g^{-1} after 200 cycles at a 0.1C rate with 67% capacity retention. The better electrochemical performance was attributed to the tubular morphology, high surface area, pore volume, N, O and iron functionalities of the porous architecture of HPC.

The fifth chapter discusses on N, O heteroatom doped hierarchical porous activated carbon, prepared from pinecone by ZnCl_2 activation and followed by carbonization. The carbon material has a high surface area of $2065 \text{ m}^2 \text{ g}^{-1}$ and a pore volume of $1.5 \text{ cm}^3 \text{ g}^{-1}$. Three different combinations of sulphur loading 54, 68 & 73% were studied as cathode material for LSBs. In this chapter, the sulphur loading and distribution in this matrix is correlated with the electrochemical performance of the cell. Carbon with 54% sulphur displayed better electrochemical performance than carbon with 68 and 73% of sulphur. The initial discharge capacity was 1606 mA h g^{-1} and obtained a reversible capacity of 1269 mA h g^{-1} after 100 cycles with 79% capacity retention at the 0.1C rate. The better electrochemical performance of the 54% sulphur loaded carbon was due to the better dispersion of sulphur in the porous carbon network.

The sixth chapter elaborates on another strategy to alleviate PS shuttling. Heteroatom doped microporous carbon (HMC-1) with a surface area of $969 \text{ m}^2 \text{ g}^{-1}$ and a pore volume of $0.43 \text{ cm}^3 \text{ g}^{-1}$ was used to modify the separator. Orange peel derived carbon-sulphur composite (OPCSC) was prepared to host sulphur. Capacity degradation in the OPCSC cathode films was improved by separator modification. The modified separator was acted as a polysulphide inhibitor and accountable for the excellent electrochemical performance when compared with the MWCNT coated separator. The cell with HMC-1 coated separator exhibited 85% capacity retention while MWCNT coated displayed 74.8% capacity retention (100 cycles). The thin layer coating of HMC on separator effectively block the migration of polysulphides towards the anode, thereby decreasing the capacity loss and improving the rate performance.

The seventh chapter concerns on a better host material for sulphur, N and O co-doped honeycomb derived hierarchically porous carbon (HC) along with SiO_2 . HCS

(80%) displayed a high stable capacity of 1101 mA h g⁻¹ after 200 cycles at a 0.1C rate and 82% capacity retention. The HCS (80%) cathode was coated with a thin layer of HC, exhibited 92% capacity retention at 0.1C rate after 200 cycles. The role of the interlayer (HC coating) to improve the electrochemical performance of the cell was investigated in detail. The HCS (80%)-HC exhibited 1009 mA h g⁻¹ at the 2C rate. It is a potential positive electrode material for LSBs.

Finally, in the conclusion, a comparison of the developed materials, summary of the complete work and the future perspectives are brought out.

TABLE OF CONTENTS

DESCRIPTION	P. No.
CERTIFICATE	v
DECLARATION	vii
ACKNOWLEDGEMENT	ix
ABSTRACT	xi
TABLE OF CONTENTS	xv
LIST OF TABLES	xxi
LIST OF FIGURES	xxiii
ABBREVIATIONS	xxxiii
SYMBOLS AND UNITS	xxxvii
1 INTRODUCTION	1
1.1 Introduction	1
1.2 Li-ion Battery	2
1.3 Li-S Battery	4
1.4 Working mechanism of Li-S battery	5
1.5 Challenges and drawbacks of Li-S battery	7
1.6 Effective strategies adopted to improve the cycle life of Li-S Battery	9
1.6.1 Design of cathode architecture	9
1.6.1.1 Carbon materials	9
1.6.1.2 Conducting polymers	21
1.6.1.3 Metal oxides/metal sulphide	23
1.6.1.4 Hybrid materials	26
1.6.2 Functional-modification of separators	29
1.6.2.1 Polymer modified separator	30
1.6.2.2 Carbon modified separator	31
1.6.2.3 Metal oxide modified separator	32

1.6.2.4	Hybrid materials modified separator	33
1.6.3	Anode protections	34
1.6.3.1	In situ protection	35
1.6.3.2	Ex situ	35
1.6.3.3	Li-host material	36
1.6.4	Trends in electrolyte	36
1.7	Electrochemical capacitor	38
1.8	Scope and objectives	45
1.9	Organization of the Thesis	46
2	MWCNT/SULPHUR/POLYINDOLE COMPOSITE AS CATHODE MATERIAL FOR LITHIUM-SULPHUR BATTERY	49
2.1	Introduction	49
2.2	Materials and Methods	50
2.2.1	Materials	50
2.2.2	Composite synthesis	51
2.2.3	Material characterization	51
2.2.4	Fabrication of coin cell	52
2.2.5	Electrochemical measurements	53
2.3	Results and Discussion	53
2.3.1	Material characterization	53
2.3.2	Electrochemical performance of the composite	59
2.4	Conclusion	65
3	4, 4'-DIAMINO-DIPHENYL SULPHONE DERIVED CARBON FOR SUPERCAPACITOR ELECTRODE AND LITHIUM-SULPHUR BATTERY	67
3.1	Introduction	67
3.2	Materials and Methods	70
3.2.1	Materials	70
3.2.2	Material synthesis	71

3.2.2.1	Preparation of porous carbon	71
3.2.2.2	Preparation of porous carbon-sulphur composite	71
3.2.3	Material characterization	71
3.2.4	Electrochemical measurements	71
3.2.4.1	Sulphur cathode preparation and characterization	71
3.2.4.2	Preparation of gel polymer electrolyte	72
3.2.4.3	Supercapacitor electrode preparation and characterization	72
3.2.4.3	Calculations of specific capacitance, energy and power densities	72
3.3	Results and discussion	73
3.3.1	Physicochemical properties of HMCs	73
3.3.2	Electrochemical performance of HMCs	81
3.3.2.1	HMCS as cathode material for lithium-sulphur batteries	81
3.3.2.2	HMCs as supercapacitor electrode	91
3.4	Conclusion	99
4	VETIVER DERIVED CARBON FOR SUPERCAPACITOR ELECTRODE AND LITHIUM SULPHUR BATTERY	101
4.1	Introduction	101
4.2	Materials and Methods	104
4.2.1	Materials	104
4.2.2	Material synthesis	104
4.2.2.1	Preparation of porous carbon	104
4.2.2.2	Preparation of carbon-sulphur composite	105
4.2.2.3	Polysulphide adsorption study	105

4.2.3	Material characterization	105
4.2.3.1	Preparation of supercapacitor electrodes and electrochemical characterization	105
4.2.3.2	Sulphur cathode preparation and characterization	106
4.3	Results and discussion	107
4.3.1	Physicochemical properties of HPCs	107
4.3.2	Electrochemical performance of HPCs	115
4.3.2.1	HPCs as supercapacitor electrodes	115
4.3.2.2	HPCS as cathode material for lithium- sulphur batteries	122
4.4	Conclusion	131
5	PINECONE DERIVED CARBON-SULPHUR COMPOSITE FOR LITHIUM-SULPHUR BATTERY	133
5.1	Introduction	133
5.2	Materials and Methods	135
5.2.1	Materials	135
5.2.2	Material synthesis	135
5.2.2.1	Preparation of porous carbon	135
5.2.2.2	Preparation of carbon-sulphur composite	135
5.2.3	Material characterization	136
5.2.4	Fabrication of coin cell and electrochemical measurements	136
5.3	Results and discussion	136
5.3.1	Material characterization	136
5.3.2	Electrochemical performance of the composite	146
5.4	Conclusion	153
6	ORANGE PEEL DERIVED CARBON FOR LITHIUM- SULPHUR BATTERY	155

6.1	Introduction	155
6.2	Materials and Methods	158
6.2.1	Materials	158
6.2.2	Material synthesis	158
6.2.2.1	Preparation of porous carbon	158
6.2.2.2	Preparation of carbon-sulphur composite	158
6.2.3	Preparation of modified separator	158
6.2.4	Material Characterization	159
6.2.5	Fabrication of coin cell and electrochemical measurements	159
6.3	Results and discussion	159
6.3.1	Characterization of OPC and OPCSCs	159
6.3.2	Electrochemical performance of the composite	165
6.3.2.1	OPCSC as cathode material for Li-S batteries	165
6.3.2.2	Structural and electrochemical evaluation of LSB with modified separator	168
6.4	Conclusion	182
7	HONEYCOMB DERIVED CARBON FOR LITHIUM-SULPHUR BATTERY	183
7.1	Introduction	183
7.2	Materials and Methods	185
7.2.1	Materials	185
7.2.2	Material synthesis	185
7.2.2.1	Preparation of porous carbon	185
7.2.2.2	Preparation of carbon-sulphur composite	186
7.2.2.3	Preparation of HC coated cathode	186
7.2.3	Material characterization	186
7.3	Results and discussion	186
7.3.1	Material Characterization	186

7.3.2	Electrochemical performance of the composite	196
7.3.2.1	HCS as cathode material for Li-S batteries	196
7.3.2.2	Impact of HC interlayer on HCS cathode material	200
7.4	Conclusion	207
8	CONCLUSIONS AND FUTURE PERSPECTIVES	209
8.1	Conclusions	209
8.2	Future Perspectives	214
	References	217
	List of Publications	271

LIST OF TABLES

TABLE	TITLE	P. No.
1.1	Comparison of specific capacitance of the biomass derived carbon	45
2.1	Comparison of performance for MWCNT/sulphur/ conducting polymer materials reported previously	63
2.2	Impedance parameters obtained from the electrochemical equivalent circuit analysis	64
3.1	Textural properties of HMCs	76
3.2	CHNS analysis of HMCs	77
3.3	CHNS analysis of HMCS	83
3.4	Impedance parameters obtained from the electrochemical equivalent for HMCSs before and after cycling	89
3.5	Impedance parameters obtained from the electrochemical equivalent circuit analysis with 6M KOH electrolyte	94
3.7	Comparison of the specific capacitance of porous carbon with three electrode system	95
4.1	XRF analysis of vetiver root	107
4.2	Elemental composition of HPCs from CHNS Analysis	107
4.3	ICP-AES analysis for HPCs	107
4.4	Surface area of HPCs without activation	109
4.5	Surface area of HPCs with activation	109
4.6	Impedance parameters obtained from the electrochemical equivalent circuit analysis with 1M Na ₂ SO ₄ electrolyte	118
4.7	Impedance parameters obtained from the electrochemical equivalent circuit analysis with 1M LiTFSI electrolyte	120
4.8	Comparison of energy densities of porous carbon materials with various organic electrolytes	121

4.9	Impedance parameters obtained from the electrochemical equivalent circuit analysis for HPCS before and after cycling	130
5.1	Surface area and pore volume of PC and PCSCs	138
5.2	Elemental content of PC and PCSCs obtained from CHNS Analysis	141
5.3	Elemental composition of PC and PCSC (54%) obtained XPS Analysis	141
5.4	Comparison of biomass derived carbon/sulphur hybrid materials for LSBs	149
5.5	Impedance parameters obtained from the equivalent circuit for the PCSCs before and after cycling	153
6.1	Surface area and pore volume of OPC/OPCSCs	160
6.2	Porosity details of MWCNT and HMC-1	170
6.3	Comparison of capacity retention of LSB with heteroatom-doped carbon modified separator	176
6.4	Equivalent circuit for the OPCSC-73% cathodes with MWCNT and HMC-1 coated separator before and cycling	179
7.1	Surface area and pore volume of HCs/HCSs	188
7.2	CHNS analysis of HC and HCS	192
7.3	Elemental composition from XPS Analysis	195
7.4	Impedance parameters obtained from the equivalent circuit for the HCSs cathodes before and cycling	200
7.5	Impedance parameters obtained from the equivalent circuit for the HCS (80) %-HC cathodes before and after cycling	204
8.1	Comparison of electrochemical performance of the developed material	213

LIST OF TABLES

TABLE	TITLE	P. No.
1.1	Comparison of specific capacitance of the biomass derived carbon	45
2.1	Comparison of performance for MWCNT/sulphur/ conducting polymer materials reported previously	63
2.2	Impedance parameters obtained from the electrochemical equivalent circuit analysis	64
3.1	Textural properties of HMCs	76
3.2	CHNS analysis of HMCs	77
3.3	CHNS analysis of HMCS	83
3.4	Impedance parameters obtained from the electrochemical equivalent for HMCSs before and after cycling	89
3.5	Impedance parameters obtained from the electrochemical equivalent circuit analysis with 6M KOH electrolyte	94
3.7	Comparison of the specific capacitance of porous carbon with three electrode system	95
4.1	XRF analysis of vetiver root	107
4.2	Elemental composition of HPCs from CHNS Analysis	107
4.3	ICP-AES analysis for HPCs	107
4.4	Surface area of HPCs without activation	109
4.5	Surface area of HPCs with activation	109
4.6	Impedance parameters obtained from the electrochemical equivalent circuit analysis with 1M Na ₂ SO ₄ electrolyte	118
4.7	Impedance parameters obtained from the electrochemical equivalent circuit analysis with 1M LiTFSI electrolyte	120
4.8	Comparison of energy densities of porous carbon materials with various organic electrolytes	121

4.9	Impedance parameters obtained from the electrochemical equivalent circuit analysis for HPCS before and after cycling	130
5.1	Surface area and pore volume of PC and PCSCs	138
5.2	Elemental content of PC and PCSCs obtained from CHNS Analysis	141
5.3	Elemental composition of PC and PCSC (54%) obtained XPS Analysis	141
5.4	Comparison of biomass derived carbon/sulphur hybrid materials for LSBs	149
5.5	Impedance parameters obtained from the equivalent circuit for the PCSCs before and after cycling	153
6.1	Surface area and pore volume of OPC/OPCSCs	160
6.2	Porosity details of MWCNT and HMC-1	170
6.3	Comparison of capacity retention of LSB with heteroatom-doped carbon modified separator	176
6.4	Equivalent circuit for the OPCSC-73% cathodes with MWCNT and HMC-1 coated separator before and cycling	179
7.1	Surface area and pore volume of HCs/HCSs	188
7.2	CHNS analysis of HC and HCS	192
7.3	Elemental composition from XPS Analysis	195
7.4	Impedance parameters obtained from the equivalent circuit for the HCSs cathodes before and cycling	200
7.5	Impedance parameters obtained from the equivalent circuit for the HCS (80) %-HC cathodes before and after cycling	204
8.1	Comparison of electrochemical performance of the developed material	213

LIST OF FIGURES

FIGURE	TITLE	P. No.
1.1	Comparison diagram of rechargeable battery technologies	3
1.2	Schematic diagram of LIB	4
1.3	Schematic diagram of LSB	6
1.4	Electrochemical voltage profile for LSB and sulphur bonding chemistry during charge-discharge process	7
1.5	Ragone plot for various electrical energy storage devices	39
1.6	Schematic representation for the classification of electrochemical capacitors	40
2.1	Schematic illustration of MWCNT/S/PIN composite preparation	52
2.2	(a) Raman spectrum for MWCNT and functionalized MWCNT (b) TGA for MWCNT and functionalized MWCNT and (c) FTIR spectrum of functionalized MWCNT	53
2.3	(a) FTIR spectrum of the PIN and MWCNT/S/PIN (b) TGA of PIN, MWCNT-COOH, MWCNT/S/PIN, MWCNT/S and sulphur (c) XRD of sulphur, MWCNT/S/PIN and PIN	55
2.4	SEM images of (a) MWCNT/S, (b) MWCNT/S/PIN and (c-f) Elemental mapping of MWCNT/S/PIN	56
2.5	TEM images of (a-b) MWCNT/S, (c-d) MWCNT/S/PIN, EDS analysis of (e) MWCNT/S and (f) MWCNT/S/PIN	57
2.6	XPS for MWCNT/S/PIN (a) Survey scan, (b) C1s, (c) N1s, (d) O1s and (e) S2p	59
2.7	CV curves in the first six cycles of (a) MWCNT/S (b) MWCNT/S/PIN (c) GCD pattern of (a) MWCNT/S (b) MWCNT/S/PIN at 0.1C rate (e) Cycle performance and coulombic efficiency for MWCNT/S and MWCNT/S/PIN at	61

	0.1C rate and (f) Rate capability studies for MWCNT/S and MWCNT/S/PIN	
2.8	(a) Survey scan of cathode before and after cycling and (b) High resolution Li1s spectra of cathode after 100 cycles	62
2.9	Electrochemical impedance spectra of MWCNT/S and MWCNT/S/PIN before and after 100 cycles at 0.1C rate and its equivalent circuit	64
2.10	SEM images of (a) MWCNT/S/PIN before cycling (b) MWCNT/S/PIN after cycling (c) MWCNT/S before cycling and (d) MWCNT/S after cycling	65
3.1	Schematic illustration of the preparation of HMC and HMCS	73
3.2	(a) N ₂ adsorption-desorption isotherm and (b) DFT pore size distribution	75
3.3	(a) X-ray diffractograms and (b) Raman spectrum for HMCs	77
3.4	SEM images (a-b) HMC-1 and (c-d) HMC-2	78
3.5	(a) TEM image (b) EDS spectrum of HMC-1 and (c) TEM image (d) EDS spectrum of HMC-2 [inset showing the SAED pattern]	78
3.6	High resolution XPS of HMC-1 (a) Survey scan (b) C1s (c) N1s and (d) O1s	79
3.7	High resolution XPS of HMC-2 (a) Survey scan (b) C1s (c) N1s (d) O1s and (e) Schematic illustration of nitrogen and oxygen containing porous carbon	80
3.8	(a) XRD pattern for sulphur, HMCS (b) Raman spectra of sulphur and HMCS and (c) TGA of sulphur, HMC and HMCS	82
3.9	SEM images of (a-b) HMC-1S (c-d) HMC-2S	84
3.10	TEM image of (a) HMC-1, (b) EDS of HMC-1S TEM image of (c) HMC-2 and EDS of (d) HMC-2S	84
3.11	High resolution XPS of HMC-2S (a) survey scan (b) C1s (c) N1s (d) O1s and (e) S2p	85

3.12	CV of the (a) HMC-1S (b) HMC-2S, GCD curves of (c) HMC-1S (d) HMC-2S (e) Cycle performances & coulombic efficiency at 0.1C rate and (f) Rate capability studies at different C-rate	86
3.13	(a) EIS of HMC-1S and HMC-2S before and after cycling and (b) fitted equivalent circuit	89
3.14	SEM images (a) HMC-1S cathode film before cycling (b) HMC-1S cathode film after cycling (c) HMC-2S cathode film before cycling and (d) HMC-2S cathode film after cycling	89
3.15	(a) Survey scan and (b) High resolution Li1s spectrum of HMC-2S after 200 cycles	90
3.16	(a) CV curves and (b) GCD of HMCs at a scan rate of 10 mV s ⁻¹ and current density of 0.8 A g ⁻¹ (c) CV curves at different scan rates of HMC-2 and (d) GCD of HMC-2 at various current densities (e) A line chart of specific capacitances Vs current density and	92
3.17	EIS of HMC-1 and 2 before and after cycling at the open circuit potential in the frequency range from 100 mHz to 100 kHz. and (b) its equivalent circuit	94
3.18	Electrochemical characteristics of HMC-2 electrode as symmetrical supercapacitor using PVA+KOH gel electrolyte (a, b) CV and GCD curves of the symmetric cell (c) Specific capacitances of symmetric cell at various current densities; (d) Ragone plot of symmetrical cell and (e) Cycling stability at a current density of 0.6 A g ⁻¹ (inset shows GCD curves of initial 14 cycles)	96
3.19	Electrochemical characteristics of an HMC-2 electrode as symmetrical capacitor using PVA+ Na ₂ SO ₄ gel electrolytes (a) CV curves at scan rate of 50 mV s ⁻¹ within different voltage windows (b) GCD curves at current densities of 0.6–4 A g ⁻¹ (c) Specific capacitances of the symmetric cell at	98

	various current densities (d) Ragone plot of symmetrical cell and (e) Cycling stability at a current density of 0.6 A g^{-1} (inset shows a white LED powered by three symmetrical devices in series).	
4.1	Schematic illustration for the preparation of (a) HPC and (b) HPCS	106
4.2	FTIR spectra of HPCs at various temperature	108
4.3	(a) N_2 adsorption-desorption isotherm (b) DFT pore size distribution analysis, CO_2 adsorption at (c) 27°C (d) 0°C (e) X-ray diffractograms and (f) Raman spectrum for HPCs	111
4.4	(a) SEM image (b) and (c) TEM images of HPC- 600°C (d) SEM image (e) and (f) TEM images of HPC- 700°C (g) SEM image (h) and (i) TEM images of HPC- 800°C (j) SEM image (k) and (l) TEM images of HPC- 900°C [Inset: corresponding TEM - EDS spectrum]	112
4.5	XPS of HPC- 800°C (a) Survey scan, High resolution (b) $\text{C}1\text{s}$ (c) $\text{N}1\text{s}$ (d) $\text{O}1\text{s}$ (e) $\text{Fe}2\text{p}$ and (f) Schematic illustration of nitrogen, oxygen and iron containing porous carbon.	114
4.6	Elemental mapping of HPC- 800°C	115
4.7	CV curves of HPCs at different scan rates (a) 600°C (b) 700°C (c) 800°C (d) 900°C and (e) GCD curves of HPCs at a current density of 0.8 A g^{-1} ;	116
4.8	Electrochemical characteristics of HPC- 800°C based symmetrical capacitor with $1\text{M Na}_2\text{SO}_4$ electrolyte (a,b) CV and GCD curves of the symmetric cell at various scan rates and various current densities in aqueous electrolyte (c) specific capacitances of symmetric cell at various current densities (d) EIS analysis (e) Ragone plot of symmetrical cell and (f) Cycling stability at a current density of 0.5 A g^{-1}	118
4.9	Electrochemical characteristics of HPC- 800°C based symmetrical capacitor with 1M LiTFSI electrolyte (a,b) CV and GCD curves of the symmetric cell at various scan rates	120

	and various current densities in aqueous electrolyte (c) specific capacitances of symmetric cell at various current densities (d) EIS analysis at the open circuit potential in the frequency range from 0.1 to 10 K Hz (e) Ragone plot of symmetrical cell and (f) Cycling stability at a current density of 0.5 A g ⁻¹ (inset shows a white LED that was powered by two symmetrical devices in series with 1M LiTFSI electrolyte	
4.10	(a) XRD pattern for sulphur, HPCS (b) Raman spectra of sulphur and HPCS (c) N ₂ adsorption/desorption isotherm HPCS (b) [inset: Pore size distribution curve of HPCS] and (d) Thermogram of sulphur, HPC and HPCS	123
4.11	XPS for HPCS (a) Survey scan, High resolution (b) C1s (c) N1s (d) O1s (e) Fe2p and (d) S2p	125
4.12	(a-c) SEM of HPC-800 °C, (d) TEM of HPC-800 °C (e-g) SEM of HPCS and (h) TEM of HPCS	126
4.13	Elemental mapping of HPCS	126
4.14	(a) GCD curves of HPCS (b) Cyclic stability performances and coulombic efficiency of HPCS (c) CV of the HPCS after 200 cycles (d) Rate capability studies of the HPC at different C rate and (e) EIS analysis of the cell before discharge and after 200 cycles at the OCV [inset: equivalent circuit diagram]	127
4.15	(a) Control of the lithium polysulphide solution and (b) Lithium polysulphide mixed with PC after 15 minutes	130
4.16	(a) HPCS cathode film before analysis (b) HPCS cathode film after 200 charge discharge cycles (c) Survey scan and (d) High resolution Li1s spectrum of HPCS after 200 cycles	131
5.1	Schematic illustration of the preparation of PC and PCSC	137
5.2	(a) N ₂ adsorption/desorption isotherm and (b) Pore size distribution curve of PC [inset: enlarged at 0-10nm]	138

5.3	(a) X-ray diffractograms of sulfur, PC, and PCSCs (b) Raman spectra for PC and PCSCs [inset: Raman spectrum of sulphur]	139
5.4	(a) TGA of sulphur, PC and PCSCs (b) FTIR spectrum of PC and PCSCs	140
5.5	Survey scan of PC and PCSC (54%)	141
5.6	XPS for PC (a) C1s (b) O1s (c) N1s and (d) Schematic illustration of nitrogen and oxygen-containing porous carbon	142
5.7	XPS for PCSC (54%) (a) C1s (b) O1s (c) N1s and (d) S2p	144
5.8	SEM of (a) PC (b) and (c) are enlarged portion of (a) and (d) TEM image of PC (inset: SAED pattern)	145
5.9	SEM of (a) PCSC (54%) (b) PCSC (68%) (c) PCSC (73%) and (d) TEM image of PCSC (54%) (Inset: SAED pattern)	145
5.10	Elemental mapping of PC and PCSC (54%)	146
5.11	CV of the PCSCs (a) 54%, (b) 68% and (c) 73%	147
5.12	GCD curves of PCSCs (a) 54% (c) 68% and (c) 73%	147
5.13	Cyclic stability performances and coulombic efficiency of PCSCs (a) PCSCs and (b) Rate capability studies of the PCSCs at different C-rate	150
5.14	UV-vis absorption spectra of polysulphide solution with PC. Inset is the digital images of the polysulphide adsorption test [(a) Lithium polysulphide solution (b) Lithium polysulphide mixed with PC after 0 min. and (c) Lithium polysulphide mixed with PC after 10 min.]	151
5.15	EIS analysis of the electrodes (a) Before discharge and (b) After 100 cycles at the OCV [inset: equivalent circuit diagram]	153
6.1	Schematic illustration of the preparation of OPC and OPCSCs	159
6.2	(a) N ₂ adsorption/desorption isotherms of OPC and OPCSCs (b) Pore size distribution curves of OPC and OPCSCs [inset: enlarged portion of pore size distribution] (c) XRD pattern	161

	for S and OPCSCs (d) Raman spectra of OPC, OPCSCs [inset: Raman spectrum of sulphur] and (e) TGA of OPC, OPCSCs and S	
6.3	XPS analysis of OPC (a) survey scan (b) C1s (c) N1s and (d) O1s	163
6.4	XPS analysis of OPCSC (73%) (a) survey scan (b) C1s (c) N1s (d) O1s and (e) S2p	164
6.5	SEM images (a-c) OPC and (d-f) OPCSC (73%)	165
6.6	Images of (a) TEM (b) EDS analysis of OPC and (c) TEM (d) EDS analysis of OPCSC (73%) [inset showing the corresponding SAED pattern]	165
6.7	CV of the OPCSCs (a) 61% and (b) 73%, GCD curves of OPCSCs (c) 61% (d) 73% (e) Cyclic stability performances and coulombic efficiency and (f) Rate capability studies at different C-rate	167
6.8	SEM Images of PP (a) Lower magnification and (b) Higher magnification [inset showing digital photograph]	168
6.9	Schematic illustration of LSB and polysulphide shuttling (a) with bare separator and (b) With separator coating	169
6.10	Characterization of MWCNT and HMC-1 (a) N ₂ adsorption/desorption isotherms (b) Pore size distribution curves [inset: enlarged portion of pore size distribution] (c) XRD pattern (d) Raman spectra and (e) XPS survey scan analysis	170
6.11	Images of (a) SEM, (b) TEM (c) EDS analysis of MWCNT and (d) SEM, (e) TEM (f) EDS analysis of HMC-1	171
6.12	Cross sectional Images of SEM images (a-b) MWCNT and (c-d) HMC-1 [inset a and c shows the digital photographs of the modified separator] [inset b and d demonstration of the flexibility and mechanical strength]	171
6.13	CV of the OPCSC-73% with separator coating (a) MWCNT (b) HMC-1, GCD curves of OPCSC-73% with separator	174

	coating (c) MWCNT (d) HMC-1 (e) Cyclic stability performances and coulombic efficiency and (f) Rate capability studies at different C-rate	
6.14	Electrochemical performances of OPCSCs, MWCNT, HMC separator coating (a) EIS analysis of the electrodes before discharge and (b) after 100 cycles at the OCV	177
6.15	SEM of OPCSC (73%) cathode film (a) before cycling (b) With bare separator after 100 cycles (c) With MWCNT modified separator after 100 cycles and (d) With HMC-1 modified separator after 100 cycles	179
6.16	Digital images of the polysulphide adsorption test (a) Lithium polysulphide solution (b) Lithium polysulphide mixed with MWCNT after 15min and (c) Lithium polysulphide mixed with HMC after 15 min	180
6.17	(a) The survey scan analysis of HMC-1 coated separator before and after 100 charge-discharge cycles and (b) High-resolution Li 1s spectrum of coated separator after 100 cycles	181
7.1	Schematic illustration of the preparation of HC and HCS	187
7.2	(a) N ₂ adsorption/desorption isotherms of HC and HCS (b) Pore size distribution curves of HC (c) XRD pattern for S and HCSs (d) Raman spectra of HC, HCSs [inset: Raman spectrum of sulphur] and (e) TGA of HC, HCSs and S	189
7.3	SEM Images of (a-b) HC and (c-d) HCS (80%)	190
7.4	TEM Images of (a) HC and (b) EDS analysis of HC: (c) HCS (80%) and EDS analysis	190
7.5	Elemental mapping of (a) HC and (b) HCS (80%)	191
7.6	XPS analysis of HC (a) Survey scan (b) C1s (c) N1s (d) O1s and (e) Si 2p	193
7.7	XPS analysis of HCS (80%) (a) Survey scan (b) C1s (c) N1s (d) O1s (e) Si 2p and (f) S 2p	195
7.8	GCD curves of HCSs (a) 70% (b) 80% and CV of the HCSs (c) 70% (d) 80%	197

7.9	(a) Cyclic stability performances and coulombic efficiency (b) Rate capability studies at different C-rate (c) EIS analysis of the electrodes at the OCV of HCSs before cycling and (d) EIS analysis of the electrodes at the OCV of HCSs after cycling [inset: equivalent circuit]	199
7.10	Schematic illustration of a working mechanism (a) Cathode film and (b) With interlayer on the cathode	201
7.11	Cross sectional image of (a) HCS (80%) cathode film and (b) HCS (80%)-HC (interlayer) cathode film	201
7.12	(a) GCD curves at 0.1C rate (b) CV (c) Cyclic stability performances and coulombic efficiency (d) Rate capability studies at different C-rate and (e) EIS analysis of the electrodes at the OCV of HCS (80%)-HC coated cathode before cycling and (f) EIS analysis of the electrodes at the OCV of HCS (80%)-HC coated cathode before cycling [inset: corresponding equivalent circuit]	203
7.13	Digital images of the polysulphide adsorption test (a) Lithium polysulphide solution and (b) Lithium polysulphide mixed with HC after 10 min.	205
7.14	XPS analysis of HCS (80%) cathode film after 200 cycles (a) Survey scan analysis and (b) High resolution Li 1s	205
7.15	Cathode surfaces of (a) HCS film before cycling (b) HCS film after 200 cycling (c) HC coated HCS cathode films before cycling and (d) HC coated HCS cathode films after 200 cycling	206

ABBREVIATIONS

3D	Three-dimensional
a.u.	Arbitrary unit
AN	Acetonitrile
BET	Brunauer, Emmett, and Teller
BMIMBF ₄	1-butyl-3-methylimidazolium tetrafluoroborate
CNFs	Carbon nanofibers
CV	Cyclic voltammetry
DFT	Density functional theory
DME	1,2-dimethoxy ethane
DOL	1,3-dioxolane
EC/PC	Ethylene carbonate/propylene carbonate
EDLC	Electrical double layer capacitor
EDS	Energy dispersive spectroscopy
EIS	Electrochemical impedance spectroscopy
EMITFSI	(1-Ethyl-3-methylimidazolium bis(trifluoromethylsulfonyl)imide)
FTIR	Fourier transform infrared spectroscopy
GCD	Galvanostatic charge-discharge
GO	Graphene oxide
HC	Honeycomb derived carbon
HCS	Honeycomb derived carbon-sulphur composite
HMC-1	Heteroatom doped microporous carbon (1 h pyrolysis time)
HMC-1S	HMC-1-sulphur composite
HMC-2	Heteroatom doped micro/mesoporous carbon (2 h pyrolysis time)
HMC-2S	HMC-2-sulphur composite
HPC	Hierarchically porous carbontube
HPCS	Hierarchically porous carbontube-sulphur composite
ICP-AES	Inductive coupled plasma-atomic emission spectrometry
IUPAC	International union of pure and applied chemistry

LED	Light emitting diode
LIB	Lithium ion battery
LiClO ₄	lithium perchlorate
LiTFSI	lithium bis(trifluoromethane)sulphonimide
LPS	Lithium polysulphide
LSBs	Lithium-sulphur battery
MOF	Metal-organic framework
MWCNT	Multiwalled carbon nanotube
MWCNT/S	Binary composite
MWCNT/S/PIN	Ternary composite
NMP	N-methyl pyrrolidone
OPC	Orange peel derived carbon
OPCSC	Orange peel derived carbon-sulphur composite
PAA	Polyacrylicacid
PAH	Polyallyl amine hydrochloric acid
PAN	Polyacrylonitrile
PANI	Polyaniline
PC	Pinecone derived carbon
PCSC	Pinecone derived carbon-sulphur composite
PE	Polyethylene
PEG	Polyethylene glycol
PEO	Polyethylene oxide
PIN	Polyindole
PP	Polypropylene
PPy	Polypyrrole
PS	Polysulphide
Pt	Platinum
PTh	Polythiophene
PVA	Poly-(vinyl alcohol)
PVDF	Polyvinylidene fluoride
PVP	Polyvinylpyrrolidone
rGO	Reduced graphene oxide

SAED	Selective area diffraction
SC	Supercapacitor
SDS	Sodium dodecyl sulphate
SEM	Scanning electron microscopy
TEABF ₄	tetraethylammonium tetrafluoroborate
TEM	Transmission electron microscopy
TGA	Thermogravimetric analysis
UV	Ultra-violet
Wt. %	Weight percentage
XPS	X-ray photoelectron spectroscopy
XRD	X-ray diffraction

SYMBOLS AND UNITS

Symbol	Name	Unit
T	Temperature	°C
t	Time	s/h
V	Voltage	V
I	Current	A
λ	Wavelength	nm
	Wavenumber	cm ⁻¹
Θ	Angle of diffraction	°/degree
m	Active material weight	g
P	Equilibrium pressure	Pa
P _o	Saturation pressure	Pa
C	Specific capacitance	F g ⁻¹
%	Percentage	
	Specific capacity	mA h g ⁻¹
C-rate	Charge/discharge rate	mA h g ⁻¹
	Specific energy	W h kg ⁻¹
	Specific power	W kg ⁻¹
Z	Impedance	Ω /ohm
Z'	Real part of impedance	Ω /ohm
Z''	Imaginary part of impedance	Ω /ohm
W	Warburg parameter	Ω s ^{-1/2}
R _s	Resistance of the electrolyte	Ω
R _{ct}	Charge transfer resistance	Ω
CPE	Constant phase element	Ω^{-1}
C _{dl}	Electrical double layer capacitance	F
Y ₀	Admittance	Ω^{-1} s ^{1/2}

CHAPTER 1

INTRODUCTION

Development of new electronic devices and hybrid electric vehicles need an improved energy storage system, in terms of energy density, durability, flexibility, safety and costs. Thus, it is necessary to explore and develop new materials that can fulfill and satisfy current and future energy needs. Lithium-sulphur batteries (LSBs) and supercapacitors (SCs) have received more attention due to their high energy and power densities compared to conventional energy storage devices such as lithium-ion battery (LIB). In this chapter, a brief summary of the state of art is presented with more consideration on the aspects related to strategies to enhance cycling stability of LSB and carbon based electrodes for electrical double layer capacitor (EDLC). Further, the objectives and outline of thesis focussed on existing challenges and the future research directions are also described.

1.1 Introduction

The technology development in the 21 st century leads to energy and environmental issues. The energy economy depends upon the fossil fuel, consequently, it's reserves are depleted much faster than the new formations. Increase in consumption of fossil fuel directly linked to environmental degradation due to the emission of pollutants (Lopes et al., 2012). Based on the available literature, it is evident that the electrochemical energy storage is the most important technology when uninterrupted energy or power supply is required. Rapid development in the portable devices, electronics, computers and electric vehicles would not be possible without efficient energy storage devices. Electrochemical energy storage is the dominant technology in the electrified fields. Batteries and supercapacitors (SC) are considered as two types of the most prospective electrochemical energy storage devices with a number of unique advantages and wide potential applications (Zuo et al., 2017; Dunn et al., 2011; Bruce et al., 2012). Electrode materials are the core of any electrochemical device, which quantify the energy and power in the system.

An electrochemical cell is a device that converts chemical energy into electrical energy and vice versa (Brett 2009). It consists of the assembly of the cathode and anode electrodes, which is separated by a porous layer having both

ionic conducting and an electrical insulating properties. The operation of a cell is based on the difference between the chemical potential of an active material between the two electrodes. There are several parameters need to be discuss for monitoring the electrochemical performance and operating conditions of an electrochemical cell (Winterand Brodd, 2004).

The specific capacity (mA h g^{-1}) of a cell is defined as the total amount of current available when the battery is fully discharged or total ampere-hours available when the battery is discharged at a certain discharge current normalized by the mass of active material.

$$\text{Specific capacity} = \frac{nF}{M} \quad (1.1)$$

Where 'n' is the number of electrons involved in the redox reaction, 'F' is the Faraday constant (96500 C mol^{-1}) and 'M' is the molecular mass of the active material (g mol^{-1}).

C-rate, the discharge current is expressed in C rate. It is a measure of the rate at which a battery is discharged relative to its maximum capacity.

The gravimetric and volumetric energy density (W h kg^{-1} or W h L^{-1}) are the values of the amount of energy stored in the material per mass/volume or the total Watt-hours available when the battery is discharged at a certain discharge current, normalized by the mass of active material and by the volume, respectively.

The columbic efficiency refers to the ratio of discharged capacity over the preceding charged capacity. It indicates the reversibility of the redox process.

1.2 Lithium ion Battery

According to the recent literatures, lithium-ion batteries (LIB), are currently becoming the dominant technology for powering portable devices, mostly due to their capability of delivering electrical energy with high power and energy densities (Figure 1.1) (Xin et al., 2012).

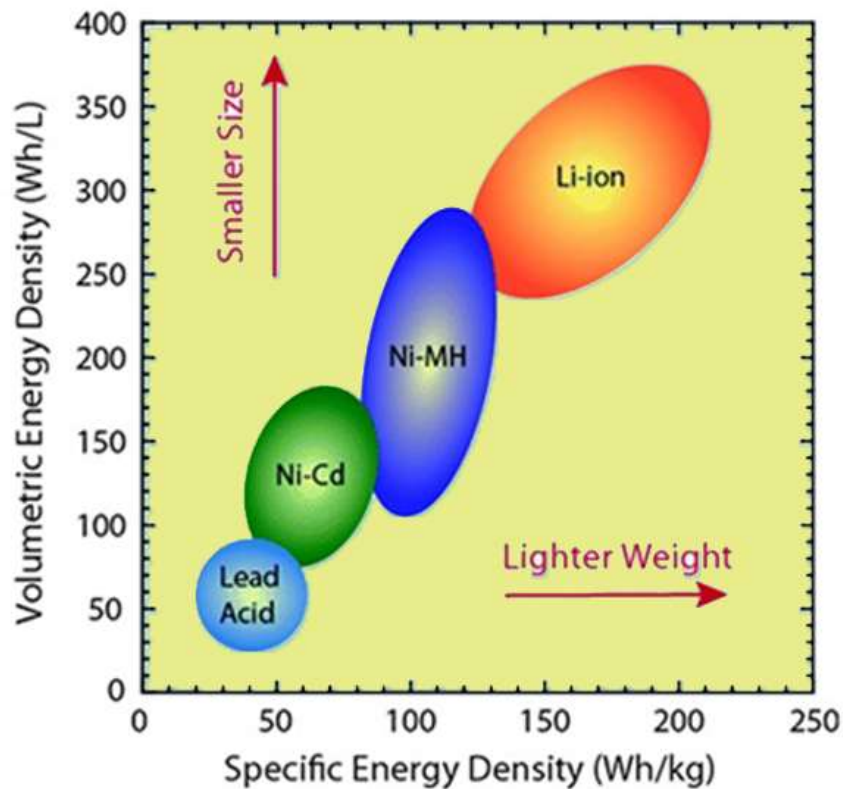


Figure 1.1. Comparison diagram of rechargeable battery technologies

A conventional LIB consists of four parts: anode material, cathode material, electrolyte and separator. Here the anode for LIB is graphite, cathode as lithium transition metal oxide (E.g.: LiCoO_2 , LiMnO_2 , LiFePO_4 and LiNiO_2), separator is a fine porous polymer film and the electrolyte is Li containing salt in carbonate based organic solvents (Goodenough and Park, 2013). The LIB works on the basis of the intercalation mechanism. During the charging process, the Li ions move from the metal oxide and intercalate into the graphitic anode. The discharging step involves the deintercalation from the anode and intercalation into the cathode (Figure 1.2). For example, the representative reaction takes place during the charging and discharging process is as follows when using as lithium cobalt oxide as cathode and graphite as the anode (Gopalakrishnan et al., 2017).



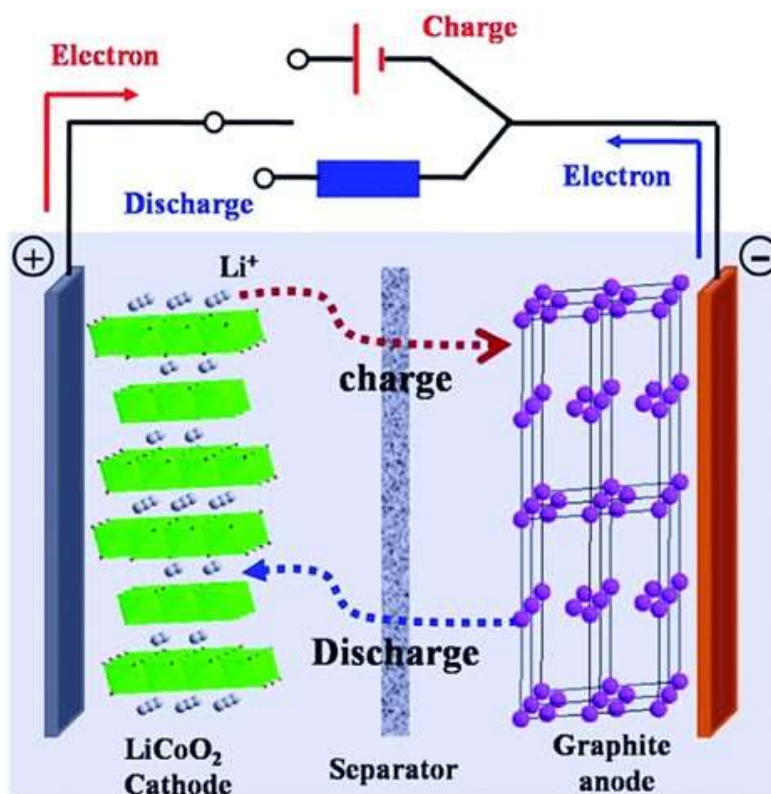


Figure 1.2. Schematic diagram of LIB (Gopalakrishnan et al., 2017)

The traditional LIB uses the intercalation based cathode materials such as metal oxides, phosphates and vanadate gives the maximum energy density of ~ 200 – 400 W h kg^{-1} (274 mA h g^{-1}), while the anode materials gives the specific capacity of $\sim 372 \text{ mA h g}^{-1}$ (Scrosati, 1992). Due to their lightweight, high open circuit voltage, high capacity, and non-memory effect, LIBs have been commercialized since 1990s by Sony corporation and dominated in the market for portable electronic devices (Aricò et al., 2005). However, the energy and specific capacity values are not sufficient for satisfying the ever increasing energy demand. The commonly used cathode materials are quite expensive and low rate capability is observed at higher current rates. So, new cathode alternatives are required for the better performance of the future LIBs.

1.3 Lithium-Sulphur Battery

Other possibilities for energy storage in Li-ion cell chemistries are alloying and conversion reactions besides the intercalation mechanism. This reaction occurs

in a manner that two materials react to form compounds with new properties. For example, in the lithium-sulphur battery (LSB), lithium and sulphur react to form Li_2S . Sulphur is an abundant, nontoxic, and environmentally benign, possessing advantages compared to the limited and pollution-yielding fuel oil (Bruce et al., 2011). More importantly, its ultra-high theoretical capacity (1675 mA h g^{-1}) and theoretical energy density (2600 W h kg^{-1}) distinguish it from other cathode materials (Manthiram et al., 2014; Song et al., 2013). The concept of elemental sulphur as a positive electrode material was first introduced by Helbert and Ulam in 1962 and the first demonstration of LSB was presented in the late 1960s. In a Li-S cell, the overall reaction during discharge process can be described as



1.4 Working Mechanism of Li-S Battery

In LSB, Li metal acts as an anode, sulphur act as cathode, lithium bis(trifluoromethane)sulphonimide (LiTFSI) in ether based solvents used as electrolyte and a polypropylene (PP) membrane used as separator (Figure 1.3). The reaction between metallic lithium and elemental sulphur is a multistep process (Arias et al., 2018). During the discharge process the octaatomic cyclic sulphur, S_8 ring broken and it will form long chain polysulphide (PS) chain. The reduction continued till the formation of lower order PSs and finally the lowest end discharge product Li_2S_2 or Li_2S . During the recharging step, the whole reaction will occur in a reversible manner. During discharging process, the Li ions are stripped from the anode, moves towards the cathode and form lithium PSs. As a result of the complete discharge, the Li_2S is formed. During the recharge, the Li ions are stripped back to the anode. During the continuous charge-discharge cycle, PS species shuttle between cathode and anode (Figure 1.4) (Wild et al., 2015). The multistep process are given below.



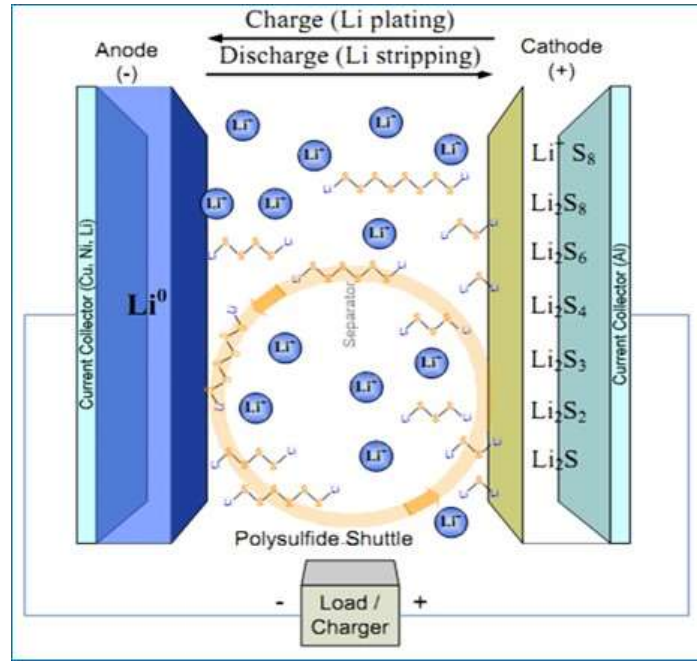


Figure 1.3. Schematic diagram of LSB (Mikhaylik et al., 2010)

In the first three steps, the reaction occurs in a voltage range of 2.2-2.4 V, and the lithium polysulfides (LPSs) (Li_2S_x , $4 < x \leq 8$) are soluble in the electrolyte. The last two-step process occurs below the 2.1V (Li_2S_x , $1 < x \leq 3$) and it will precipitates on the cathode and generally it is insoluble in the electrolyte. The first 4 step reactions are kinetically faster, while the last step is a slow process, which will impede the battery performance (Ogoke et al., 2017). The discharge curve of LSBs shows two plateaus, the first plateau lies in the voltage range of 2.2-2.4 V and corresponds to the conversion of elemental sulphur to high valence state PS ions, S_{n-2} where $n=8, 7$ and 6 . The second plateau lies below 2.1V, which corresponds to the conversion of low valence state of PS ions, $n=4$ and 3 (Figure 1.4).

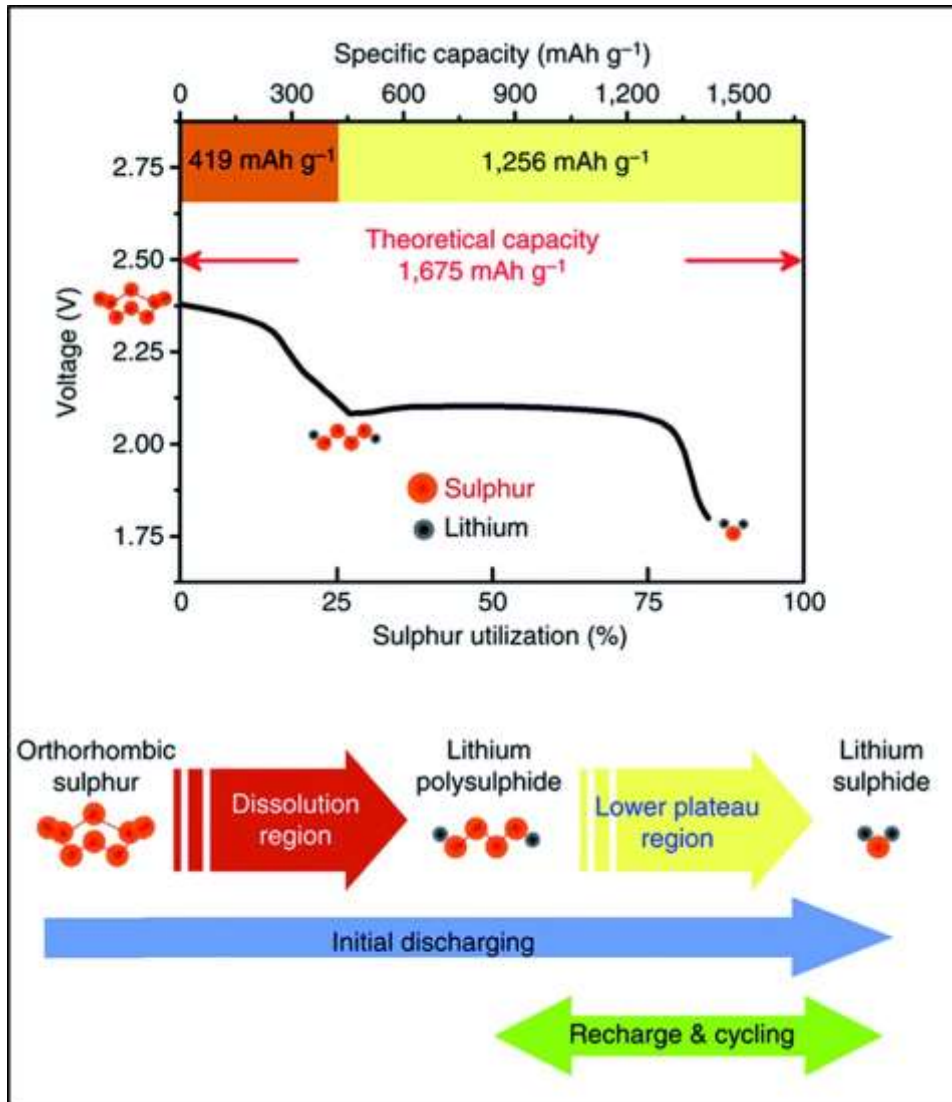


Figure 1.4. Electrochemical voltage profile for LSB and sulphur bonding chemistry during charge-discharge process (Su et al., 2013)

1.5 Challenges and Drawbacks of Li-S Battery

The following are the few challenges associated with LSB, which are really obstruct its commercial values (Aurbach et al., 2009; Mikhaylik et al., 2010; D.-W. Wang et al., 2013).

(1) The inherent insulating nature of sulphur (electrical conductivity is 5×10^{-30} S cm^{-1}) (D.-W. Wang et al., 2013) and lowest end discharge product, Li_2S , which restrict the movement of ions and electrons. Sulphur is soluble in most of the

organic solvents used in the electrolyte, which leads to self-discharge and OCV potential decrease and lowered discharge capacity after storage.

(2) The insoluble lower order discharge products like Li_2S_2 and Li_2S deposit on the surfaces of the conductive framework leads to progressive capacity fading, and reduce the effective active surface area to perform the electrochemical reactions.

(3) Intermediate PSs formed during discharging are soluble in the most of the organic electrolyte, which can easily pass through the separator to the anode and it will react (get reduced) to form low-order PSs on the surface of the Li anode, attributed to the passivation of anode surface. These short chain PSs can then diffuse back to the cathode during the reverse process where they can be oxidized back to high-order species. The process can be further repeated, resulting in prolonged charge-discharge process. This mechanism of LSB is called “*shuttle phenomenon*”. As a result, the charging process cannot complete, further lowers the coulombic efficiency considerably. Presence of ‘shuttle mechanism’ results in the deposition of solid species (Li_2S) on the metallic lithium surface, leading to a capacity fade because of the irreversible active material losses.

(4) Volume changes of sulphur during the cycling process bring the collapse of the electrode structures.

(5) The dendrites growth can result in micro short-circuits during battery charging, which incites cell death and safety problems. Even though few studies reported that the reactivity of PSs with lithium restrain the dendrites growth, it is an unsolved issue in LSBs.

The above mentioned processes create a lot of serious problems in LSBs, including the Li deterioration, unstable solid–electrolyte interface, irreversible loss of active material and increases in the interfacial resistance between the anode and electrolyte. This shuttle phenomenon leads to low coulombic efficiency, rapid capacity waning, low rate performance and short cycle life (Yibo He, Chang, et al., 2018). Thus various approaches and methods are reported in the literature to tackle the PS issues and degradation of battery performances.

1.6 Effective Strategies Adopted to improve the Cycle Life of Li-S Battery

There are various strategies adopted in the literature to improve the electrochemical performance of LSB. They are

- (1) Design and development of new sulphur host/ modification of cathode film for trapping PS by physical adsorption and chemical binding.
- (2) Modification of separator to immobilize the PS on cathodic region.
- (3) Protection of Li metal anode from the passivation and lithium dendrite growth.
- (4) Investigation of new electrolytes/electrolyte composition to restrict the dissolution of PSs in the electrolyte.

1.6.1 Design of cathode architecture

One of the most important aspect for improving the performance of LSB is the fabrication of novel cathode materials with new sulphur composite for trapping the PSs. Among the massive host materials for sulphur, carbon materials like porous carbon, heteroatom doped porous carbon, graphene, carbon nanofiber, carbon nanotubes, conducting polymers, metal oxides and the combination of above materials are commonly used (R. Chen et al., 2015; G. Xu, B. Ding, J. Pan, et al., 2014). This thesis discuss on carbon-sulphur composites as cathodes for LSBs. Hence the literature review mainly focussed on carbon-sulphur composite cathode materials and strategies to restrict the PSs in the cathodic region.

1.6.1.1 Carbon materials

The interesting structural advantageous like high inertness, conductivity, high pore volume, large exposed surface area, different dimensions (0-3 dimensions), natural abundance, low cost which make the carbon materials as one of the important hosts for sulphur and widely used as cathode material for LSB applications (Manthiram et al., 2014).

Carbon nanomaterials

Carbon nanomaterials are the materials which have at least one dimension in the nanoscale. Carbon nanotube, graphene, carbon nanofiber and carbon nanoparticles/quantum dots belongs to this category (J. Liang et al., 2016). Since from the discovery of carbon nanotube in 1991, it is used for a wide variety of applications in the field of electronics. The multiwalled carbon nanotube (MWCNT) is used as cathode material for LSB application without binder and current collector which reduces the cost of the electrode manufacturing. Here, 60% sulphur was deposited on the walls of the carbon and obtained an initial discharge capacity of 1352 mA h g⁻¹ at 1C. The high conductivity of MWCNT helped to improve the active material utilization and the electrochemical performance (Su et al., 2012). Binder free high density carbon nanotube forest was able to enhance the interfacial adsorption, confine the PS species and accommodate volume changes of sulphur and obtained a stable discharge capacity of 812 mA h g⁻¹ after 200 cycles with 0.054% capacity retention (Xi et al., 2015). High sulphur content (85%) of carbon nanotube/sulphur composite was prepared by ball milling followed via heating in an argon atmosphere. Due to high electrical conductivity and stable structure of the composite, active material utilization increased to 76% (J.-z. Chen et al., 2014). A disordered carbon nanotube with sulphur impregnated via vapour infusion method, was used as cathode material and obtained 96% coulombic efficiency (Juchen Guo et al., 2011). Vertical aligned carbon nanotube/sulphur composite was prepared without binder with 95% sulphur content. The sulphur loading on the cathode was 20 mg cm⁻². It delivered the capacity of 900 mA h g⁻¹ at the current density of 0.64 mA cm⁻² (Hagen et al., 2012; Hagen et al., 2013; McDonough and Gogotsi, 2013). Carbon onion with several concentric graphitic spheres was prepared and sulphur was deposited on the wall of the carbon onion by melt diffusion. It delivered a reversible capacity of 700 mA h g⁻¹ at 0.1C rate (Choudhury et al., 2017).

Carbon nanofibers (CNFs) are one-dimensional material, similar to carbon nanotube with larger diameter. Hollow carbon nanofiber encapsulated with sulphur was used for PS trapping and exhibited 730 mA h g⁻¹ at 0.2C rate after 150 cycles

(Zheng et al., 2011). Hierarchical porous carbon embedded with 80% sulphur was used as cathode, the porosity of the carbon fiber helped efficient trapping of PS and to inhibit shuttle effect. This composite delivered $601.5 \text{ mA h g}^{-1}$ at 2C rate after 350 cycles (W. Kang et al., 2018). Binder-free sulphur distributed carbon nanofiber with 65% sulphur obtained a stable capacity $\geq 700 \text{ mA h g}^{-1}$ in LSB cathode application (K. Fu et al., 2014). Mesoporous carbon nanofibers were successfully prepared by electrospinning method as host for sulphur, with 74.35% sulphur exhibited a stable capacity of 721 mA h g^{-1} after 500 cycles at 1C rate (Zhenheng Cao et al., 2018). Hollow carbon nanofiber sulphur composite prepared via mixed solvent process, 60.8% sulphur loading was achieved. Due to these hollow structures which alleviate the PS migration and obtained a stable capacity of 600 mA h g^{-1} after 100 cycles at the 1C rate (Q. Li et al., 2014)

A single layer of graphite is termed as graphene and 2D carbon nanomaterial. Its excellent properties made them as superior candidate for electrochemical applications. Sulphur/graphene sheet was prepared by the thermal reduction between the sulphur and graphene oxide (GO). Graphene acts as a conducting and adsorbing agent, obtained a reversible capacity of $\geq 670 \text{ mA h g}^{-1}$ after 80 cycles (Feifei et al., 2012). Graphene/sulphur composite was synthesized by heating the mixture of elemental sulphur and graphene sheet, with 17.6% sulphur loading obtained 96.35% sulphur utilization (J.-Z. Wang et al., 2011). Unstacked double layer templated graphene was prepared via chemical vapour deposition method. Sulphur composite was prepared by the melt diffusion method and displayed a stable capacity of 380 mA h g^{-1} after 1000 cycles (M.-Q. Zhao et al., 2014). Dielectric barrier discharge plasma and high energy ball milling were used to fabricate ultrafine sulphur nanoparticle, which was anchored on in-situ exfoliated graphene with 69.2% sulphur content. Graphene offered sufficient sites for capturing the PSs. It delivered a stable capacity of $618.6 \text{ mA h g}^{-1}$ after 500 cycles at the 0.1C rate (Z. Ma et al., 2017). Graphene nanoplatelets edge functionalized with sulphur were prepared by ball milling process, obtained a high reversible capacity of $966.1 \text{ mA h g}^{-1}$ at 2 C with a low capacity decay rate of 0.099% after 500 cycles (J. Xu et al., 2014). Binder and current collector free, flexible graphene sulphur paper was used with 67% sulphur loading obtained a reversible capacity of

600 mA h g⁻¹ after 100 cycles with 83% capacity retention (J. Jin et al., 2013). A freestanding sulphur-graphene composite delivered an initial capacity of 1393 mA h g⁻¹ at 0.1 C (X. Huang et al., 2013). A free standing binder sulphur reduced graphene oxide (rGO) was prepared by the freeze-drying method with 67% sulphur, with high areal capacity and good sulphur utilization (Nitze et al., 2016). Graphene-Sulphur nanocrystal composite with 63% sulphur loading exhibited a stable capacity of ~700 mA h g⁻¹ after 50 cycles at a current density of 300 mA g⁻¹ (G. Zhou et al., 2013).

Porous Carbon materials

Porous carbon is another class of carbon material different from the carbon nanomaterials, generally, they are amorphous in nature with low degree of graphitization with tunable properties. It is well known that porous carbon materials are capable for adsorbing PS, and enhancing the sulphur utilization due to its enhanced surface area, pore volume and conductivity. According to their pore size they can be divided into microporous carbon (< 2 nm), mesoporous carbon (2-50 nm) and macroporous carbon (> 50 nm). The pores can be generated spontaneously during the carbonization, physical or chemical activation and by the soft/hard templating method (Zan Gao et al., 2017). The carbon precursor from various sources like biomass residue, the animal residue can be converted into high surface area nanostructured carbon by facile methods (Gao et al., 2017; C. Zhang et al., 2016). Pyrolysis and hydrothermal carbonization are the methods used for the preparation of porous carbon. The carbon materials obtained using these methods have low surface area and porosity. But high surface area and porosity are the required parameters for better electrochemical performance of LSB. Pyrolysis of template embedded carbon source followed by template removal yield, carbon with high surface area compared to the above methods and obtained a well-developed uniform pore size distribution (Ogoke et al., 2017). To tune, the morphology and structure of carbon material physical/chemical activation methods were used. (Contreras et al., 2010; Kwiatkowski and Broniek, 2017). Commonly used physical activators are O₂, CO₂ or steam and chemical activators are KOH, H₃PO₄ or ZnCl₂ (Demiral et al., 2011; J. I. Hayashi et al., 2000). ZnCl₂ is the widely used activator owing to its non-corrosive nature, better carbon yield, the high specific surface area

carbon with excellent adsorption property and the hierarchical porosity (J. I. Hayashi et al., 2000). The selection of precursor, activation method and temperature for carbonization are significantly affect the surface area, pore size, heteroatom doping which in turn amend the electrochemical performance of the prepared porous carbon material.

Porous carbon materials are really helpful to accommodate high sulphur loading and house the volume changes of sulphur during the charge-discharge process. This porous carbon can act as a physical barrier for sulphur and PS species, at the same time it can provide the access to liquid electrolytes and porous carbon can adsorb the PS from the electrolyte (D.-W. Wang et al., 2013).

A breakthrough progress have been first made by S/CMK-3 (highly ordered mesoporous carbon) (sucrose and SBA-15) composite with 70% sulphur loading exhibited an initial capacity of 1000 mA h g^{-1} with a coulombic efficiency of 99.94% (Ji et al., 2009). Inspired by this report, a bimodal mesoporous carbon/S composite (phenol and triblock copolymer) with 50% sulphur was investigated and obtained a reversible capacity of 550 mA h g^{-1} after 100 cycles at the 1C rate. Here, small mesopores formed during the preparation process, which act as PS reservoir and improved its performances (G. He et al., 2011). A high surface area of $2102 \text{ m}^2 \text{ g}^{-1}$ ordered mesoporous carbon was used for sulphur host, 60% sulphur loading displayed 70% sulphur utilization, high rate capability at 6C and long electrochemical stability for 400 cycles (S.-R. Chen et al., 2011). Unique hollow carbon nanosphere/sulphur composite exhibited stable capacity of 626 mA h g^{-1} at 0.2C after 200 cycles (Shao-Zhong et al., 2018). Sucrose derived microporous carbon was used as a host for sulphur 600 mA h g^{-1} after 4020 cycles with 0.0014% capacity degradation (Yunhua et al., 2015). Hierarchically porous carbon derived from soluble starch using $\text{Mg}(\text{OH})_2$ as template was prepared. Carbon with 84% sulphur exhibited an initial discharge capacity of 1249 mA h g^{-1} and a reversible capacity of 562 mA h g^{-1} after 100 cycles at high current density of 1675 mA g^{-1} (G. Xu, B. Ding, P. Nie, et al., 2014). A high surface area bimodal carbon was prepared by soft template method followed by KOH activation to host sulphur, obtained a high initial discharge capacity of 1584 mA h g^{-1} at a current density of

2.5 A g⁻¹. This bimodal structured carbon provided a synergetic effect of meso and microporosity to accommodate PSs in the cathode region (C. Liang et al., 2009). Sulphur-carbon sphere composite with 42% sulphur loading exhibited a reversible capacity of 650 mA h g⁻¹ after 500 cycles at a current density of 400 mA g⁻¹ (B. Zhang et al., 2010). Double-shelled hollow carbon sphere used for confining the sulphur and exhibited a stable capacity of 410 mA h g⁻¹ at 0.3C after 100 cycles (Chaofeng et al., 2012). Microporous carbon sulphur composite resulted in 616 mA h g⁻¹ at 1C after 600 cycles (Lei et al., 2017). Acetylene black is a well-known conductive agent, used for the preparation of sulphur composite and showed 500 mA h g⁻¹ after 50 cycles (B. Zhang et al., 2009; Yongzheng Zhang et al., 2018). Here sulphur was deposited on the surface of the nanopores of conductive black. 52% sulphur loaded composite showed a reversible capacity of 1012 mA h g⁻¹ after 100 cycles with a capacity retention of 75.1% at a 0.1C rate (W. G. Wang et al., 2014). An ultra-lightweight 3-D sulphur-few layered graphene foam composite was developed without binder and conducting additive with 52% sulphur loading. It exhibited a stable capacity of 300 mA h g⁻¹ after 400 cycles even at a current density of 3200 mA g⁻¹ (Xi et al., 2014). A high surface area of 2600 m² g⁻¹ was developed from zinc citrate source and used as sulphur host, 950 mA h g⁻¹ after 100 cycles even with a low amount of electrolyte (6.8 µl mg⁻¹) (Strubel et al., 2016). Sulphur infiltrated porous carbon microspheres from sucrose exhibited 904 mA h g⁻¹ after 100 cycles at the the 1C rate (C. Zhao et al., 2014).

Metal-organic framework (MOF) provided carbon materials when it was heated in an inert atmosphere due to the presence of organic moieties in the MOF, owing to its unique morphology, large surface area and high pore volume. MOF derived carbon was prepared as an ideal host for the sulphur due to the hierarchical porosity of the carbon material gives an easy pathway for the Li⁺ ion transportation. The-high pore volume can refuse PS dissolution into the electrolyte and accommodate volume changes of sulphur during the charge-discharge process (X. Qian et al., 2016; G. Xu et al., 2013). Carbon derived from zinc fumarate with 55% sulphur showed a capacity of 592 mA h g⁻¹ after 40 cycles. Both meso and micropores helps to hold sulphur and to improve the active material utilization (Xi et al., 2013).

Carbon nanorod shaped Zn-MOF with 68% sulphur exhibited 700 mA h g^{-1} after 200 cycles at a current rate of 0.5C. This conductive carbon nanorod improved the electron transport and the pores generated during the carbonization is highly helpful for electrolyte infiltration and to encapsulate the sulphur (X. Qian et al., 2016). MOF-5 derived hierarchical porous nanoplates (54% sulphur) showed 730 mA h g^{-1} of reversible capacity after 50 cycles at 0.5C rate (G. Xu et al., 2013). French fries like hierarchical porous carbon was derived from Al-MOF and used as sulphur host. It displayed a capacity retention of 68% at 0.5 C after 200 cycles (Xiaofei Yang et al., 2015). Amylose derived carbon-sulphur hybrid exhibited 798 mA h g^{-1} after 200 cycles at the 0.1C rate (X. Li et al., 2017). A low-cost ultra microporous carbon from macadamia nutshell was used as sulphur host and provided a reversible capacity of 1254 mA h g^{-1} after 100 cycles at 0.1C rate with 80% capacity retention (J. Han et al., 2018).

Biomass is used as an energy source for long years ago as wood and charcoal. Scientific progress creates new methods to excavation energy and chemicals from biomass. The bio-derived porous carbons are more interested due to its low cost, ease of availability and good product yield. The produced carbon are green, cheap and energy efficient (Imtiaz et al., 2016). Nanostructured porous carbon derived from biomass used as sulphur host for various LSB (Imtiaz et al., 2016; J. Li et al., 2014).

Bamboo, a natural biomass, was converted into the hierarchical porous structure using KOH activation followed by carbonization. The carbon-sulphur composite (50% sulphur) displayed an initial discharge capacity of 1262 mA h g^{-1} at a current density of 160 mA g^{-1} (Gu et al., 2015). Sulphur-bamboo charcoal composite with 57.7% sulphur showed a stable capacity of 414 mA h g^{-1} after 500 cycles with 0.079% capacity degradation for the 0.5C rate (J. J. Cheng et al., 2015). Ultrahigh specific surface area ($3164 \text{ m}^2 \text{ g}^{-1}$) porous carbon was derived from litchi shell by KOH activation method. 60% sulphur-carbon composite displayed 51% capacity retention after 800 cycles at current density of 800 mA g^{-1} with a fading rate of 0.06% per cycle (S. Zhang et al., 2014). 40.7 wt% product yield was obtained from Apricot shell derived porous carbon with 57.7% sulphur provided a discharge

capacity of 613 mA h g^{-1} at a high current density of 1C may be achieved after 200 charges/discharge cycles (K. Yang et al., 2015). Microporous carbon nanosheet derived from corn cob displayed a reversible capacity of 554 mA h g^{-1} after 50 cycles. This two dimensional porous, high surface area carbon facilitated to improve the utilization of sulphur (Jinxin Guo et al., 2015). Coconut shell derived carbon with high surface area of $2258 \text{ m}^2 \text{ g}^{-1}$ was obtained by KOH activation and exhibited a reversible capacity of 929 mA h g^{-1} after 100 cycles with 62% sulphur (M. Liu et al., 2014). Porous coconut shell derived carbon displayed a stable capacity of 517 mA h g^{-1} after 400 cycles at the 2C rate (Z.-H. Chen et al., 2017). A unique hierarchical porous carbon was obtained from the pig bone derived carbon using KOH activation and exhibited 1267 mA h g^{-1} as initial discharge capacity and 51% capacity retention after 50 cycles (S. Wei et al., 2011). Starch derived porous carbon with 81.29% sulphur showed a stable capacity of 683 mA h g^{-1} after 100 cycles at the 0.5C rate (J. Li et al., 2014). A three-dimensionally (3D) connected micro/mesoporous carbon was prepared from pomelo peel and used as cathode material without using any binder or conducting additives with 60% sulphur content. It delivered 700 mA h g^{-1} at the 2C rate (J. Zhang et al., 2014). A bio-inspired fabrication of fish scale like carbon nanotile was developed from the green source of kapok fiber and a high amount of 93.2% sulphur is loaded. It showed a stable capacity of 524 mA h g^{-1} after 90 cycles at a current density of 0.4 A g^{-1} (Tao et al., 2014). Poplar catkin considered as a kind of air pollutant and zero cost. A mesoporous carbon microtubes were prepared from poplar catkin and these tubes are highly efficient for trapping the PSs during cycling and exhibited 810 mA h g^{-1} reversible specific discharge capacity after 100 cycles at 0.1 C (Y. Zhang et al., 2015). Wall nut shell derived porous carbon sulphur composite delivered 910 mA h g^{-1} after 100 cycles at the 0.1C rate (J. Liu et al., 2017). Fish scale derived porous carbon sulphur composite showed 1039 mA h g^{-1} as discharge capacity and maintained a capacity of 1023 mA h g^{-1} 70 cycles at a current density of 1675 mA g^{-1} (S. Zhao et al., 2013). Sisal fiber derived carbon sulphur composite displayed 950 mA h g^{-1} as initial discharge capacity at 0.1C rate (Raja et al., 2016). Banana peel derived carbon exhibited 65% sulphur loading and displayed 872 mA h g^{-1} after 100 cycles at 0.1C rate with 71% capacity retention (Kai et al., 2016). Another

report from the banana peel derived carbon with 67% sulphur composite exhibited 707 mA h g⁻¹ after 100 cycles at 0.2C (F. Li et al., 2017). Cotton derived carbon sulphur composite with 80% sulphur loading showed 788 mA h g⁻¹ as reversible capacity after 100 cycles for 0.1C rate with 67% capacity retention (Chung et al., 2016). Bamboo leaves derived carbon-sulphur composite exhibited 707 mA h g⁻¹ as final capacity after 200 cycles for 1C with 0.014% capacity degradation per cycle (Yuanyuan Li et al., 2017). Bark tree derived carbon architecture without any additive was used as cathode material and exhibited a stable capacity of 608 mA h g⁻¹ after 60 cycles at a current density of 0.2 A g⁻¹ (Jiaqi Xu et al., 2016). Waste fruit peel derived carbon was used as a stabilizing agent for the sulphur composite 886 mA h g⁻¹ at 0.1 C, which remained remarkably stable over subsequent 50 charge/discharge cycles (Pólrolniczak et al., 2016). Olive stone derived porous carbon sulphur composite displayed 670 mA h g⁻¹ as final capacity after 50 cycles with 80% sulphur content (Moreno et al., 2014). A sheet like carbon matrix obtained from shaddock peel was used as sulphur host which displayed 722.5 mA h g⁻¹ at 0.2C after 100 cycles (S. Lu et al., 2016). *Aspergillusflavus* *Conidia*-derived Carbon/Sulphur Composite displayed 940 mA h g⁻¹ at 0.2C after 120 cycle (M. Xu et al., 2016). Mangosteen peel derived carbon-sulphur composite with 65% sulphur content exhibited a stable capacity of 509 mA h g⁻¹ at 0.5C after 500 cycles (M. Xue et al., 2018). Mangostone derived activated carbon with high surface area of 3334 m² g⁻¹ was obtained and 71% sulphur content composite exhibited 45% capacity retention after 1000 cycles with a current density of 1600 mA g⁻¹ (S. Zhang et al., 2016). Rapeseed shell derived carbon with 60% sulphur loading composite exhibited 49% capacity retention after 1000 cycles at 1600 mA g⁻¹(M. Zheng et al., 2017). Cherry pit waste derived carbon sulphur composite exhibited 410 mA h g⁻¹ after 200 cycles at 1C rate (Hernández-Rentero et al., 2018). Peanut shell derived carbon-sulphur composite with 50.5% sulphur loading composite showed 571 mA h g⁻¹ after 1000 cycles at the 2C rate (Zhou et al., 2018). Rice husk derived carbon-sulphur composite delivered 500 mA h g⁻¹ at the 5C rate (Rybarczyk et al., 2016). Soybean hull derived carbon with 67% sulphur content achieved 450 mA h g⁻¹ after 200 cycles at the 0.5C rate (Y. Zhu et al., 2017). Wheat straw derived carbon was used as sulphur host and displayed 445 mA h g⁻¹ after 200 cycles at 1C rate (Y.

Cheng et al., 2015). MWCNT microsphere was prepared by spray drying and its sulphur composite (70% sulphur) exhibited an initial discharge capacity of 983 mA h g⁻¹ and a stable capacity of 858 mA h g⁻¹ after 100 cycles at a current rate of 0.2C (Ye et al., 2016). Carbon nanobelt with ultra-high surface area of 3445 m² g⁻¹ sulphur composite exhibited 690 mA h g⁻¹ after 300 cycles at 5C and a capacity decay of 0.052% per cycle. The sulphur content in the composite was 60% (S.-Z. Zeng et al., 2017).

Heteroatom doped porous carbon materials

The surface chemistry of porous carbon is more important in the LSB for restricting the PS dissolution in the electrolytes. The porous carbon can restrict the movement of PSs only by physical means, thus the modification of porous carbon with heteroatoms is necessary. The density functional theory, diffusion experiments and X-ray photoelectron spectroscopy (XPS) observation admitted the introduction of heteroatom improves the PS chemisorption and conductivity of the carbon matrix (Paraknowitsch and Thomas, 2013). Recently heteroatoms like N, B, P, O and S doped carbon network received significant attention due to its enhanced electrochemical properties in LSB (Seh et al., 2016). The inclusion of heteroatoms in the hexagonal rings of carbon improves the conductivity, basicity and oxidation stability via conjugation between the lone pairs and π -system of the carbon network (Paraknowitsch and Thomas, 2013). Presence of heteroatom functionalities improves the electron-donor capability, thereby enhances polarity and wettability of the carbon surfaces, causing variation in an electrode-electrolyte contact area which further reduces the diffusion path length and support to improve the electrochemical performance (Shiguo et al., 2015). Strong interactions between the hetero elements like N, O, B, S, P, etc and PS anchors improve the sulphur utilization in the prolonged cycles and enhancing the electrochemical performance (Y. Peng, Y. Zhang, J. Huang, et al., 2017; He et al., 2018). Heteroatoms can be introduced into the carbon framework by in-situ pyrolysis of heteroatoms containing compounds or post-treatment of carbonaceous material with heteroatoms containing gas. Post-treatment may cause the destruction of carbon morphology and unwanted pore stalling. The structural stability of the carbon

material greatly influences the final heteroatoms content, graphitic structure, surface area, electronic conductivity, etc. (Shiguo et al., 2015). In general, heteroatom doped carbon preparation by post-treatment is a sophisticated process, it requires costly chemicals. So the preparation of inherently doped porous carbon is economical and easy to scale up.

GO- sulphur composite exhibited an initial discharge capacity of 1550 mA h g⁻¹ at 0.02C and retained a capacity of 900 mA h g⁻¹ after 50 cycles at 0.1C. It was due to the bonding between GO and sulphur (L. Zhang et al., 2012). MOF derived N doped microporous carbon was used as sulphur immobilizer and exhibited a reversible capacity of 936.5 mA h g⁻¹ after 100 cycles at a current density of 335 mA g⁻¹ with coulombic efficiency of 100% (Z. Liand Yin, 2015). Mushroom derived carbon showed an initial discharge capacity of 1357.8 mA h g⁻¹ at 0.1 C and high capacity retention of 729 mA h g⁻¹ after 100 cycles due to its specific porous structure of the carbon along with the hetero elements P and N which effectively improve the specific capacity and PS dissolution (H. Wu et al., 2016). Goat hair is an eco-friendly low cost, easily available sustainable material. N, O and P tri-doped porous carbon was obtained from the goat hair by H₃PO₄ activation. Due to the synergistic effect of porous nature and doping of heteroatom displayed a reversible capacity of 509 mA h g⁻¹ at 0.2C after 300 cycles (J. Ren et al., 2018). Silk cocoon derived porous carbon exhibited 804 mA h g⁻¹ at 0.5C after 80 cycles (B. Zhang et al., 2014). Natural silk cocoon derived N doped carbon sulphur composite with 55.7% sulphur loading displayed high reversible capacity of 594 mA h g⁻¹ after 100 cycles at 0.5C rate (M. Xiang et al., 2017). N-doped porous carbon microspheres from microalgae exhibited 1030.7 mA h g⁻¹ at a current density of 0.1 A g⁻¹ after 100 cycles (Xia et al., 2017). A high surface area N-doped microporous carbon was prepared from sol-gel polymerization followed by carbonization and used as sulphur host. The sulphur cathode delivered a reversible capacity of 1054 mA h g⁻¹ at 0.5C after 100 cycles with 40% sulphur content (Huichao Chen et al., 2015). N and S co-doped mesoporous carbon from polyaniline with 54% sulphur content exhibited a capacity of 693 mA h g⁻¹ at 10 C rate (F. Wu et al., 2015). Biological cell derived N doped microporous carbon with 67% sulphur exhibited 912 mA h g⁻¹ at 0.1C after 150 cycles with a capacity decay of 0.06%

(Xie et al., 2017). N and O dual doped 3D hierarchical porous carbon derived from nori based biochar was used as sulphur host (81.2%, sulphur). It exhibited a reversible capacity of 618 mA h g⁻¹ at 2C rate after 1000 cycles with 0.022% capacity decay per cycle (X. Wu et al., 2017). N enriched porous carbon was used as sulphur host from polyimide waste and shows a stable capacity of 620 mA h g⁻¹ at 0.5C rate after 350 cycles with 0.071% capacity decay per cycle (S. Zhu et al., 2016). S doped mesoporous graphene microspheres were prepared from chemical vapour deposition process and sulphur was incorporated by steam impregnation process, it exhibited better rate capability and high capacity of 830 mA h g⁻¹ at 8C (X. Ma et al., 2018). N doped yolk shell carbon spheres with 75.4% sulphur loading exhibited a stable capacity of 909 mA h g⁻¹ after 500 cycles at 0.2C rate (J. Xu et al., 2018).

Polyurethane is a polymer and its waste was used for the preparation of N doped porous carbon with an interconnected sheet-like structure for the sulphur incorporation. 75% sulphur was loaded and it showed a stable capacity of 460 mA h g⁻¹ after 100 cycles at 5C rate (S. Xiao et al., 2015). S and N co-doped mesoporous graphene platelets with 43.4% sulphur loading exhibited an initial discharge capacity of 1433 mA h g⁻¹ and obtained a stable capacity of 684 mA h g⁻¹ after 200 cycles at 2C rate (X. Yuan, Liu et al., 2017). N doped microporous carbon sphere prepared from polypyrrole by ZnCl₂ activation. It exhibited a stable capacity of 1002 mA h g⁻¹ after 200 cycles at 0.3C rate with 53% sulphur content (Niu, Zhou, et al., 2016). N doped single walled nanohorn with 80% sulphur content exhibited a reversible capacity of 573 mA h g⁻¹ after 200 cycles at 0.1C rate (Gulzar et al., 2018). N doped porous coralloid carbon was derived from aniline source and used as sulphur host. It displayed 607.2 mA h g⁻¹ after 200 cycles at 800 mA g⁻¹ (J. Yang et al., 2015). N and B co-doped graphene nanoribbon-sulphur composite with 65% sulphur loading showed an initial discharge capacity of 977 mA h g⁻¹ and after 300 cycles it reached 740 mA h g⁻¹ at 0.2C with 0.08% capacity decay rate (L. Chen et al., 2017). B and O co-doped MWCNT sulphur composite showed a final capacity of 937 mA h g⁻¹ after 100 cycles at a current density of 100 mA g⁻¹ with an average decay rate of 0.34% (Jin et al., 2017). Biomass waste gelatin derived N-doped carbon with 53.3% sulphur content showed a stable capacity of 600 mA h g⁻¹ after

100 cycles at 1C (Qu et al., 2015). Hydroxylated N-doped carbon nanotube was prepared from polypyrrole and it was used for 79% sulphur loading. This carbon-sulphur composite provided 754 mA h g^{-1} after 200 cycles at 0.2C rate with 77% capacity retention (J. S. Lee and Manthiram, 2017). N-doped hierarchically porous carbon derived from o-phenylenediamine sulphur composite provided 520 mA h g^{-1} as final capacity after 300 cycles at 0.2C (R. Wu et al., 2018). N-doped carbon nanofiber-sulphur composite displayed $749.8 \text{ mA h g}^{-1}$ after 180 cycles at 0.2C rate (J. Yang et al., 2014). Coralline-like N-doped hierarchically porous carbon derived from enteromorpha was used as host for sulphur and exhibited 734 mA h g^{-1} after 100 cycles at 0.1C rate with 40% sulphur content (Shengnan et al., 2017). N and O co-doped hollow carbon nanospheres from polyamine/catechol with 66% sulphur content delivered 851 mA h g^{-1} as final capacity at 0.2C rate after 200 cycles and a capacity decay of 0.08% per cycle (Y. Peng, Y. Zhang, J. Huang, et al., 2017). N-doped porous carbon bowls-sulphur composite with 69.9% sulphur content exhibited a reversible capacity of 706 mA h g^{-1} at 1C rate after 400 cycles (Fei et al., 2016).

1.6.1.2 Conducting polymers

The merits of employing polymers in LSBs are the following (1) Polymers have the good mechanical flexibility to solve the issues related in charge-discharge process in LSB, volume expansion and dissolution of PSs into the electrolyte. (2) Polymers are usually synthesized by lower temperature using oxidative polymerization (3) Polymer chains displayed physical and chemical confinement for the sulphur and PSs (Cheng and Wang, 2014). Conducting polymers like polyaniline (PANI), polypyrrole (PPy), polythiophene (PTh), polydopamine, amylopectin and their modified materials were widely used for the cathode material preparations. The thickness of the coating layer of polymer on sulphur is greatly influenced the electrochemical properties of sulphur during the cycling process (Eftekhari and Kim, 2017).

PPy nanowire was synthesized via cationic surfactant as soft template and 1222 mA h g^{-1} as the initial discharge capacity, retained 570 mA h g^{-1} after 20th cycles (M. Sun et al., 2008). A thin layer of PTh is coated over the surfaces of the

sulphur powder (71.9%) and delivered a stable capacity of 830.2 mA h g⁻¹ after 80 cycles at a current density of 100 mA g⁻¹ (F. Wu, Chen, Chen, et al., 2011). PANI coated sulphur with Yolk shell type structure exhibited 765 mA h g⁻¹ after 200 at 0.2C rate with 82% sulphur content (W. Zhou, Y. Yu, et al., 2013). A mixed ionic-electronic conductor of PPy synthesized with poly(2-acrylamido-2-methyl-1-propanesulfonic acid) and it was explored as an additive for sulphur cathode. 75% sulphur composite delivered a stable capacity of 500 mA h g⁻¹ after 50 cycles at 5C rate (Y. Fuand Manthiram, 2012). A PPy hollow nanosphere with ultra-thin wrinkled shell exhibited a high capacity of 536.5 mA h g⁻¹ at 5C rate with 60.7% sulphur loading (Y. Liu et al., 2018). In situ vulcanization process was used for the preparation of sulphur-PANI composite. It exhibited 837 mA h g⁻¹ after 100 cycles at a 0.1 C rate (Lifen et al., 2012). A nanostructured sulphur-PPy composite was prepared without ball milling and 65% sulphur was loaded. It showed a final capacity of about 500 mA h g⁻¹ after 40 cycles at a current density of 100 mA g⁻¹ (Y. Zhang et al., 2012). PTh lamella wrapped sulphur nanoparticle composite with 86.1% sulphur exhibited an initial discharge capacity of 1074 mA h g⁻¹ and reached 595.5 mA h g⁻¹ at 0.1C rate after 90 cycles (C. Li et al., 2018). Core-shell structured sulphur-PPy with 80% sulphur loading displayed a stable capacity of 805 mA h g⁻¹ after 50 cycles at 0.1 C rate (Y. Xie et al., 2016). PPy/sulphur/PPy composite with 65.6% sulphur exhibited 554 mA h g⁻¹ after 50 cycles with 68.8% capacity retention (X. Liang et al., 2015). Sulphur coated with polydopamine exhibited a final capacity of 385 mA h g⁻¹ at 0.5 C rate with 54% capacity retention after 400 cycles (X. Liu et al., 2016). Porous poly(3, 4-ethylenedioxythiophene)/sulphur composite exhibited 883 mA h g⁻¹ at 0.5 C rate with 71% capacity retention after 200 cycles with 61% sulphur loading (B. Ding et al., 2016). Sulphur hollow PPy spheres exhibited a stable capacity of 620 mA h g⁻¹ after 100 cycles at 0.5C rate (Z. Dong et al., 2013). Urchin sulphur-PANI composite delivered an initial discharge capacity of 1095 mA h g⁻¹ at 0.1C rate (Q. Lu et al., 2015). Sulphur-PPy core-shell type composite showed an initial discharge capacity of 1039 mA h g⁻¹ with 59% capacity retention after 50 cycles at 0.1C rate (G. Yuan and Wang, 2014). Layer by layer deposition of Polyallylamine/polyacrylic acid (PAA) and polyethylene oxide (PEO)/PAA on sulphur, delivered a stable capacity of 806 mA h g⁻¹ after 100 cycles

at 0.5C rate (E. T. Kim et al., 2016). Sulphur deposited on a hollow PANI composite (54.6% sulphur content) and showed a reversible capacity of 601.9 mA h g⁻¹ after 100 cycles at 170 mA g⁻¹ (P. Wei, Fan, Chen, Yang, et al., 2016). Hollow PANI sphere sulphur composite with 62% sulphur content exhibited a stable capacity of 602 mA h g⁻¹ after 1000 cycles at 0.5C rate (G. Ma, Wen, Jin, Lu, Wu, et al., 2014). The Ultrafine nanoparticle of sulphur with a diameter of 10-20 nm is coated with poly (3, 4-ethylenedioxythiophene). It delivered a stable capacity of 930 mA h g⁻¹ after 50 cycles at 400 mA g⁻¹ with 83% capacity retention (H. Chen et al., 2013). Core-shell structured sulphur composite covered by polydopamine with 74.8% sulphur content exhibited a stable capacity of 708.6 mA h g⁻¹ after 890 cycles at 0.8 A g⁻¹ and 81.7% capacity retention was observed (Y. Deng et al., 2015).

1.6.1.3 Metal oxides/metal sulphide

Transition metal oxides, sulphides and carbides are belong to non-carbon polar host category. Compared to the above mentioned sulphur hosts less reports are available presently. The nanostructured materials of oxides and sulphides with exposed surfaces and 3D architecture are more effective and efficient for trapping the PSs. Metal oxide/sulphides were used as conductive polar host, they can adsorb the PSs during discharge process and restrict LPSs into the electrolyte. In addition to that, these materials accelerate the conversion of lower order PSs to higher order PSs and vice versa due to its catalytic effect (Yibo He, Chang, et al., 2018; Manthiram et al., 2014; Ould Ely et al., 2018; L. Xue et al., 2017).

Nanosized Mg_{0.6}Ni_{0.4}O was the first report in metal oxide additive along with sulphur in LSB for adsorbing PSs. It exhibited a reversible capacity of 1000 mA h g⁻¹ after 50 cycles at 0.1C rate with 20% sulphur loading (Manthiram et al., 2014). SiO₂ was added as an additive to improve the electrochemical performance of carbon sulphur composite, It provided a final capacity of 650 mA h g⁻¹ after 40 cycles with 65% capacity retention. Here the sulphur content in the composite was 59.85% (Ji et al., 2011). Si/SiO₂ was added onto the hierarchical carbon sulphur composite with 69.6% sulphur content exhibited an initial discharge capacity of 1215 mA h g⁻¹ and ultraslow capacity decay of only 0.063% per cycle during 500

cycles at 0.1C rate (Sarish et al., 2016). TiO₂ with various morphologies have been tried as sulphur host viz, TiO₂ nanoparticle, nanofiber, nanotube and hollow sphere etc. Hollow TiO₂ sphere with 68% sulphur provided 71% capacity retention after 100 cycles at 1C rate. TiO₂ nanofiber-sulphur composite with 57.5% sulphur content exhibited a reversible capacity of 530 mA h g⁻¹ after 50 cycles at 335 mA g⁻¹. TiO₂ nanotube-sulphur with 65% sulphur content exhibited an initial discharge capacity of 913 mA h g⁻¹ and retained 93% capacity retention after 100 cycles. TiO₂ nanoparticle with 60% sulphur content exhibited an initial discharge capacity of 1460 mA h g⁻¹ and 680 mA h g⁻¹ after 100 cycles at a current density of 335 mA g⁻¹ (L. Xue et al., 2017). Sulphur-TiO₂ yolk-shell structure exhibited an initial specific capacity of 1030 mA h g⁻¹ at 0.5 C and coulombic efficiency of 98.4% over 1,000 cycles was achieved. Ti₄O₇ with 51% sulphur content displayed an initial capacity of 623 mA h g⁻¹ and 97% capacity retention after 250 cycles at 0.5C rate. The nanoparticle of Ti₄O₇ with 48% sulphur loading exhibited a stable capacity of 850 mA h g⁻¹ after 500 cycles at 2C rate with a capacity decay of 0.06% per cycle (L. Xue et al., 2017). Ti₆O₁₁ nanowire exhibited a specific capacity of 713 mA h g⁻¹ after 100 cycles at 0.1C rate with 52% sulphur loading. MnO₂ nanosheet with 56% sulphur loading displays an initial capacity of 1120 mA h g⁻¹ after 200 cycles at 0.2C rate (Yazhou et al., 2018). Yolk shell type MnO₂ sulphur composite with 59% sulphur content exhibited a final capacity of 780 mA h g⁻¹ after 800 cycles at 0.2C rate (Arias et al., 2018). 50% sulphur content with MnO₂ nanosheet showed 920 mA h g⁻¹ after 300 cycles at 0.5C rate (L. Xue et al., 2017). Nanosheet of NiFe₂O₄ with 55% sulphur content MWCNT composite displayed a final capacity of 900 mA h g⁻¹ after more than 500 cycles at 1C rate with extra high cycle stability and ~0.009% capacity decay per cycle (Q. Fan et al., 2015). Al₂O₃ used an ultra-thin layer on graphene sulphur composite with 64% sulphur content. It displayed a final capacity of 646 mA h g⁻¹ after 100 cycles at 0.5C rate (M. Yu et al., 2014). Co₃O₄, V₂O₅ and VO₂ nanoparticles added on graphene sulphur composite with 75% sulphur content (L. Xiao et al., 2016). Co₃O₄ exhibited an initial discharge capacity of ~826 mA h g⁻¹ and obtained a final capacity of ~300 mA h g⁻¹ after 200 cycles at 0.5C rate with 0.34% capacity decay per cycle. V₂O₅ displayed an initial discharge capacity of 1000 mA h g⁻¹ and retained 76% capacity

retention after 150 cycles at 0.5C rate. VO₂ displayed an initial discharge capacity of 1000 mA h g⁻¹ and retained 74% capacity retention after 150 cycles at 0.5C rate (L. Xiao et al., 2016). Co₃O₄ nanotube with 15.35% sulphur exhibited a final capacity of 778 mA h g⁻¹ after 100 cycles at a current density of 0.05 mA cm⁻² (Arias et al., 2018). MoO₂ mesoporous particle with 32% sulphur loading displayed an initial discharge capacity of 1100 mA h g⁻¹ and obtained 52% capacity retention after 250 cycles at 0.1C rate (L. Xue et al., 2017). SiO₂ with 72% sulphur loading exhibited a final capacity of 814 mA h g⁻¹ after 50 cycles at 0.1C rate and 99% columbic efficiency was observed (Hou et al., 2017). La₂O₃ was added to mesoporous carbon sulphur composite with 48% sulphur content. It delivered a final capacity of 792 mA h g⁻¹ with 76% capacity retention at 1C rate (Yazhou et al., 2018). Ultra-thin layer of ZnO and MgO were added on graphene sulphur composite with 55% sulphur content (L. Xue et al., 2017). Composite with ZnO displayed an initial discharge capacity of 949 mA h g⁻¹ and retained 89% capacity retention after 100 cycles at 0.2C rate. Composite with MgO displayed an initial discharge capacity of 923 mA h g⁻¹ and retained 83% capacity retention after 100 cycles at 0.2C rate. La_{0.6}Sr_{0.4}CoO_{3-δ} was used PS immobilizer in the carbon-sulphur composite with 66.3% sulphur content. It exhibited a stable capacity of 996 mA h g⁻¹ after 400 cycles at 0.5C rate with 0.039% capacity decay per cycle (Z. Hao et al., 2017). K₃PW₁₂O₄₀ sulphur-composite with 50.6% sulphur content exhibited a reversible capacity of 767.4 mA h g⁻¹ after 70 cycles at 0.1C rate (N. Yan et al., 2018). Other metal oxides like Mg_{0.8}Cu_{0.2}O, Li₄Ti₅O₁₂, BaTiO₃, LiFePO₄, ZrO₂, MoO₃, Nb₂O₅, W₁₈O₄₉, CeO₂, Fe₂O₃, CaO, In₂O₃, V₂O₅, and SnO₂ were used as additives in cathode material (Guand Lai, 2018; L. Xue et al., 2017; Yazhou et al., 2018). Recently, metal sulphides are used as sulphur hosts such as Co₉S₈, CoS₂, TiS₂, FeS₂, FeS, SnS₂, NiS₂, MnS, CuS, ZnS, Ni₂S₃, Cu₃Bi₅S₃, etc. (X. Fan et al., 2018; L. Xue et al., 2017; Donghai et al., 2018; Yazhou et al., 2018) due to the catalytic effect for the redox reactions. Most of the metal oxides/sulphides were mixed with polymeric or carbon materials to improve the conductivity and thereby improving the active material utilization during the cycling process.

1.6.1.4 Hybrid materials

Hybrid materials are the composites comprising two or three constituents of above mentioned sulphur hosts. Variety of hybrid materials were demonstrated as sulphur hosts viz the composites of carbon nanotube and graphene, carbon nanotube and conducting polymers, graphene and conducting polymers, porous carbon and graphene, porous carbon and carbon nanotube, porous carbon and conducting polymers, etc. Hybrid materials are preferred for cathode materials due to the enhancement in properties like high conductivity, surface area, tunable micro-mesoporosity, surface functionalities etc. These materials rationally integrate the properties together which facilitates to overcome the intrinsic drawbacks of one material by complementary enhancement. It brings a synergistic effect. Altogether it can give multiple confinement of PSs during the cycling process which further enhances the sulphur utilization and improves the electrochemical performance of the LSB.

CMK-3-graphene hybrid sulphur composite exhibited a reversible capacity of 867 mA h g^{-1} after 300 cycles at a current density of 335 mA g^{-1} with 82% capacity retention (X.-n. Tang et al., 2018). One step synthesis of carbon nanosheet decorated carbon nanofiber with 63% sulphur exhibited a stable capacity of 607 mA h g^{-1} after 500 cycles at 0.5C rate (S. Feng et al., 2017). rGO and hollow carbon spheres with 90% sulphur content exhibited a stable capacity of 662 mA h g^{-1} after 78 cycles at 0.1C rate with 77% capacity retention (S. Liu et al., 2016). MOF derived N doped porous carbon along with graphene sheet was served as sulphur host. The cell delivered a stable capacity of 608 mA h g^{-1} after 300 cycles at 1C rate (Ke et al. 2018). A 3D MOF and carbon nanotube hybrid with 64% sulphur content displayed 750 mA h g^{-1} after 500 cycles at 1C rate with 0.02% capacity decay per cycle (Zhang Hui et al., 2018). A hybrid of hierarchically N doped porous graphene and fluoro graphene sulphur composite with 63.2% sulphur exhibit a final capacity of 300 mA h g^{-1} after 800 cycles at 0.5C rate with 0.068% capacity decay per cycle (Z. Liu et al., 2017). A bifunctional carbon host, a hierarchical porous carbon and ultrathin graphene achieved a specific capacity of 694 mA h g^{-1} after 200 cycles at 0.5C rate with 81.2% capacity retention (W. Deng

et al., 2017). Self-supported graphene encapsulated hollow mesoporous carbon nanosheet hybrid with 73% sulphur exhibited 719 mA h g⁻¹ after 500 cycles at 1C rate with 79.9% capacity retention (Pei et al., 2017). Micro/mesoporous dual carbon-sulphur composite with 69.57% sulphur exhibited 402.2 mA h g⁻¹ after 1000 cycles at 1C rate with 0.057% capacity decay per cycle (H. Li et al., 2016). MnO₂/GO/MWCNT hybrid was with 80% sulphur exhibited 963 mA h g⁻¹ after 100 cycles at 0.2C rate (Yong Li et al., 2016). Carbon nanotube clusters had grown in 3D porous graphene network with a surface area of 1645 m² g⁻¹ was used as sulphur host (81.6%) which exhibited an initial discharge capacity of 1229 mA h g⁻¹ at 0.5C rate with a capacity decay of 0.044% over 500 cycles (S. Huang et al., 2018). Fe₃C/N doped graphene/carbon nanotube scaffold with 73% sulphur displayed a stable capacity of 158 mA h g⁻¹ after 1000 cycles at 10C rate (Dawei et al., 2017). Freestanding N and O co-doped carbon film composed of porous carbon nanofiber and carbon nanotube with 62% sulphur exhibited a stable capacity of 859 mA h g⁻¹ after 100 cycles at 5.15 mA h cm⁻² (Y.-Z. Zhang et al., 2018). A multi-dimensional N doped graphene and porous carbon hybrid was used as the sulphur host with 60.79 % sulphur. This sulphur composite delivered a stable capacity of 579 mA h g⁻¹ after 500 cycles at 1C rate (H. Wu et al., 2018). B-doped porous carbon and graphene hybrid with 70% sulphur delivered 740 mA h g⁻¹ after 500 cycles at 0.5C rate and achieved 78% capacity retention (W. Ai et al., 2018). The above investigations demonstrate the potential usage of hybrids based on graphene, porous carbon and carbon nanotube as sulphur host (Yibo He, Chang, et al., 2018; Kumar et al., 2018; Rehman et al., 2017; X. Zhang et al., 2017; Yunya Zhang et al., 2018).

Another approach is based on conducting polymers and carbon materials. A coating of PANI over the binary composite MWCNT/S exhibited a stable capacity of 932.4 mA h g⁻¹ after 80 cycles at 0.1C rate with 56.3% capacity retention (F. Wu, Chen, Li, et al., 2011). Polyethylene glycol (PEG), wrapped graphene sulphur composite exhibited a stable capacity of ~600 mA h g⁻¹ after 100 cycles at 0.5C rate. The polyethylene glycol and graphene coating layer helped to accommodate the volume expansion of PSs during charge discharge process (H. Wang et al., 2011). Carbon sulphur composite coated with rGO exhibited a stable capacity of 421 mA h g⁻¹ after 100 cycles at a current density of 0.2 A g⁻¹ (N. Li et

al., 2012). Dual core-shell structured sulphur composite was made using MWCNT and PPy, in which sulphur was deposited by the reaction between sodium thiosulphate and HCl. The composite with 68.3% sulphur, exhibited a final capacity of 917 mA h g⁻¹ after 60 cycles at a current density of 200 mA g⁻¹ (C. Wang et al., 2013). Amylopectin wrapped graphene sulphur composite exhibited a stable capacity of 430 mA h g⁻¹ after 60 cycles at 0.5C rate (W. Zhou, H. Chen, et al., 2013). Binder free phenyl sulphonated graphene-sulphur composite with 69% sulphur exhibited a final capacity of ~465 mA h g⁻¹ after 40 cycles at 0.2C rate (L. Zhou et al., 2014). Reduced carbon wrapped acetylene black sulphur composite with 56.8% sulphur displayed a stable capacity of 808 mA h g⁻¹ after 100 cycles at 200 mA g⁻¹ (Xuebing Yang et al., 2015). Microporous carbon polyhedron encapsulated polyacrylonitrile (PAN) with 52% sulphur exhibited 370 mA g⁻¹ at 4C rate (Y.-Z. Zhang et al., 2017). PANI coated hollow carbon nanofiber hybrid demonstrated as an effective PS trapper with 75% sulphur content. It exhibited a stable capacity of 535 mA h g⁻¹ after 200 cycles at 0.5C rate (Zhian Zhang et al., 2014). rGo/S/PANI with 51% sulphur content exhibited a stable capacity of 600.8 mA h g⁻¹ after 100 cycles at 0.1C rate (M. Fan et al., 2018; J. Cai et al., 2017). A freestanding PAN/S/CNT hybrid delivered an initial capacity of 1610 mA h g⁻¹ and retained a stable capacity of 1400 mA h g⁻¹ after 200 cycles at 0.2C rate (Abdul Razzaq et al., 2019). A double wrapped graphene and polydopamine with porous carbon sulphur composite exhibited a stable capacity of 821 mA h g⁻¹ after 100 cycles at a current density of 0.3 A g⁻¹ with 52% sulphur content (Y. Dong et al., 2017). Watermelon derived carbon sphere sulphur composite wrapped tubular PPy delivered a reversible capacity of 685.8 mA h g⁻¹ after 500 cycles at 0.5C rate (Qihong et al., 2017; Y. Zhang et al., 2017). Sulphur/rGo/polydopamine composite with 67.4% sulphur loading exhibited a final capacity of 647 mA h g⁻¹ after 100 cycles at a current density of 200 mA g⁻¹ and stable coulombic efficiency of 98% (Y. Zhang et al., 2017). Polydopamine coated N-doped hollow carbon sphere-sulphur composite with 55% sulphur displayed 600 mA h g⁻¹ after 600 cycles at 0.6C rate (W. Zhou et al., 2014). Graphene/polydopamine/sulphur composite with 70% sulphur loading delivered 984 mA h g⁻¹ after 500 cycles at 0.5C rate and 100% coulombic efficiency was observed (L. Zhou et al., 2016). Poly (3, 4-

ethylene-dioxythiophene): poly(styrenesulfonate) coated rGO-sulphur composite with 56.4% sulphur displayed 701 mA h g⁻¹ at high rate performance of 4C (Peitao et al., 2017). Polydiallyldimethylammonium chloride coated rGO-sulphur composite exhibited 652 mA h g⁻¹ after 100 cycles at 0.2C rate (H.-Y. Lee et al., 2016). Polyvinylpyrrolidone (PVP) coated graphene aerogel sulphur composite exhibited 508.2 mA h g⁻¹ after 200 cycles at 0.5C rate (B. Li et al., 2017). Polyanthraquinonyl sulphide wrapped rGO sulphur composite exhibited an initial discharge capacity of 1225 mA h g⁻¹ and 61.5% capacity retention after 1200 cycles. It delivered a reversible capacity of 615 mA h g⁻¹ at 8C rate. The combination of graphene and polyanthraquinonyl sulphide facilitated electron and ion transport and thus provided reduction in PS shuttling (Hongwei Chen et al., 2015). MWCNT/Sulphur/PANI composite with 67.8% sulphur exhibited 600 mA h g⁻¹ after 100 cycles with 61.8% capacity retention at 0.2C rate (X. Li et al., 2015). MWCNT and PPy supported sulphur composite displayed a reversible capacity of 751 mA h g⁻¹ after 100 cycles, with 60% capacity retention at 0.2C rate (Y. Zhang, Y. Zhao, Z. Bakenov, et al., 2014). Pluronic F-127 block copolymer coated carbon sulphur composite with 63.5% sulphur content exhibited a stable capacity of 470 mA h g⁻¹ after 20 cycles and it maintained upto 80 cycles at 4C rate (Y. Fu et al., 2012). MWCNT/S/PANI delivered a capacity of 640 mA h g⁻¹ at 2C and provided a stable capacity of 760 mA h g⁻¹ after 400 cycles at 0.25C with 65% sulphur content (C. Wang et al., 2014). Various conducting polymers in combination with carbon materials were reported to improve the electrochemical performance by PS entrapment during the cycling process (Cheng and Wang, 2014; L. Li et al., 2015; X. Liang et al., 2012; S. Lim et al., 2015; G. Ma, Wen, Jin, Lu, Rui, et al., 2014; Peng et al., 2018; W. Qian et al., 2017; Wu Yang et al., 2018; Yongguang et al., 2018; Yunya Zhang et al., 2018; X. Zhao et al., 2013; X. Zhou et al., 2015).

1.6.2 Functional Modification of Separators

The separator is a necessary part of the battery, which is an electron insulator placed between the electrodes to prevent the short circuit. In the case of battery, the primary function of a separator is to separate the anode and cathode. The separator is the medium for the transportation of Li ion. Commercial separators

are polyethylene (PE), PP and PE/PP with a large number of nanoscale pores which is larger than the size of PS anion. Thus the soluble PSs can easily diffuse through the separator and can react with Li anode, which causes corrosion of Li metal. An effective approach to reduce the PS shuttling is the modification of separator in such a way to block the migration of PS. An overview of various approaches adopted in literature to modify separator are discussed below (W. Fan et al., 2018; Shaibani et al., 2017).

1.6.2.1 Polymer modified separator

Celgard 2400 coated nafion effectively improved the electrochemical behaviour of LSB. Nafion is a sulphonated tetrafluoro ethylene based fluoro polymer. The pores present in the separator allows the movement of Li cation, and restrict the movement of PS anion. 0.15 mg cm⁻² coating of nafion on normal separator delivered an initial discharge capacity of 781 mA h g⁻¹ and 60% capacity retention was observed after 500 cycles with 0.08% capacity decay per cycle at 1C rate (J.-Q. Huang et al., 2014). Carboxyl group modified PP separator displayed an initial discharge capacity of 1250 mA h g⁻¹ with 89.2% capacity retention after 100 cycles at 0.1C rate (X. Yu et al., 2016). Lithium perfluorinated sulphonyl dicyanaomethide modified separator was used for blocking the PS anion (Z. Jin et al., 2013). Ion selective membrane modified separator was fabricated by layer by layer assembly of polyallyl amine hydrochloric acid (PAH) and PAA exhibited 100% coulombic efficiency and a high discharge capacity of 1418 mA h g⁻¹ (Z. Jin et al., 2013). Oxygen plasma modification on PP produced a lots of electronegative functional groups along with grafting of styrene sulphonate blocked PSs successfully (Conder et al., 2015; Z. Li, Q. Jiang, et al., 2015). A PPy conducting film was inserted in between the separator and cathode as an interlayer to avoid the migration of PSs towards anode and provided a stable capacity of 846 mA h g⁻¹ after 200 cycles at 0.2C rate (G. Ma, Wen, Jin, Wu, et al., 2014). Polydopamine coated separator exhibited 1020.3 mA h g⁻¹ after 30 cycles at 0.2C rate which showed 77% improvement compared to the uncoated separator (G. C. Li et al., 2015). PAA modified separator exhibited an ultra-slow 0.074% capacity decay per cycle for 600 cycles at 0.5C rate (S. Song et al., 2018).

1.6.2.2 Carbon modified separator

Conductive carbon modified separator exhibited an initial discharge capacity of 1045 mA h g⁻¹ and obtained a stable capacity of 701 mA h g⁻¹ at 2C rate after 200 cycles with 0.12% capacity decay per cycle (Sheng-Heng and Arumugam, 2014). This carbon material acts as upper current collector and offered an additional electron pathway for improving the sulphur utilization. The resulted carbon coated separator was 0.2 mg cm⁻², which avoid the unnecessary increase of cell weight and unsatisfactory energy density. Mesoporous carbon coated separator exhibited a stable capacity of 723 mA h g⁻¹ after 500 cycles at 0.5C with 0.08% capacity decay per cycle. Mesoporous carbon facilitated the trapping of PSs and volume changes of sulphur (Juan et al., 2015). MWCNT coated separator displayed a stable capacity of 621 mA h g⁻¹ after 300 cycles at 1C rate with 0.14% capacity decay per cycle. The coating weight was 0.17 mg cm⁻² (Chung and Manthiram, 2014). SWCNT modified separator exhibited a high discharge capacity of 1132 mA h g⁻¹ with a low-capacity fade rate of 0.18% per cycle after 300 cycles. The prominent cycle stability attributed to the SWCNT coating that directly reduced the fast PS migration and hence indirectly ameliorates the Li-metal anode degradation (Chi-Hao et al., 2016). GO membrane have inherently good mechanical strength, which contains a large number of functional group which can act as ion hooping sites of positively charged Li⁺ ions and reject the negatively charged PS anion. GO membrane cell exhibited an initial discharge capacity of 920 mA h g⁻¹, which was higher than the value of the cell without GO membrane. While using the GO membrane the capacity decay was reduced from the 0.49 to 0.23% capacity decay per cycle (J.-Q. Huang et al., 2015). Coating of rGO on PP provided 3D structure and exhibited a stable capacity of 878 mA h g⁻¹ after 100 cycles at 0.2C rate with 0.18% capacity decay per cycle (W. Lin et al., 2015). Porous graphene modified separator delivered an initial discharge capacity of 1135 mA h g⁻¹ at 0.1C with 65% sulphur utilization and capacity become stable in the remaining cycle (P.-Y. Zhai et al., 2017). The incorporation of rGO with high reduction degree modified on glass fiber membrane separator reduced the PS shuttling. It exhibited a stable capacity of 733 mA h g⁻¹ after 100 cycles at 0.2C and delivered a high capacity of 519 mA h g⁻¹ at 2C, which were 42% and 90% higher than those of cells with

separators coated with low reduction degree rGO. Mesoporous nature and abundant oxygen functionalities on rGO provided chemical adsorption to the PSs and immobilized on cathode side. It exhibited an initial discharge capacity of 1515.7 mA h g⁻¹ and long term cycling stability was observed for 600 cycles with 0.057% capacity decay per cycle (Linlin Zhang et al., 2018). Activated carbon nanofiber coated onto PP demonstrated an initial discharge capacity of 1270 mA h g⁻¹ at 0.5C rate and obtained a stable capacity of 819 mA h g⁻¹ after 200 cycles with a capacity decay of 0.13% per cycle (Sheng-Heng et al., 2015). Carbon fiber cloth was applied as interlayer in between the cathode and separator exhibited a reversible capacity of 560 mA h g⁻¹ at 5C rate and 0.025% capacity decay per cycle over 1000 cycles (Y. Yang et al., 2016). N doped carbon nanowire modified PP delivered an initial discharge capacity of 1430 mA h g⁻¹ at 0.2C rate and long term cycling stability with 0.08% capacity decay per cycle (X. Zhou et al., 2016). B and N doped rGO improved cyclability, discharge capacity and which create polar sites to anchor PSs (P. Han and Manthiram, 2017). N and P co-doped honeycomb like carbon modified separator delivered an initial discharge capacity of 1387 mA h g⁻¹ at 0.2C and maintained a reversible capacity of 930 mA h g⁻¹ after 200 cycles (P. Zeng, Huang, Zhang, Zhang, et al., 2018). N-doped porous carbon sphere provided a stable capacity of 542 mA h g⁻¹ after 500 cycles at 1C rate (Zhian Zhang et al., 2015). Novel carbon flower like modified separator exhibited high reversible capacity of 730 mA h g⁻¹ with a degradation rate of 0.061% per cycle after 500 cycles at 0.5C (Liao et al., 2017). Hollow carbon spheres with nano shell modified separator displayed high discharge capacity of 806 mA h g⁻¹ at 4C rate and an ultra-long cycle life with a low capacity decay rate of 0.037% after 1500 cycles at 2C rate (S. Liu et al., 2018). N, S and O co doped porous carbon modified separator delivered an initial discharge capacity of 1395 mA h g⁻¹ at 0.2C rate and maintain a stable capacity of 599.9 mA h g⁻¹ after 700 cycles at 1C rate with 0.064% capacity fading per cycle (F. Ai et al., 2017).

1.6.2.3 Metal oxide modified separator

Oxygen rich inorganic metal oxides and sulphide rich inorganic metal sulphides are generally used as PS adsorber in LSB (Donghai et al., 2018). By

modifying the separator with inorganic metal oxide/sulphides not only adsorb the PSs but also act as a physical obstacle for the movement of PS anion. Vermiculite is a clay mineral, which was used for the modification of the separator. The cell with vermiculite separator exhibited an initial discharge capacity of 1000 mA h g⁻¹ at 0.1C rate after 50 cycles it provided 90.3% capacity retention (R. Xu et al., 2017). Hollow spherical La₂O₃ modified PP separator exhibited a stable capacity of 720 mA h g⁻¹ at 1C after 200 cycles (X. Qian et al., 2017). V₂O₅ modified separator in a 2 cm × 2 cm pouch cell demonstrated with a capacity of 800 mA h g⁻¹ without noticeable degradation for >300 cycles over ~1 year (W. Li et al., 2014). Similarly, other metal oxides/sulphides reported to modify separator for blocking the PSs and catalyse the reactions were ZrO₂, Al₂O₃, TiO₂, BaTiO₃, MnO, MoO₂, and Ni Fe based double oxides (N. Deng et al., 2016; W. Fan et al., 2018; Yibo He, Qiao, et al., 2018; Yunya Zhang et al., 2018).

1.6.2.4 Hybrid materials modified separator

Chitosan is a polysaccharide with abundant hydroxyl and amine groups. The combination of carbon and chitosan modified separator exhibited 675 mA h g⁻¹ after 200 cycles at 1C rate with 0.11% capacity decay per cycle (Y. Chen et al., 2015). MWCNT/PEG modified separator provided an initial discharge capacity of 1283 mA h g⁻¹ at 0.5C rate with 0.12% capacity decay per cycle for 500 cycles (G. Wang et al., 2015). Polyvinylidene fluoride (PVDF)-carbon layer modified separator exhibited 339 mA h g⁻¹ even at high current density of 5C rate (H. Wei et al., 2014). Functional carbon layer coated separator (PVP and carbon black) high reversible capacity of 778 mA h g⁻¹ at 0.5C rate after 100 cycles (Zhiyong Zhang et al., 2015). A spray coating of mixture of GO and MWCNT on separator with mass loading of 0.3 mg cm⁻² exhibited a stable capacity of 750 mA h g⁻¹ at 1C rate after 100 cycles (Yunbo et al., 2015). Fe-N doped carbon nanofiber and graphene modified separator delivered 601.9 mA h g⁻¹ at 0.5C rate after 500 cycles with 0.053% capacity decay per cycle (X. Song et al., 2018). Lithium sulphonate/carboxylate anchored polyvinyl alcohol modified separator displayed a stable capacity of 901 mA h g⁻¹ at 1.5 A g⁻¹ after 500 cycles with 0.016% capacity decay per cycle (K. Jiang et al., 2018). MWCNT/S/PANI modified separator

delivered a reversible capacity of 913 mA h g^{-1} at the current density of 100 mA g^{-1} after 100 cycles, which was much higher than that of the cells with pristine celgard separator (Shi et al., 2018). rGO and Co/N doped carbon nanofiber modified PP gives high rate capability of 658 mA h g^{-1} at 5C rate (G. Chen et al., 2018). Acetylene black and CoS_2 modified separator exhibited 380 mA h g^{-1} at 5C rate after 550 cycles with 0.09% capacity decay per cycle (P. Zeng, Huang, Zhang, Han, et al., 2018). A self-standing TiO_2 and Co_3O_4 embedded in the N doped porous carbon as interlayer was inserted in between the cathode and separator, delivered a stable capacity of 968 mA h g^{-1} at 0.1C rate after 100 cycles with a capacity retention of 85% (C.-Y. Fan et al., 2017). Graphene and CNT modified separator displayed a stable capacity of 551 mA h g^{-1} after 200 cycles at 4C rate (Haiwei Wu et al., 2017). rGO/MoS₂ coated separator have the thickness of $8 \mu\text{m}$ and weight of 0.25 mg cm^{-2} exhibited an initial reversible discharge capacity of 877 mA h g^{-1} and after 500 cycles, discharge capacity of 368 mA h g^{-1} was obtained with a coulombic efficiency above 95% and a low average capacity fading of 0.116% (L. Tan et al., 2018). Nano TiO_2 decorated carbon coating modified separator provided a stable capacity of 762 mA h g^{-1} after 200 cycles at 0.2C rate (Shao et al., 2018). A 3D porous C_3N_4 nanosheets/rGO modified separator displayed a stable capacity of 680 mA h g^{-1} after 800 cycles at 0.5C rate with 0.048% capacity decay per cycle (Gong et al., 2017). Carbon nanosheet/ MnO_2 modified separator exhibited a stable capacity of $856.1 \text{ mA h g}^{-1}$ after 200 cycles at 0.5 C (Lai et al., 2017). Similarly other combinations like carbon nanofiber/carbon nanotube, graphene/GO, carbon black/various metal oxides, porous carbon/metal oxides, polymer/metal oxide, polymer/porous carbon, polymer/carbon nanotube, polymer/graphene, etc were reported to modify the separator for improving the electrochemical performance.

1.6.3 Anode protection

Apart from cathode modification, functional modification of separator need more concentration towards the Li metal anode. These Li metal is more attractive due to its high specific capacity (3860 mA h g^{-1}), low reduction potential and low density (0.59 g cm^{-3}). Most of the LIBs failed due to the deactivation of the Li anode. During the charge-discharge process, the Li metal experience repeated

plating and stripping. This will cause volume change in the Li metal anode. Li metal is highly reactive, it will react with organic electrolyte and form solid electrolyte interface (SEI) on anode. The SEI film present on the anode can easily be disturbed and repeated volume fluctuation leads to SEI cracking and reconstruction. On the other hand it causes constant Li and electrolyte loss. In addition, the SEI damage causes the entry of Li to the organic electrolyte and leads to the formation of uncontrolled growth of lithium dendrite, which has the capability to penetrate through the separator resulting in a short circuit. This will lead to battery degradation and low coulombic efficiency of the cell. Various strategies were reported for the protection of Li anode and to improve the cycle life by adding additives to the electrolyte (in situ), adjusting the electrolyte components (modification of lithium anode) and insertion of artificial layers (ex situ) (Kumar et al., 2018).

1.6.3.1 In situ

Variety of additives were used in the electrolyte for the protection of anode through SEI formation. LiNO_3 is the most effective additive to improve the cycle performance of LSB. LiNO_3 in the electrolyte solution reacts with Li metal anode and forms a surface passivation layer, which consists of LiN_xO_y , ROLi and ROCOOLi . N_2O and N_2 gases formed during SEI layer formation have a positive effect during the charge/discharge process. PS and LiNO_3 have a synergistic role to prevent lithium dendrite formation, which creates the SEI layer composed of Li_2SO_3 and Li_2SO_4 . LiNO_3 containing electrolyte greatly suppresses the lithium dendrite growth and improves the sulphur utilization (Suo et al., 2013). The other additives used in the electrolytes were Lithium bis (oxalate) borate (LiBOB), thiol-based electrolyte with the additive of biphenyl-4,4'-dithiol (BPD), SiCl_4 , Tris(trimethylsilyl) phosphite-Vinylene carbonate (TMSP-VC) for getting the better electrochemical performance in LSB (H. Zhao et al., 2018).

1.6.3.2 Ex situ

In addition to the formation of SEI layer with different additives, modification of anode surface (Li metal) was adopted to improve the electrochemical performance of LSBs. Formation of a coating or protective film

prior to fabrication of cell, distinguishing it from electrolyte modification to protect anode from the soluble PSs. The protective film shield the anode from the side reactions with the electrolytes and PSs with the Li metal. It also restricts the unsafe Li stripping and plating. A colloidal solution was prepared by using Cu₃N nanoparticles in THF with styrene butadiene (SBR) was applied on Li anode by doctor blade method or direct coating. A protective film of Li₃N was formed when Cu₃N contact with Li metal and it was named as artificial SEI. As a result, the coulombic efficiency was increased to 97.34% at a current density of 1 mA cm⁻² and cycle life was increased to 40% (Yayuan et al., 2017). Other reported materials and methods for forming protective film were porous Al₂O₃ layer on Li anode, PPy and Li powder prepared by planetary ball milling method, benzenedicarboxylic acid and cobalt nitrate based MOF, Li_{1.5}Al_{10.5}Ge_{1.5}(PO₄)₃ (LAGP) film on anode by drop casting method, dipping of Li foil into poly(dimethylsiloxane) (PDMS) containing DOL/DME solution, etc. (H. Zhao et al., 2018).

1.6.3.3 Li-host materials

A variety of host materials have been intended to stabilize the Li anode during the charge-discharge process. Graphene sphere film, hollow carbon sphere and graphene oxide were used as host to restore the Li (D. Lin et al., 2017; K. Yan et al., 2016). A free standing Li_xM/graphene (M= Si, Sn or Al nanoparticles) foil was prepared to enhance the stability of Li anode in the air (J. Zhao et al., 2017).

1.6.4 Trends in Electrolyte

The electrolyte which is necessary part of the battery, it is a medium for Li ion transport. It is considered as a key component in the battery system, the electrochemical performance of the battery greatly influenced by the electrolyte compositions and additives. Liquid organic electrolytes are the most commonly used electrolyte used in LSB. Liquid organic electrolyte contains a lithium salt and an organic solvent. The commonly used lithium salt is lithium bis(trifluoromethanesulfonyl)imide (LiTFSI) and the solvents are tetrahydrofuran (THF), fluoroethylene carbonate (FEC), 1,2-dimethoxymethane (DME), 1, 3-dioxolane (DOL) tetraethyleneglycoldimethylether (TEGDME), etc. The higher

order PSs are soluble in the electrolyte and freely move towards the anode through the separator. The restriction of PS dissolution in the electrolyte is an effective method to inhibit the PS transport. Gel polymer electrolytes (GPE) and solid electrolytes are preferred for this purpose (Judez et al., 2018; Scheers et al., 2014; X. Yu and Manthiram, 2017).

GPE generally consists of LiTFSI and polymer matrices. The polymer can trap the liquid components. GPE able to reduce the lithium dendrite growth and improve the performance of the battery. Pentaerythritol tetraacrylate (PETEA) based GPE delivered an initial discharge capacity of $653.5 \text{ mA h g}^{-1}$ at 1C and 82.1% capacity retention observed even after 500 cycles (M. Liu et al., 2016). The polymer matrices used in the GPE were Poly (vinylidene fluoride–hexafluoropropylene) (PVDF–HFP), poly (butyl acrylate)/poly (ethylene glycol) diacrylate (P(BA-co-PEGDA)), PEO, PAN and poly methyl methacrylate (PMMA) etc. (Angulakshmi and Stephan, 2015; Yibo He, Chang, et al., 2018).

Solid electrolytes made up of both inorganic and organic components were used by researchers to improve the cycle life and coulombic efficiency. Solid ceramic electrolytes are non-flammable and stable at high temperature. Recently several types of ceramic (sulphides, oxides and phosphates) and polymer-ceramic composites electrolytes such as NASICON ($\text{Li}_{1.4}\text{Al}_{0.4}\text{Ge}_{1.7}(\text{PO}_4)_3$, (LICGC), $\text{Li}_{1.3}\text{Al}_{0.3}\text{Ti}_{1.7}(\text{PO}_4)_3$ (LATP)), $(\text{Li}_{1+x+y}\text{Al}_x\text{Ti}_{2-x}\text{Si}_y\text{P}_{3-y}\text{O}_{12})$, perovskite ($\text{Li}_{0.33}\text{La}_{0.557}\text{TiO}_3$ (LLTO)), and garnet ($\text{Li}_7\text{La}_3\text{Zr}_2\text{O}_{12}$ (LLZO)) were reported with enhanced mechanical and electrochemical properties. The solid state cell fabricated using these electrolytes exhibited excellent cycling and rate performance. But, their huge impedance resistance and chemical compatibility between electrolytes and electrodes, poor processability, still needs to be solved. However, all-solid-state LSBs are safer than liquid electrolytes, also this configuration is proposed to be better to achieve higher gravimetric energy density than the state of- art of LIBs (Zhonghui Gao et al., 2018; Judez et al., 2018; Agostini et al., 2013; A. Hayashi et al., 2008; Judez et al., 2018; Judez et al., 2017; Kobayashi et al., 2008; Nagao et al., 2016; Y.-Z. Sun et al., 2017).

1.7 Electrochemical Capacitor

Batteries and electrochemical capacitor are considered as the two major energy storage devices. Electrochemical capacitor is also termed as SC or ultra-capacitor. Ragone plot compares the energy density and power density of SCs and batteries (Figure 1.5) (François et al., 2014). SCs are differentiated from the battery in terms of power density i.e. the ability to rapidly charge and discharge during life span, indicates how quickly charge is stored and discharged with short interval of time. So, the applications of SCs are mainly concentrated in the area of power breaking section, industrial energy management, power back up devices and hybrid electric vehicles (Dubal et al., 2018). SC consists of a positive electrode, negative electrode, and separator in between the positive and negative electrode to prevent the short circuit, with the electrolyte. (F. Wang et al., 2017; Y. Wang et al., 2016)

On the basis of charge storage mechanism, SCs are differentiated as electrical double layer capacitors (EDLC) and pseudocapacitors (François et al., 2014; Zhong et al., 2015). In EDLC charge is stored in between electrode-electrolyte interface by a non-faradaic process, an electrical double layer formed is due to the adsorption of ions. The process is highly reversible and long cycle life. But charge storage takes place in pseudocapacitors are due to faradaic process on the electrode surface, which is a fast surface oxidation-reduction reactions or possible intercalation in the electrode (Conway and Pell, 2003).

The performance of electrochemical capacitors are determined by the combination of the electrode material and electrolyte used. There are three main categories of electrode materials used for ECs, namely (1) carbon-based materials, (2) transition metal oxides, and (3) conductive polymers. Similarly, three types of electrolyte materials are used for ECs including (1) aqueous electrolytes, (2) organic electrolytes, and (3) ionic liquids (Borenstein et al., 2017). Carbon based materials are under the category of EDLC and transition metal oxides and conducting polymers belongs to the pseudocapacitor category. Carbon materials provide high power density with low energy density due to the low electric charge separation between the electrode-electrolyte interfaces. Metal oxides provide high

energy density with low power density due to the fast redox reactions (H. Fan et al., 2016). Carbon materials with heteroatom such as N, P, S and B enhance the capacitance due to the pseudocapacitive behaviour of heteroatoms and thereby the energy density (Y. Deng et al., 2016; Paraknowitsch and Thomas, 2013; M. Xu et al., 2017; S. S. Zhang, 2015; G. Zhu et al., 2017). In addition the heteroatom boosts the wettability and electronic conductivity. So, this type of carbon material is used as SCs to obtain both higher power and energy densities.

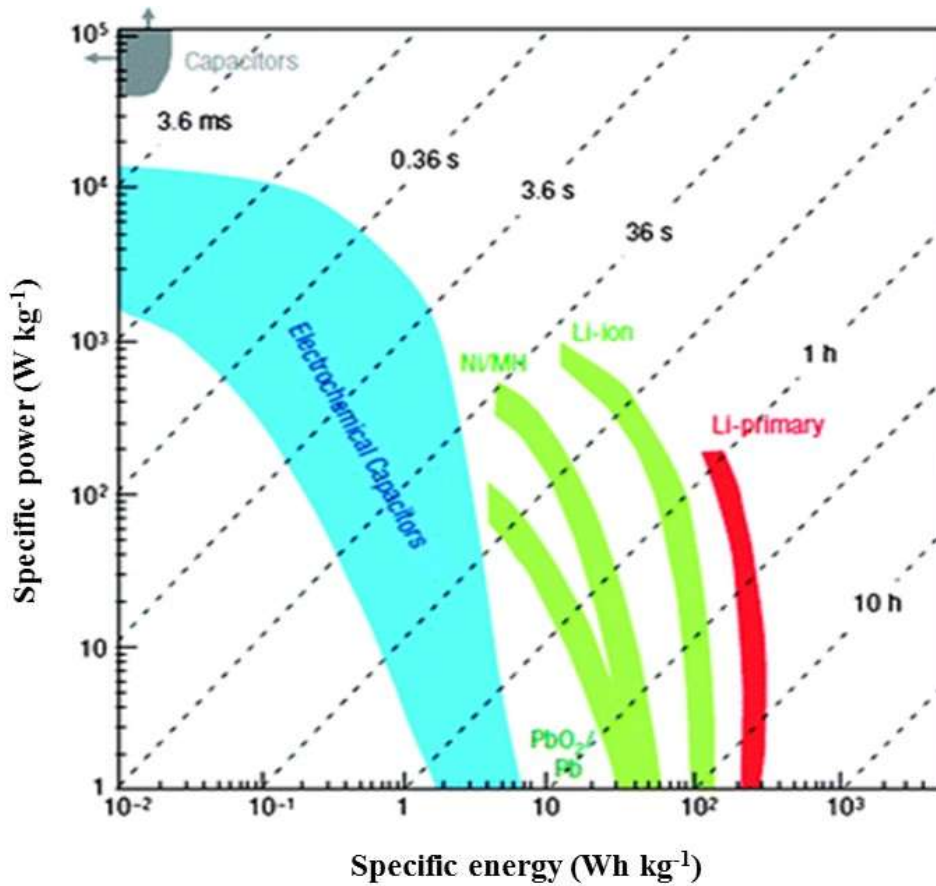


Figure 1.5. Ragone plot for various electrical energy storage devices (Service, 2006)

The key parameters affecting the energy and power density of SC are specific capacitance and operating voltage window. Generally the maximum operating voltage window is depend upon the stability of the electrolyte used. EDLCs based SCs are commercially available due to its characteristics such as long-term cycling stability, durability, high power density, non-toxicity and environmental friendliness (Dubal et al., 2018; François et al., 2014). EDLCs are considered as green energy technologies and it emerges as a promising solution for the thirst of the energy demand

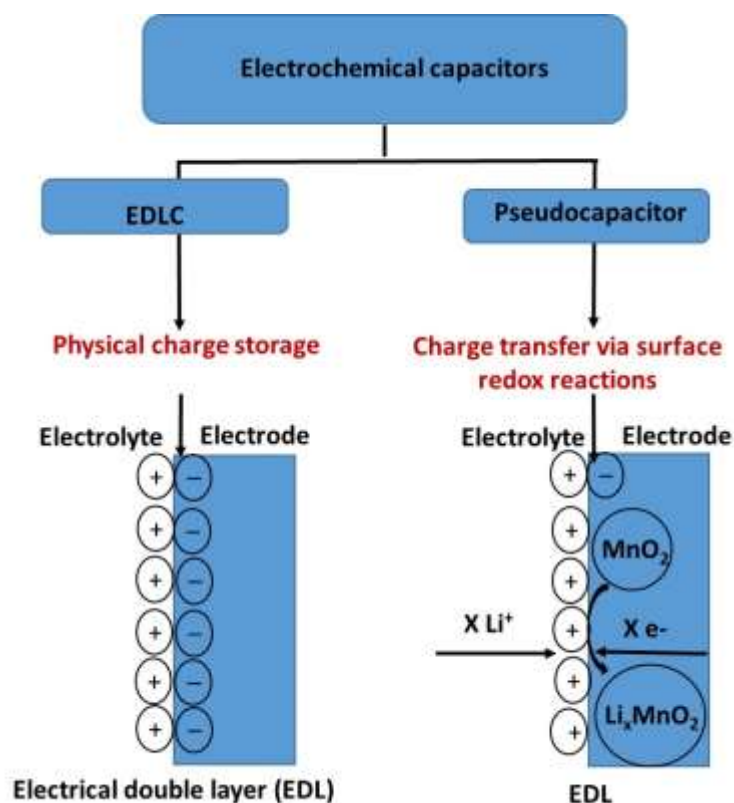


Figure 1.6. Schematic representation for the classification of electrochemical capacitors

The carbon materials are widely used in SCs due to the peculiar properties associated with it such as their abundance, easy processing, non-toxicity, high specific surface area, tunable microstructure, low density, low cost, electronic conductivity, chemical stability and wide operating temperature. Carbon nanotube, porous carbon, carbon aerogel, nanofiber, graphene etc., are the common electrode materials for EDLCs (Borenstein et al., 2017; X. Guo et al., 2017; Z. Yu et al., 2015; Yunpu et al., 2011). High surface area carbons with wide pore size distribution are highly explored to improve the electrochemical performance by employing new synthetic approaches for the development of porous carbon with diverse precursors. The specific capacitance of EDLC increases with specific surface area and the relationship is not always linear, since the capacitance depends on other factors such as pore size, interconnectivity, electrical conductivity, materials surface chemistry, method of preparation, electrolyte, electrode testing methods, etc. (Enock et al., 2017). Pore structure is also plays a vital role to improve the electrochemical performance of EDLC. Hierarchical pores with micro/meso and macro is highly beneficial to obtain high specific capacitance. Macropores reduces the ion diffusion

length, which act as an ion reservoir. Short range mesopores offers low resistance for ions to reach the electrode surface. Micropores contribute to increase the specific surface area (J. Wang et al., 2017). The distribution of micro to macropore size, shape and its interconnectivity affect the mass transport and diffusion of ions. If the micro/mesopores are too narrow/deep and it is difficult for the ions to penetrate into the pores to form the double layer. However wide and shallow pores ease the pathway of ion diffusion (Fuertes and Sevilla, 2015; Y. Lu et al., 2017).

Multi porous N doped carbon was prepared from PANI using SiO₂ template. Porous carbon with high surface area obtained at 800 °C exhibited maximum specific capacitance value of 413 F g⁻¹ by three electrode system with 6M KOH and obtained specific capacitance of 327 F g⁻¹ at a current density of 1 A g⁻¹ using CR 2032 type button cell (95% capacity retention after 10000 charge discharge cycles (Li et al., 2017). 1,10 phenanthroline disulphate derived N, S co-doped mesoporous carbon with the surface area of 1161 m² g⁻¹ using colloidal silica as template delivered a specific capacitance of 156.4 F g⁻¹ and 145.2 F g⁻¹ for 1M H₂SO₄ and 6M KOH respectively at a current density of 1 A g⁻¹ (Shiguo et al., 2015). In situ activated N-doped mesoporous carbon was obtained from protic salt benzimidazoletriflate with calcium and sodium citrate. The surface area of the carbon was 1788 m² g⁻¹ and the specific capacitance was 111F g⁻¹ with 1M tetraethylammonium tetrafluoroborate/acetonitrile (TEABF₄/AN) as electrolyte at a current density of 0.5 A g⁻¹. 86% capacitance retention was obtained at a current density of 10 A g⁻¹ (Mendes et al., 2016). Poly(o-phenylenediamine) derived porous carbon exhibited a specific capacitance of 690 F g⁻¹ at 0.1 A g⁻¹ current density using 1M H₂SO₄ as electrolyte in three electrode set up. A 96% capacitance retention was observed after 1200 cycles at a current density of 5 A g⁻¹ (Zhu Hui et al., 2012). 3D high surface area graphene like carbon material was derived from PANI with the surface area of 1645 m² g⁻¹. Symmetric supercapacitor delivered a specific capacitance of 235 F g⁻¹ at a current density of 1 A g⁻¹ using 6M KOH as electrolyte (Sheng et al., 2016). Dead leaves derived porous carbon delivered a specific capacitance 400 F g⁻¹ at a current density of 500 mA g⁻¹ with 1M H₂SO₄ as electrolyte (Biswal et al., 2013). Hierarchical porous carbon materials from nanosized metal-organic complex displayed an energy density of 43W h Kg⁻¹ in 1M

BMIMBF₄/AN (S. Zhang et al., 2018). N containing novoloc derived carbon bead exhibited maximum energy density of 22 W h Kg⁻¹ in 1M TEABF₄/AN (Krüner et al., 2018).

Among the porous carbon materials activated carbon is widely used in energy storage application, owing to its commendable characteristics such as high surface area, high strength, less corrosive, wide operating temperature, easiness of the preparation etc. (Biswal et al., 2013; Puthusseri et al., 2014; Marta Sevilla and Mokaya, 2014). Nowadays, biomass derived activated carbon received more attention due to its inherently doped of heteroelements and simple, low cost preparation methods. Recent studies show that biomass-derived activated carbons exhibited better electrochemical performance than the conventional activated carbon (Ranjith et al., 2017).

Pinecone petal derived activated carbon was prepared with the surface area of 3950 m² g⁻¹ by KOH activation. A symmetric cell exhibited a specific capacitance of 142 F g⁻¹ at a current density of 1 A g⁻¹ by using 1M Lithium hexafluorophosphate (LiPF₆) in ethylene carbonate/dimethyl carbonate (EC/DMC). 90% capacitance retention was obtained after 20000 cycles at a current density of 3 A g⁻¹ (energy density of 61 W h kg⁻¹) (Karthikeyan et al., 2014). Hemp derived activated carbon exhibited the specific capacitance of 142 F g⁻¹ at a current density of 100 A g⁻¹ using ionic liquid electrolyte. It delivered a higher power density of 20 kW kg⁻¹ (H. Wang et al., 2013). Grape fruit peel derived N-doped carbon nanosheet exhibited a specific capacitance of 311 F g⁻¹ with 1M H₂SO₄ as electrolyte and 94.05% capacitance retention after 10, 000 cycles. It exhibited a maximum energy density of 34.05 W h kg⁻¹ at a power density of 180 W kg⁻¹ with 1M Na₂SO₄ aqueous electrolyte (Wang et al., 2016). Palm kernel shell derived N, P and S co doped activated carbon with a surface area of 2760 m² g⁻¹ and exhibited a specific capacitance of 380 F g⁻¹ at a current density of 1 A g⁻¹ by 3M KOH as electrolyte. It exhibited cycle stability for 10000 cycles with 96% capacitance retention (M. Xu et al., 2017). Lotus seed pod derived activated carbon displayed a specific capacitance of 402 F g⁻¹ with 6M KOH as electrolyte at a current density of 0.5 A g⁻¹ and 95.4% capacitance retention was observed after 10000 cycles. The

symmetric cell delivered a high energy density of 12.5 W h kg^{-1} at a power density of 260 W kg^{-1} (B. Liu et al., 2016). Corn cob derived activated carbon with a specific surface area of $1471.4 \text{ m}^2 \text{ g}^{-1}$ exhibited a specific capacitance of 293 F g^{-1} at a current density of 1 A g^{-1} with 6M KOH as electrolyte and 99.9% capacitance retention after 4000 cycles (S. Yang and Zhang, 2018). Waste fig fruit derived foam like activated carbon with surface area of 2000 delivered a specific capacitance of 340 F g^{-1} at a current density $\text{m}^2 \text{ g}^{-1}$ of 0.5 A g^{-1} by $0.5\text{M H}_2\text{SO}_4$ as electrolyte and 99% capacitance retention (Housseinou et al., 2018). N doped Neem leaves derived activated carbon with a surface area of $705 \text{ m}^2 \text{ g}^{-1}$ displayed 74 F g^{-1} specific capacitance at a current density of 1 mA cm^{-2} using 1M lithium perchlorate (LiClO_4) in EC/propylene carbonate (PC). The cell delivered a maximum energy density of $10.33 \text{ W h kg}^{-1}$ at a power density of 4.66 kW kg^{-1} (Sultan, Parvaz, et al., 2018). N-doped pea skin derived activated carbon with the surface area of $1828 \text{ m}^2 \text{ g}^{-1}$ exhibited 141 F g^{-1} specific capacitance at current density of 1.3 A g^{-1} using 1 M LiTFSI in EMITFSI (1-Ethyl-3-methylimidazolium bis(trifluoromethylsulfonyl) imide) solution as electrolyte. The cell delivered a maximum energy density of 19.6 W h kg^{-1} at a power density of 25.4 kW kg^{-1} (Sultan, Ahsan, et al., 2018). Rotten carrot derived activated carbon with a surface area of $1154 \text{ m}^2 \text{ g}^{-1}$ delivered a specific capacitance of 142 F g^{-1} at a current density of 1mA cm^{-2} by using 1M LiClO_4 in EC/PC as electrolyte. The cell delivered a maximum energy density of 28.4 W h kg^{-1} at a power density of 89.1 kW kg^{-1} (Ahmed et al., 2018). N and O co-doped cotton derived activated carbon with the surface area of $1022 \text{ m}^2 \text{ g}^{-1}$ exhibited a specific capacitance of 270 F g^{-1} at a current density of 0.5 A g^{-1} . The symmetric cell delivered 18 W h kg^{-1} energy density at a power of 250 W kg^{-1} (Lan Zhang et al., 2018). N doped lotus stem derived activated carbon with the surface area of $1322 \text{ m}^2 \text{ g}^{-1}$ displayed a specific capacitance of 360.5 F g^{-1} at a current density of 0.5 A g^{-1} and 96% capacitance retention after 5000 cycles by using 6M KOH as electrolyte (S. Yan et al., 2018). Wild rice stem derived activated carbon with the surface area of $1288 \text{ m}^2 \text{ g}^{-1}$ exhibited a specific capacitance of 301 F g^{-1} at a current density of 1 A g^{-1} using 6M KOH as electrolyte. The symmetrical cell delivered $13.05 \text{ W h kg}^{-1}$ as energy density at a power of 250 W kg^{-1} (Q. Tian et al., 2018). Moringa derived N and O co-doped activated carbon with the surface area

of $2312 \text{ m}^2 \text{ g}^{-1}$ exhibited a specific capacitance of 355 F g^{-1} at a current density of 0.5 A g^{-1} using 6M KOH as electrolyte and 95% capacitance retention after 20000 cycles at higher current density of 20 A g^{-1} . The symmetrical cell delivered 20 W h kg^{-1} as energy density while using $1\text{M Na}_2\text{SO}_4$ as electrolyte (Y. Cai et al., 2016). Cotton stalk derived activated carbon provided a surface area of $1964.46 \text{ m}^2 \text{ g}^{-1}$ and exhibited a specific capacitance of 254 F g^{-1} at a current density of 0.2 A g^{-1} using $1\text{M Na}_2\text{SO}_4$ as electrolyte. It delivered 96% capacitance retention after 10000 cycles at a higher current density of 1 A g^{-1} . The symmetrical cell delivered $18.14 \text{ W h kg}^{-1}$ as energy density at a power of 450.37 W kg^{-1} while using $1\text{M Na}_2\text{SO}_4$ as electrolyte (X. Tian et al., 2017). Straw derived activated carbon fiber with the surface area of $2013 \text{ m}^2 \text{ g}^{-1}$ exhibited a specific capacitance of 230 F g^{-1} at a current density of 0.5 A g^{-1} using 6M KOH as electrolyte. The symmetrical cell delivered 16 W h kg^{-1} as energy density at a power of 450.4 W kg^{-1} using $0.5\text{M Na}_2\text{SO}_4$ as electrolyte (X. Zheng et al., 2017).

Biomass from agricultural and forest crop residues and other renewable sources such as rice husk (Yong et al., 2017), sunflower seed (Xiao Li et al., 2011), waste paper (Kalpana et al., 2009), willow catkin (L. Xie et al., 2016), celtuce leaves (R. Wang et al., 2012), sewage sludge (H. Feng et al., 2015), wood saw dust (L. Wei et al., 2011), tobacco rod (Y.-Q. Zhao et al., 2016), fallen leaves, (Y.-T. Li et al., 2015), water hyacinth (K. Wu et al., 2016), cherry stone (Olivares-Marín et al., 2009), hemi cellulose (Falco et al., 2013), fungi (Hui Zhu et al., 2011), fungus (Long et al., 2015), pumpkin (Bai et al., 2016), water melon rind (Mo et al., 2016), etc were successfully converted into porous carbon and demonstrated as electrode materials for EDLC applications. Bio-waste derived from animal origin like, cow dung (Bhattacharjya and Yu, 2014), human hair (W. Qian et al., 2014), chicken feathers (Q. Wang et al., 2013), sheep manure (C. Zhang et al., 2016), egg yolk (J. Li et al., 2015) etc were also reported for energy storage applications. The surface area and electrochemical properties of these material are listed in Table 1.1.

Table 1.1: Comparison for the specific capacitance of biomass derived carbon

Precursor	Surface area (m ² g ⁻¹)	Specific capacitance (F g ⁻¹)	Current density (A g ⁻¹)	Electrolyte
Rice husk	2242	429	0.5	6M KOH
Sunflower seed	1235	144	10	30wt% KOH
waste paper	416	180	2	6M KOH
Willow catkin	1775	292	1	6M KOH
Celtuce leaves	3404	421	0.5	2M KOH
Seawage sludge	2839	379	20	1M Na ₂ SO ₄
Wood saw dust	2967	175	20	1M TEABF ₄
Tobacco rod	-	286	0.5	6M KOH
Fallen leaves	2869	242	0.3	6M KOH
Water hyacinth	1308	273	1	6M KOH
Cherry stone	1300	230	-	2M H ₂ SO ₄
Hemi cellulose	2300	300	0.2	0.5M H ₂ SO ₄
Fungi	80.8	196	0.17	6M KOH
Fungus	1103	360	0.5	6M KOH
Bamboo waste	1472	301	0.1	6M KOH
Microalgae	2190	200	0.1	6M LiCl
Pumpkin	2968	419	1	6M KOH
Watermelon rind	2277	333	1	6M KOH
Cow dung	2000	117	1	Et ₄ NBF ₄
Human hair	1306	340	1	6M KOH
Chicken feathers	1839	168	10	1M H ₂ SO ₄
Sheep manure	1000	486	1	6M KOH
Egg yolk	2277	220	20	6M KOH

1.8 Scope and Objectives

LIBs have revolutionised in the market of portable electronic devices. However, due to the ever increasing demand of energy storage devices with high energy and power densities, new materials and chemistries are evolved. Among the promising futuristic technologies, LSBs and SCs are widely discussed for lightweight applications (e.g., aircraft, artificial satellite, and unmanned aerial vehicles), and large-scale stationary energy storage, owing to their high gravimetric energy density (2-3 fold, LSB), power density (1-2 orders, SC), long life cycle (1–3 orders, SC), low cost, safety and eco- friendliness compared to conventional LIBs. The use of LSBs in the commercial market is hampered by the insulating nature of sulphur and lithium sulphide, shuttle effect and Li dendrites formation upon

cycling. Researchers and industries made significant progress during last decades, still unresolved problems existing which hinder the deployment of LSBs for various applications. This doctoral research has been focused on the design and development of carbon based electrode materials for LSB and SC systems. Considering the excellent properties of porous carbon materials, we attempted to address few of the above mentioned challenges for LSB, using heteroatom containing porous carbon as host for active material and to modify separator and cathode film electrodes for LSBs. The main objectives of the research work are

- To develop a high performance cathode material for Li-S battery with high specific capacity and cycling stability
 - To prepare renewable, hybrid cathode materials with high specific capacity, stable cycling and high rate.
 - To investigate the feasibility of high capacity cathode based on sulphur concentration and porous carbon with surface functionalities.
 - To investigate the impacts of surface functional groups on the PSs shuttling and the electrochemical performance of energy storage device.
 - Structural and electrochemical evaluation of the functionalized porous carbon-sulphur composite cathode materials.
- To develop symmetric SC based on electrical double-layer charge storage with high energy density and long term cycling performance.

1.9 Organization of the Thesis

The thesis describes the preparation, characterization of pyrolytic heteroatom containing high surface area porous carbon, conducting polymer and its electrochemical evaluation. Two of the developed materials evaluated for its capacitive behaviour (EDLC) in addition to the exploration of its characteristics towards LSB application. The thesis composed of eight chapters in which the results obtained are presented. A brief description of the chapters are outlined as follows:

Chapter 1 provides a general introduction on LSB and SC systems and a comprehensive literature review on the strategies adopted to overcome the challenges of LSBs, specifically on cathodic region and various porous carbon materials for EDLC. It describes objectives and outline of the thesis.

Chapter 2 presents systematic preparation and characterisation of MWCNT/sulphur/Polyindole (PIN) composite as cathode material for LSB. This chapter focused on the function of MWCNT and PIN to mitigate PS shuttling.

Chapter 3 describes one pot synthesis of heteroatom doped carbon derived from 4, 4'-diamino-diphenyl sulphone as electrode material for LSB and SC.

Chapter 4 reports the impact of pyrolysis temperature onto porous carbon network during the preparation of functionalized hierarchically porous carbon with iron, nitrogen and oxygen derived from vetiveria zizanioides (vetiver) for high-performance LSB and SC.

Chapter 5 describes the preparation and evaluation of sulphur-immobilized nitrogen and oxygen co-doped hierarchically porous carbon derived from pinecone for LSB application. This study aimed to investigate the importance of sulphur distribution into the porous structure on cycling stability.

Chapter 6 presents the preparation and evaluation of heteroatom doped porous carbon derived from orange peel as sulphur host. To achieve better performance and to enhance the cycling stability the separator was modified with MWCNT and porous carbon derived from DDS. An extensive comparison between the separator modified and unmodified cells was also included.

Chapter 7 investigates on hierarchical porous carbon material derived from honeycomb and its sulphur composite as cathode material for LSB. To improve the electrode performance, the same carbon material is coated on the cathode film (interlayer) and the performance was compared with the bare cathode.

In *Chapter 8*, conclusions are summarized and perspectives are proposed for further research work based on this doctoral work.

References are listed after Chapter 8, followed by publications received during the period of my PhD study.

CHAPTER 2

MWCNT/SULPHUR/POLYINDOLE COMPOSITE AS CATHODE MATERIAL FOR LITHIUM- SULPHUR BATTERY

In this chapter novel multiwalled carbon nanotube/sulphur/polyindole (MWCNT/S/PIN) nanocomposite is investigated as a cathode material for LSBs to reduce the shuttle effect. In MWCNT/S/PIN sulphur was prepared by reaction between sodium thiosulphate and hydrochloric acid onto functionalized MWCNT followed by in-situ polymerization of indole monomer. The advantage of wrapping polyindole onto MWCNT/S was brought out with the help of experimental details. MWCNT/S/PIN nanocomposite exhibited 1490 mA h g^{-1} as initial specific capacity and displayed a capacity of 1043 mA h g^{-1} after 100 cycles at 0.1C rate with 70% capacity retention compared to the binary nanocomposite (MWCNT/S). The better electrochemical performance of ternary nanocomposite cathode material is attributed to the synergistic effect of functionalized MWCNT and polyindole which provides improved conductivity and effective fencing of intermediate PSs.

2.1 Introduction

LSBs received the attention of researchers due to its fascinating properties mainly the theoretical capacity of sulphur. However the LSB technology faces a few challenges such as insulating nature of sulphur, shuttle effect, passivation of Li anode, etc. In order to tackle LSB issues, various approaches have been adopted (Carbone et al., 2017; Manthiram et al., 2013), which include combining sulphur with electrically conducting species such as metal oxides (Pan et al., 2015), carbon nanotube (Xi et al., 2015), graphene (J. Feng et al., 2016; L. Sun et al., 2015), carbon nanofiber (K. Fu et al., 2014; Singhal et al., 2015) carbon onions (Choudhury et al., 2017), porous carbons (D. Li et al., 2013; G.-L. Xu et al., 2013; S. Zhang et al., 2014), conducting polymers with core and yolk-shell structure, etc. (F. Wu, Chen, Chen, et al., 2011; Y. Fu and Manthiram, 2012a; H. Chen et al., 2013; W. Zhou, Y. Yu, et al., 2013; Y. Fu; Chulliyote et al., 2017a and Manthiram, 2012c). The high conductivity of the cathode material is advantageous to improve the kinetics of the Li-S redox reactions (L. Sun et al., 2015; F. Wu, Chen, Li, et al., 2011; W. Zhou, Y. Yu, et al., 2013). Recently, attempts have been made to develop ternary cathode

materials, where sulphur is trapped between two conductive elements, which improves the capacity and cycling performance. Literature reports in this area includes, sulphur wrapped with carbon nanotube and graphene (L. Sun et al., 2015; J. He et al., 2015), graphene and porous carbon (S. Liu et al., 2015; M. Yu et al., 2015), carbon nanotube and conducting polymers such as polyaniline (F. Wu, Chen, Li, et al., 2011; X. Li et al., 2015), polypyrrole (C. Wang et al., 2013; Y. Zhang, Y. Zhao, Z. Bakenov, et al., 2014) etc. The improved electrochemical performance of ternary composite cathodes are due to the enhanced conductivity and the ceiling effect of PS in the cathodic region. In addition, achieving high sulphur loading and the uniform polymer coating on to sulphur are few more challenges to be addressed. In this chapter, polyindole (PIN) as one of the conductive layers in ternary composite along with multiwall carbon nanotubes (MWCNT) aiming to achieve uniform coating and better sulphur loading. PIN is one of the well-known conducting electroactive polymers with an electrical conductivity of 0.1 S cm^{-1} and stable at normal conditions which exhibits good electrochemical characteristics as cathode material (Zhijiang et al., 2013). Hence, a coating of PIN onto sulphur is beneficial to trap PSs. Owing to its good electrical conductivity, thermal and mechanical properties (C. Wang et al., 2013), MWCNT also plays an advantageous part in the ternary system. Here, we discuss MWCNT/S/PIN nanocomposite with dual core-shell structure as the ternary cathode material for LSBs. The composite preparation involves simple chemical precipitation of sulphur onto MWCNT followed by in-situ polymerization of the monomer indole. An initial discharge capacity as high as 1490 m Ah g^{-1} at a rate of 0.1C, with a good cycling stability up to 100 cycles and a very feeble capacity fading rate (0.5%) is achieved. This demonstrates the enhanced electrochemical performance of the ternary composite due to PIN coating.

2.2 Materials and Methods

2.2.1 Materials

MWCNT (Sigma Aldrich, 95% purity), indole monomer (Aldrich, 99% purity), FeCl_3 (Merck, 96%), sodium dodecyl sulphate (SDS, Merck, 99%), sodium

thiosulphate ($\text{Na}_2\text{S}_2\text{O}_3 \cdot 5\text{H}_2\text{O}$) (Merck, 99.5%), hydrochloric acid (HCl, Merck, 35%), nitric acid (HNO_3 , Merck, 69%), 1,3-dioxolane/1,2-dimethoxy ethane (DOL/DME, Sigma Aldrich), super P carbon (Alfa Aesar), polyvinylidenedifluoride (PVDF, Sigma-Aldrich), N-methyl pyrrolidone (NMP, Sigma-Aldrich) as Li metal (Foote Minerals), lithium nitrate (LiNO_3 , Sigma-Aldrich), bis(trifluoromethane)sulfonimide lithium salt (LiTFSI, Sigma-Aldrich), 2032 type coin cell, Al foil, polypropylene film (Celgard, 2400).

2.2.2 Composite synthesis

The MWCNT/S/PIN composite preparation is schematically represented in Figure 2.1. PIN was synthesized by chemical oxidative polymerization (S. An et al., 2008) of indole monomer using FeCl_3 as the oxidant. Oxidation of MWCNT was carried out using HNO_3 . MWCNT/S composite was prepared by a chemical precipitation method. Oxidised MWCNT was dispersed in sodium dodecyl sulphate aqueous solution in an ultrasonicated bath. $\text{Na}_2\text{S}_2\text{O}_3 \cdot 5\text{H}_2\text{O}$ was added and stirred for 10 minutes followed by dropwise addition of hydrochloric acid and stirred for 1 hour. The product was separated and dried under vacuum oven at 60 °C. To this material, 0.53 g of indole in 10 ml of ethanol was added, stirred for 10 minutes, then FeCl_3 was added to the reaction mixture dropwise in the N_2 atmosphere and stirred for 24 hours in 0 °C. The pristine polymer was prepared using indole and FeCl_3 (1:5). Finally, the product was dried in vacuum at 70 °C for 24 hours.

2.2.3 Material characterization

Powder X-ray diffraction (XRD) patterns were obtained with a Bruker D-8 diffractometer (Xpert Pro, Philips, USA) using $\text{Cu K}\alpha$ radiation over the 2θ range 10°- 80° (40 kV, 30 mA, $\lambda=1.54 \text{ \AA}$). The surface morphology of the composite was studied using a high-resolution scanning electron microscope (HRSEM, Quanta FEG200, FEI, USA) equipped with Energy Dispersive Spectroscopy (EDS) and elemental mapping. High-resolution transmission electron microscopy (HRTEM, JEM-2100, JEOL, and Japan) analysis was carried out with an acceleration voltage of 200 kV. Raman spectra were recorded from 100 to 3000 cm^{-1} on a Raman spectrometer (INVIA, England) with a 514 nm argon ion laser. Thermogravimetric

analyzer (TGA, Q-50, TA Instruments, and the USA) was used to collect the data at a heating rate of $10\text{ }^{\circ}\text{C min}^{-1}$ in the temperature range of $30\text{--}600\text{ }^{\circ}\text{C}$ nitrogen atmosphere. The composites were characterized using Fourier transform infrared spectrometer (FTIR, Perkin Elmer) with KBr pellet method. The presence of oxygen and nitrogen atoms in the composite was evaluated by Kratos–Analytical Axis Ultra X-ray photoelectron spectrophotometer (XPS) with a monochromatic Al-K α -X-ray source.

2.2.4 Fabrication of coin cell

The composite was mixed with super P carbon, PVDF in a weight ratio of 70:20:10 using NMP as the solvent. The slurry was coated on Al foil and dried in an oven at $60\text{ }^{\circ}\text{C}$ for 12 hours. The film was punched into a circular disk for assembling cell in a glove box with Ar atmosphere. The electrolyte was prepared by using 0.7 M LiTFSI and 0.07 M LiNO₃ in an equal volume of DME/DOL as a solvent. 2032 type coin cell was assembled using the composite film on Al foil as cathode and Li metal as an anode with the electrolyte, porous PP film as a separator. The areal mass loading of composite electrode is $\sim 2\text{ mg cm}^{-2}$.

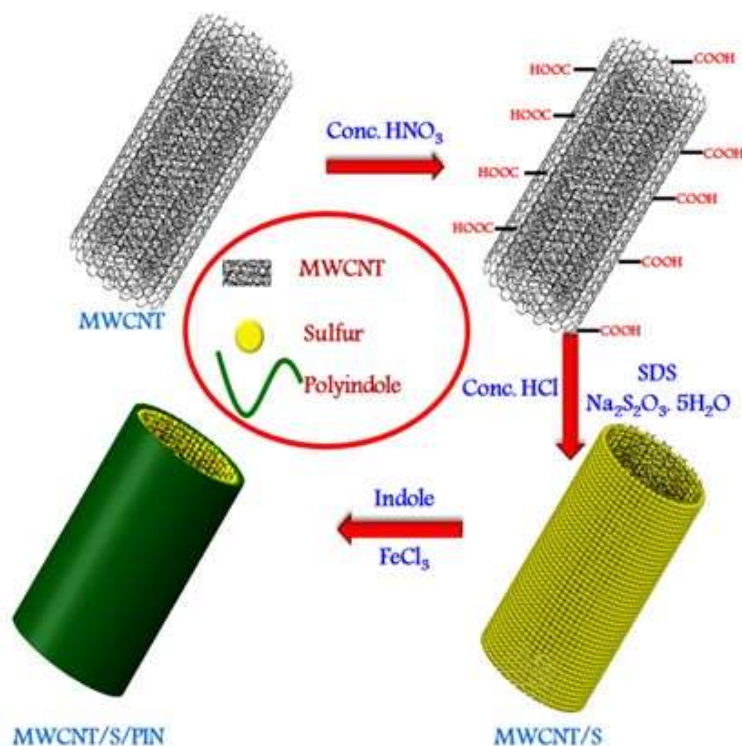


Figure 2.1. Schematic illustration of MWCNT/S/PIN composite preparation

2.2.5 Electrochemical measurements

The cyclic voltammetric (CV) studies were carried out using PGSTAT302N electrochemical workstation (Autolab, Metrohm, Switzerland). CV was performed in the potential window of 1.6 to 3 V at a scan rate of 0.1 mV s^{-1} . Electrochemical impedance studies (EIS) were carried out between 100 mHz and 100 kHz at the open circuit voltage. The galvanostatic charge-discharge (GCD) studies were conducted at a voltage range of 1.6-3 V using the computer controlled battery testing unit (Arbin, USA).

2.3 Results and Discussion

2.3.1 Material characterization

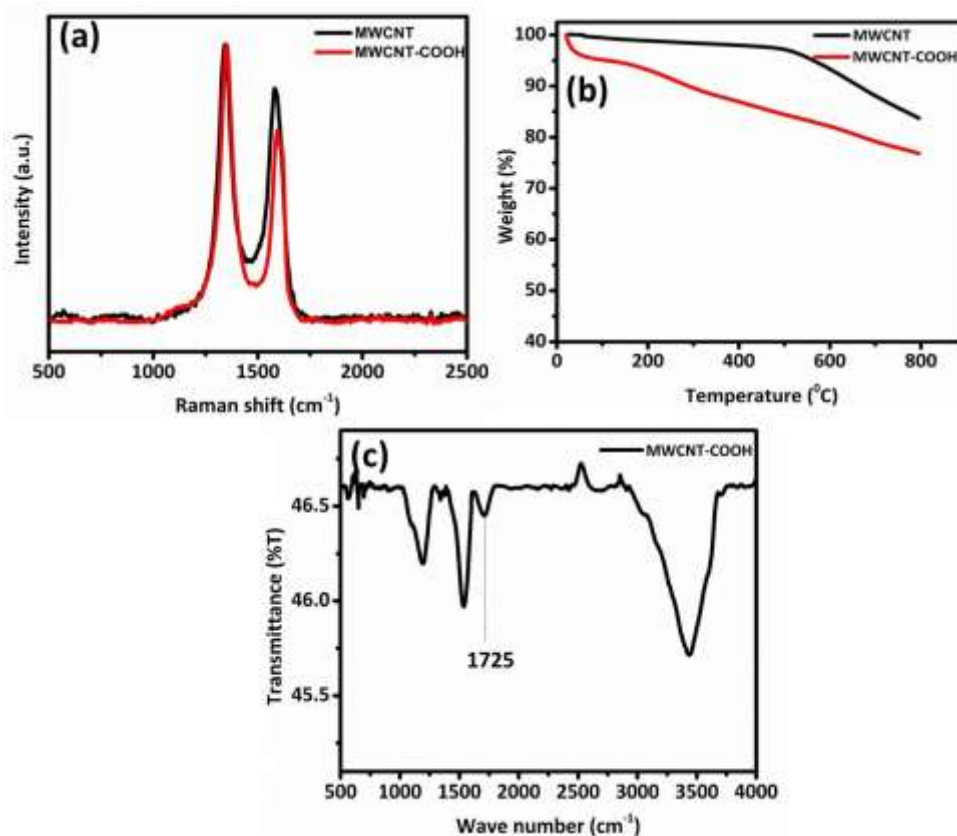


Figure 2.2. (a) Raman spectrum for MWCNT and functionalised MWCNT (b) TGA for MWCNT and functionalised MWCNT and (c) FTIR spectrum of functionalised MWCNT

To confirm the functionalization of carboxylic acid on the walls of MWCNT Raman spectroscopy, TGA and IR spectroscopy was employed (Figure

2.2). Figure 2.2 (a) shows the Raman spectrum of MWCNT and functionalised MWCNT. It contains two bands at 1345 cm^{-1} called D band or disordered band and at 1549 cm^{-1} called G band or graphitic band. It was observed that the G band intensity reduced after chemical modifications of MWCNT, suggesting the surface modification of carbon nanotube after acid treatment.

The carboxylated carbon nanotube has less thermal stability than pristine MWCNT (Figure 2.2 (b)). A decomposition observed below $100\text{ }^{\circ}\text{C}$ due to the elimination of water from the sample. A sharp decomposition observed in the case of carboxylated carbon nanotube in the temperature range of $130\text{ }^{\circ}\text{C}$ to $350\text{ }^{\circ}\text{C}$ is an evidence for the presence of carboxylic acid on the surface of MWCNT. Figure 2.2 (c) shows the IR spectrum for the carboxylated MWCNT. The peak at 1722 cm^{-1} is due to the carbonyl stretching in the carboxylic acid. It confirms the presence of carboxylic acid over the surface of MWCNT.

FTIR spectroscopy is used to determine the presence of PIN in the composite. The characteristic peaks in the IR spectra of PIN (Figure 2.3 (a)) are in good agreement with the literature reports (S. An et al., 2008; Reshma and Mary Gladis, 2015; Zhijiang and Chengwei, 2011). The strong and broad peak at 3437 cm^{-1} is the characteristic absorption of the N–H bond. The band at 1368 cm^{-1} is related to modes involving the C8–N–C2–C3 group. The band at 741 cm^{-1} indicates that the benzene ring is not affected during the polymerization process of indole. The single peak located at 1450 cm^{-1} is assigned to the stretching of the benzene ring. The band at 1621 cm^{-1} is ascribed to the C–C vibration on indole ring. The above mentioned characteristic peaks for polyindole are also observed in the MWCNT/S/PIN which confirms the formation of polyindole on the surface of MWCNT/S composite.

Figure 2.3 (b) shows the TGA analysis of polyindole, functionalized MWCNT, sulphur, MWCNT/S and MWCNT/S/PIN under a nitrogen atmosphere. The composites display weight loss from $118\text{ }^{\circ}\text{C}$ to $240\text{ }^{\circ}\text{C}$ due to the evaporation of sulphur from the composite. Polyindole undergoes continuous weight loss up to $400\text{ }^{\circ}\text{C}$ due to its gradual decomposition. The sulphur content is calculated after eliminating the weight loss due to polyindole and functionalized MWCNT (C. Wang

et al., 2013). The sulphur content of MWCNT/S and MWCNT/S/PIN is about 83.4 wt. % and 79.06 wt. %, respectively.

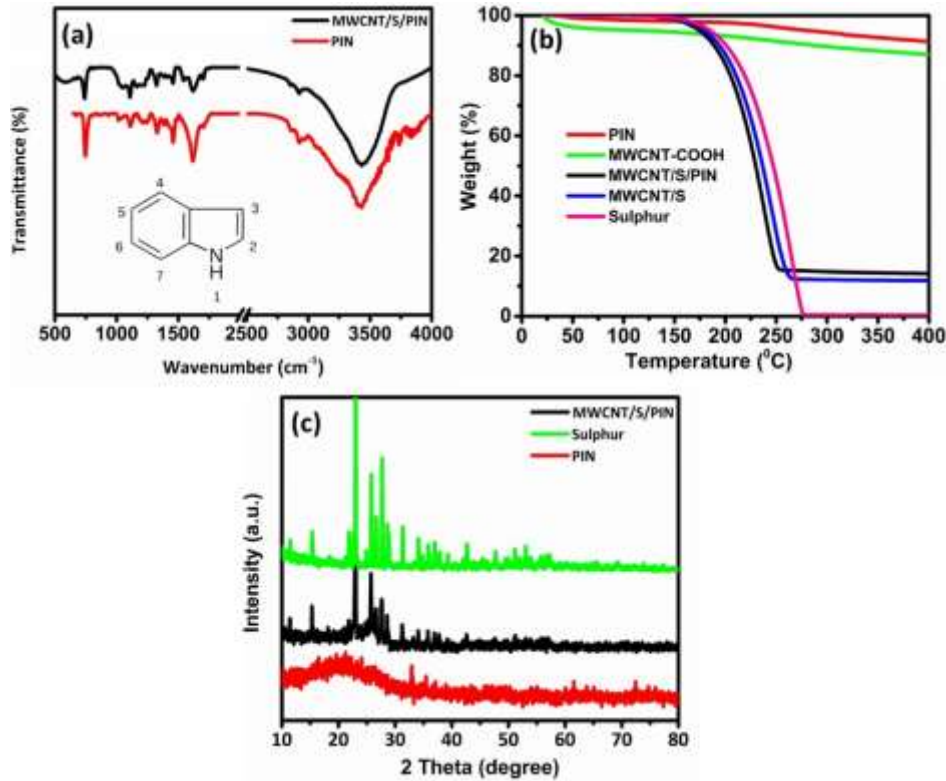


Figure 2.3. (a) FTIR spectrum of the PIN and MWCNT/S/PIN (b) TGA of PIN, MWCNT-COOH, MWCNT/S/PIN, MWCNT/S and Sulphur (c) XRD of sulphur, MWCNT/S/PIN and PIN

Figure 2.3 (c) shows the XRD patterns of sulphur, as prepared polyindole and MWCNT/S/PIN. The broad peak at $2\theta=20^\circ$ exhibits the amorphous nature of the polymer (Raj et al., 2015; Ryuand Kim, 2008). The peaks at 2θ values of 23.08° , 25.73° , 27.66° , 28.75° , 31.36° , 34.10° and 36.98° are in good agreement with the (222), (026), (117), (135), (044), (137) and (317) reflections of the Fddd orthorhombic phase (JCPDS No.: 00-001-0478) of sulphur. The sharp and intense diffraction signals indicate the crystallines of sulphur. XRD pattern of MWCNT/S/PIN exhibits similar diffraction pattern as that of sulphur but with low intensity, evidenced that sulphur is coated with the PIN.

Figure 2.4 (a and b) gives surface morphology of MWCNT/S/PIN and MWCNT/S composites. Figure 2.4 (c–f) displays the elemental mapping of MWCNT/S/PIN. It is observed that the MWCNT/S and MWCNT/S/PIN

composites have a tubular structure with no agglomerated sulphur particles. It is difficult to differentiate between sulphur and PIN coatings from the micrograph. The elemental distribution maps assert that polyindole is coated onto MWCNT/S composite.

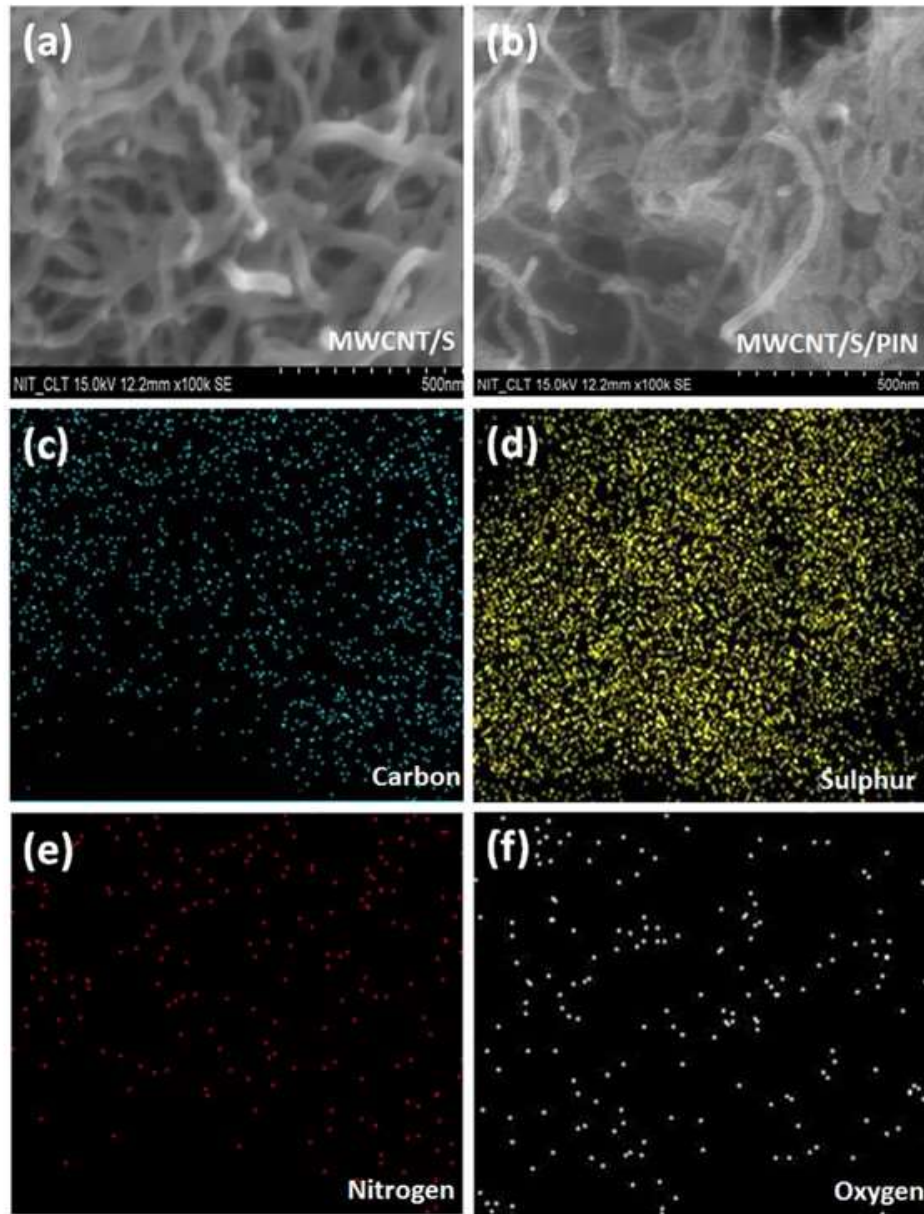


Figure 2.4. SEM images of (a) MWCNT/S, (b) MWCNT/S/PIN and (c-f) Elemental mapping of MWCNT/S/PIN

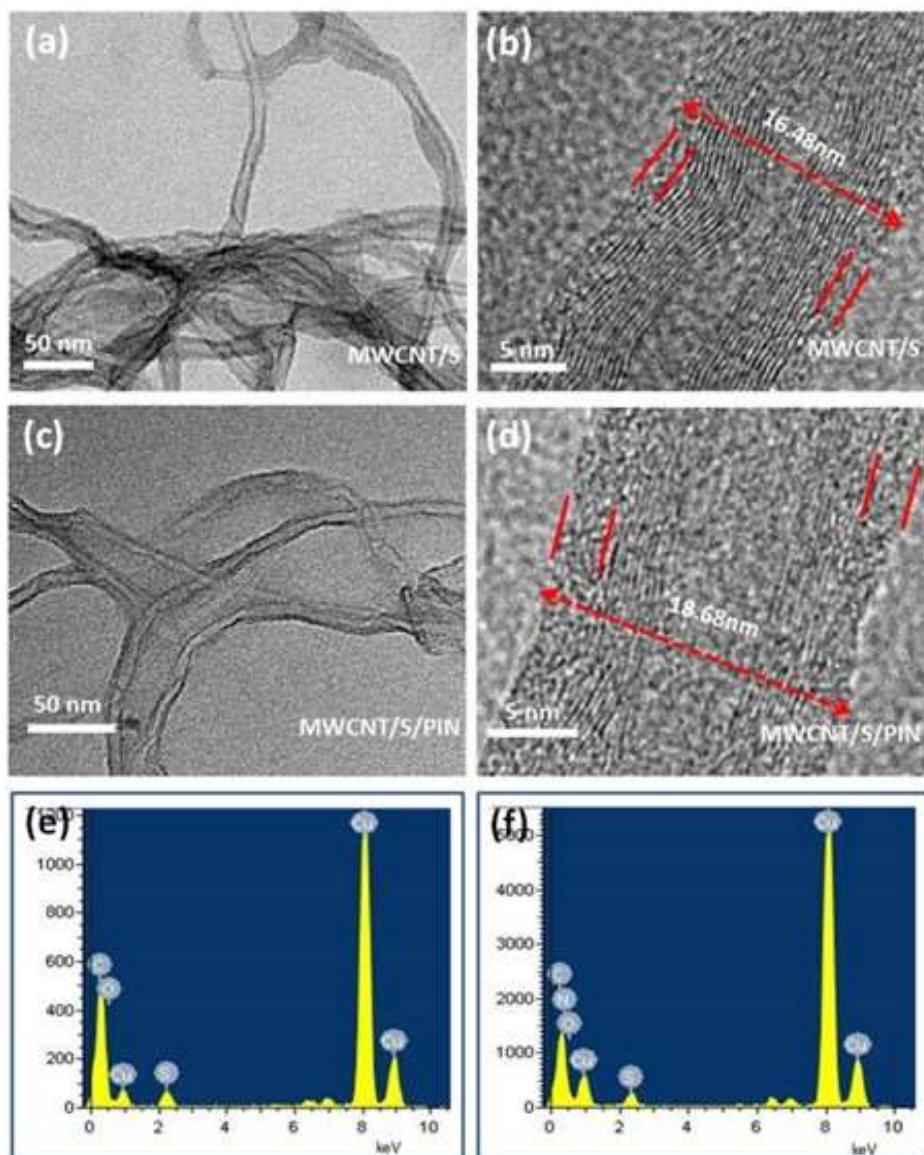


Figure 2.5. TEM images of (a-b) MWCNT/S, (c-d) MWCNT/S/PIN, EDS analysis of (e) MWCNT/S and (f) MWCNT/S/PIN

It is further confirmed by the TEM images of MWCNT/S and MWCNT/S/PIN composites as shown in Figure 2.5. It is observed that the sulphur is coated over the surface of MWCNT and increase in tube diameter affirms the information obtained from SEM. A thin layer of polyindole is wrapped over the surface of MWCNT/S attributed to the coating of polyindole onto MWCNT/S, which further confirms the dual core-shell structure. The thickness of the ternary composite is increased after polymerization. Moreover, TEM images display (Figure 2.5 (d)) a thickness increase of ~ 2 nm in the ternary composite after polyindole coating. It is clearly seen in the EDS analysis, the presence of sulphur,

oxygen and sulphur, nitrogen, oxygen in the binary and ternary composite, respectively (Figure 2.5 (e and f)).

A wide scan energy spectrum for the MWCNT/S/PIN indicates the presence of C, O, N and S which agrees well with the elemental mapping. The survey scan (Figure 2.6 (a)) reveals the presence of C1s, O1s, N1s, S2s and S2p in the composite. The peak at 164 eV, 240 eV, 285.1 eV, 400 eV and 533.1 eV corresponds to the S2p, S2s, C1s, N1s and O1s, respectively (L. Chen et al., 2017). The high-resolution C1s (Figure 6.6 (b)) peak deconvoluted into 5 components, C-C bond (284.6 eV) of sp^2 , C-O bond, C-S bond (285.8 eV), C-N bond (286.7 eV) and O-C=O bond (289.1 eV) (Datsyuk et al., 2008; Niu et al., 2015). The high resolution O1s spectrum (Figure 2.6 (c)) is deconvoluted into three components: C-O bond (531.43 eV), C=O bond (532.55 eV) and carboxyl (533.6 eV) (Datsyuk et al., 2008; Roy et al., 2014). The N1s spectrum (Figure 6.6 (d)) contains two contributions at 399.6 eV and 401.68 eV (Koiry et al., 2007) which are assigned to the N-C and N-H bonds. These results are in good agreement with the FTIR spectra. The presence of pyrrolic nitrogen may influence the electrochemical properties. The basic pyrrolic nitrogen (N-H) in the composite enhances the adsorption of polysulphides through its interaction with nitrogen atoms. Moreover, this five-membered pi system with lone pairs enhance the surface adsorption sites for polysulphides. (J. Yang et al., 2014; Xia Liand Sun, 2014) The high resolution spectra of S2p (Figure 2.6 (e)) is deconvoluted into four peaks. S2p_{3/2} (163.7 and 164.9 eV) and S2p_{1/2} (164.2 and 165.4 eV) with an energy separation of 1.2 eV corresponds to the S-S and S-O bond in the composite (L. Zhang et al., 2012; G. Zhou et al., 2013). This binding energy shift ascribed to the changes in the electronic distribution on the sulphur atom evidenced the binding between the sulphur and functionalized MWCNT via S-O bond, which helps to prevent active material loss by trapping the polysulphides during charge-discharge process (Demir-Cakan et al., 2011; W. G. Wang et al., 2014).

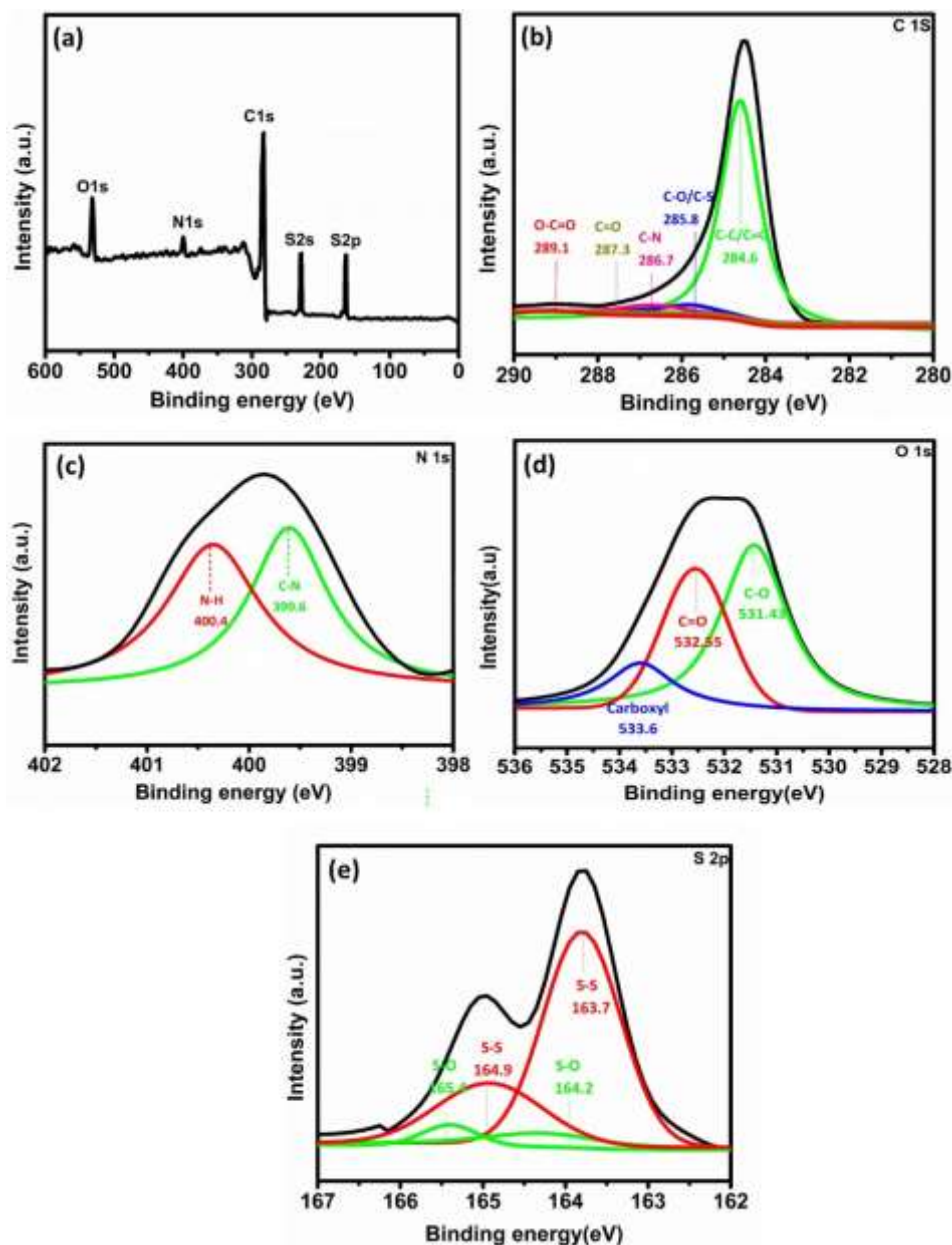


Figure 2.6. XPS for MWCNT/S/PIN (a) survey scan, (b) C1s, (c) N1s, (d) O1s and (e) S2p

2.3.1 Electrochemical performance of the composite

The Cyclic voltammetry studies of MWCNT/S and MWCNT/S/PIN composite electrode was carried out at a scan rate of 0.1 mV s^{-1} to understand the electrochemical reaction of nanocomposite cathode in between the voltage window of 1.6-3 V. Two reduction and one oxidation peaks are observed (Figure 2.7 (a & b)) in both the composites due to multiple reactions between sulphur and lithium, as reported previously (Y. Zhang, Y. Zhao, and Z. Bakenov, 2014). The cathodic

peak at 2.37 V is due to the conversion of octaatomic sulphur to higher order lithium polysulphides (Li_2S_n , $4 \leq n \leq 8$), further reduction at 2.0 V is due to the conversion of these higher order polysulphides to lower order polysulphides (Li_2S_n , $3 \leq n \leq 4$) finally into insoluble Li_2S_2 and Li_2S (K. Fu et al., 2014; J. Jiang et al., 2015; N. Li et al., 2012; Y.-X. Wang et al., 2013; Y. Zhang, Y. Zhao, and Z. Bakenov, 2014). The subsequent oxidation process is provided with a broad oxidation peak at 2.42 V mainly due to the conversion of Li_2S_2 and Li_2S to higher order polysulphides and finally to sulphur (J. Lee et al., 2015; Pan et al., 2015; S. Zhang et al., 2014). The increase in peak intensity of MWCNT/S/PIN composite is attributed to good electrochemical contact which in turn boosts the utilization of active material (K. Fu et al., 2014; J. Jiang et al., 2015; N. Li et al., 2012; Y.-X. Wang et al., 2013; Y. Zhang, Y. Zhao, and Z. Bakenov, 2014). The increment in the peak area compared to the binary composite proves the increase in active material utilisation (J. Feng et al., 2016; Zhijiang et al., 2013). Also, the CV curves are more stable in the subsequent cycles indicating better cyclability. The result obtained from the CV is in good agreement with GCD curves.

Figure 2.7 (c & d) represents the typical GCD behaviour of MWCNT/S and MWCNT/S/PIN composite electrode in rechargeable LSB at room temperature. The figure shows charge-discharge capacities of 1, 2, 10, 20, 30, 40, 50, 60, 70, 80, 90 and 100th cycles of ternary and binary composites. The performance of the MWCNT/S/PIN composite is enhanced due to polyindole coating compared to MWCNT/S. Ternary composite delivered an initial capacity of 1490 mA h g⁻¹ with an average capacity degradation of 0.5% per cycle and 70% capacity retention with respect to initial discharge capacity, and 97% with respect to 50th discharge capacity up to 100 cycles. But in the case of the binary composite, an initial discharge capacity of 1267 mA h g⁻¹ with 61% capacity retention with respect to initial discharge capacity is observed. PIN coating onto the composite prevents the loss of active material by blocking the PSs. The nitrogen atoms in the polyindole is helpful to prevent the loss of sulphur as PSs during cycling and continuous utilization of sulphur in the composite (Demir-Cakan et al., 2011; W. G. Wang et al., 2014; Xia Liand Sun, 2014). The coulombic efficiency of MWCNT/S/PIN cathode (~100%)

is higher than that of MWCNT/S (~97%), due to the reduction in the shuttling behaviour of PSs (Figure 2.7 (e)).

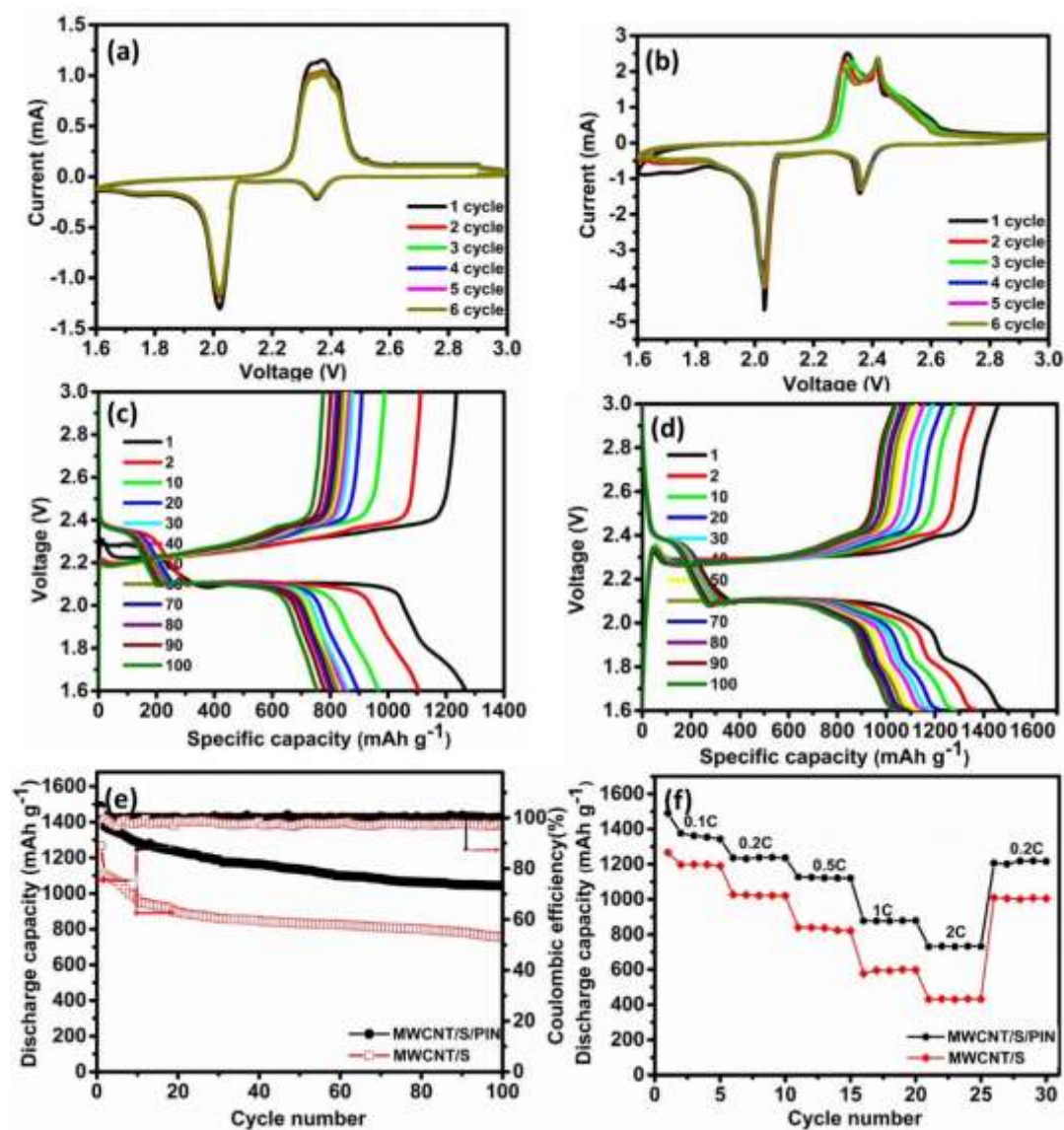


Figure 2.7. CV curves in the first six cycles of (a) MWCNT/S (b) MWCNT/S/PIN (c) GCD pattern of (c) MWCNT/S (d) MWCNT/S/PIN at 0.1C rate (e) Cycle performance and coulombic efficiency for MWCNT/S and MWCNT/S/PIN at 0.1C rate and (f) Rate capability studies for MWCNT/S and MWCNT/S/PIN

The electrochemical performance of the binary and ternary composites at different current densities were investigated in detail, which is shown in Figure 2.7(f). The ternary composite exhibits excellent performance at different C rates when compared with the binary composite. The initial discharge capacity is 1490 mA h g⁻¹ at the 0.1C rate. It exhibits 1236, 1124, 878 and 730 mA h g⁻¹ at the current densities of 0.2C, 0.5C, 1C and 2C, respectively. When returned to 0.2C rate its

discharge capacity retained to 1218 mA h g⁻¹ with 98.5% capacity retention which indicates robustness and stability of ternary composite.

The binary composite shows the discharge capacities of 1232, 1024, 840, 590 and 430 mA h g⁻¹ at 0.1C, 0.2C, 0.5C, 1C and 2C, respectively when switched back to 0.2C discharge capacity becomes 996 mA h g⁻¹. The high solubility of LPSs in the electrolytes greatly influence the cyclic stability of LSBs, insulating nature of sulphur and lowest end discharge products, which will also negatively affect the performance of composites when we switched into higher current rates. Herein the case of ternary composite both MWCNT and PIN provides an effective conducting network to move electrons, thereby enhance the rate performance. The superior performances of the ternary composite are due to the polyindole coating and MWCNT to confine the PSs from dissolving into the electrolyte. Here, sulphur is sandwiched between polyindole and MWCNT. Such a protective thin layer coating is absent in the case of the binary composite, and sulphur deposited over the surface of MWCNT. Consequently, there exist more chances to lose sulphur as PSs due to dissolution in the electrolyte and therefore reduce its performance.

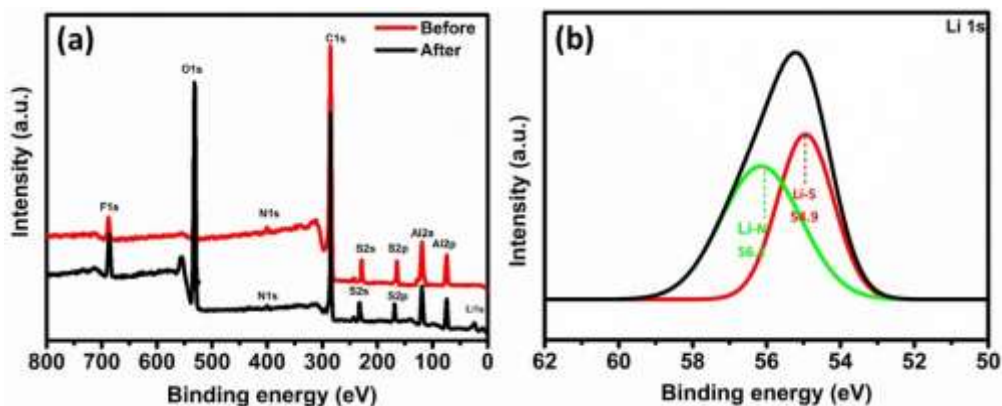


Figure 2.8. (a) Survey scan of cathode before and after cycling and (b) High-resolution Li1s spectra of cathode after 100 cycles

XPS spectra of electrodes MWCNT/S/PIN cathode before and after 100 cycles was carried out to support this rationalization as shown in Figure 2.8. The presence of aluminium and fluorine in the survey scan spectrum (Figure 2.8 (a)) are due to the Al collector and PVDF binder in the cathode. There is changes in the binding energy of N1s from 400 eV to 399.43 eV ascribing the interaction of Li with the lone pair in the N. The high-resolution spectra of Li1s are deconvoluted

into two components (Figure 2.8 (b)). The peak at 54.9 eV is ascribed to electrons in the lithium sulphide. The interaction between lithium and nitrogen in the polyindole is proved by the peak at 56.1 eV which corresponds to Li-N bond. (F. Chen et al., 2018; X. Fan et al., 2018; Xia Li and Sun, 2014; Seh et al., 2014). These interactions favour polyindole to restrain the discharge products. Further, the conductive nature of PIN helps to enhance the utilization of active material (Su and Manthiram, 2012a; C. Wang et al., 2014; Jiawei Zhang et al., 2015).

Table 2.1: Comparison of performance for MWCNT/sulphur/conducting polymer materials reported previously

Sl no.	Cathode materials	Current rate /Current density	Cycles	Final capacity (mA h g ⁻¹)	Capacity retention (%)	References
1	MWCNT/S/PANI	0.1C	80	932.4	56.3	F. Wu, Chen, Li, et al., 2011
2	MWCNT/S/PANI	0.2C	100	600	61.8	X. Li et al., 2015
3	MWCNT/S/PPy	200 mA g ⁻¹	60	917	60	C. Wang et al., 2013
4	MWCNT/S/PPy	0.2C	100	751	60	Y. Zhang, Y. Zhao, Z. Bakenov, et al., 2014
5	MWCNT/S	0.1C	100	772	61	Our work
6	MWCNT/S/PIN	0.1C	100	1043	70	Our work

The electrochemical performance of ternary composite is significantly greater than the control material–MWCNT/S, and other ternary composites reported elsewhere (Table 2.1) (X. Li et al., 2015; C. Wang et al., 2013; F. Wu, Chen, Li, et al., 2011; Y. Zhang, Y. Zhao, Z. Bakenov, et al., 2014). Wu et al reported a coating of polyaniline over the binary composite MWCNT/S exhibited 932.4 mA h g⁻¹ after 80 cycles and 56.3% capacity retention with respect the initial discharge capacity at the 0.1C rate (F. Wu, Chen, Li, et al., 2011). Similarly, Li et al studied sulphur supported with MWCNT and coated with polyaniline (~600 mA h g⁻¹ after 100 cycles) with 61.8% capacity retention at the 0.2C rate (X. Li et al.,

2015). A dual core-shell structured cathode material using MWCNT and polypyrrole exhibited capacity of 917 mA h g^{-1} after 60 cycles and 60% capacity retention at a current density of 200 mA g^{-1} was described by Wang et al (C. Wang et al., 2013). Another type of MWCNT and polypyrrole reported by Zhang et al displayed a reversible capacity of 751 mA h g^{-1} after 100 cycles, with 60% capacity retention at 0.2C rate (Y. Zhang, Y. Zhao, Z. Bakenov, et al., 2014).

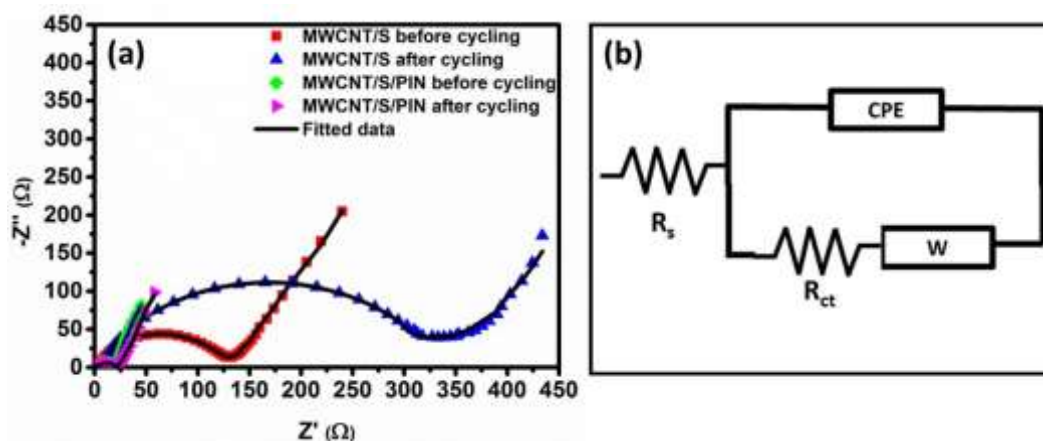


Figure 2.9. (a) EIS of MWCNT/S and MWCNT/S/PIN before and after 100 cycles at a 0.1C rate and (b) corresponding equivalent circuit

Table 2.2: Impedance parameters obtained from the electrochemical equivalent circuit analysis

Material description	R_s (Ω)	CPE $\times 10^{-5}$ (Ω^{-1})	R_{ct} (Ω)	Y_0 $\times 10^{-6}$ ($\Omega^{-1} \text{ s}^{1/2}$)
MWCNT/S before cycling	7.6	4.8	129.13	8.9
MWCNT/S after cycling	5.4	3.8	323.22	4.32
MWCNT/S/PIN before cycling	0.61	14446	18.82	7400
MWCNT/S/PIN after cycling	0.66	17	20.47	7200

To investigate the superior performance of MWCNT/S/PIN over MWCNT/S, EIS measurements were carried out at OCV. Figure 2.9 shows Nyquist plots (EIS spectra) of ternary composite and binary composite before and after 100 cycles. The EIS spectra was fitted by electrochemical equivalent circuit with ZSimpWin software (Figure 2.9(b)). The longest diameter of an impedance semicircle at the high-frequency region is associated with higher charge transfer resistance (R_{ct}) and straight line at low-frequency region corresponds to ion diffusion resistance (W) within the cathode (C. Wang et al., 2013; G.-L. Xu et al., 2013; S. Zhang et al., 2014; H. Chen et al., 2013; Y. Fu and Manthiram, 2012c). The resistance of the electrolyte (R_s) determined from the intersection of the front

end of the semicircle on the Z' axis. R_{ct} is the measure of the difficulty in transfer the electron/charge between the electrode and electrolyte interface. CPE is the constant phase element, which is associated with the non-ideal behaviour of capacitance. The impedance parameters are shown in the Table 2.2. Here the Warburg impedance is written in terms of admittance ($Y_0, \Omega^{-1} s^{1/2}$), which is related to Warburg coefficient, $\sigma = \frac{1}{\sqrt{2} Y_0}, \Omega s^{-1/2}$. As shown in Table 2.2 R_{ct} and ion diffusion resistance of ternary composite is less than the binary composite before and after cycling, which is expected due to its high initial discharge capacity. Sulphur is sandwiched between conducting MWCNT and polyindole, facilitating an easy pathway to electron transfer.

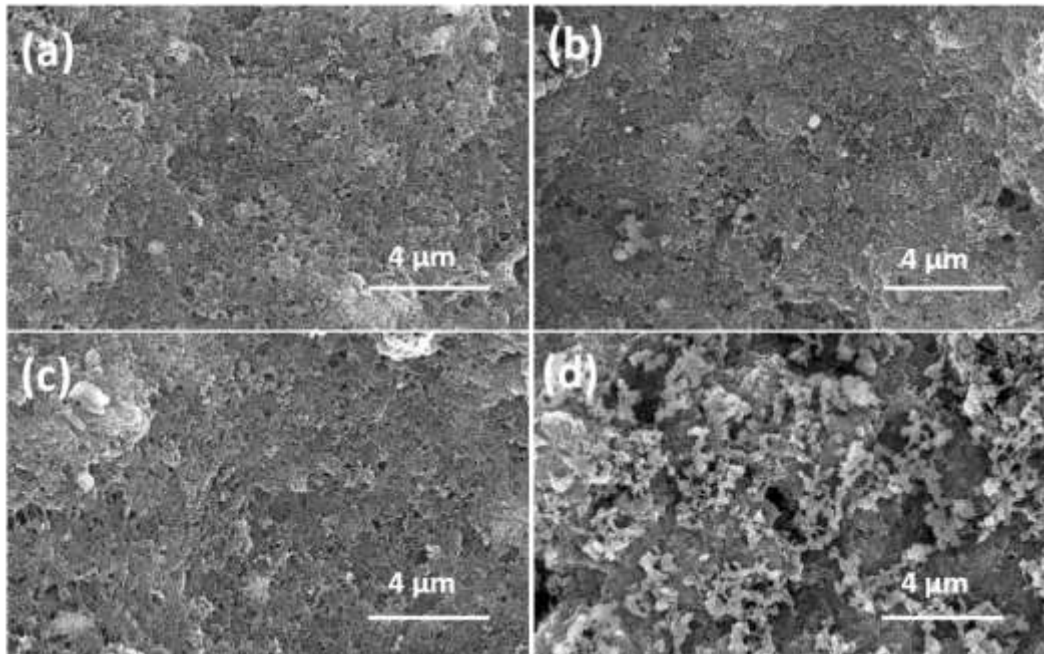


Figure 2.10. SEM images of (a) MWCNT/S/PIN before cycling (b) MWCNT/S/PIN after cycling (c) MWCNT/S before cycling and (d) MWCNT/S after cycling

In the case of binary composite the R_{ct} and ion diffusion resistance increases due to the dissolution of PSs in the electrolyte and the irreversible deposition of discharge products (Li_2S/Li_2S_2) leading to loss of active materials (J. Feng et al., 2016; C. Wang et al., 2014). The negligible change in the R_{ct} and ion diffusion resistance of ternary composite ascribed to the conductive architecture surrounded by sulphur maintains its structural integrity during the charge-discharge process (C. Wang et al., 2014; Jiawei Zhang et al., 2015). Moreover, the porous

structure of conducting polyindole helps easy transport of Li^+ ions. It is further supported by the similar morphology of ternary composite cathode even after 100 cycles (Figure 2.10). The changes on the surface of the binary composite cathode are attributed to the impact of electrochemical reactions resulting in the increased R_{ct} values (Su and Manthiram, 2012a; C. Wang et al., 2013). The reason for the better rate capability and cyclability of the ternary composite is correlated with low charge transfer and diffusion resistances. Also, there is sufficient interaction among MWCNT and polyindole with sulphur which enhances the electronic conduction.

2.4 Conclusion

In summary, a novel ternary composite MWCNT/S/PIN was prepared by in situ oxidative polymerization of indole onto MWCNT/S. It is a promising cathode material for LSB. The electrochemical performance has been improved especially, specific capacity, cyclability and rate capability by wrapping polyindole on sulphur. It may be due to reduced charge transfer resistance of the material, which facilitates easy transport of lithium ion into the cathode material and reduced shuttling effect. MWCNT/S/PIN composite attains 1490 mA h g^{-1} initial capacity and 1043 mA h g^{-1} reversible capacity after 100 cycles at 0.1C with 100% columbic efficiency. The good electrochemical performance is due to the functionalized MWCNT/S/PIN dual core-shell type structure, both MWCNT and polyindole are supporting to trap the PSs and to enhance the capacity retention during cycling.

CHAPTER 3

4, 4'-DIAMINO-DIPHENYL SULPHONE DERIVED CARBON FOR SUPERCAPACITOR ELECTRODE AND LITHIUM-SULPHUR BATTERY

Carbon materials with favourable porous architecture and heteroatom functionalities are considered for energy storage applications due to its excellent structure and electrochemical properties. In this chapter, porous carbon-composite cathode for LSB and an all solid-state symmetric SC using heteroatom (nitrogen and oxygen) inherently co-doped microporous carbon (HMC) was investigated. HMC was prepared by simple carbonization without any additives and multistep experimental procedures. 4, 4'-diamino-diphenyl sulphone (DDS) was pyrolyzed at 950 °C in a single step and HMC with surface area of 1766 m² g⁻¹ and a total pore volume of 0.87 cm³ g⁻¹ was obtained. The structural characteristics and the content of heteroatom functionalities are manipulated with pyrolysis time to improve the electrochemical behaviour. The prepared carbon material-sulphur composite was demonstrated as cathode material for LSB. These materials exhibited better capacity retention due to the synergistic effect of porous carbon with high surface area, pore volume, heteroatom N and O, which facilitate to restrain the PS movement. The symmetrical supercapacitor was fabricated with polyvinyl alcohol (PVA) supported 6M KOH and 1M Na₂SO₄ as gel electrolytes. The performance of solid-state supercapacitors showed good cycling stability and high energy density. Finally, the device using porous carbon electrode material with PVA+1M Na₂SO₄ able to light a LED after charging of ~5sec.

3.1 Introduction

LSBs and SCs have been considered as the most prospective energy storage devices with ample potential applications (Borenstein et al., 2017; C. Xu et al., 2013; Zan Gao et al., 2017). Amongst the various materials, carbon-based electrodes are usually studied extensively owing to their high specific surface area, tunable microstructure, low density, low cost, electronic conductivity and chemical stability (Borenstein et al., 2017; Bose et al., 2012). Porous carbons, carbon onions, carbon sphere, carbon aerogel, carbon nanotube and graphene are the commonly used carbon electrodes in the high-performance LSBs and SCs (Borenstein et al., 2017; Dubal et al., 2018; X. Fan et al., 2018; C. Xu et al., 2013; Z. Yu et al., 2015). Among these, porous carbon-based electrode materials are most interested, due to

the simple preparation process, tunable morphologies and high surface area (Stein et al., 2009; François et al., 2014; D.-W. Wang et al., 2013; Yunpu et al., 2011; S. S. Zhang, 2015).

High surface area carbons with the wide pore size distribution are highly explored to improve the electrochemical performance by employing new synthetic approaches for the development of porous carbon with diverse precursors. The distribution of micro to macropore size, shape, and its interconnectivity affect the mass transport and diffusion of ions. If the micro/mesopores are too narrow/deep, it is difficult for the ions to penetrate into the pores for the contribution towards EDLC. However wide and shallow pores ease the pathway of ion diffusion. (Fuertes and Sevilla, 2015; Y. Lu et al., 2017). To achieve such micro/mesoporous carbon with desired structure several approaches are reported, which includes carbonization at high temperature (Fuertes and Sevilla, 2015) methods using soft and hard templates (Y. Lu et al., 2017), template carbonization followed by activation (Bhattacharjya and Yu, 2014), bio-inspired methods (C. Zhang et al., 2016), etc. In comparison with SCs, LSBs can provide high energy density (2600 Wh kg^{-1}) (Zan Gao et al., 2017). However, PS shuttling during the charge-discharge process is the major problems associated with LSBs, causing capacity fading and poor cyclability. Various materials developed to address this issue and to improve the electrochemical performance of the LSBs by encapsulating sulphur within the matrix. Carbon nanotube (J.-z. Chen et al., 2014; Juchen Guo et al., 2011), rGO (N. Li et al., 2012; S. Liu et al., 2016), metal oxides (Donghai et al., 2018), conducting polymers (Dirlam et al., 2017) and hybrid materials (Yibo He, Chang, et al., 2018) were tried to alleviate Ps shuttling. LSBs still have shortcomings in terms of sulphur content and the capability of composite to hold sulphur/PS (H. Chen et al., 2018). In chapter 2, we used the PIN coating to improve the LSB performance, However, the PIN coating was not thick enough to capture all the PS during the shuttling process and non-uniform coating of PIN onto sulphur, resulting loss of active material, capacity fading as the cycle number increased.

Recently heteroatoms like N, B, P, O, and S doped carbon network received significant attention due to its enhanced electrochemical properties (Y.

Deng et al., 2016; Paraknowitsch and Thomas, 2013; M. Xu et al., 2017; S. S. Zhang, 2015; G. Zhu et al., 2017). The inclusion of heteroatoms in the hexagonal rings of carbon improves the conductivity, basicity and oxidation stability via conjugation between the lone pairs and π -system of the carbon network. Heteroatom doped carbons are utilized for various applications like catalysis, fuel cells, Li-ion batteries, and adsorption (Paraknowitsch and Thomas, 2013; M.-H. Sun et al., 2016). The presence of heteroatom functionalities improves the electron-donor capability, thereby enhances polarity and wettability of the carbon surfaces, causing variation in an electrode-electrolyte contact area which further reduces the diffusion path length and support to improve the electrochemical performances (X. Kang et al., 2018; Xin Zhou et al., 2017). Heteroatoms enhance the electronic conductivity and contribute towards pseudocapacitance and facilitate PS mitigation (Paraknowitsch and Thomas, 2013; Wang Yang et al., 2018; S. S. Zhang, 2015). Heteroatoms can be introduced into the carbon framework by in-situ pyrolysis of heteroatoms containing compounds or post-treatment of carbonaceous material with heteroatoms containing gas. Post-treatment may cause the destruction of carbon morphology and unwanted pore stalling (Yanzhen He et al., 2016; S. Zhang et al., 2015). The organic precursors used for in-situ pyrolysis are PANI (Yudong Li et al., 2017), PPy (L. Wei et al., 2012) and protic salts 1, 10-phenanthroline dicationic bisulfate (Shiguo et al., 2015), benzimidazole triflate (Mendes et al., 2016), in which multistep synthetic procedures, templates/metal salts/oxidizing agents are used during carbonization. In some cases, a trace amount of impurities are detected in the resultant carbon materials. A major challenge in the preparation of in-situ doped porous carbon is the instability of the organic precursors during the carbonization process. The structural stability of the carbon material greatly influences the final heteroatoms content, graphitic structure, surface area, electronic conductivity, etc. (C. H. Kim et al., 2004; Y. Zhai et al., 2008). We report a simple method for the preparation of a three dimensional hierarchical porous carbon-containing in-situ doped sulphur, oxygen and nitrogen through a single step carbonization process and its application as an electrode material for LSBs and SCs.

In this chapter, we employed 4, 4'-diamino-diphenyl sulphone (DDS) as a carbon source for the first time. DDS has been widely reported as a precursor material for the preparation of Polyimide and epoxy resin (Konnola et al., 2015). DDS is beneficial to use as a carbon resource for the synthesis of the high surface area and well balanced porous structured material. The gases evolved during the carbonization process are responsible for the considerable amount of the pore formation (Mendes et al., 2016; L. Wei et al., 2012; S. Zhang et al., 2015). Heteroatom doped micro/mesoporous carbon (HMC) with inherently doped, N and O functionalities was prepared via simple carbonization without any sophisticated/multistep experimental procedures using DDS as a precursor material. The effect of pyrolysis time on the content of heteroatoms and pore formation is investigated. The prepared electrode materials were characterized structurally and electrochemically. HMC-sulphur composite cathode was demonstrated as a cathode material to enhance the cyclability. The porous structure with inherent hetero atom doping can facilitate effective accommodation of elemental sulfur and strong confinement of LPS. The subsequent electrochemical measurements confirmed the improved specific capacity and cycling stability of the cell. The N heteroatom doping induces the pseudocapacitance and boosts the performance of the SC (F. Hu et al., 2016; J. Li et al., 2016; Yiju Li et al., 2016). The performance characteristics of the SCs have been evaluated by EIS, CV and GCD analysis in aqueous electrolyte (6M KOH). The symmetrical SC was fabricated with PVA supported 6M KOH and 1M Na₂SO₄ as gel electrolytes and evaluated.

3.2 Materials and Methods

3.2.1 Materials

4, 4'-diamino-diphenyl sulphone (DDS, Merck, 99%), polyvinyl alcohol (PVA, Merck, 99%), potassium hydroxide (KOH, Merck, 99%), sodium sulphate (Na₂SO₄, Merck, 99%) and all other chemical are as mentioned in chapter 2. 2.1.

3.2.2 Material synthesis

3.2.2.1 Preparation of porous carbon

4, 4'-diamino-diphenyl sulphone was used as a novel precursor material to prepare microporous carbon material with heteroatoms (HMC). DDS powder was carbonized at 950 °C at the pyrolysis timings of 1, 2 & 3 h in a heating rate of 2 °C min⁻¹ in an inert atmosphere. The schematic representation of the preparation of HMC is given in Figure 3.1.

3.2.2.2 Preparation of porous carbon-sulphur composite

Heteroatom doped microporous carbon-sulphur composites (HMC-1S and HMC-2S) were prepared by melt diffusion method. The carbon and sulphur were mixed using an agate mortar with 1:3 ratio (w/w). Then, the composite was heated to 155 °C in an inert atmosphere for 12 hours in a sealed vessel. During this process, sulphur melts and diffuses into the pores of carbon (Figure 3.1).

3.2.3 Material characterization

Nitrogen adsorption-desorption studies were carried out using a surface area analyzer (Gemini 2375, Micromeritics, USA). The specific surface area and pore size distribution of HMCs and HMCS were obtained using Brunauer, Emmett and Teller (BET) method and Density functional theory (DFT), respectively. The amount of C, H, N and S were characterized by using CHNS elemental analyser (Elementar VarioMICROselect, Germany) and other characterization tools were as discussed in the section 2.2.3.

3.2.4 Electrochemical measurements

3.2.4.1 Sulphur cathode preparation and characterization

The HMC-1S and HMC-2S cathodes were prepared using the same procedure described in the section 2.2.4. The areal mass loading on the composite electrode is ~5 mg cm⁻² and fabricated the coin cell using the procedure described in the section 2.2.5.

3.2.4.2 Preparation of gel polymer electrolyte

Gel electrolytes were prepared by mixing polyvinyl alcohol (PVA) with, sodium sulphate and KOH as described elsewhere (Ping et al., 2016). First, 1M Na₂SO₄ and 10 wt.% PVA (1:1 v/v) were magnetically stirred at (5 ml each) 85 °C until a homogeneous viscous mixture was obtained and cooled at room temperature. KOH based gel electrolyte was also prepared as mentioned above by replacing sodium sulphate.

3.2.4.3 Supercapacitor electrode preparation and characterization

Electrodes were prepared by mixing 80 wt. % of active material (HMCs), 10 wt.% of super P and 10 wt.% of PVDF (Sigma -Aldrich) as a binder and NMP as a solvent. The slurry was coated on nickel foam and was dried in an oven at 100 °C for 24 hours. The electrode was pressed into a thin film by applying 10 MPa pressure. The mass loading of the active material was 2 mg cm⁻². Electrochemical performance of HMCs was measured by the three-electrode system with 6M KOH as the aqueous electrolyte. PVA with KOH and Na₂SO₄ based gel electrolyte was used for symmetric electrode studies. The electrochemical properties of the electrodes were evaluated using an electrochemical analyser PGSTAT302N (Autolab, Metrohm, Switzerland). EIS measurements were performed in the frequency range 0.1Hz to 100 KHz.

3.2.4.4 Calculations of specific capacitance, energy and power densities

In three electrode system configuration specific capacitance (C), was calculated by the following equation.

$$C = \frac{I\Delta t}{m\Delta v} \quad (3.1)$$

The two electrode system configuration, specific capacitance, F/g was calculated by the following equation (symmetrical capacitor)

$$C = \frac{I\Delta t}{M\Delta v} \quad (3.2)$$

The energy density E (W h kg^{-1}) and power density P (W kg^{-1}) were calculated by the following equation

$$E = \frac{C\Delta V^2}{2} \quad (3.3)$$

$$P = \frac{E}{t} \quad (3.4)$$

Where I (A) is the discharge current, Δt (s) is the discharge time, ΔV (V) is the potential window difference and m (g) is the mass of active material, M (g) is the total mass of the active material.

3.3 Results and Discussion

3.3.1 Physicochemical properties of HMCs

The preparation of HMC is illustrated in Figure 3.1. A simple carbonization method includes pyrolysis of the DDS precursor at 950°C without any chemical activation was used to prepare HMC. DDS is a source of carbon, oxygen, sulphur and nitrogen. The porous carbon obtained at various pyrolysis time (1, 2 and 3h) are denoted as HMC-1, HMC-2 and HMC-3, respectively. It is observed that the yield of HMC-3 is lesser than that of HMC-1 and HMC-2 which is attributed to the oxidation of reactive sites to form a more porous surface (Daud et al., 2001; C. L. Lee et al., 2017).

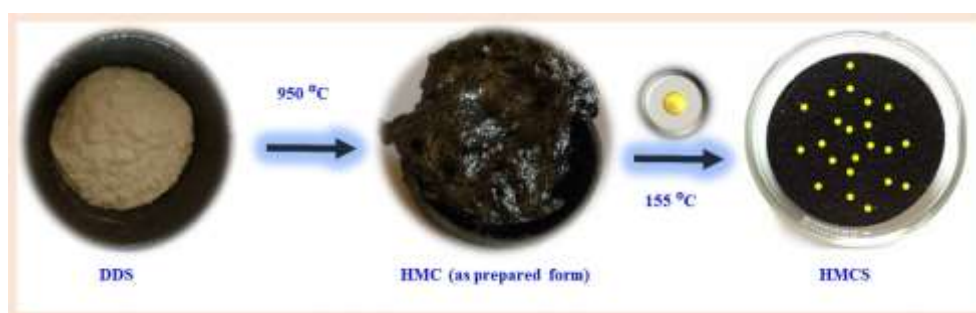


Figure 3.1. Schematic illustration of the preparation of HMC and HMCS

The textural properties of HMCs are investigated using N_2 adsorption-desorption isotherms. Figure 3.2 (a) shows the N_2 adsorption-desorption isotherm of HMC-1, HMC-2 and HMC-3 and the porosity properties are displayed in Table

3.1. According to the International Union of pure and applied chemistry (IUPAC) classification, According to the International Union of Pure and Applied Chemistry (IUPAC) classification, there are 6 types of isotherms Type 1, Type II, Type III, Type IV, Type V and Type VI. In Type 1 monolayer adsorption of the gaseous molecule over the surface is occur, which mainly for the micro porous adsorbents. Type II exhibit monolayer with unrestricted multilayer formation and exhibit for the types of mixed situations of micropores and open structures. Examples for that non porous and macroporous adsorbents. Type III no monolayer formation occurs, direct multilayer formation will take place and the formation is unrestricted. This type of isotherm exhibited in the adsorbed molecules having the strong interactions than the interactions between adsorbent surface and adsorbate. In Type IV is similar to Type II isotherm, here monolayer adsorption followed by multilayer formation with capillary condensation and exhibited the type of mesopores. Type V is similar to Type III, here direct multilayer formation with capillary condensation is occurring and for the mesoporous materials and Type VI isotherm exhibit stepwise multilayer adsorption and each step height determines the monolayer capacity of the gaseous molecule to adsorb on the adsorbent. This type of isotherms observed in the samples having the extreme homogenous surfaces. In the case of isotherm of non-porous materials, the desorption curve traces the adsorption curves. But in the case of meso/macro porous materials desorption curve is not retracing the absorption curve, which create a loop. It is known as hysteresis loop, which is corresponds to the capillary condensation of adsorbate in the multilayer region, pore filling and emptying mechanism. The nature of hysteresis loop associated with different pore geometry. There are 4 types, H1, H2, H3 and H4. H1 contains cylindrical or tubular and H2 exhibit the bottle neck type of pores. H3 and H4 describes the slit type of pores (J. Li et al., 2016; Yiju Li et al., 2016; W. Yu et al., 2016).

Here HMC-1 shows the Type I isotherm. The isotherms show a sharp uptake at relatively low pressure ($P/P_0 \sim 0$) indicating the existence of micropores. HMC-1 shows a horizontal plateau parallel to X-axis at a high relative pressure confirms the presence of micropores. HMC-2 shows the combination of Type I and Type IV isotherms. A narrow small hysteresis loop in the isotherm of HMC-2 is

due to the existence of mesopores. The isotherm of HMC-2 exhibits a small deviation from HMC-1 indicates the development of mesopores and new pores when the pyrolysis time increases (J. Li et al., 2016; Yiju Li et al., 2016; W. Yu et al., 2016). It was observed that the N₂ adsorption capacity increases, comparing HMC-1& 2 as the pyrolysis time rise. This results in an enhancement in the surface area and pore volume of HMC-2. This may be due to the increase in the volatility of carbon deposits between and within the pores or removal of gases from the surface functionalities (Yudong Li et al., 2017; Mendes et al., 2016; S. Zhang et al., 2015). When the pyrolysis time increases the fusion of micropores, pore widening (micro to meso/larger pores) and the conception of new pores occur (J. Li et al., 2016; Yiju Li et al., 2016). HMC-3 exhibit Type I isotherm. However further increase in the carbonization time (3 hour) results in a decrease in surface area and pore volume due to the deterioration in the porous structure, which is shown in Table 3.1. The deterioration is owing to the coalescence of neighbouring pores initiate annihilation of porous structure.

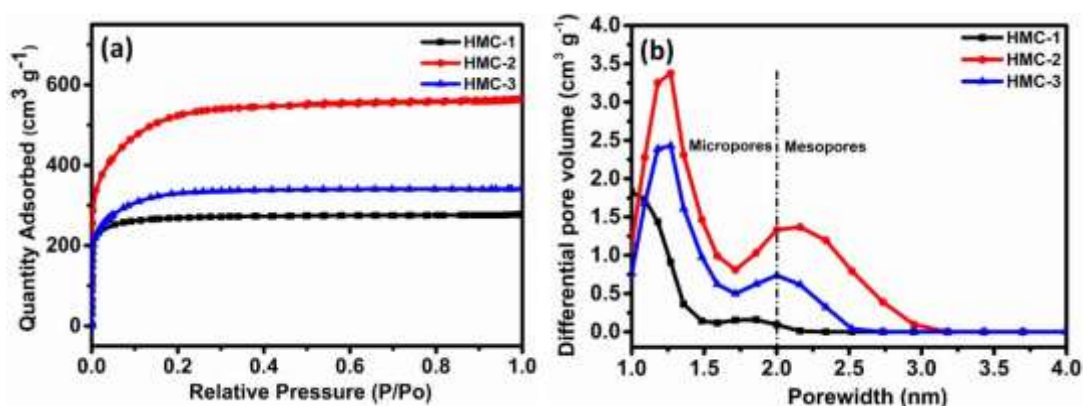


Figure 3.2. (a) N₂adsorption-desorption isotherm and (b) DFT pore size distributions of HMCs

DFT pore size distribution analysis clearly exemplifies these observations which is shown in Figure 3.2 (b). The BET surface area is calculated from the linear portion having a relative pressure range from 0.05 to 0.25. HMC-1 possesses BET surface area of 969 m² g⁻¹ and a total pore volume of 0.43 cm³g⁻¹, while the BET surface area increases to 1766 m² g⁻¹ and total pore volume expanded to 0.87 cm³ g⁻¹ when pyrolysis time increases to 2 hour (HMC-2). The surface area and pore volume reduced to 1082 m² g⁻¹ and 0.52 cm³ g⁻¹, respectively due to the destruction of the porous structure when pyrolysis time increased to 3 h (HMC-3). Hence,

pyrolysis time is an important factor for tuning pore size distribution along with the temperature and heating rate (Bouchelta et al., 2008; Shaaban et al., 2014; H. Yuan et al., 2014). HMC-1 & 2 are considered for further structural and electrochemical characterizations due to the very low yield of HMC-3 (10%) (Table 3.1). Micro and mesopores support significantly the double layer formation and fast ion transport due to low diffusion length (François et al., 2014).

Table 3.1: Textural properties of HMCs

Sample	HMC-1	HMC-2	HMC-3
BET surface area ($\text{m}^2 \text{g}^{-1}$)	969	1766	1082
Total pore volume ($\text{cm}^3 \text{g}^{-1}$)	0.43	0.87	0.52
Yield (%)	20	13	6.66

The crystallographic structure of HMC-1 and HMC-2 are investigated using XRD and Raman analysis. Figure 3.3 (a) shows a broad band at $2\theta=24.6^\circ$, is due to the reflection of (002), another diffraction peak at $2\theta = 44^\circ$ corresponding to the reflection of (100) plane, indicating amorphous structure with low graphitic nature. HMC-1 and HMC-2 exhibit a similar behavior indicates the prepared carbons are amorphous in nature with low degree of graphitization (H. Yuan et al., 2014; Tzeng and Chr, 2002; Jie Zhang et al., 2015). The Raman spectra of the HMCs (Figure 3.3 (b)) exhibits two peaks at 1336 cm^{-1} (D band) and 1595 cm^{-1} (G band) representing the disordered amorphous carbon, lattice defect of the carbon atoms and stretching vibration of graphitic carbon, respectively. It is widely accepted that the relative intensity ratio of “D-band” and “G-band” (I_D/I_G) demonstrates the disorder or defects in carbon structures. The I_D/I_G ratio for HMC-1 is 0.91 and HMC-2 is 0.96 which indicates the disordered crystalline carbon structure of the material (Y. Cai et al., 2016; Bai et al., 2016). However, I_D/I_G ratio of HMC- 2 is relatively more than that of HMC-1 which indicates that the defects get increased with the increase of pyrolysis time to 2h (Bai et al., 2016; Praveen et al., 2017; Wang et al., 2016).

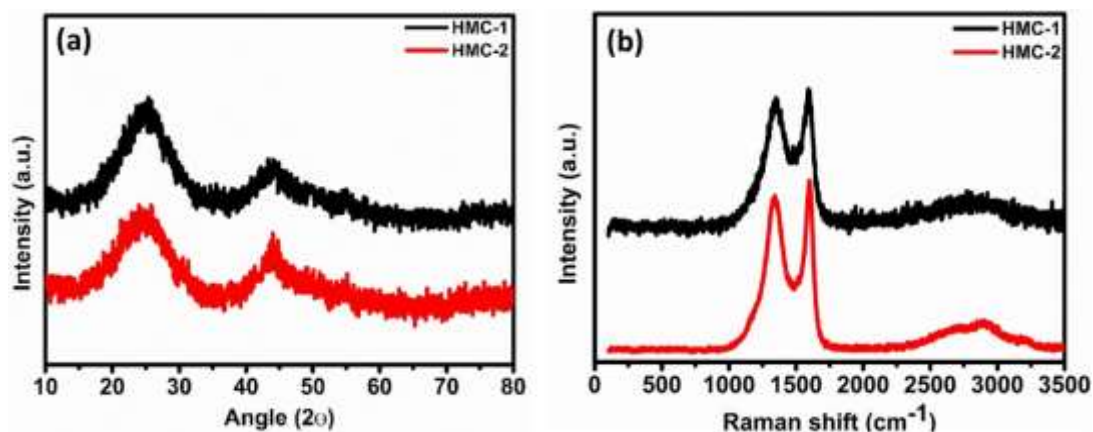


Figure 3.3. (a) X-ray diffractograms and (b) Raman spectrum for HMCs

CHNS analysis (Table 3.2) results show the presence of C, H, N and O in the HMCs. The content of these elements (H, N) except carbon decreased with the rise of pyrolysis time due to the thermal degradation of heteroatom functionalities.

Table 3.2: CHNS analysis of HMCs

Sample	C (%)	H (%)	N (%)	O (%)	S (%)
HMC-1	78.24	3.88	3.88	14	0
HMC-2	82.62	2	1.55	13.88	0

FESEM and TEM were employed to obtain the morphology and microstructure of the porous carbons. EDS analysis was carried out to confirm the presence of the heteroatoms. Figure 3.4 shows the SEM images of the HMCs. When the pyrolysis time increases there is no change in the sheet-like morphology of the prepared HMC-2 (Figure 3.4 (c-d)) compared to HMC-1, (Figure 3.4 (a-b)). The observation of pores in Figure 3.4 (b & d), evidencing the results of the pore distribution analysis. Figure 3.5 (a and c) displays the TEM images of HMCs, which reveals a highly interconnected porous carbon layers with nanopores. Inset of Figure 3.5 (a and c) shows the selected area electron diffraction (SAED) pattern, which confirms the amorphous nature of HMC-1 and 2, respectively. On comparing HMC-1 and 2, as the pyrolysis time increases (1 to 2h) defects in the porous network is increased (Tzeng and Chr, 2002; Jie Zhang et al., 2015). The SEM and TEM images corroborate with the results obtained from the N₂ adsorption-desorption isotherms.

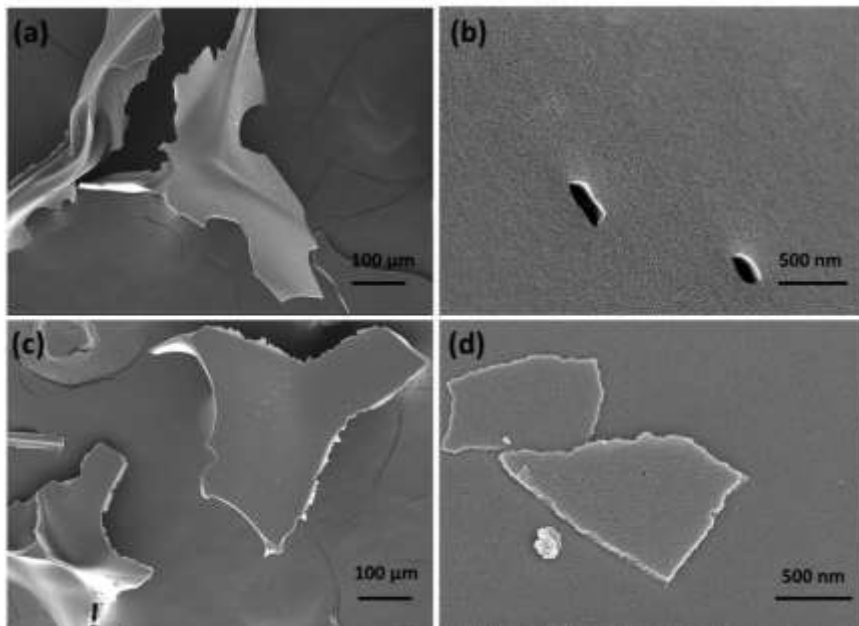


Figure 3.4. SEM images (a-b) HMC-1 and (c-d) HMC-2

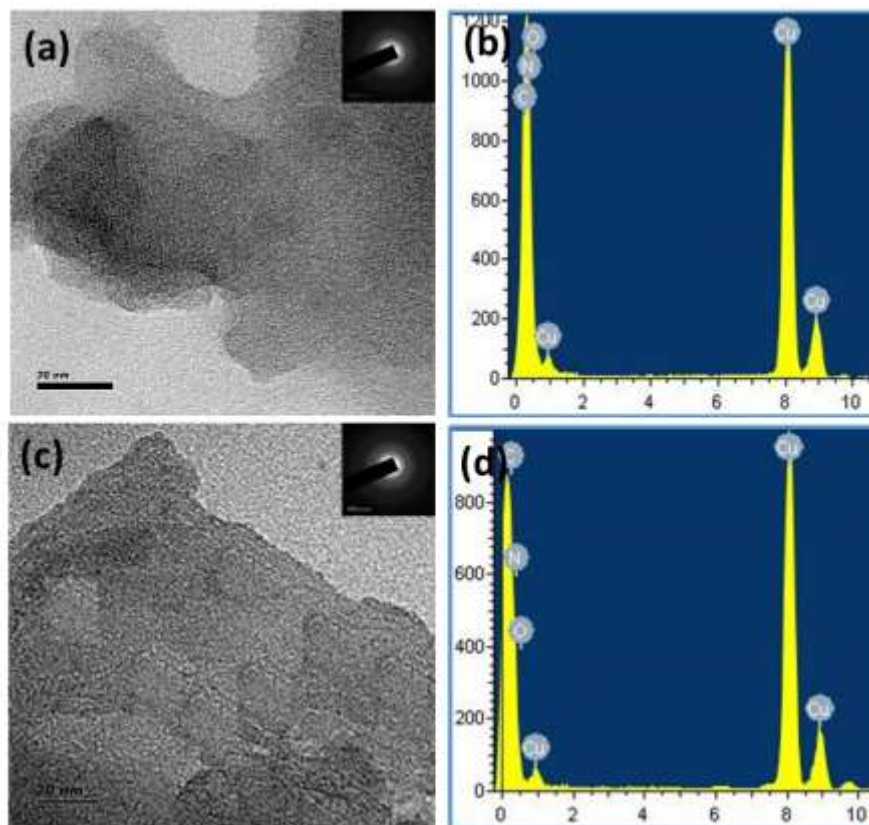


Figure 3.5. (a) TEM image (b) EDS spectrum of HMC-1 and (c) TEM image (d) EDS spectrum of HMC-2 [inset showing the SAED pattern]

EDS analysis (Figure 3.5 (c and f)) confirms the presence of N and O in the HMCs. These heteroatoms functionalities contribute towards the improvement

in the electrochemical performance of the material (Y. Cai et al., 2016; X. Fan et al., 2018).

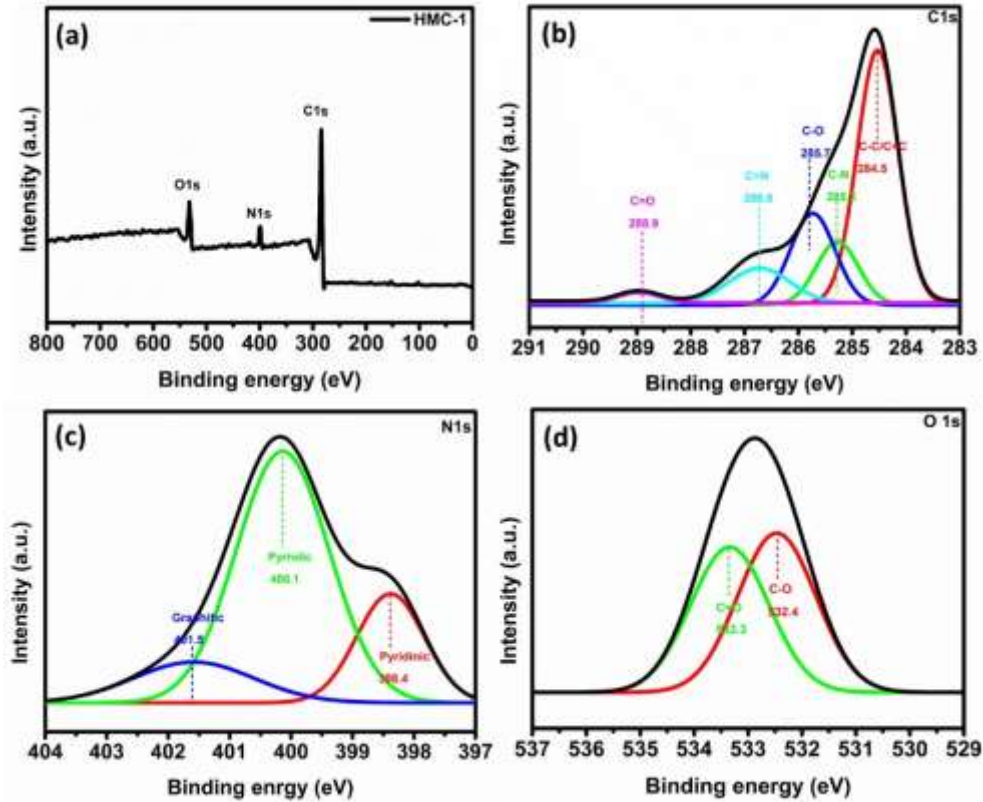


Figure 3.6. High resolution XPS of HMC-1 (a) Survey scan (b) C1s (c) N1s and (d) O1s

To study the electronic state of the surface atom and chemical composition in the HMC-1 and HMC-2, XPS measurements were employed. Figure 3.6 (a) and 3.7 (a) shows the survey scan of both HMC-1 and HMC-2, reveals the presence of C1s, N1s and O1s in the porous carbon matrix at 283.7 eV, 400 eV and 533.1 eV, respectively. Compared with HMC-1, the contents of the N elements in the HMC-2 is decreased and the C content increased when pyrolysis time increased to 2h (Yiju Li et al., 2016). Figure 3.6 (b, c and d) shows the high-resolution C, N and O spectra of HMC-1. The deconvoluted C1s (Figure 3.6 (b)) spectrum exhibits 5 peaks, C-C bond (284.5 eV) of sp^2 , C-N (285.2 eV), C-O bond (285.7 eV), C=N bond (286.6 eV) and C=O (288.9 eV). The N1s spectrum (Figure 3.6 (c)) is resolved into 3 peaks at the binding energies of 398.4 eV, 400.1 eV and 401.5 eV which are assigned to the pyridinic, pyrrolic and graphitic nitrogen, respectively. The high-resolution O1s spectrum (Figure 3.6 (d)) has two peaks: C-O bond (532.1 eV), and

C=O bond (533.5 eV) (Jin et al., 2017; Shao et al., 2016; G. Zhou et al., 2015; C. Tang et al., 2017; X. Yuan, Liu et al., 2017).

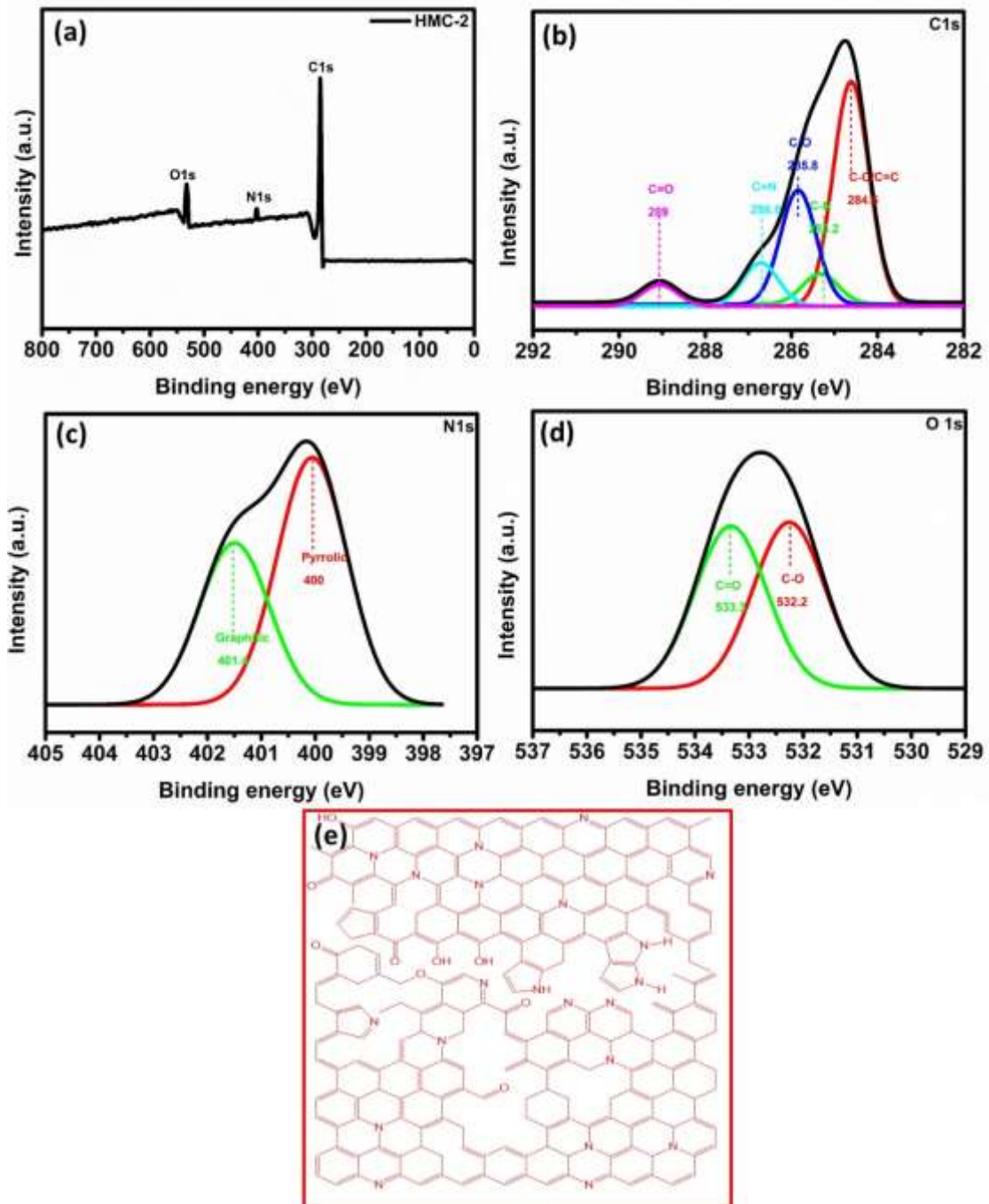


Figure 3.7. High resolution XPS of HMC-2 (a) Survey scan (b) C1s (c) N1s (d) O1s and (e) Schematic illustration of nitrogen and oxygen containing porous carbon

Figure 3.7 (b, c and d) shows the high-resolution C, O and N spectra of HMC-2. The high-resolution C1s spectrum (Figure 3.7 (b)) is resolved into 5 components, C-C bond (284.6 eV) of sp^2 , C-N (285.4 eV), C-O bond (285.8 eV),

C=N bond (286.8 eV) and C=O (289.3 eV). The N1s spectrum (Figure 3.7 (c)) contains 2 peaks at 400.1 eV and 401.5 eV due to the pyrrolic and graphitic nitrogen, respectively. The high-resolution O1s spectrum (Figure 3.7 (d)) exhibits two peaks: C-O bond (532.1 eV), and C=O bond (533.5 eV) The above XPS results confirm the intrinsic doping of nitrogen & oxygen onto a porous carbon matrix during pyrolysis (X. Yuan, Liu et al., 2017; G. Zhou et al., 2015; Tang et al., 2017). Based on these observations a schematic representation of HMC-2 is exhibited in Figure 3.7 (e) (Jing Xu et al., 2016; Jin et al., 2017; Shao et al., 2016). It is reported that the presence of heteroatoms like N and O on the surface of the porous carbon affects the electrical conductivity, wettability, etc. (S. S. Zhang, 2015)

3.3.2 Electrochemical performance of the HMCs

The obtained carbon materials are used as host for sulphur in LSBs. The porous carbon material is highly advantageous for ion buffering and PS ponding. The sulphur composites (HMC-1S and HMC-2S) were prepared by melt diffusion method. The structure and morphology of the composites were evaluated followed by the study of charge-discharge characteristics.

3.3.2.1 HMCS as cathode material for lithium-sulphur batteries

Figure 3.8 (a) displays the XRD patterns of HMC-1S, HMC-2S and sulphur. Sulphur shows the reflections from the orthorhombic phase (JCPDS no. 00-008-0247). HMC-1S and HMC-2S show sharp lines correspond to the crystalline phases of sulphur. These observations confirm the presence of sulphur in the HMCs. HMC-2S shows all the crystalline phases of sulphur with the lowest intensity than HMC-1S, attributed to adsorption of sulphur into the pores of carbon matrix, while in HMC-1 most of the sulphur crystal may present on the surface of carbon matrix due to its lower surface area and small pore size when compared to HMC-2 (S. Zhang et al., 2014; S. Zhao et al., 2013).

Figure 3.8 (b) shows Raman spectrum of HMCS, which consist of D band (disordered band) at $\sim 1346\text{ cm}^{-1}$ and G band (graphitic band) at $\sim 1595\text{ cm}^{-1}$ (Dresselhaus et al., 2007; Tao et al., 2014). Crystalline sulphur displays three bands

at 125cm^{-1} , 200cm^{-1} and 475cm^{-1} (Ward, 1968). These sulphur bands are observed in HMC-1S and HMC-2S indicates successful incorporation of sulphur in the carbon matrix. HMC-1S shows sulphur bands with higher intensity than HMC-2S, due to the existence of more sulphur crystals on the surface of porous carbon than the interior network (Niu et al., 2015; Xuebing Yang et al., 2015). These results are corroborated by the XRD observations.

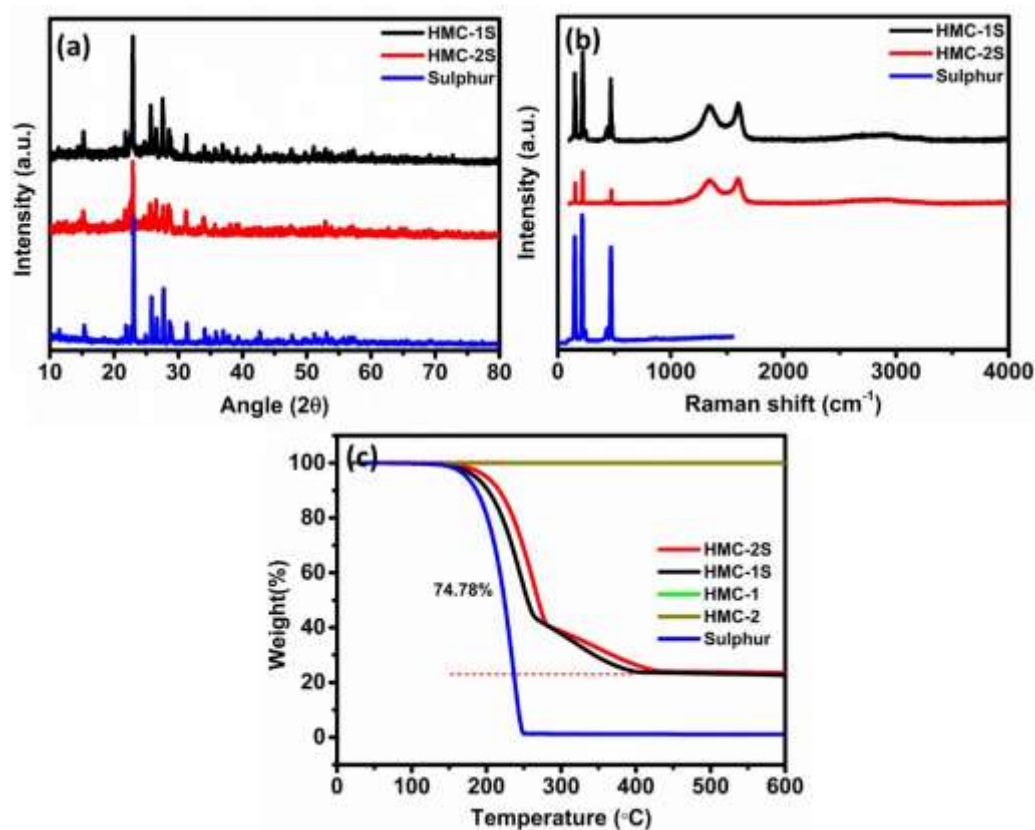


Figure 3.8. (a) XRD pattern for sulphur, HMCS (b) Raman spectra of sulphur and HMCS (c) TGA of sulphur, HMCs and HMCS

The amount of sulphur in the HMCS is determined by using sulphur and its thermal decomposition characteristics at a heating rate of 10 °C min^{-1} (Figure 3.8(c)). TGA of HMC-1 and HMC-2 are thermally stable after the weight loss below 100 °C is due to the elimination of the adsorbed water. For HMCS the decomposition temperature starts at higher than that of sulphur, it due to the strong interaction between the porous carbon and sulphur, as a result, the weight loss for sulphur starts at a lower temperature than both HMC-1S and HMC-2S. The decomposition for the composite occurred in the two-step process, due to the evaporation of sulphur at the surface (below 280 °C) and pores of porous carbon

(Gu et al., 2015; W. G. Wang et al., 2014). The sulphur content in the composite was determined, ~74wt% for both the composites.

Much variation in the morphology is not observed from the SEM, before (Figure 3.4) and after the sulphur loading (Figure 3.9) of HMCs, except the sulphur crystals on the surface of carbon sheet, which is comparatively more in HMC-1 (Figure 3.9 (c and d)), confirming the results from XRD and TGA.

Figure 3.10 shows the TEM images of HMCS and their corresponding EDS analysis. No agglomerated visible sulphur particle is seen in the TEM images, due to the good dispersion of sulphur particle inside the carbon matrix for the both of HMC-1S and HMC-2S.

The presence of sulphur in the carbon matrix is confirmed from EDS analysis. EDS analysis confirms nitrogen and oxygen functionalities along with sulphur (Figure 3.10 b and d). CHNS analysis confirms the presence of C, N, S and O in the HMC-1S and HMC-2S, which is shown in Table 3.3.

Table 3.3: CHNS analysis of HMCS

Sample	C (%)	H (%)	N (%)	S (%)	O (%)
HMC-1S	15.19	0	2.6	74.87	7.34
HMC-2S	16.2	0	1.5	74.68	7.62

Figure 3.11 shows the XPS analysis of HMC-2S. XPS survey scans analysis reveals the presence of C1s, N1s, O1s, S2s and S2p functional groups at 285.1 eV, 400 eV, 533.1 eV, 240 eV and 164 eV, respectively in the HMC-2S. (Figure 3.11 (a)). The high-resolution C1s spectra (Figure 3.11(b)) contains six components. C-C (284.6 eV), C-S (284.9), C-N (285.3 eV), C-O (285.7 eV), C=N (286.6eV) and C=O (289 eV) (M. Chen et al., 2017; Jin et al., 2017; Jing Xu et al., 2016). Oxygen and nitrogen functionalities are highly favourable for trapping of PSs on the carbon host. It is supported by the emergence of new N-S (402.8 eV) and S-O (530.3 eV) bonds in the high-resolution N1s (Figure 3.11 (c)) and O1s (Figure 3.11 (d)) spectrum, respectively in addition to the pyrrolic (400 eV), graphitic (401 eV), C=O bond (532.2 eV) and C=O bond (533.3 eV) (Jin et al., 2017; Z. Wang et al., 2014; X. Yuan, Liu et al.,2017; G. Zhou et al., 2015).

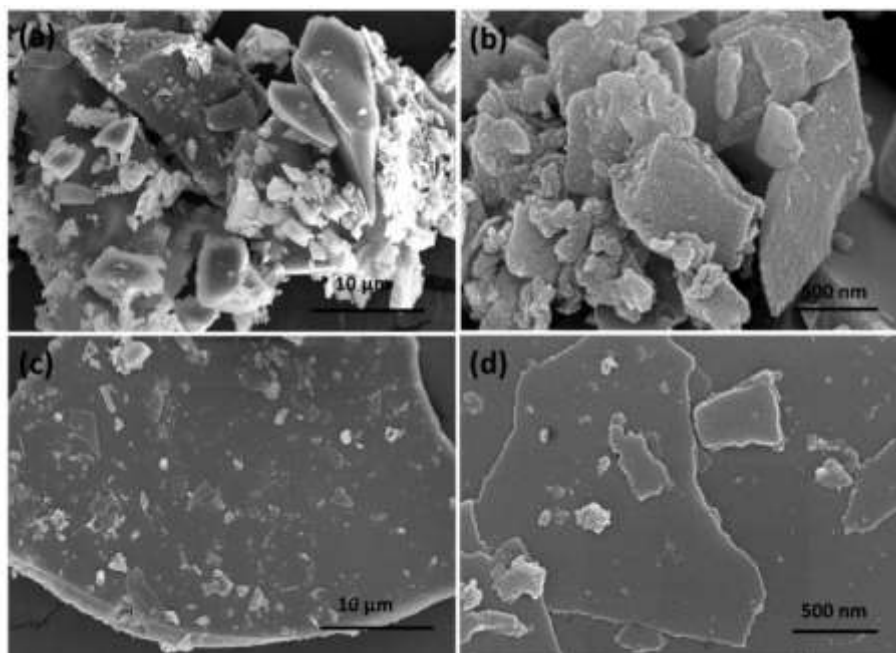


Figure 3.9. SEM images of (a-b) HMC-1S (c-d) HMC-2S

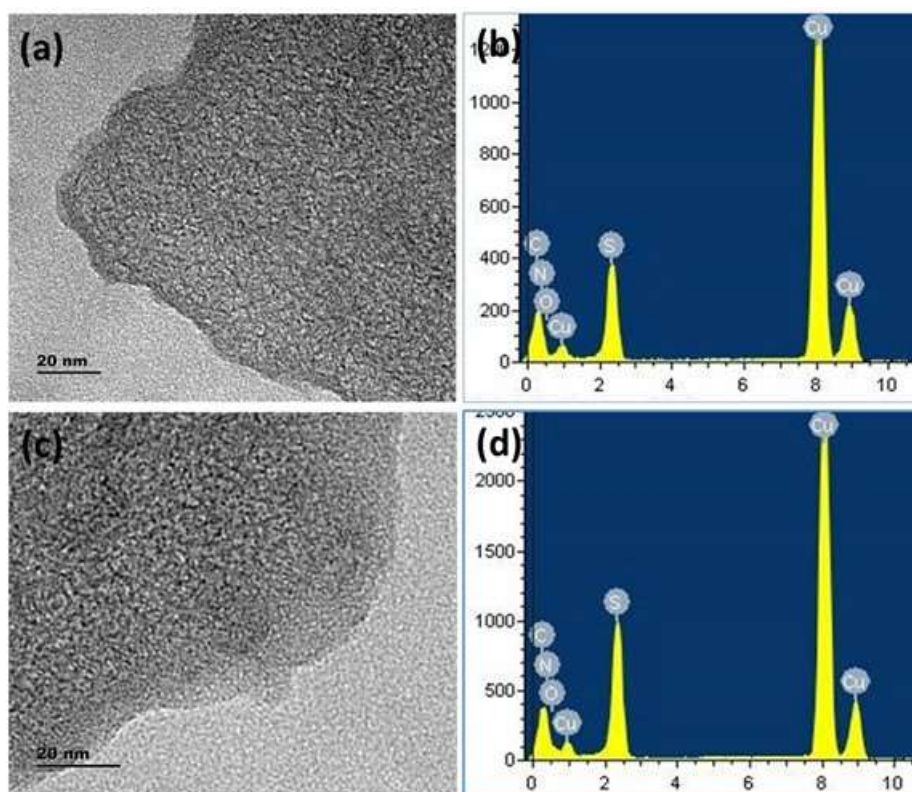


Figure 3.10. TEM image of (a) HMC-1S, (b) EDS of HMC-1S (c) TEM image of HMC-2S and (d) EDS of HMC-2S

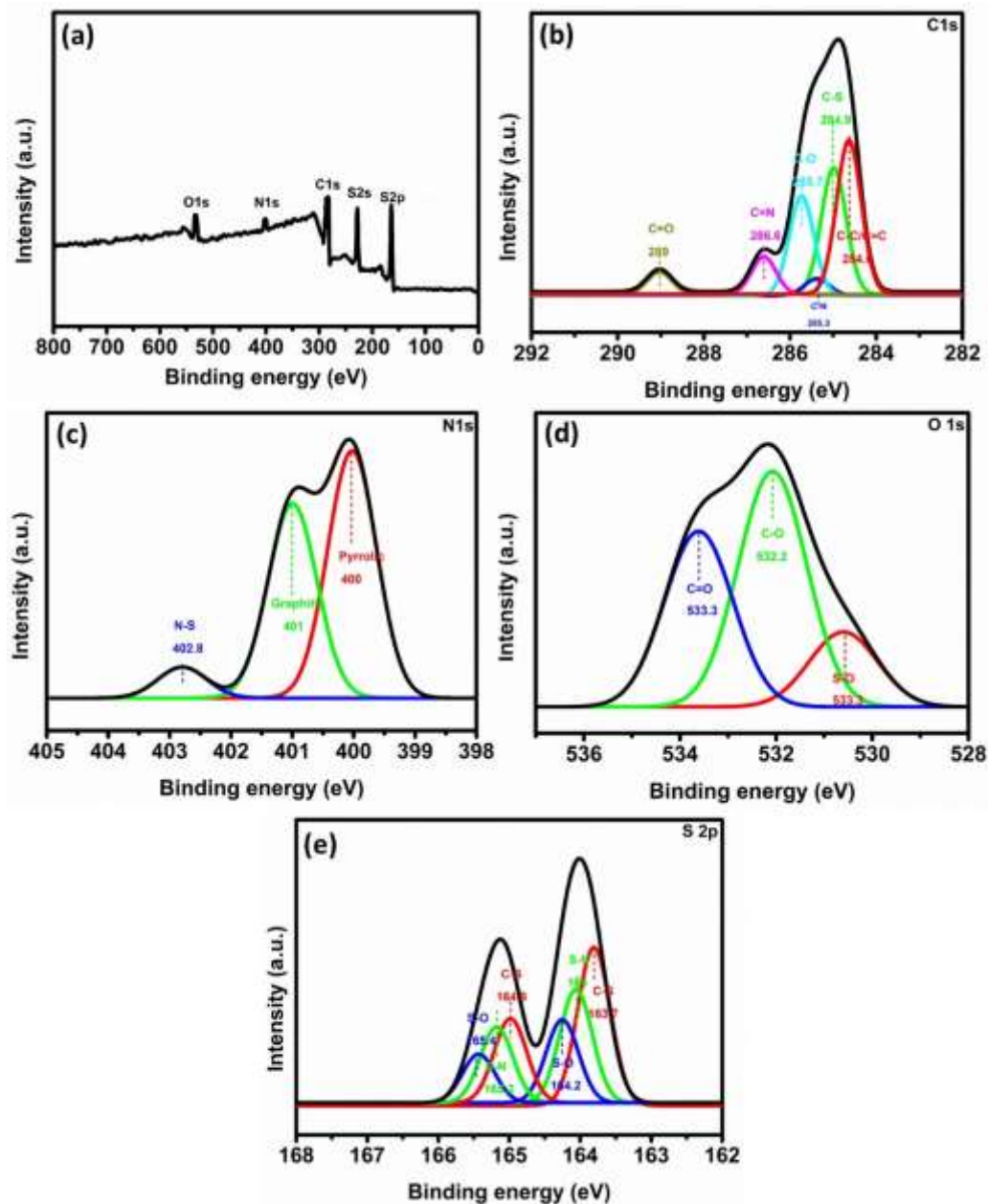


Figure 3.11. High resolution XPS of HMC-2S (a) Survey scan (b) C1s (c) N1s (d) O1s and (e) S2p

The high-resolution S2p spectrum (Figure 3.11 (e)) gives the confirmations of interactions between sulphur with oxygen and nitrogen (J. Yang et al., 2016). The S2p deconvoluted into two S2p_{3/2} and S2p_{1/2} with an energy separation of 1.2 eV (Niu et al., 2015; L. Zhang et al., 2012). S2p_{3/2} is deconvoluted into three (163.7, 164 and 164.2 eV) components and S2p_{1/2} is deconvoluted into three peaks (165.9, 165.2 and 165.4 eV) corresponds to the C-S, S-N and S-O bonds in the HMC-2S (Niu et al., 2015; L. Zhang et al., 2012).

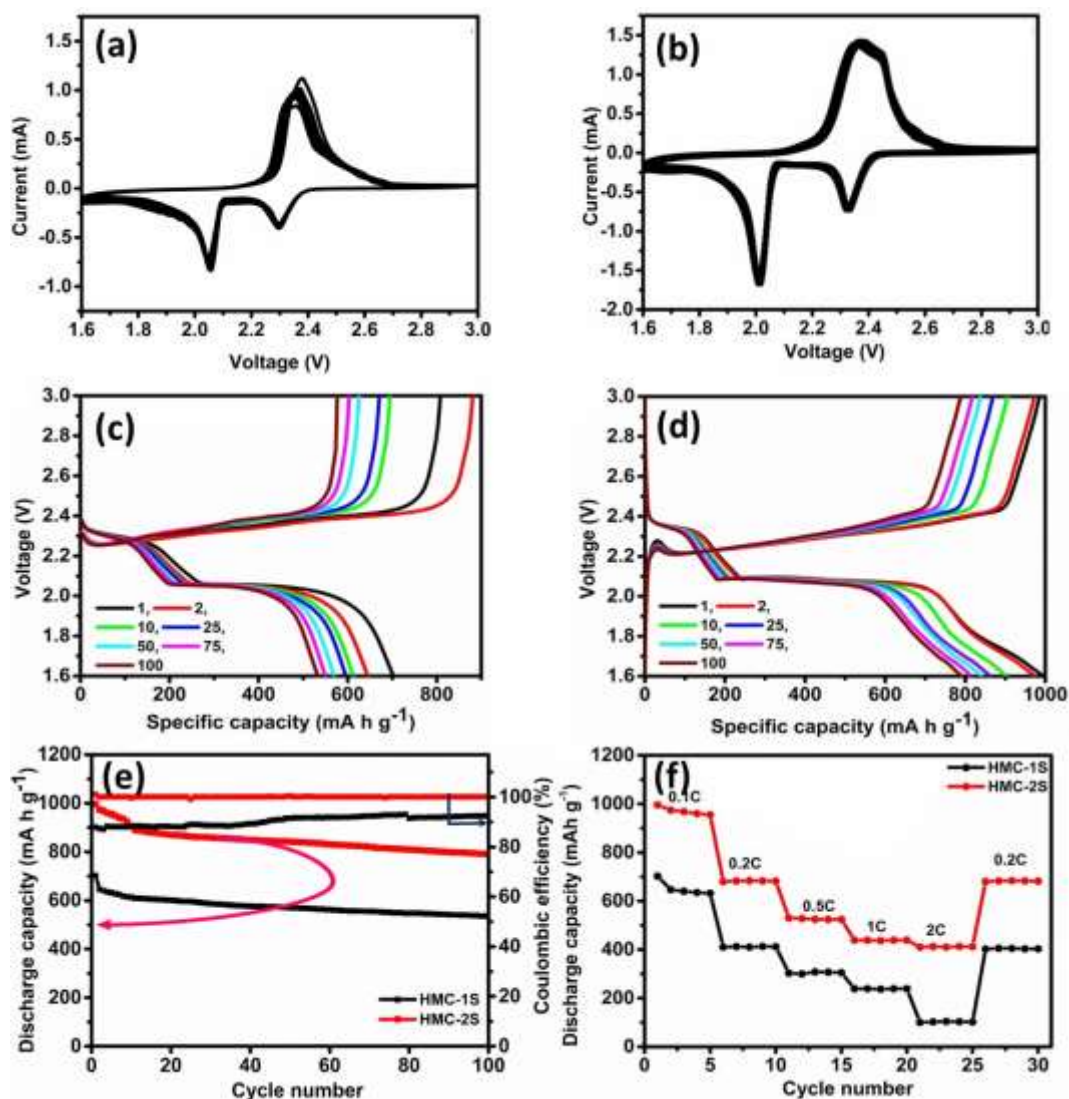


Figure 3.12. CV of the (a) HMC-1S (b) HMC-2S, GCD curves of (c) HMC-1S (d) HMC-2S (e) Cycle performances & coulombic efficiency at 0.1C rate and (f) Rate capability studies at different C rate

CV was used to investigate the oxidation-reduction behaviour of HMC-1S and HMC-2S as cathode material in the lithium-sulphur cell. Figure 3.12 (a and b) shows the CV curves of HMC-1S and HMC-2 at a scan rate of 0.1 mV s^{-1} in the voltage window of 1.6-3 V. It exhibits two reduction and one oxidation peaks. As observed in the literature, in the cathode scan, the reduction peak at 2.3 V and 2 V is due to the reduction of sulphur to higher order LPSs and further reduction to lower order polysulphides. In the subsequent anodic scan, an oxidation peak at 2.39 V is observed due to the oxidation of lithium polysulphides to sulphur (Gu et al., 2015; S. Zhang et al., 2014). The oxidation peak position is slightly changed for HMC-1S due to the instability of the electrode, later it is stable (Zhengjiao Liu et

al., 2018). In the case of HMC-2S, the peak position and current is not changed in the successive cycles indicating the robustness and reversibility of the material. Moreover, the current density is increased for HMC-2S than HMC-1S due to the improved active material utilization (J. Yang et al., 2015; S. Zhang et al., 2014). CV results show that the high surface area and pore volume of porous carbon material along with N, O functionalities quite effective to prevent the loss of active material into the electrolyte (G. Ren et al., 2016; Jing Xu et al., 2016).

To further understand the electrochemical performance of the HMCS cathodes, GCD experiments at 0.1C rate were carried out. The GCD curves of HMC-1 and HMC-2S (Figure 3.12 (c and d) exhibit two reduction and one oxidation plateaus as observed in the CV curves. GCD curve shows 1, 2, 25, 50, 75 and 100th charge-discharge cycles. HMC-1S shows 702 mA h g⁻¹ as initial discharge capacity after 100 cycles, the capacity is reduced to 536 mA h g⁻¹ with 76% capacity retention. HMC-2S shows 995 mA h g⁻¹ as initial discharge capacity and 790 mA h g⁻¹ as the 100th capacity with 79% capacity retention. Moreover, the charge-discharge plateaus are stable throughout the 100 cycles, indicating the excellent electrochemical stability of HMC-2S (Jinxin Guo et al., 2015; G. Ren et al., 2016).

The above results are comparable with the carbon-sulphur composite reported previously where the porous carbon was prepared without activation. Xu et al reported soluble starch derived hierarchical porous carbon as sulphur host with 84% sulphur loading exhibited 1269 mA h g⁻¹ as the initial discharge capacity and a reversible capacity of 406 mA hg⁻¹ after 100 cycles at a 0.1C rate with 32% capacity retention (G. Xu, B. Ding, P. Nie, et al., 2014). Wang et al demonstrated kejent black derived carbon sphere with 75% sulphur exhibited 1300 mA h g⁻¹ as initial capacity and 70 % capacity retention at the 0.1C rate (M. Wang et al., 2015). Xia et al reported microalgae-derived N doped microspheres with 65% sulphur provided a reversible capacity of 1030 mA h g⁻¹ after 100 cycles at a current density of 0.1 A g⁻¹ with 91% capacity retention (Xia et al., 2017). Yang et al reported N doped carbon nanofiber web from PPy with 77% sulphur loading displayed a final capacity of 749 mA h g⁻¹ after 180 cycles at a 0.2C rate with 69.6% capacity

retention (J. Yang et al., 2014). Mi et al reported melamine derived N doped 3D flexible carbon as sulphur host for 36.3% sulphur displayed 556 mA h g⁻¹ as final capacity after 100 cycles at a 0.05C rate with 87% capacity retention (Mi et al., 2016). Liu et al reported PPy derived N doped carbon with 61% sulphur composite provided ~40% capacity retention after 200 cycles at a 0.2C rate (C. Liu et al., 2017). Liang et al described N doped carbon nanofiber from PVP-sulphur composite exhibited a reversible capacity of 1093 mA h g⁻¹ after 300 cycles at a 0.5C rate with 76% capacity retention (Y. Liang et al., 2018). Wu et al reported PAN and PMMA derived N doped carbon nanofiber sulphur composite with 60% sulphur loading exhibited a final capacity of 715 mA h g⁻¹ after 70 cycles at a 0.1C rate with 88% capacity retention (Y. Wu et al., 2014). These results suggested that heteroatom doping on the carbon network enhance the performance of LSBs.

The cycling performance of the HMC-1S and HMC-2S is shown in Figure 3.12(e) at 0.1C rate. HMC-2S exhibit 100% coulombic efficiency throughout the 100 cycles with 0.12% capacity decay per cycle, while HMC-1S provides 87% coulombic efficiency in the initial cycles with 0.48% capacity decay per cycle and it is increased to ~ 92.5% after 100 cycles, attributed to the loss of active material (sulphur at the surface of carbon) during initial cycles (S. Zhang, 2013; C. Hu et al., 2017).

The rate performance of the HMC-1S and HMC-2S at different current densities are displayed in Figure 3.12 (f). HMC-1S delivers the capacities of 702, 410, 303, 238 and 100 mA h g⁻¹ at 0.1, 0.2, 0.5, 1 and 2C, respectively. HMC-1S delivers 402 mA h g⁻¹ with 1.95% capacity degradation when it is reduced back to 0.2C rate. However, HMC-2S exhibits 995, 680, 525, 439 and 410 mA h g⁻¹ at 0.1, 0.2, 0.5, 1 and 2C, respectively. It maintains 100% capacity retention when the current density is reduced back to 0.2C. In the case of HMC-1S most of the sulphur crystals may be on the surface and not uniformly distributed in the micro porous network due to the low specific surface area and pore volume, so the active material utilization decreases, it is reflected in the poor discharge capacity values at different current densities. The excellent electrochemical performance of the HMC-2S is due to the presence of meso/microporosity, high pore volume and the heteroatom

functionalities, which effectively trap the PSs during the charge-discharge process which reduces the active material loss.

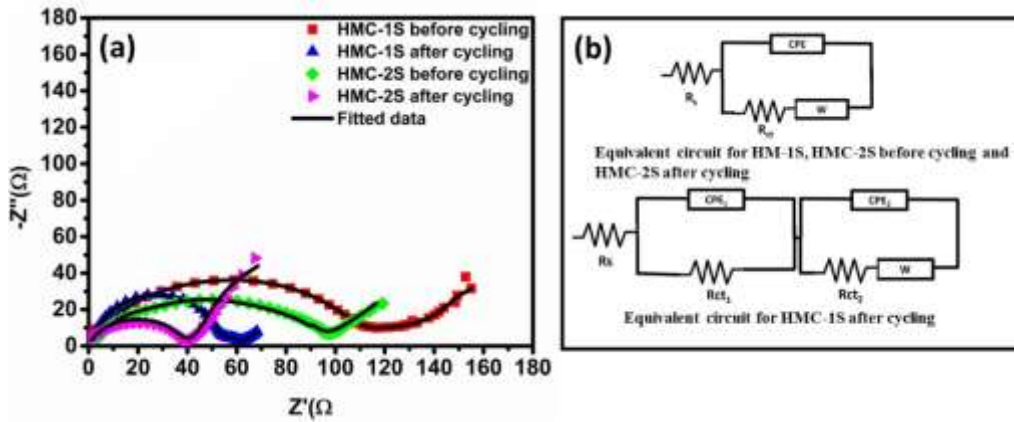


Figure 3.13. (a) EIS of HMC-1S and HMC-2S before and after cycling and (b) its equivalent circuit

Table 3.4: Impedance parameters obtained from the electrochemical equivalent circuit analysis for HMCSs before and after cycling

Material description	R_s (Ω)	$CPE \times 10^{-6}$ (Ω^{-1})	R_{ct} (Ω)	$CPE_2 \times 10^{-7}$ (Ω^{-1})	R_{ct2} (Ω)	Y_0 ($\Omega^{-1}s^{1/2}$)
HMC-1S before cycling	0.65	3.02	118.4	-	-	0.087
HMC-1S after cycling	1.6	7.32*	53.27**	9	6	0.18
HMC-2S before cycling	0.52	10.78	61.01	-	-	0.080
HMC-2S after cycling	3.54	1.69	36.33	-	-	0.53

* CPE_1 , ** R_{ct1}

To understand the electrochemical performance of HMC-1S and HMC-2S electrodes, electrochemical impedance spectroscopy is employed before and after 100 cycles (Figure 3.13). It is observed that R_{ct} and ion diffusion resistance for HMC-2S is less than HMC-1S due to the enhanced electronic conductivity and dispersion of sulphur in the porous network before and after cycling (Table 3.4) After cycling the charge transfer resistance and ion diffusion resistance are decreased for both HMC-1S and HMC-2S attributed to the enhancement of ion transport after cycling due to the increase in accessibility of electrolyte to the intricacies of porous network and the pore volume accommodate the volume changes of sulphur during the charge-discharge process (W. G. Wang et al., 2014). HMC-1S shows 2 semicircles after cycling, a large semicircle at high-frequency region (R_{ct1}) and a very small circle at medium frequency region (R_{ct2}), related to

the resistance offered from the deposition of insoluble lower order PSs on the surface of the cathode, which results in poor electrochemical performance of the HMC-1S than HMC-2S. Such behaviour is not observed in HMC-2S, evidencing its better electrochemical performances (Gu et al., 2015; Raghunandan et al., 2018; W. Zhang et al., 2017.) (W. G. Wang et al., 2014). Such behaviour is not observed in HMC-2S, evidencing its better electrochemical performance (Gu et al., 2015; Raghunandan et al., 2018; W. Zhang et al., 2017.)

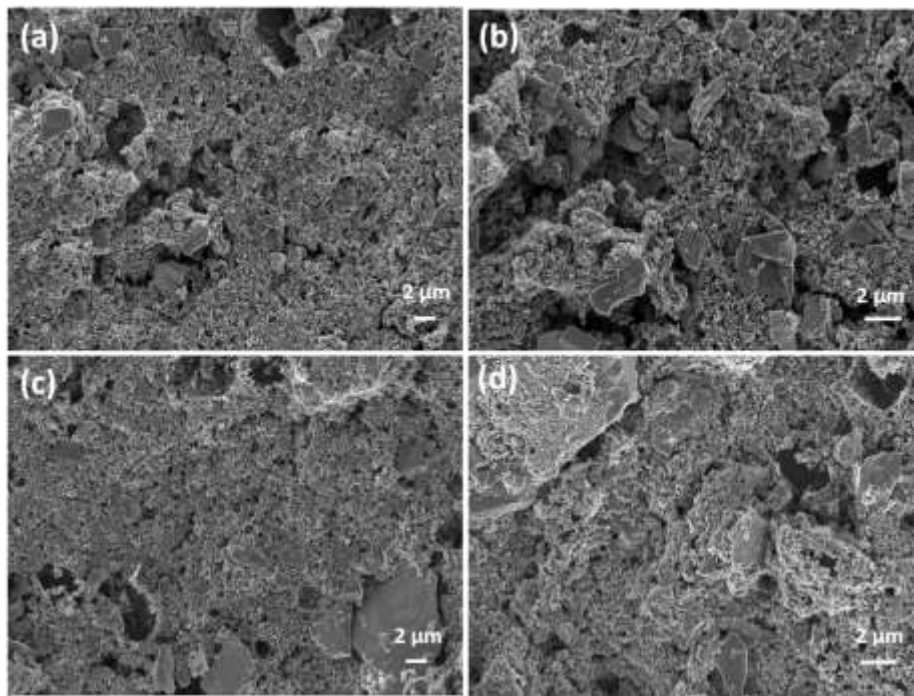


Figure 3.14. SEM images (a) HMC-1S cathode film before cycling (b) HMC-1S cathode film after cycling (c) HMC-2S cathode film before cycling and (d) HMC-2S cathode film after cycling

To study the structural stability of the cathode film, coin cells were dismantled after 100 cycles and HMC-1S & 2S cathode films were characterized. Figure 3.14 depicts the morphology of HMC-1S and HMC-2S of as prepared and cycled cathode surfaces. Morphological differences are observed in HMC-1S after cycling whereas HMC-2S maintains its structural integrity after 100 cycles (S. Wei et al., 2011). The reason behind is that the hetero atom doped carbon with high surface area and pore volume restrict the solubility of higher order PSs into the electrolytes and thereby reduces the loss of deposition of Li_2S (insulator) on the cathode surface and enhance the electrochemical performance resulting high

capacity retention, coulombic efficiency for HMC-2S compared to HMC-1S (Miao et al., 2013).

The excellent electrochemical performance of HMC-2S is further supported by XPS analysis of the cathode film after 100 charge-discharge cycles at the 0.1C rate. Figure 3.15 shows the XPS analysis of HMC-2S after cycling. The survey scan analysis reveals C1s, O1s, N1s, S2s, S2p and F1s (from PVDF binder) (Figure 3.15 (a)). High-resolution Li 1s spectra (Figure 3.15 (b)) is deconvoluted into the three contributions Li-S (55.7eV), Li-N (56.2 eV) and Li-O (56.7 eV) (X. Fan et al., 2018; Xia Liand Sun, 2014; Son et al., 2015). The interactions between lithium with oxygen and nitrogen through Li-N and Li-O bond strongly affirms PS anchoring by the heteroatoms (X. Fan et al., 2018; Son et al., 2015). The meso/microporosity and high pore volume of HMC-2 along with N and O functionalities help to restrict the movement of PSs on cathode rim during the charge-discharge process (Son et al., 2015).

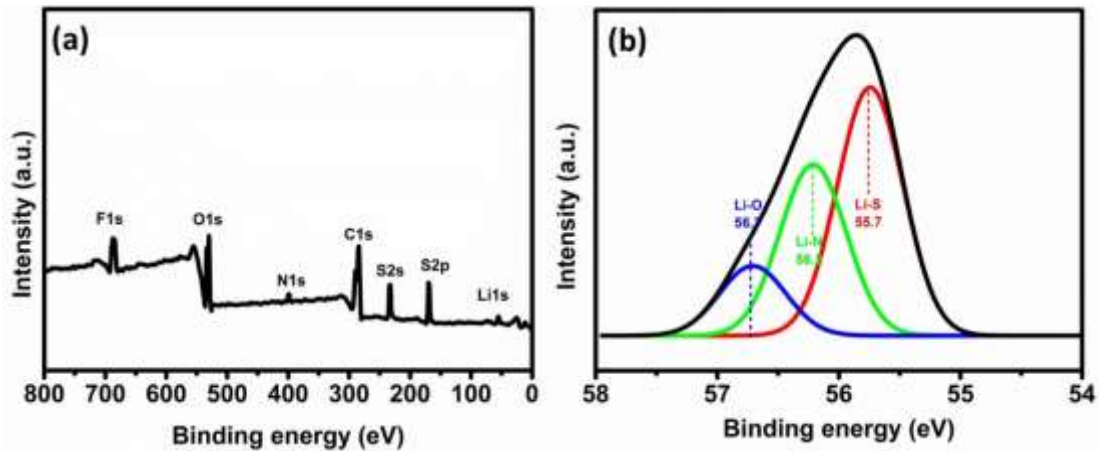


Figure 3.15. (a) Survey scan and (b) High-resolution Li1s spectrum of HMC-2S after 200 cycles

3.3.2.2 HMCs as supercapacitor electrode

The developed HMC-1 and HMC-2 is used for supercapacitor application. Initial electrochemical characterization of single electrode was carried out by three electrode system, following two electrode fabrication.

Three electrode system

A three electrode system is used for the initial evaluation of the electrode materials prepared at different pyrolysis time using Hg/Hg₂Cl₂ as reference electrode, Pt mesh as counter electrode and aqueous 6M KOH electrolyte. Figure 3.16 (a) shows the CV curves of HMC-1 and HMC-2 at a voltage window of -1 to 0 V at a scan rate of 10 mV s⁻¹. By comparing HMC-2 with HMC-1, it is observed that HMC-2 has more integrated area than HMC-1 due to the high surface area and the porous architecture. Figure 3.16 (b) shows the GCD of HMC-1 and HMC-2 at a current density of 0.8 A g⁻¹. Specific capacitance was calculated from the discharge time using the equation 3.1. The calculated specific capacitances of HMC-2 and HMC-1 are 431 F g⁻¹ & 250 F g⁻¹, respectively. Figure 3.16 (c) demonstrates CV profile of HMC-2 electrode materials at different scan rates. All the curves are rectangular in shape, indicating electrical double layer capacitive behaviour. Current density is increased when scan rate increases from 10 to 100 mV s⁻¹ and maintains its rectangular shape even at higher scan rate 100 mV s⁻¹, indicating low polarization and fast response during electrode processes (Yiju Li et al., 2016). Figure 3.16 (d) represents the GCD curves for different current densities from 0.8 A g⁻¹ to 4 A g⁻¹. The GCD curves are symmetrical indicates the electrical double layer capacitance (Yiju Li et al., 2016; Mo et al., 2016). The specific capacitance is calculated from the equation (3.1) using the discharge time. The relationship between specific capacitance and current densities is shown in Figure 3.16 (e). When the current density is increased to 4 A g⁻¹ specific capacitance reaches to 420 F g⁻¹, excitingly 3.2% capacity degradation is observed with respect to the specific capacitance at 0.8 A g⁻¹. However, HMC-1 exhibit 17% capacity degradation when the current density is increased to 4 A g⁻¹.

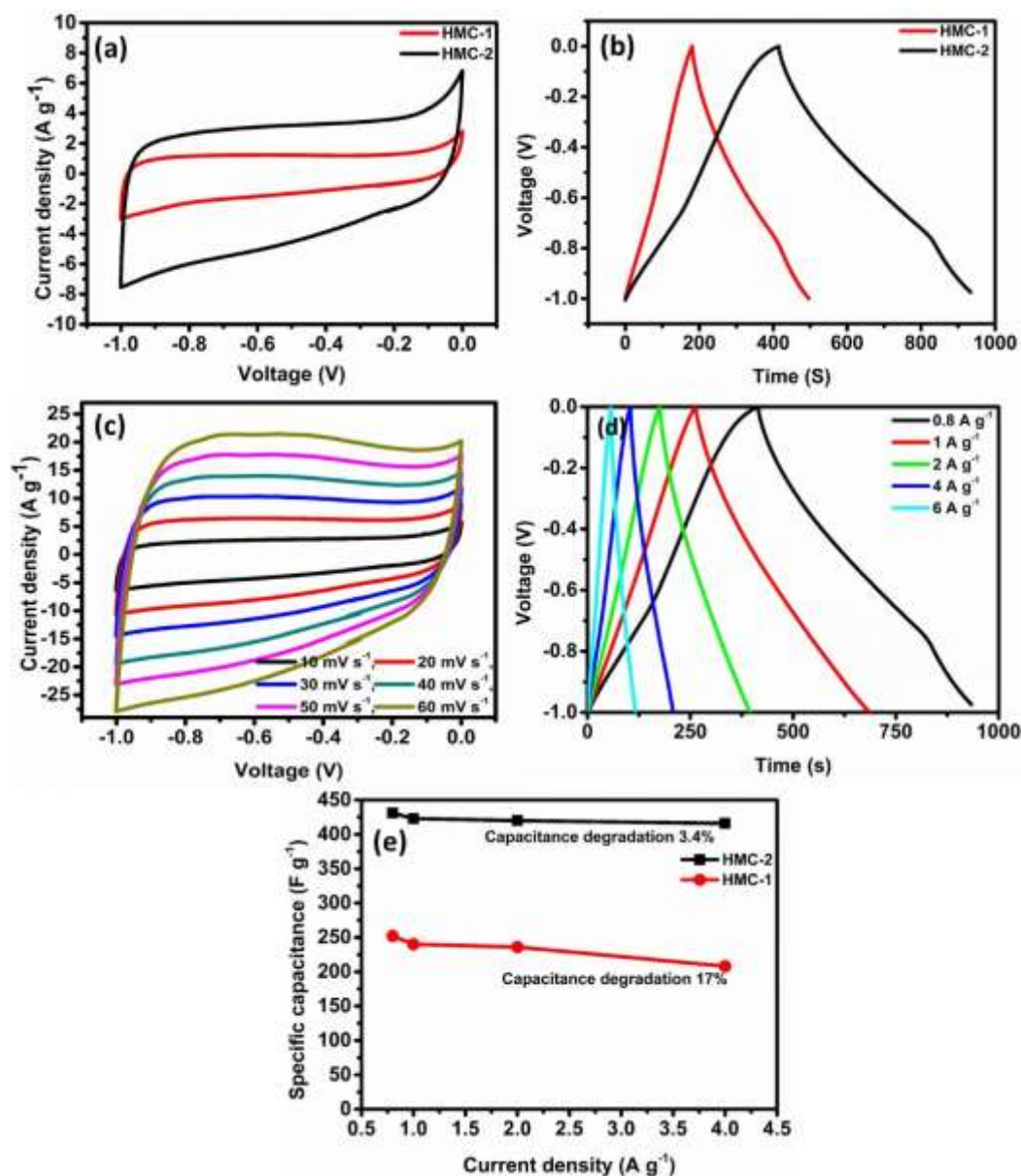


Figure 3.16. (a) CV curves and (b) GCD of HMCs at a scan rate of 10 mV s⁻¹ and current density of 0.8 A g⁻¹ (c) CV curves at different scan rates of HMC-2 and (d) GCD of HMC-2 at various current densities and (e) A line chart of specific capacitance Vs current density

EIS was carried out before and after cycling at the OCV voltage to understand the electrode-electrolyte interfacial interactions (Figure 3.17). The inset shows the EIS plot of the HMC-1 before and after 1000 cycles at a current density of 0.6 A g⁻¹. The tail of the HMCs before and after cycling is almost parallel to the Y axis, greater than 45 ° indicating its ideal capacitive behaviour with low Warburg resistance. There is more variation from ideal behaviour was noted in HMC-1 compared to HMC-2 after cycling (Table 3.5), attributed to the better electrochemical performance of HMC-2 (Bai et al., 2016; Xin Zhou et al., 2017;

Ranjith et al., 2017). It is due to the adsorption and diffusion of ions into the well-connected micro- meso pores with high surface area is retained after long cycling. The deviation in HMC-1 may be due to the comparatively more functional groups in less surface area increases corrosiveness. Moreover, not much decrease in ionic diffusion on the electrode surface on prolong cycling, which is observed from Nyquist plots, facilitate better performance for long period of time.

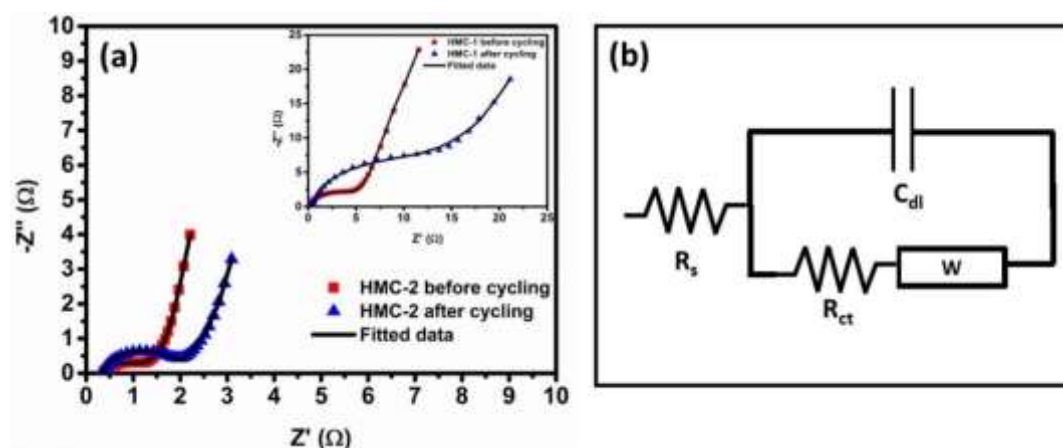


Figure 3.17. (a) EIS of HMC-1 and 2 before and after cycling at the open circuit potential in the frequency range from 100 mHz to 100 kHz and (b) its corresponding equivalent circuit

Table 3.5: Impedance parameters obtained from the electrochemical equivalent circuit analysis with 6M KOH electrolyte

Material description	R_s (Ω)	C_{dl} (F)	R_{ct} (Ω)	Y_0 ($\Omega^{-1}s^{1/2}$)
HMC-1 before cycling	0.2	1.6	5	0.023
HMC-1 after cycling	0.27	1.08	14.78	0.019
HMC-2 before cycling	0.52	1.78	0.95	0.041
HMC-2 after cycling	3.54	1.76	1.48	0.039

The electrochemical performance of HMC-2 is comparatively better than similar carbon materials reported elsewhere which is shown in the Table 3.6 (Y. An et al., 2017; Ma et al., 2016; L. Wang et al., 2013; Wang et al., 2016; X. Zheng et al., 2017). The excellent electrochemical performance of the HMC-2 is due to the high surface area, pore size distribution, high pore volume, which helps the electrolyte ions to reach electrode surface to create charge-dipoles (Bai et al., 2016; Y. Cai et al., 2016). The HMC-2 is considered for further electrochemical evaluations due to its better performance.

Table 3.7: Comparison of the specific capacitance of porous carbon with three electrode system

Precursor	Surface area (m ² g ⁻¹)	Specific capacitance (F g ⁻¹)	Current density (A g ⁻¹)	Electrolyte	References
Rice husk	2242	429	0.5	6M KOH	Yong et al., 2017
Willow catkin	1775	292	1	6M KOH	L. Xie et al., 2016
Celtuce leaves	3404	421	0.5	2M KOH	R. Wang et al., 2012
Tobacco rod	-	286	0.5	6M KOH	Y.-Q. Zhao et al., 2016
Fallen leaves	2869	242	0.3	6M KOH	Y.-T. Li et al., 2015
Water hyacinth	1308	273	1	6M KOH	K. Wu et al., 2016
Hemi cellulose	2300	300	0.2	0.5M H ₂ SO ₄	Falco et al., 2013
Fungi	80.8	196	0.17	6M KOH	Hui Zhu et al., 2011
Fungus	1103	360	0.5	6M KOH	Long et al., 2015
Pumpkin	2968	419	1	6M KOH	Bai et al., 2016
Watermelon rind	2277	333	1	6M KOH	Mo et al., 2016
Human hair	1306	340	1	6M KOH	W. Qian et al., 2014
HMC-1	969	431	0.8	6M KOH	Our work
HMC-2	1766	250	0.8	6M KOH	Our work

Two electrode System

To evaluate the real-life application, a symmetrical SC is fabricated using HMC-2 on Ni foam (mass of single electrode ~2 mg cm⁻²) as electrode and PVA+KOH gel as electrolyte. All the measurements were carried out in the room temperature. Figure 3.18 (a) shows the CV curves of HMC-2//HMC-2 symmetric SC. The curves are close to rectangular shape similar to three electrode system at the lower scan rate. When scan rate increases from 10 to 100 mV s⁻¹, it maintains the rectangular shape which indicates the fast charge-discharge and rate capability of the material.

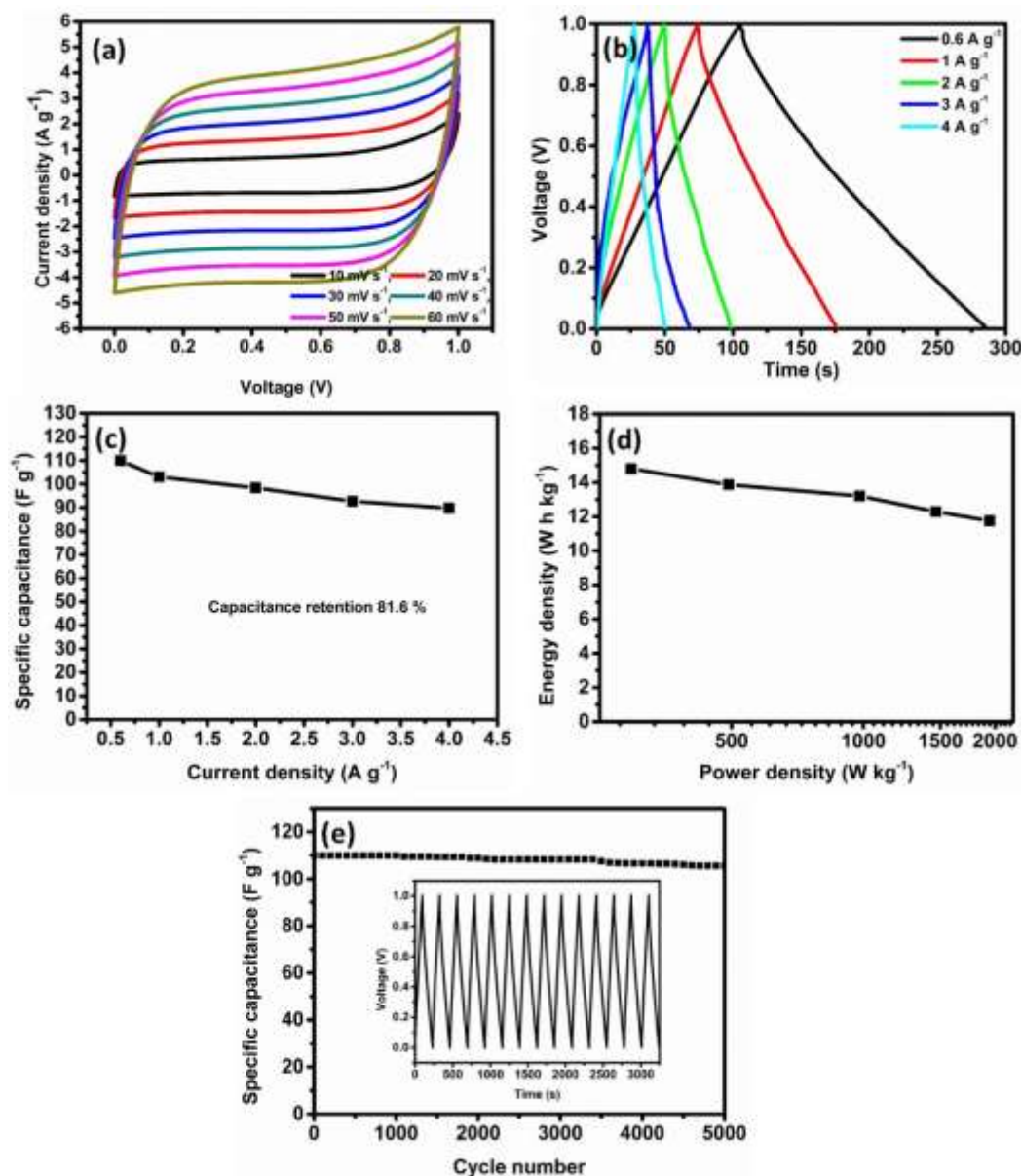


Figure 3.18. Electrochemical characteristics of HMC-2 electrode as symmetric supercapacitor using PVA+KOH gel electrolyte (a, b) CV and GCD curves of the symmetric cell (c) Specific capacitances of symmetric cell at various current densities (d) Ragone plot of symmetrical cell and (e) Cycling stability at a current density of 0.6 A g⁻¹ (inset shows GCD curves of initial 14 cycles)

Figure 3.18 (b) represents the GCD curve at different current densities, it is triangular, highly symmetrical and a small deviation from linearity with a very small voltage drop over various current densities. Both CV and GCD curves reflect a perfect EDLC with exceptional electrochemical reversibility. The specific capacitance was calculated from the galvanostatic discharge time by equation 3.2. The Figure 3.18 (c) demonstrates the relationship between specific capacitance and current density. HMC-2//HMC-2 shows a high specific capacitance of 110 F g⁻¹ at

a current density of 0.6 A g^{-1} , and the capacitance remains 89.8 F g^{-1} at a higher current density of 4 A g^{-1} . HMC-2//HMC-2 demonstrate 81.6% capacity retention at the current density of 4 A g^{-1} . From the Ragone plot (Figure 3.18 (d)), it is observed that HMC-2//HMC-2 offers a maximum specific energy density of 14.8 W h kg^{-1} (calculated using equation (3.3)) at a power density of 295 W kg^{-1} (calculated using equation (3.4)). Moreover, it exhibits 11.7 W h kg^{-1} energy density at the power density of 1942 W kg^{-1} ascribed to the short diffusion pathway and less charge transfer resistance (Karthikeyan et al., 2014; Mendes et al., 2016). It is one of the potential electrode material for symmetric SC using KOH gel electrolyte. HMC-2//HMC-2 shows better cycle stability of at a current density of 0.6 A g^{-1} (Figure 3.18 (e)) with 98% capacity retention after 5000 cycles compared to the initial specific capacitance.

The energy and power densities of the symmetric SC is limited, due to the lower operating voltage window (0 to 1 V) of alkaline electrolyte. To achieve higher energy density for SCs neutral sodium sulphate electrolyte was employed due to its better operating voltage window (0-1.8 V) than aq. KOH (0 to 1 V) (Bai et al., 2016; Y. Cai et al., 2016; Wang et al., 2016) is well known that energy density is directly related to specific capacitance and operating voltage window. The symmetrical SC provided 11 W h kg^{-1} of maximum energy density while using PVA+KOH based gel electrolyte. In order to achieve maximum energy density, it is evaluated at the high voltage window (0-1.8 V) using PVA+ Na_2SO_4 as the electrolyte. Figure 3.19 (a) shows the CV curves of symmetric SC, HMC-2//HMC-2 at a scan rate of 50 mV s^{-1} (0 to 1V to 0 to 1.8 V). It maintains a quasi-rectangular shape even when the voltage window is increased.

Figure 3.19 (b) shows the GCD curves at different current densities from 0.6 to 4 A g^{-1} . The relationships between specific capacitance and current density is given in Figure 3.19 (c). GCD curves are triangular in shape with IR drop provides a maximum capacitance of 79 F g^{-1} at 0.6 A g^{-1} current density and demonstrate 68.6% capacity retention when the current density is 4 A g^{-1} .

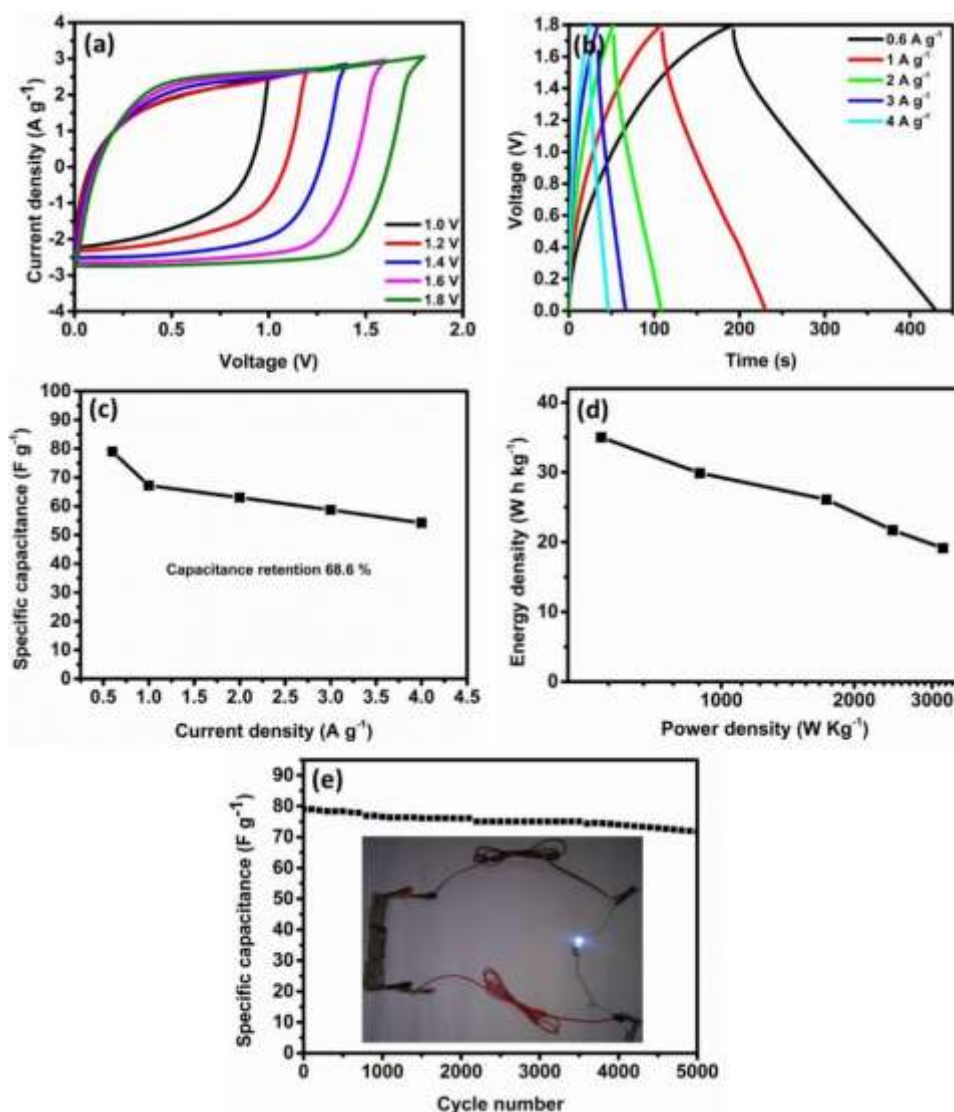


Figure 3.19. Electrochemical characteristics of an HMC-2 electrode as symmetrical capacitor using PVA+ Na₂SO₄ gel electrolytes (a) CV curves at scan rate of 50 mV s⁻¹ within different voltage windows (b) GCD curves at current densities of 0.6–4 A g⁻¹ (c) Specific capacitances of the symmetric cell at various current densities (d) Ragone plot of symmetrical cell and (e) Cycling stability at a current density of 0.6 A g⁻¹ (inset shows a white LED powered by three symmetrical devices in series)

Figure 3.19 (d) shows the relationship between energy density and power density. The device exhibits a maximum energy density of 35 W h kg⁻¹ at a power density of 529 W kg⁻¹ and it retains 20 W h kg⁻¹ at a power of 3180 W kg⁻¹, these results are better than similar reports (Y. Cai et al., 2016; X. Tian et al., 2017; Wang et al., 2016; X. Zheng et al., 2017). Figure 3.19 (e) shows the cycle stability of the symmetric SC, HMC-2//HMC-2, it exhibits 91.1% capacity retention after 5000 cycles at a current density of 0.6 A g⁻¹. The inset of Figure 3.19 (f) shows lighting

up of a white-light-emitting diode (LED) by using symmetric SC, HMC-2//HMC-2 and it glows for 2 minutes after charging ~5sec.

The excellent electrochemical performance of the HMC-2 as SC electrode and sulphur host is due to the following unique properties. 1) The higher surface area and pore volume help to improve the interaction between electrode surface and electrolyte at the porous region; HMC-2 can accommodate more volume changes of sulphur during the charge-discharge process. 2) It possesses a sheet-like morphology which helps to access the electrolytes easily, helps the diffusion and transmission of ions. 3) The overall specific capacitance gets improved due to the presence of N and O in the carbon matrix helps to trap the PSs during the cycling process of LSBs.

3.4 Conclusion

N and O inherently doped a high surface area carbon material was prepared by simple one-step carbonization from DDS without any additives. It is demonstrated that pyrolysis time plays a vital role to achieve high surface area and interconnected porous architecture. The carbon material (HMC-2) obtained with two hours of pyrolysis at 950 °C provide high BET surface area ($1766.9 \text{ m}^2 \text{ g}^{-1}$) and demonstrated as a functional host for sulphur with 995 mA h g^{-1} as initial discharge capacity and 790 mA h g^{-1} after 100 cycles with 79% capacity retention at 0.1C rate. HMC-2 electrode provides a specific capacitance of 431 F g^{-1} at a current density of 0.8 A g^{-1} . In addition, the symmetric SC has good rate capability and maximum energy density of 35 W h kg^{-1} and power density of 3175 W kg^{-1} using PVA+Na₂SO₄ gel electrolyte. HMC-2 with an interconnected porous network comprising of N and O functionalities is a promising energy storage material for future applications.

CHAPTER 4

VETIVER DERIVED CARBON FOR SUPERCAPACITOR ELECTRODE AND LITHIUM SULPHUR BATTERY

Hierarchically porous carbon tubes (HPC) inherently doped with iron oxide nanoparticles and heteroatoms (nitrogen and oxygen) was prepared from vetiver roots by ZnCl₂ activation method. The influence of pyrolysis temperature on the textural and energy storage characteristics of HPC was investigated in detail. HPC prepared at 800 °C (HPC-800 °C) achieved 1879 m² g⁻¹ BET surface area and a total pore volume of 0.91 cm³ g⁻¹. The tubular morphology and the inherently functionalized hierarchical pore structure augment the transport of ions in the carbonaceous matrix, demonstrating an excellent electrochemical performance. A symmetric supercapacitor is fabricated using aqueous Na₂SO₄ and organic LiTFSI electrolytes. The device exhibited a maximum energy density of 67.8 W h kg⁻¹ with maximum power density of 15000 W kg⁻¹ and ~ 88% capacity retention after 10,000 cycles when using 1M LiTFSI as the electrolyte. In addition, the HPC-800 °C acts as a conductive host for sulphur and the interconnected tubular porous network enables the rapid transport of lithium ions and electrons. The fabricated coin cell provides excellent cycling stability of 462 mA h g⁻¹ at 3C with 0.85% capacity decay per cycle. The synergistic effect of porous architecture and inherently co-doped iron, N & O facilitate to restrain the diffusion of PSs.

4.1 Introduction

Various strategies have been proposed to improve the electrochemical performance of LSBs by configuring the cathode (structure and composition), anode protection and electrolyte optimization (Yibo He, Chang, et al., 2018). Among these, engineering the cathode configuration is the most interesting topic of research in LSBs. The conductivity of sulphur is improved by incorporating or enfolding the materials such as carbon nanotube (L. Sun et al., 2015; Xi et al., 2015; Ye et al., 2016), graphene (H. Wang et al., 2011; Y.-X. Wang et al., 2013), graphene oxide (M. Xiao et al., 2013), carbon nanofiber (K. Fu et al., 2014; W. Kang et al., 2018; Zhengjiao Liu et al., 2018), carbon onions (Choudhury et al., 2017; Zeiger et al., 2016), porous carbon (Fei et al., 2016; Imtiaz et al., 2016; J. Li et al., 2014; X. Qian et al., 2016), metal oxides (Arias et al., 2018; Donghai et al., 2018; Guand Lai,

2018), conducting polymers (Cheng and Wang, 2014; Dirlam et al., 2017; Seh et al., 2016) etc., thereby augmenting the kinetics of Li-S redox reactions. These materials can improve the electrical conductivity of the active material, amount of active material utilization, and reduced the dissolution of PSs thus improving the capacity retention.

Porous carbon material doped with heteroatoms are extensively used as sulphur host due to its high surface area, pore volume, electrical conductivity can accommodate volume changes during the charge-discharge process and can confine LPS during shuttling through weak physical interactions (S. S. Zhang, 2015). The chemical confinement of LPS through chemical bonds is an advantage, which offers bonding between sulphur atom or PSs and other heteroatoms like N, O, S, B, P etc. (Seh et al., 2016). The anchored PSs are restrained on cathode host itself and defended from shuttling, reducing the active material loss and improving the electrochemical performance of the LSBs. Heteroatoms can be introduced into the carbon matrix by in-situ pyrolysis or post-treatment of the carbonaceous material with heteroatom containing substances. Post-treatment may destruct the carbon morphology and provoke unwanted pore obstructions. Insitu doped porous carbon gives a better electrochemical performance in LSBs. It is already reported that transition metals along with hetero (N, O, S and P) atom doped porous carbon improve the electrochemical performance (Hasegawa et al., 2015). This type of materials are capable of confining PS in the cathode side which enhance capacity retention while using as sulphur host in the LSB applications (Xia Liand Sun, 2014; Pang et al., 2015). Similarly, metals/metal oxides are preferred as additives in LSBs to improve its performance. Commonly used metal oxides are MnO, MnO₂, Ti₄O₇, TiO₂, Fe₂O₃, ITO and compounds like MXene, TiC, MS_x, M(OH)_x, etc. The strong bonding between metal-based materials and LPS prevents the diffusion and dissolution of LPS into the electrolyte (Arias et al., 2018; Donghai et al., 2018).

However, there is no consistency and scalability for the preparation of porous carbon and the production process is generally tedious and costly. Hence, it is essential to find well-organized and low-cost sources of porous carbon for the investigation of sulphur based composites for LSBs. Porous carbon from biomass

has its own advantageous such as high abundance, being renewable, rather inexpensive, environmentally friendly and sustainability. KOH or ZnCl₂ assisted activation and followed by carbonization is the common method for the preparation of bio-derived porous carbon (Zan Gao et al., 2017). Various examples are demonstrated in the literature to develop porous biochar from shaddock peel (S. Lu et al., 2016), bamboo (J. J. Cheng et al., 2015; Gu et al., 2015; Yuanyuan Li et al., 2017), apricot shell (K. Yang et al., 2015), silk cocoon (M. Xiang et al., 2017), pig bone (S. Wei et al., 2011), fish scale (S. Zhao et al., 2013), banana peel (F. Li et al., 2017), etc., and studied as cathode materials for LSBs. These carbon-sulphur composites have yet solved all the problems, still, improvement is required in terms of capacity fading and rate capability (Ould Ely et al., 2018; X. Zhang et al., 2017). Natural materials with organised structures and functionalities will be useful to produce better host material for sulphur to reduce the shuttling effect (Xia Liand Sun, 2014; X. Fan et al., 2018). Porous carbon with polar functionalities and doped metal oxides may synergistically boost the chemical adsorption ability (Eftekhari and Kim, 2017). Hence, the selection of carbon source plays a vital role to prepare hierarchically porous inherently functionalized carbon material. The aromatic root of vetiver (*Vetiveria zizanioides* L.), is a complex organic and inorganic compounds which inspired us to choose as a raw material for porous carbon. Vetiver is a well-known natural root available all over the world. Vetiver roots have a tufted vertically growing root structure. The roots are one of the most important organizational systems that make vetiver a miracle for its multifarious applications in soil and water conservation. It is a raw material for vetiver root handicrafts, environmental and perfumery products. In addition to absorbing water and maintaining soil moisture, vetiver roots are also capable of absorbing toxic substances, chemical fertilizers, pesticide residues and heavy metals and playing a major role in soil reclamation (P. Truong and Hart, 2001).

In this chapter, we developed a 3D carbon tube-like structure with N, O heteroatoms along with iron oxide nanoparticles from vetiver roots by ZnCl₂ activation at different temperature starting from 600 °C-900 °C. The hierarchical porous carbon tube (HPC) obtained at 800 °C displayed a maximum specific surface area of 1879 m² g⁻¹ with a total pore volume of 0.91 cm³ g⁻¹.

Electrochemical studies of the developed carbon material demonstrated its capacitive behaviour with a maximum energy density of 67.8 W h kg^{-1} and power density of 15000 W kg^{-1} . HPC-800 °C is used as sulphur host and evaluated as cathode material in LSBs. The presence of Fe functionalities has a catalytic effect on the LSB redox reaction and in improving the electrochemical performance (Donghai et al., 2018; Zhenzhen Liu et al., 2018; K. Sun et al., 2017). It is demonstrated that the presence of Fe functionalities in the HPC in addition to N and O helps to improve the electrochemical performance than the materials described in the previous chapters. The large surface area and porous texture with functionalities (N, O & Fe) of HPC impart quadruple confinement effect to chemically adsorb LPS and can alleviate strain during the charge-discharge process. Moreover, the interconnected tubular porous networks enable rapid transport of lithium ions and electrons.

4.2 Materials and Methods

4.2.1 Materials

Vetiver was obtained from Thiruvananthapuram, Kerala. Lithium sulphide (Li_2S 99.9%, Alfa Aesar) and Zinc chloride (ZnCl_2 , Merck) were used as received. All other chemicals are as mentioned in section 2. 2.1 and 3.2.1.

4.2.2 Material synthesis

4.2.2.1 Preparation of porous carbon

The root of *Vetiveria zizanioides* L, commonly known as vetiver was collected from the local market, Thiruvananthapuram, Kerala, India. It was crushed into pieces, washed with distilled water followed by ethanol several times and dried at $100 \text{ }^\circ\text{C}$ for overnight. The fine powder of the root was treated with ZnCl_2 in a ratio of 1:1 (w/w) for 24 hours. It was dried and the mixture was taken in an alumina crucible and pyrolyzed in a box furnace at various temperatures such as $600 \text{ }^\circ\text{C}$, $700 \text{ }^\circ\text{C}$, $800 \text{ }^\circ\text{C}$ and $900 \text{ }^\circ\text{C}$ for 1 hour at a heating rate of $2 \text{ }^\circ\text{C min}^{-1}$ in an inert atmosphere (Figure 4.1 (a)). Then, it was washed with HCl followed by distilled water until the

filtrate became neutral. The carbon material was dried in an oven at 100 °C and stored in a desiccator. The prepared carbon is hierarchically porous carbon tube (HPC) material.

4.2.2.2 Preparation of carbon-sulphur composite

Hierarchically porous carbon tube-sulphur composite (HPCS) is prepared by the following procedure discussed in section 3.2.2.2

4.2.2.3 Polysulphide adsorption study

The polysulphide solution was prepared by mixing sublimed sulphur and Li_2S in a ratio of 5:1 in DOL/DME as the solvent. This mixture was stirred overnight to produce the purple-brown polysulphide solution at 80 °C. Test solution (5 ml) was prepared by adding the polysulphide solution with 20 mg of HPC. The solution was vigorously stirred for 15 min. All these experiments were carried out in an Ar-filled glove box.

4.2.3 Material characterization

The presence of metal oxides in the vetiver was characterized using Energy dispersive X-ray fluorescence (EDXRF) (PANalytical, Epsilon 3). The presence of metals in the carbon samples were characterized by inductively coupled plasma atomic emission spectroscopy (ICP-AES) (Perkin Elmer, 4300 V Optima) and all other characterizaion described in section 2.2.3 and 3.2.3.

4.2.3.1 Preparation of supercapacitor electrode and electrochemical characterization

Electrodes were prepared and the electrochemical characterization was studied by the procedure described in the previous chapter 3, section 3.2.4.3. The specific capacitance, energy density and power densities were calculated by the equation described in section 3.2.4.4.

4.2.4.3 Sulphur cathode preparation and characterization

The HPCS cathode was prepared with an areal mass loading on the composite electrode of $\sim 3.7 \text{ mg cm}^{-2}$ and the electrochemical characterization was studied by the procedures described in section 2.2.4 and 2.2.5.

4.3 Results and Discussion

4.3.1 Physicochemical properties of HPCs



Figure 4. 1. Schematic illustration for the preparation of (a) HPC and (b) HPCS

Figure 4.1 (a) shows the schematic illustration of the preparation of the HPCs. It is simple chemical activation method, here ZnCl_2 act as Lewis acid and it will react with oxygen or nitrogen functionalities (Lewis base) of lignocellulosic materials in the vetiver roots to form complexes which initiate degradation in the chain which will randomly oriented though out the network (J. I. Hayashi et al., 2000; Zan Gao et al., 2017). The XRF results of powdered vetiver root exhibit the presence of metal oxides accumulated by bio sorption from the soil or water where it is cultivated (Table 4.1). The hyper accumulated metal oxides and the adsorbed activating agent in the porous texture (ZnCl_2) facilitate oxidation of active sites helps to develop high surface area porous carbon architecture. HPCs with an interconnected porous network and inherent dopants (N, O and FeO) was realised

from the gases produced during pyrolysis and due to the removal of metal oxides and activation agent (reacted and unreacted) while washing with water and HCl. The amount of C, O, N in the HPCs are disclosed by CHNS analysis (Table 4.2). As the carbonisation temperature increased, the resulted HPC has more carbon content, however, oxygen and nitrogen content decreased.

Table 4.1: XRF analysis of vetiver root

Vetiver	Compound	Conc.	Unit
1	MgO	0	ppm
2	Al ₂ O ₃	4.72	%
4	P ₂ O ₅	11.624	%
5	Cl	0.409	%
6	K ₂ O	2.379	%
7	CaO	7.063	%
8	TiO ₂	0.316	%
9	V ₂ O ₅	0.128	%
10	Cr ₂ O ₃	514.1	ppm
11	MnO	0.157	%
12	Fe ₂ O ₃	65.71	%
13	NiO	472.3	ppm
14	CuO	794.3	ppm
15	ZnO	0.116	%
16	As ₂ O ₃	283.4	ppm
17	Br	136.5	ppm
18	SrO	256.6	ppm
19	BaO	450.3	ppm
20	La ₂ O ₃	0	ppm
21	Eu ₂ O ₃	0.104	%
22	PbO	125.6	ppm
23	Re	6.3	ppm

Table 4.2: Elemental composition of HPCs from CHNS Analysis

Sample	C (%)	N (%)	H (%)	S (%)	O (%)
HPC-600 °C	59.98	4.30	3.03	0.00	32.96
HPC-700 °C	76.92	3.5	2.78	0.00	16.8
HPC-800 °C	87.02	2.88	1.76	0.00	8.34
HPC-900 °C	92.89	1.08	0.79	0.00	5.24

Table 4.3: ICP-AES analysis of HPCs

Sample	Iron %
HPC-600 °C	0.93
HPC-700 °C	0.89
HPC-800 °C	0.85
HPC-900 °C	0.81

The iron present in HPCs is analysed using inductively coupled plasma-atomic emission spectrometry (ICP-AES) (Table 4.3) by leaching it with conc.HCl.

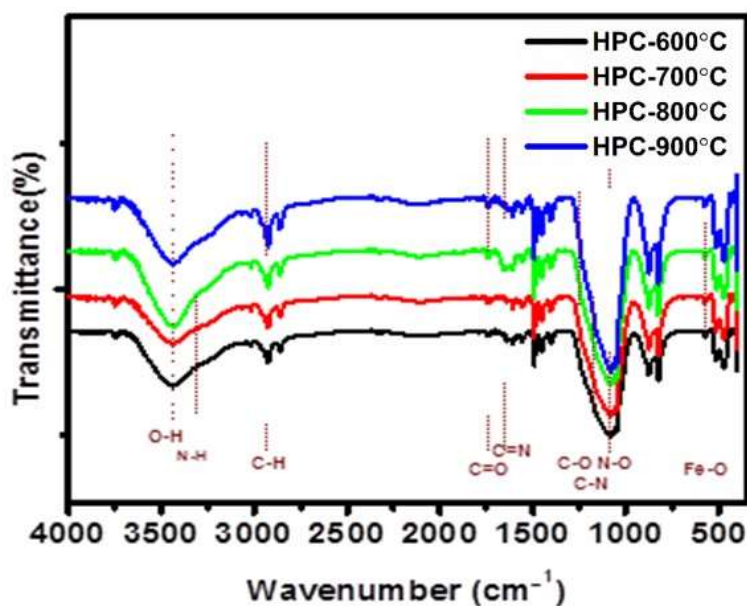


Figure 4.2. FTIR spectra of HPCs at various temperature

FTIR spectroscopy is employed to identify the functional groups in the prepared carbon (Figure 4.2). The bands at 3450 cm^{-1} and 3261 cm^{-1} are due to stretching vibrations of O-H and N-H bonds, respectively. It is observed that the intensity of these bonds declines when the carbonization temperature increases, attributed to the decrease in the concentration of nitrogen and oxygen functionalities. The band at 2932 cm^{-1} and 2850 cm^{-1} are due to symmetric and asymmetric stretching vibrations of C-H bonds. The band at 1728 cm^{-1} and 1640 cm^{-1} correspond to the stretching vibrations of C=O and C=N in the HPCs. The band at 1252 cm^{-1} , 1095 cm^{-1} are due to the stretching vibrations of C-O and C-N. The band at 586 cm^{-1} is due to the stretching vibration of the Fe-O bond (Elizabeth et al., 2012). These results prove the presence of oxygen, nitrogen and iron functionalities on the surface of HPCs.

The textural properties and the porosity of the carbon material are the most important criteria for energy storage application and CO_2 adsorption. N_2 and CO_2 adsorption-desorption analysis were used for the porosity evaluation of the

activated carbon. The activation of vetiver with ZnCl_2 yields high surface area and pore volume compared to the carbon without activation (Table 4.4 and 4.5).

Table 4.4: Surface area of HPCs without activation

Sample	BET surface area ($\text{m}^2 \text{g}^{-1}$)	Micropore surface area ($\text{m}^2 \text{g}^{-1}$)
HPC-600 °C	537	0.26
HPC-700 °C	604	0.34
HPC-800 °C	551	0.32
HPC-900 °C	493	0.27

Table 4.5: Surface area of HPCs with activation

Sample	BET surface area ($\text{m}^2 \text{g}^{-1}$)	Micropore surface area ($\text{m}^2 \text{g}^{-1}$)	Total pore volume ($\text{cm}^3 \text{g}^{-1}$)	Micropore volume ($\text{cm}^3 \text{g}^{-1}$)
HPC-600 °C	1398	797	0.67	0.28
HPC-700 °C	1678	828	0.77	0.24
HPC-800 °C	1879	772	0.91	0.18
HPC-900 °C	1628	360	0.86	0.04

ZnCl_2 activation of materials leads to more interspace between lignocellulosic materials in the vetiver which in turn increases the surface area compared to inactivated materials (Table 4.4 and 4.5). Figure 4.3 (a and b) shows N_2 adsorption-desorption isotherms and their corresponding pore size distribution analysis. The strong N_2 adsorption at low relative pressure (P/P_0) indicates the presence of micropores while a hysteresis loop in the desorption region at $P/P_0 \sim 0.4-0.8$ indicates the presence of mesopores and a slight upward tendency at $(P/P_0) \sim 1$ is due to the presence of macropores (Gu et al., 2015). The shape of N_2 adsorption-desorption isotherms varies for HPCs prepared at different pyrolysis temperature. HPC-600 °C and HPC-700 °C exhibit Type I behaviour on the other hand, HPC-800 °C and HPC-900 °C are Type IV. Type I behaviour is exhibited by microporous carbon and type IV is the combination of micro and mesoporous carbon. The results show that the carbonization temperature has a significant effect on the surface area and porosity of the material. The increase of N_2 uptake in HPC with increasing carbonisation temperature from 600 °C to 800 °C, indicating the gradual development of pores (S. Zhang et al., 2014). The BET surface area increases from 1398 to 1879 $\text{m}^2 \text{g}^{-1}$ and its total pore volume increases from 0.67 to 0.91 $\text{cm}^3 \text{g}^{-1}$. Further increase in the activation temperature from 800 °C to 900 °C, experience a

reduction in adsorption of N_2 attributed to the deterioration of the porous structure by the fusion of adjacent micropores. As a result, the surface area and pore volume is reduced to $1628 \text{ m}^2 \text{ g}^{-1}$ and $0.86 \text{ cm}^3 \text{ g}^{-1}$, respectively (S. Wei et al., 2011). From this, we conclude that the optimum condition for preparing highest surface area carbon from vetiver by zinc chloride activation is $800 \text{ }^\circ\text{C}$. The hierarchical porous structure of HPCs are further evidenced from the DFT pore size distribution analysis (inset of Figure 4.3 (b)). It is clearly observed from the pore size distribution graph, when the activation temperature increases, the pore size increases (Figure 4.3 (b)) resulting in a well-developed hierarchical porous structure (inset of Figure 4.3 (b)) (S. Wei et al., 2011).

The high surface area and low pore size distribution with N, O and Fe heteroatoms on the surfaces of carbon favour the CO_2 adsorption. Its capacity depends upon the micropore volume and heteroatom doping on the porous carbon (Praveen et al., 2017; J. Wang and Liu, 2014). The CO_2 adsorption isotherm of HPCs samples at room temperature and $0 \text{ }^\circ\text{C}$ are depicted in Figure 4.3 (c and d). It is seen that the CO_2 adsorption increases habitually with the increase of pressure. HPC- $700 \text{ }^\circ\text{C}$ has the highest CO_2 adsorption capacity at $0 \text{ }^\circ\text{C}$ and room temperature, which is about $4.92 \text{ mmol Hg}^{-1}$ and 2.8 mmol Hg^{-1} , respectively. As the micropore surface area increases for HPC- $700 \text{ }^\circ\text{C}$, the adsorption capacity increases. Further, increase in the activation temperature to $800 \text{ }^\circ\text{C}$, HPC- $800 \text{ }^\circ\text{C}$ displayed an increase in total surface area due to the development of mesopores, however, its micropore surface area decreases and exhibit less CO_2 adsorption capacity. Surface area is decreased for HPC- $900 \text{ }^\circ\text{C}$ due to deterioration of mesopores, and shows a CO_2 adsorption capacity of 4.4 mmol Hg^{-1} and 2.3 mmol Hg^{-1} room temperature and $0 \text{ }^\circ\text{C}$, respectively. This well-developed porous structures helps to develop a more active site through which ions can easily diffuse and reach the electrode surfaces.

XRD pattern of HPC exhibits two broad diffraction peaks at $2\theta = 24^\circ$ and 44° due to the reflections from (002) and (100) graphitic planes (Figure 4.3(e)). These broad peaks indicate the amorphous and disordered nature of HPCs (Gu et al., 2015; Jinxin Guo et al., 2015). In comparison (HPC- $600 \text{ }^\circ\text{C}$ to $900 \text{ }^\circ\text{C}$) the disorder induced peak broadening is observed due to the variation in the d spacing

values (Praveen et al., 2017). The sharp diffraction peaks at 36° , 42° , 61° and 76° are due to the reflections from the phase pure cubic FeO (space group: $Fm\bar{2}m$ (225)) (JCPDS 00-003-0968).

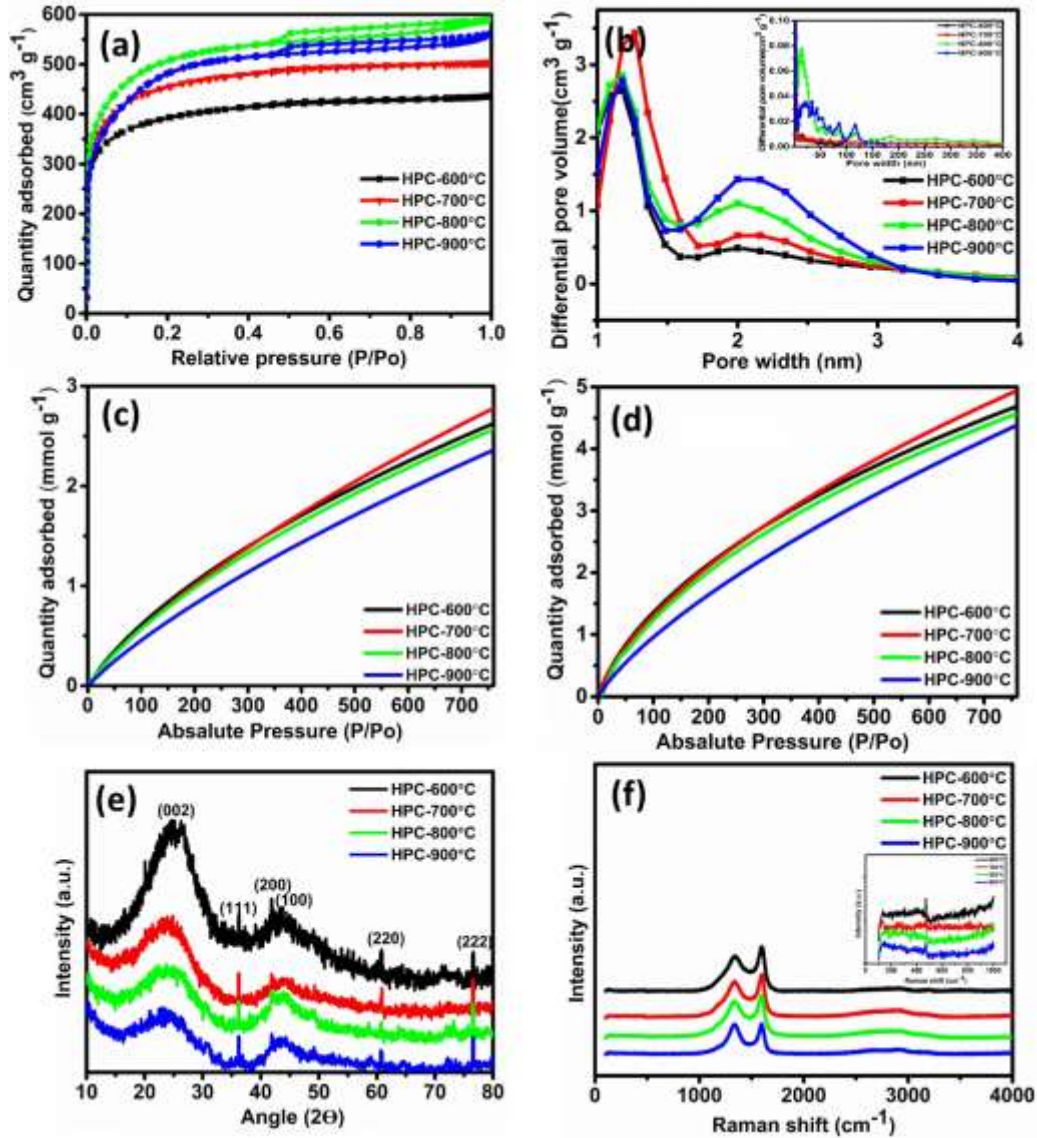


Figure 4.3. (a) N_2 adsorption-desorption isotherm (b) DFT pore size distribution analysis, CO_2 adsorption at (c) $27^\circ C$ (d) $0^\circ C$ (e) X-ray diffractograms and (f) Raman spectrum for HPCs

The amorphous and disordered nature of HPCs, further corroborated by Raman spectra , which shows two bands at 1336 cm^{-1} (D band) and 1590 cm^{-1} (G band) (Figure 4.3(f)). D band is the breathing mode vibration of A_{1g} , confirms the amorphous character. G band attributes to the E_{2g} phonon of the sp^2 carbon (Jinxin Guo et al., 2015). The ratio of the intensities of D and G bands (I_D/I_G) is a measure

of defects in the carbonaceous materials. The values of the I_D/I_G ratio, increases from 0.91 to 0.98 (HPC-600 °C to 900 °C), indicating that the defect gets more pronounced while the activation temperature increases (Praveen et al., 2017). A distinct Fe-O Raman band is observed for HPCs at $\sim 595\text{ cm}^{-1}$ (inset of Figure 4.3 (f)), indicates the presence of FeO in the carbon matrix (Hanesch, 2009). These results are in good agreement with the XRD data.

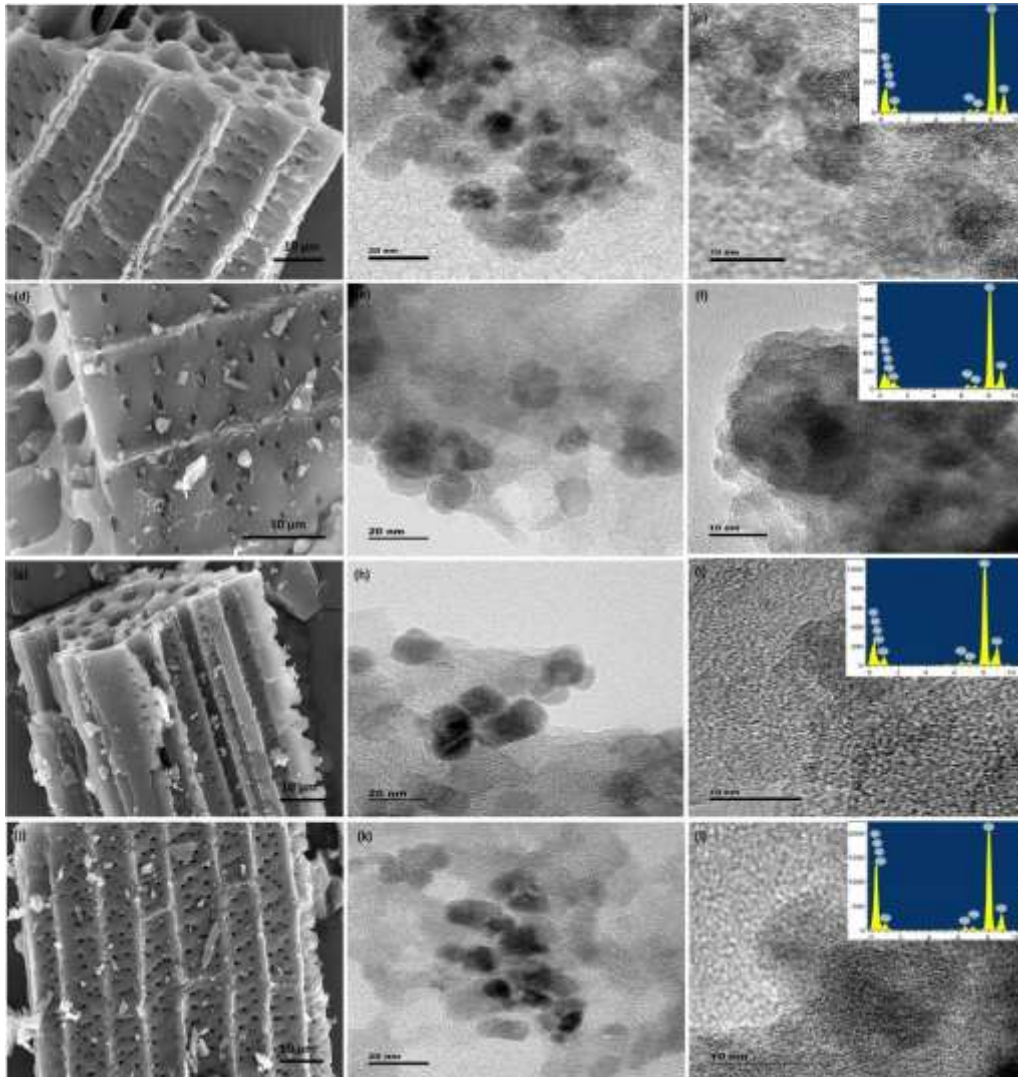


Figure 4.4. (a) SEM image (b) and (c) TEM images of HPC-600 °C (d) SEM image (e) and (f) TEM images of HPC-700 °C (g) SEM image (h) and (i) TEM images of HPC-800 °C (j) SEM image (k) and (l) TEM images of HPC-900 °C [Inset: corresponding TEM - EDS spectrum]

The FESEM images of HPCs are characterized by the well-developed interconnected porous network with macropores in a range of 1-2 μm (Figure 4.4),

which is served as an ion buffering reservoir for the transportation of the electrolyte ions (D. Zhou et al., 2017). It is observed that HPC have a micro tube-like morphology with open channels.

TEM images of the HPC show a graphene sheet-like structure with interconnected micropores, which enhance the surface area of the material (Figure 4.4 (b-c), (e-f), (h-i) & (k-j)). The pores are due to the gas bubble formation at high temperature (J. i. Hayashi et al., 2000). The presence of these micropores helps for the ion storage and better capacitive behaviour. This porous network allows fast ion diffusion and provides more active sites for the development of the EDLC. Moreover, it is observed that 13.05 nm FeO nanoparticle decorated the surface of the HPCs. This may be due to the reduction of Fe³⁺ to Fe²⁺/Fe using C/CO as a reducing agent during the ZnCl₂ activation at higher temperature in the inert atmosphere (Mondal et al., 2004).



TEM-EDS analysis (inset of Figure 4.4) confirms the presence of N, O and Fe in the porous carbon. These heteroatoms functionalities facilitate to improve the specific capacitance through the pseudocapacitive behaviour (Paraknowitsch and Thomas, 2013).

XPS measurements were used to investigate the chemical states of the elements in HPC-800 °C. Survey scan (Figure 4.5 (a)) analysis of the HPC-800 °C, reveals the presence of C1s, N1s, O1s and Fe2p in the porous carbon at 283.7 eV, 400 eV, 533.1 eV and 710 eV, respectively. The deconvoluted C1s spectrum (Figure 4.5 (b)) has 5 components, C-C/C=C (284.6 eV) of sp², C-N (285.6 eV), C-O bond (286.4 eV), C=N bond (287.2 eV) and C=O (288.6 eV). The deconvoluted N1s spectrum (Figure 4.5 (c)) contains the peak corresponding to pyridinic (398.1 eV), pyrrolic (400 eV), graphitic (401.7 eV) and nitrogen oxide (403.2 eV). The deconvoluted O1s spectrum (Figure 4.5 (d)) contains four components: Fe-O (529.3 eV), N-O (530.7 eV), C-O bond (531.9 eV), and C=O bond (533.1 eV) (Jin et al., 2017; N. Tian et al., 2016; T. Zhou et al., 2017; X. Yuan, Liu., et al., 2017; G. Zhou et al., 2015; M. Chen et al., 2017; Z. Wang., et al., 2014).

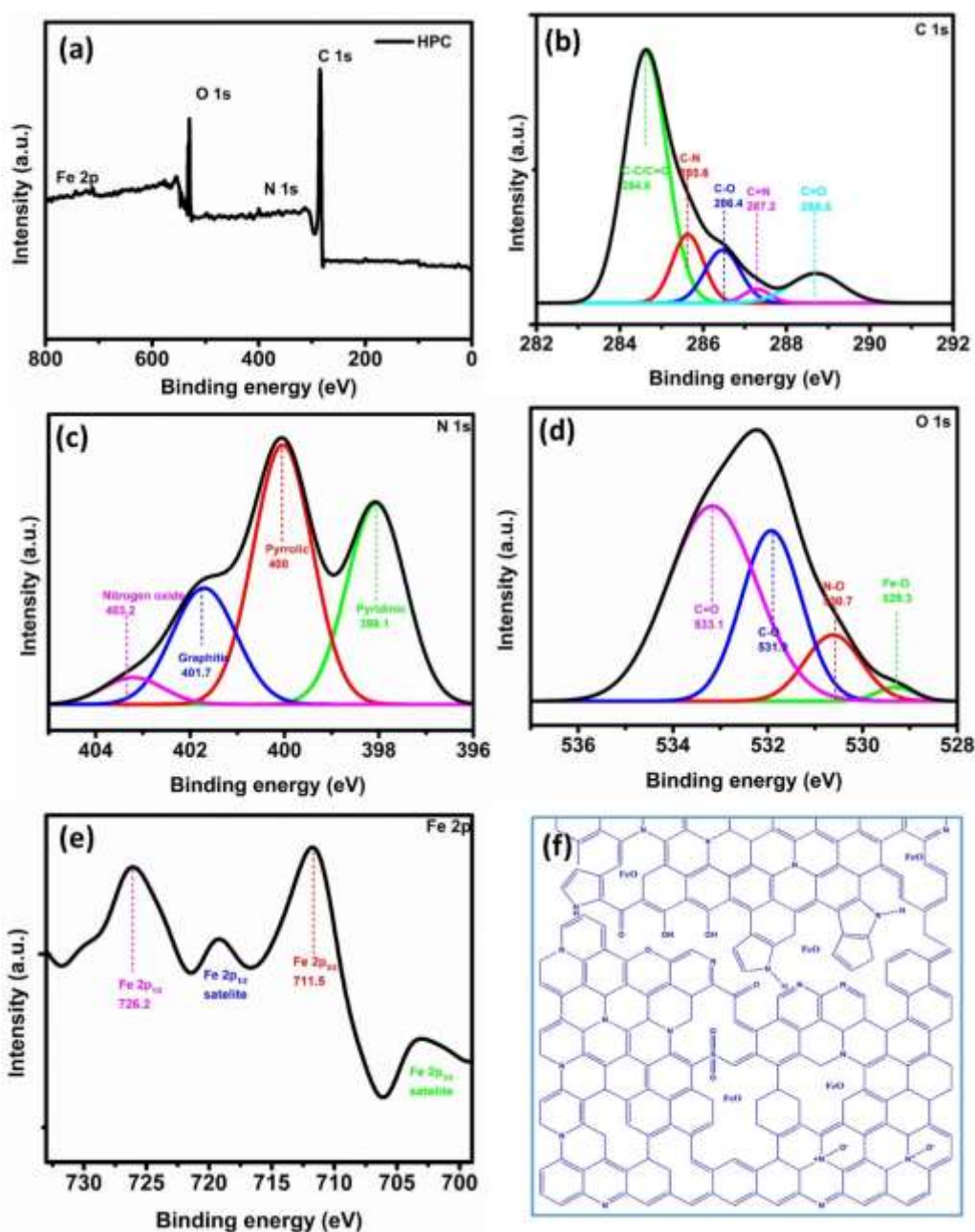


Figure 4.5. XPS spectra of HPC-800 °C (a) Survey scan, High resolution (b) C1s (c) N1s (d) O1s (e) Fe2p and (f) Schematic illustration of nitrogen, oxygen and iron-containing porous carbon

. The Fe2p spectrum (Figure 4.5 (e)) was deconvoluted to evaluate the nature of Fe in the porous carbon. Fe2p_{3/2} and Fe2p_{1/2} binding energies are located at 711.5 eV and 726.2 eV corresponds to the Fe²⁺ ionic state in the FeO (A. C. Lim et al., 2018). A small and distinguishable peaks are observed at 702.97 eV and 719.05 eV assigned as the satellite peak of Fe2p_{3/2} and Fe2p_{1/2}, respectively (Sridhar et al., 2015). Based on these observations a schematic representation for HPC is

displayed (Figure 4.5 (f)) (Y. Hao et al., 2015). The N, O and Fe functionalities will generate more electroactive sites for energy storage via pseudocapacitive contribution by creating more disorder in the carbon matrix (C. Wu et al., 2016). The HPC-800 °C is further characterized by elemental mapping analysis (Figure 4.6), which confirms the presence of oxygen, nitrogen and iron in the porous carbon. The uniform distribution of nitrogen and iron helps to improve the electrochemical performance of the capacitor.

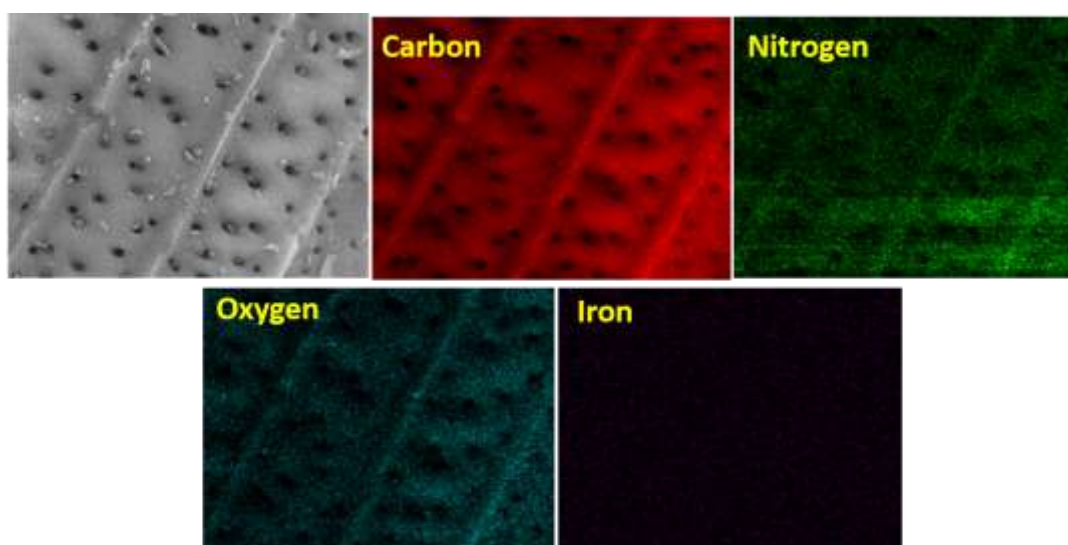


Figure 4.6. Elemental mapping of HPC-800 °C

4.3.2 Electrochemical performance of the HPCs

4.3.2.1 HPCs as supercapacitor electrodes

A three electrode system is used to evaluate the electrochemical performance of the prepared electrode materials (3 mg cm^{-2} on Ni foam) which is taken as working electrode, Ag/AgCl as reference electrode, Pt mesh as counter electrode and aqueous 1M Na_2SO_4 as electrolyte. Figure 4.7 (a-d) shows the CV curves of HPCs at different scan rates at a voltage window of -0.6 to 0.8 V at a scan rate of 5-20 mV s^{-1} . The HPCs show perfect EDLC behaviour, however, the expected pseudocapacitive behaviour from the heteroatom functionalities (nitrogen-containing functional groups and iron oxide) is not well pronounced. HPC-800 °C gives the higher integrated area due to the high surface area and increased active sites, which contribute to high specific capacitance.

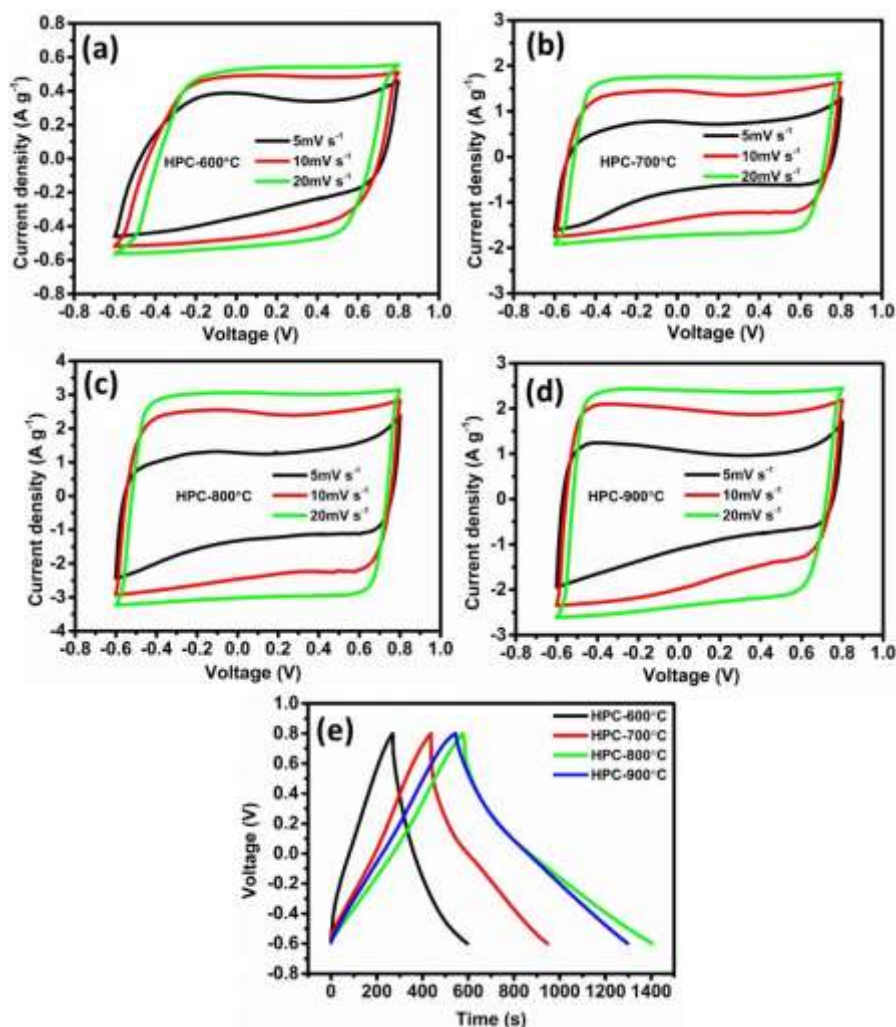


Figure 4.7. CV curves of HPCs at different scan rates (a) 600 °C (b) 700 °C (c) 800 °C (d) 900 °C and (e) GCD curves of HPCs at a current density of 0.8 A g^{-1}

The electrochemical capacitance of HPCs is further characterized by the GCD experiment at a current density of 0.8 A g^{-1} (Figure 4.7 (f)). All the samples exhibit linear and symmetric curves, indicating electrochemical reversibility and charge-discharge characteristics. The specific capacitance is calculated using the discharge branch with equation (3.1) for HPC-600 °C (116 F g^{-1}), HPC-700 °C (182 F g^{-1}), HPC-800 °C (298 F g^{-1}) and HPC-900 °C (268 F g^{-1}). A trend is observed in the specific capacitance on par with that of surface area and pore volume. Even though no much variation is observed in the surface area of HPC-700 °C ($1678 \text{ m}^2 \text{ g}^{-1}$) and HPC-900 °C ($1628 \text{ m}^2 \text{ g}^{-1}$) the disparity in the specific capacitance (182 F g^{-1} and 268 F g^{-1}) may be due to the inaccessible narrow micropores of HPC-700 °C compared to HPC-900 °C. The free movement of hydrated ion might be

restricted to reach the surface of HPC-700 °C to create electric dipoles on the surface of carbon.

The excellent electrochemical performance of the HPC-800 °C is due to the higher surface area, better pore size distribution and micro/meso/macropore which ultimately help in better ion transport. Also the presence of nitrogen, oxygen and iron heteroatoms foster the wettability of electrodes and in improving the electronic conductivity (Razmjooei et al., 2017). HPC-800 °C is chosen for symmetric capacitor fabrication due to higher specific capacitance compared to other HPCs for further electrochemical studies using 1M Na₂SO₄ electrolyte.

A symmetric SC is fabricated by using the CR2032, type coin cell using 1M Na₂SO₄ as electrolyte (mass of active material for one electrode ~ 1.5 mg cm⁻²) with cellulose material as separator. Figure 4.8 (a) shows rectangular shaped CV curves of HPC-800 °C//HPC-800 °C symmetric SC at the scan rate from 10 to 110 mV s⁻¹, certify excellent capacitive behaviour and rate capability of the material. Figure 4.8 (b) represents the GCD curve at different current densities from 0.5 A g⁻¹ to 10 A g⁻¹, which is triangular, symmetrical (F. Wang et al., 2017; Y. Wang et al., 2016; Y. Deng et al., 2016). HPC-800 °C//HPC-800 °C shows a specific capacitance of 61 F g⁻¹ at a current density of 0.5 A g⁻¹ and the capacitance remains at 53.8 F g⁻¹ at a current density of 10 A g⁻¹ demonstrates excellent rate capability with 98% capacitance retention (Figure 4.8 (c)).

EIS studies were carried out to gain information about the carbon-electrolyte interface of HPC. Figure 4.8(d) and inset shows the Nyquist plot and the equivalent circuit for HPC-800 °C//HPC-800 °C (Na₂SO₄ electrolyte) before and after 10000 cycles. The straight line in the low frequency region is almost vertical before and after cycling indicates ideal capacitive behaviour. R_{ct} and ion diffusion resistance are almost same before and after cycling attributed to its electrochemically stable nature of inherently doped functionalities and well-connected porous structure aids ionic diffusion in the electrode.

HPC-800 °C//HPC-800 °C gives a maximum specific energy density of 27 W h kg⁻¹ at a power density of 444 W kg⁻¹. Its energy density remains 23.5 W h kg⁻¹

¹ even at a higher power density of 8844 W kg⁻¹ (Figure 4.8 (e)). 98% capacity retention is observed after 10000 cycles compared to initial specific capacitance (Figure 4.8 (f)).

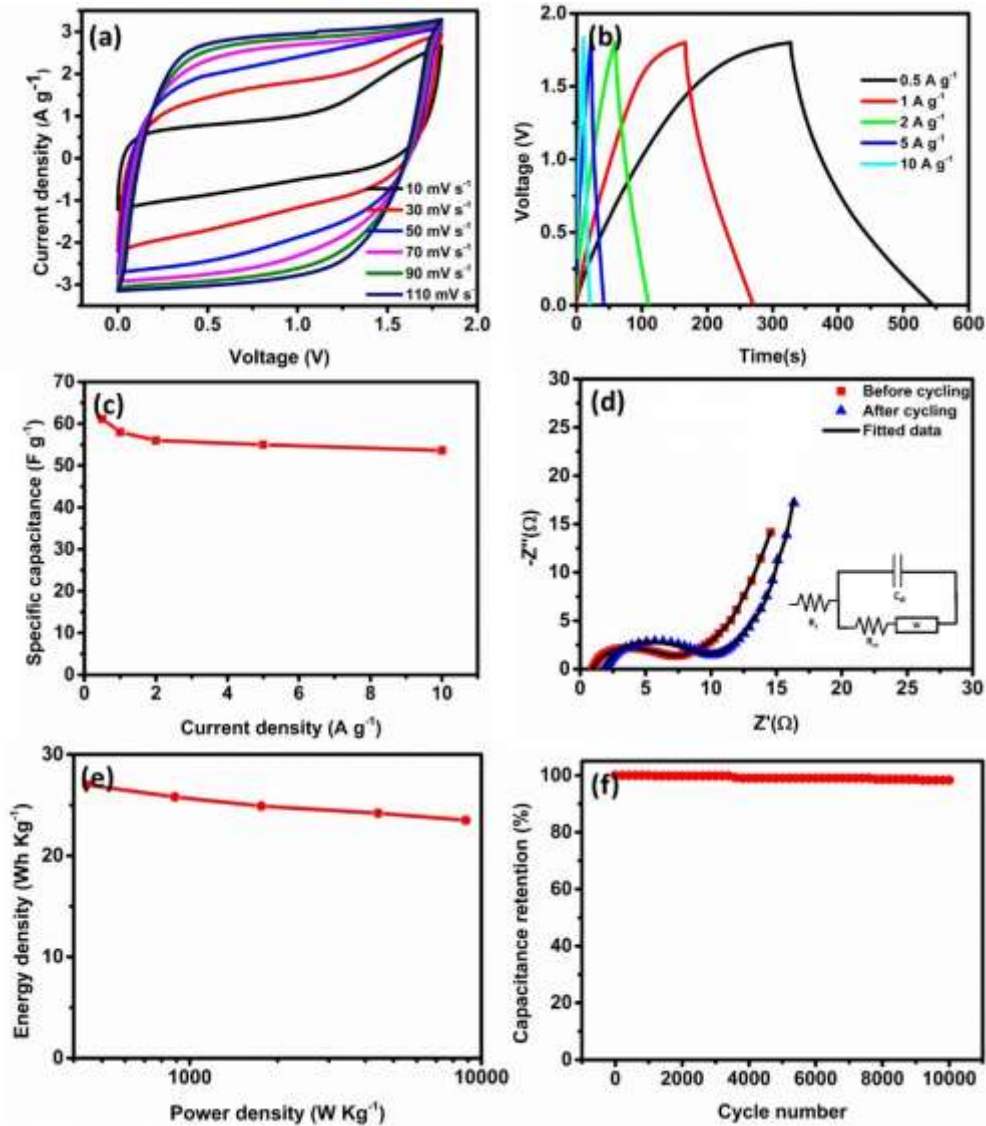


Figure 4.8. Electrochemical characteristics of HPC-800 °C based symmetrical capacitor with 1M Na₂SO₄ electrolyte (a,b) CV and GCD curves of the symmetric cell at various scan rates and various current densities in aqueous electrolyte (c) Specific capacitances of symmetric cell at various current densities (d) EIS analysis [inset: equivalent circuit]. (e) Ragone plot of symmetric cell and (f) Cycling stability at a current density of 0.5 A g⁻¹

Table 4.6: Impedance parameters obtained from the electrochemical equivalent circuit analysis with 1M Na₂SO₄ electrolyte

Material description	Rs (Ω)	Cdl (F)	Rct (Ω)	Y ₀ (Ω ⁻¹ s ^{1/2})
HPC before cycling	0.09	2.26	7.6	0.019
HPC after cycling	2.08	1.76	7.9	0.018

The energy density of supercapacitor can be increased either by increasing the specific capacitance (C) or by increasing the voltage window (V). The energy of supercapacitor in aqueous solution is lower than that of the non-aqueous solution due to the lower operating voltage window ($< 2V$) (François et al., 2014; Zhong et al., 2015). To improve the energy density (27 W h kg^{-1}) achieved using $1M \text{ Na}_2\text{SO}_4$, we chose $1M \text{ LiTFSI}$ in DOL/DME as an electrolyte has a wide operating voltage window ($0-3V$). The organic electrolyte LiTFSI is commonly used in LSBs (X. Fan et al., 2018) and SCs (Sultan, Ahsan, et al., 2018) which is stable at high potential without decomposition (Angulakshmi and Stephan, 2015). A symmetric cell is prepared using the $1M \text{ LiTFSI}$ in DOL/DME as electrolyte with PP as separator (mass of active material for single electrode $\sim 1.6 \text{ mg cm}^{-2}$). CV curves represent an ideal rectangular shape, which indicates the perfect EDLC behaviour at a scan rate of 10 mV s^{-1} between the voltage window 0 to $3V$ (Figure 4.9 (a)). When the scan rate increased to 110 mV s^{-1} , it maintains the rectangular shape indicates the excellent rate capability. GCD curves exhibit linear charge-discharge profiles at different current densities from 0.5 to 10 A g^{-1} which is in good agreement with the CV studies (Figure 4.9 (b)).

Figure 4.9 (c) shows the relationship between the specific capacitance and current density. The maximum capacitance of the symmetric cell calculated from the GCD curve is 54 F g^{-1} at a current density of 0.5 A g^{-1} , it reaches 46 F g^{-1} when current density increased to 10 A g^{-1} with 80% capacity retention which indicates good rate capability Figure 4.9 (d) and inset show the Nyquist plot of HPC-800 °C //HPC-800 °C (LiTFSI electrolyte) and its equivalent circuit model before and after cycling. It is observed that the R_{ct} and ion diffusion resistance are more than that of the cell using $1M \text{ Na}_2\text{SO}_4$ as electrolyte (Table 4.7) due to the poor ionic conductivity of LiTFSI compared to Na_2SO_4 (Hnedkovsky et al., 2005; Nishimoto et al., 1999). Since the same current collector and material is used, the change in R_s is likely contributed by the internal resistance of electrolyte. The minor change in R_{ct} and ion diffusion after cycling (10000 cycles) demonstrates that the functionalized porous architecture acts as ion adsorption sites and retains its structural integrity for a long time.

Table 4.7: Impedance parameters obtained from the electrochemical equivalent circuit analysis with 1M LiTFSI electrolyte

Material description	R_s (Ω)	Cdl (F)	R_{ct} (Ω)	Y_0 ($\Omega^{-1}s^{1/2}$)
HPC before cycling	2.37	2.26	21.4	0.016
HPC after cycling	3.55	1.76	28.22	0.010

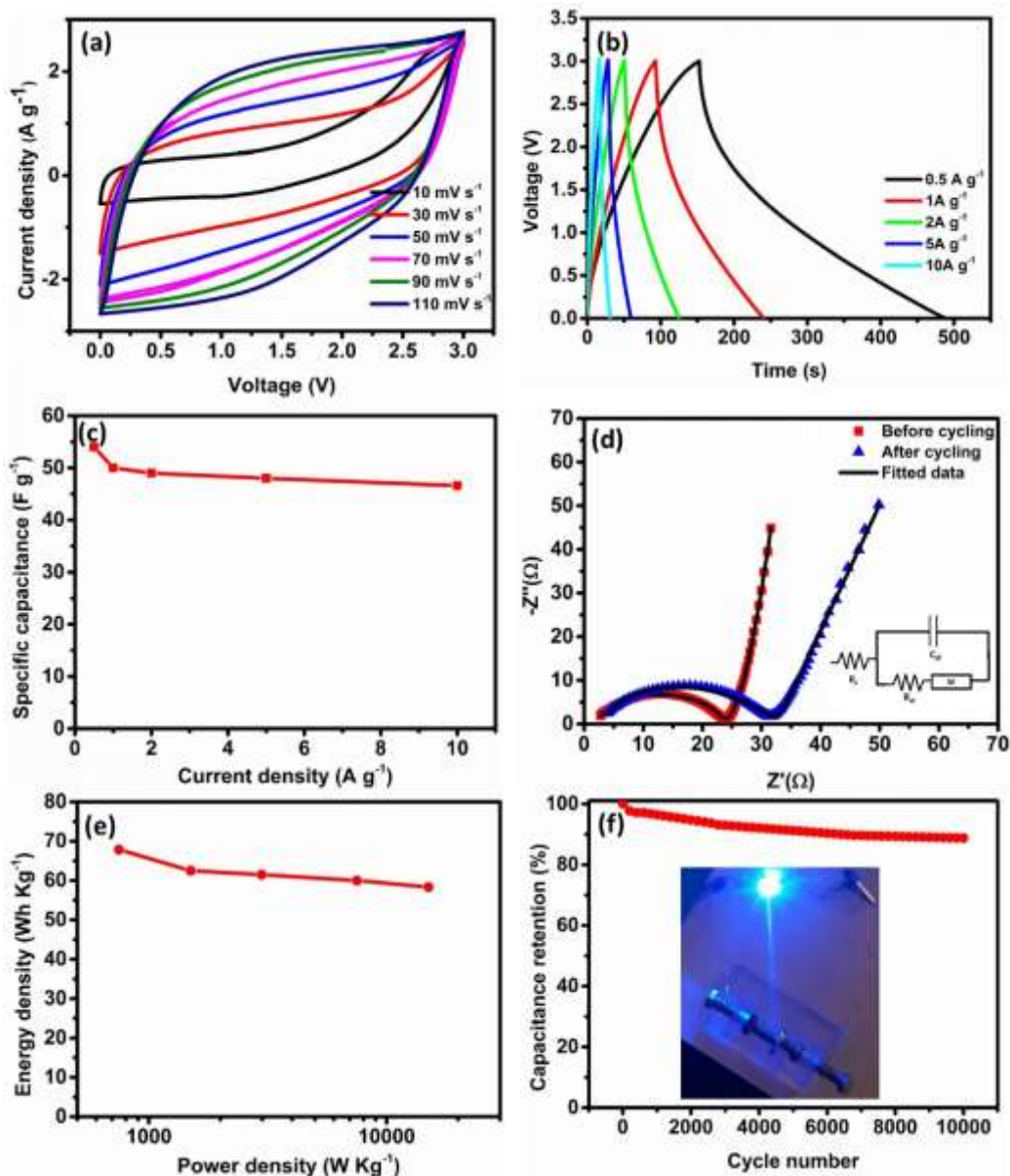


Figure 4.9. Electrochemical characteristics of HPC-800 °C based symmetrical capacitor with 1M LiTFSI electrolyte (a, b) CV and GCD curves of the symmetric cell at various scan rates and various current densities in aqueous electrolyte (c) Specific capacitance of symmetric cell at various current densities (d) EIS analysis at the open circuit potential in the frequency range from 100 mHz to 100 k Hz [inset: equivalent circuit].(e) Ragone plot of symmetric cell and (f) Cycling stability at a current density of 0.5 A g⁻¹ (inset shows a white LED powered by two symmetrical devices in series with 1M LiTFSI electrolyte

Figure 4.9 (e) shows the relationship between energy density and power density. The device exhibits a maximum energy density of 67.8 W h Kg^{-1} at a power density of 749 W kg^{-1} and it retains 46 W h kg^{-1} at a power of 15000 W Kg^{-1} , better than the values reported elsewhere (Table 4.7).

Ahmed et al reported activated carbon from rotten carrot obtained an energy density of 28.4 W h Kg^{-1} using 1M LiClO_4 in EC: PC (Ahmed et al., 2018). Neem leaves derived carbon obtained an energy density of $10.33 \text{ W h Kg}^{-1}$ with the same electrolyte (Sultan, Parvaz, et al., 2018). Wang et al studied sodium polyacrylate derived porous nanocages with the energy density of 40.7 W h Kg^{-1} in 1M TEABF_4 in AN (D. Wang et al., 2018). Ahmed et al reported pea skin-derived activated carbon with an energy density of 19.6 W h Kg^{-1} in 1M LiTFSI in EMITFSI (Sultan, Ahsan, et al., 2018). Novolac derived carbon beads exhibited maximum energy density of 22 W h Kg^{-1} in 1M TEABF_4 in AN (Krüner et al., 2018). Zhang et al reported Hierarchical porous carbon materials from the nanosized metal-organic complex with an energy density of 43 W h Kg^{-1} in 1M BMIMBF_4 in AN (S. Zhang et al., 2018). The superior electrochemical performance is attributed to N and Fe-doped high surface area carbon matrix with porous architecture which facilitates the activity of EDLC (M. Xu et al., 2017).

Table 4.8: Comparison of energy densities of porous carbon materials with various organic electrolytes

Material	Electrolyte	Energy density (W h Kg^{-1})	Power density (kW Kg^{-1})	References
Rotten Carrot	1M LiClO_4 in EC: PC	28.4	89.1	(Ahmed et al., 2018)
Neem leaves	1M LiClO_4 in EC: PC	10.33	4.66	(Sultan, Parvaz, et al., 2018)
Sodium polyacrylate	1M TEABF_4 in AN	40.7	0.675	(D. Wang et al., 2018)
Pea skin	1M LiTFSI in EMITFSI	19.6	25.4	(Sultan, Ahsan, et al., 2018)
Novoloc	1M TEABF_4 in AN	22	-	(Krüner et al., 2018)
Al-MOC	1M BMIMBF_4 in AN	43	-	(S. Zhang et al., 2018)
Vetiver	1M LiTFSI in DOL/DME	67.8	0.749	Our work

The cycling stability of SC with organic electrolyte is tested (Figure 4.9 (f)), under the current density of 0.5 A g^{-1} , where no capacity change is observed during initial cycles and it shows 88% capacity retention after 10000 cycles. The inset shows lighting up of a white-light-emitting diode (LED) using symmetrical SC, HPC-800 °C//HPC-800 °C and it was glowing for 2 minutes.

The excellent electrochemical performance of the HPC-800 °C is due to the following unique properties 1) The high surface area and pore volume with a considerable amount of micro/meso/macro porous area which positively assist in developing a more amount of electrical double layer between electrode surface and electrolyte interface. 2) Presence of highly interconnected network with hierarchical pores helps to tune a channel for the diffusion and transmission of ions. 3) The improvement in its wettability and electronic conductivity due to the presence of inherent dopants N and Fe.

4.3.2.2 HPCS as cathode material for lithium-sulphur batteries

The HPC-800 °C carbon material with the high surface area is chosen as the electrode material for LSB applications. HPC-800 °C-sulphur composite (HPCS) was prepared by melt diffusion method (Figure 4.1 (b)) as mentioned in section 3.2.2.2. The structural differences between HPC-800 °C and HPCS were investigated by XRD and Raman analysis. Elemental sulphur shows all the diffraction peaks of the orthorhombic sulphur (JCPDS 00-008-0247) (Figure 4.10 (a)). During the heating process, the sulphur particle melts and diffused into the pores due to the low viscosity of sulphur and strong adsorbing capacity of HPC. The sulphur is considered to be in the amorphous state inside the micro and mesopores (Jinxin Guo et al., 2015). The infiltrated sulphur into the macropores and on the surface of the carbon is crystalline in nature. Less intense diffraction peaks of sulphur in the HPCS denotes that sulphur is well dispersed in the pores of the carbon matrix, which is evident from the XRD studies (Jinxin Guo et al., 2015; W. G. Wang et al., 2014). Moreover, the sharp diffraction peaks at the 2θ values of 36° , 42° , 61° and 76° are due to the reflections from the phase pure cubic FeS (space group: $Fm\bar{2}m$ (225)) (JCPDS 00-003-0968) formed by the reaction of FeO with elemental sulphur during the melt diffusion reaction (Figure 4.10 (a)).

Raman spectrum of HPCS shows two prominent Raman band at ~ 1346 cm^{-1} and ~ 1595 cm^{-1} that corresponds to D band (disordered graphitic structure) and G band (ordered sp^2 hybridised graphitic structure), respectively (Figure 4.10 (b)). The I_D/I_G ratio of HPC is 0.9 and this value is increased to 0.91 in the case of HPCS. The coexistence of both G and D band suggests that the HPC is amorphous in nature (Dresselhaus et al., 2007). Three bands can be observed for crystalline sulphur at 125 cm^{-1} , 200 cm^{-1} , 475 cm^{-1} . These sulphur bands are observed in the HPCS composite with low intensity indicates that the sulphur is successfully incorporated into the porous carbon matrix and few sulphur crystals may exist on the surface of the porous carbon (Niu et al., 2015; Ward, 1968; Xuebing Yang et al., 2015). These results are in good agreement with XRD Analysis.

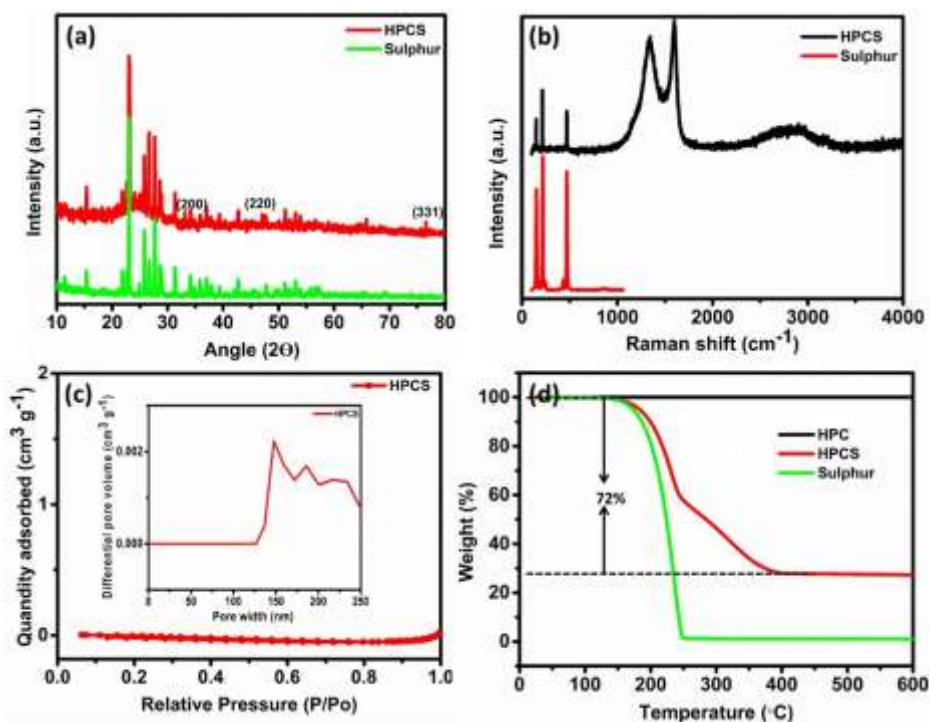


Figure 4.10. (a) XRD pattern for sulphur, HPCS (b) Raman spectra of sulphur and HPCS (c) N_2 adsorption/desorption isotherm HPCS (b) [inset: Pore size distribution curve of HPCS] and (d) Thermogram of sulphur, HPC and HPCS

Figure 4.10 (c) shows the N_2 adsorption-desorption isotherm of HPCS and inset shows the pore size distribution analysis. The BET surface area is decreased to 0.06 m^2 g^{-1} after sulphur incorporation which indicates that the sulphur is homogeneously distributed throughout the porous network (Y. Tan et al., 2017). This hierarchical porous structure is highly useful for the incorporation of sulphur and

to control the diffusion of PS ions towards Li anode during the charge-discharge process. The pore volume is close to zero after sulphur loading, signifies the successful amalgamation of sulphur into the porous network.

TGA was carried out to determine the sulphur content in the composite according to the thermal decomposition characteristics of sulphur at a heating rate of $10\text{ }^{\circ}\text{C min}^{-1}$ (Figure 4.10 (d)). TGA of HPC doesn't have any weight loss indicating the thermal stability of the prepared carbon material. The sulphur in the meso/macropores of HPCS is evaporated at $200\text{ }^{\circ}\text{C}$ to $250\text{ }^{\circ}\text{C}$ and the decomposition from $250\text{ }^{\circ}\text{C}$ to $400\text{ }^{\circ}\text{C}$ indicates that the sulphur infiltrated into the microporous region of HPC and these weight loss taken as the signal for the amount of sulphur (72%) in the composite (Y. Fu et al., 2012; W. G. Wang et al., 2014).

The chemical composition and bonding characteristics of HPCS were analysed using XPS spectrum. The survey scan analysis (Figure 4.11 (a)) reveals the presence of C1s, O1s, N1s, S2s, S2p and Fe2p functionalities. The deconvoluted C1s spectra (Figure 4.11 (b)) attributed to C-C (284.3 eV) C-S (284.9), C-N (285.3 eV), C-O (286.4 eV), C=N (287eV) and C=O (288.4 eV) from HPCS composite (M. Chen et al., 2017; Jing Xu et al., 2016).

The deconvoluted N1s spectrum (Figure 4.11 (c)) contains pyridinic (398.3 eV), pyrrolic (400.3 eV), graphitic (401.7 eV) N-S (402.6 eV) and nitrogen oxide (403.6 eV). The high-resolution O1s spectrum (Figure 4.11 (d)) is deconvoluted into S-O bond (530.7 eV), N-O bond (531.1 eV), C=O bond (531.8 eV) and C=O bond (532.4 eV) (Pang et al., 2015; Z. Wang., et al., 2014; X. Yuan, Liu et al., 2017). The deconvoluted N1s spectrum (Figure 4.11 (c)) contains into pyridinic (398.3 eV), pyrrolic (400.3 eV), graphitic (401.7 eV) N-S (402.6 eV) and nitrogen oxide (403.6 eV). The high-resolution O1s spectrum (Figure 4.11 (d)) is deconvoluted into S-O bond (530.7 eV), N-O bond (531.1 eV), C=O bond (531.8 eV) and C=O bond (532.4 eV) (Pang et al., 2015; Z. Wang., et al., 2014; X. Yuan, Liu et al., 2017). The Fe2p spectrum (Figure 4.11 (e)) was evaluated to identify the nature of Fe in the porous carbon. Fe $2p_{3/2}$ and Fe $2p_{1/2}$ binding energies are located at 713.4 eV and 728.7 eV corresponds to the Fe $^{2+}$ ionic state. Clearly distinguishable satellite peak of Fe $^{2+}$ is observed at 702.97 eV and 719.05 eV ascribed to Fe $2p_{3/2}$

and Fe2p_{1/2}, respectively (Srivastava et al., 2014). The presence of N, O and Fe in the porous carbon network is highly favourable for anchoring of PS during the charge-discharge process via chemical or physical adsorption.

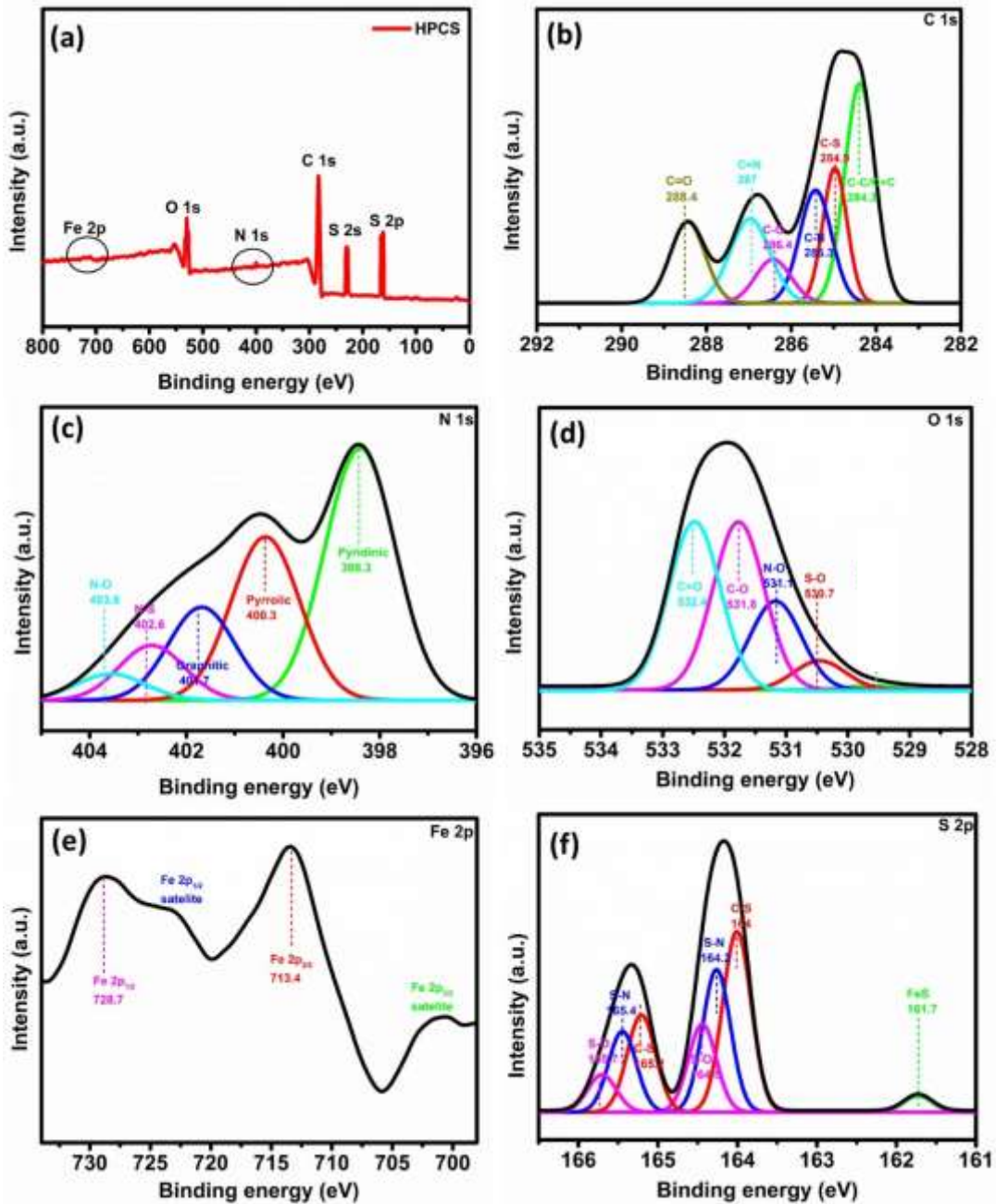


Figure 4.11. XPS for HPCS (a) Survey scan, High resolution (b) C1s (c) N1s (d) O1s (e) Fe2p and (d) S2p

The high-resolution S2p (Figure 4.11 (e)) peak at 161.7 eV reveals the presence of FeS in the composite which is in agreement with the XRD and EDS results (Srivastava et al., 2014). It is observed that S2p_{3/2} (164, 164.2 and 164.5 eV)

and $S_{2P_{1/2}}$ (165.2, 165.4 and 165.7 eV) with an energy separation of 1.2 eV corresponds to the C-S, S-N and S-O bonds in the HPCS (Demir-Cakan et al., 2011; Y. Hao et al., 2015; Niu et al., 2015; J. Yang et al., 2016; L. Zhang et al., 2012).

SEM and TEM analysis were carried out to evaluate the porous morphology of the carbon before and after sulphur loading (Figure 4.12). Not much morphological differences are observed before and after sulphur loading. Also, absence of agglomerated sulphur particle in the porous network indicates the homogenous distribution of sulphur in the porous network, the channels and pores are not blocked by the sulphur particles.

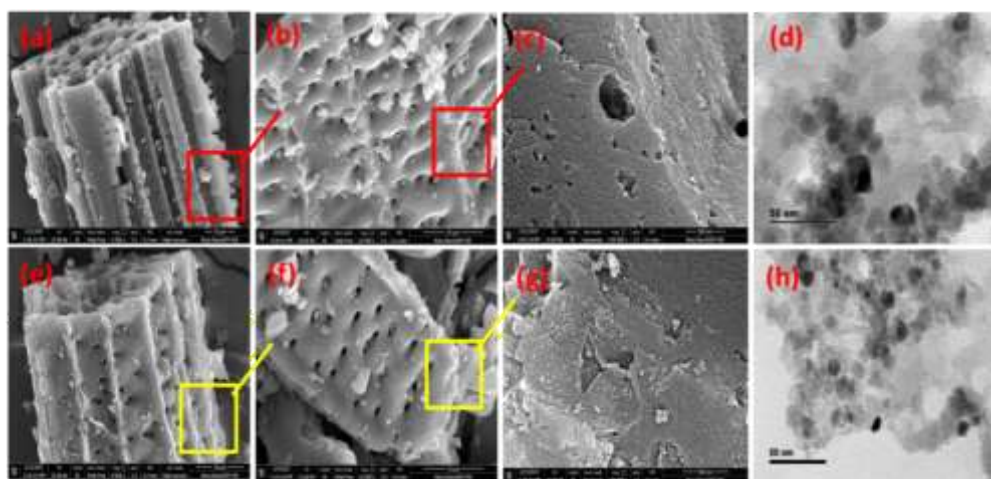


Figure 4.12. (a-c) SEM of HPC-800 °C, (d) TEM of HPC-800 °C (e-g) SEM of HPCS and (h) TEM of HPCS.

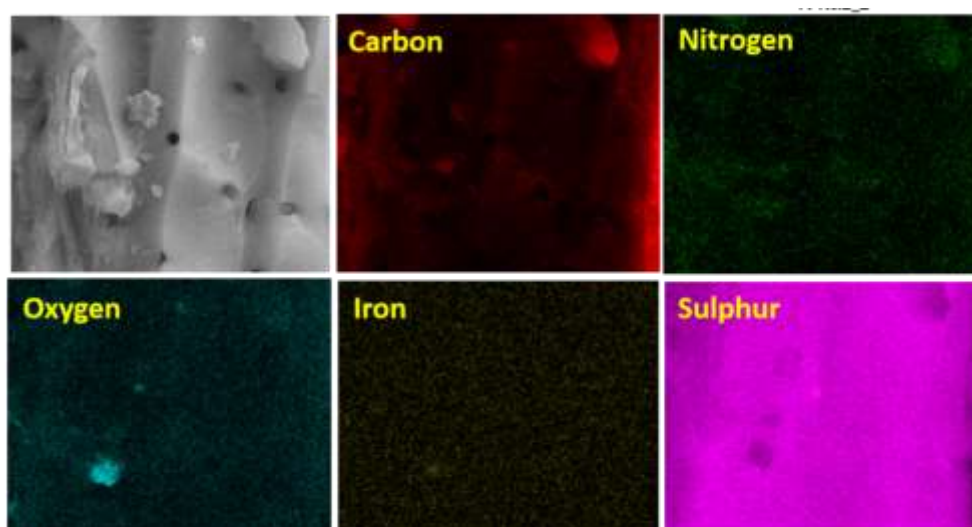


Figure 4.13. Elemental mapping of HPCS

Figure 4.13 shows the elemental mapping analysis HPCS. It is observed that the carbon, nitrogen, iron and oxygen were homogenously distributed throughout the HPCS sample. After melt diffusion, the sulphur particles are successfully incorporated into the carbon matrix. The presence of iron, nitrogen, oxygen and sulphur in the HPCS is confirmed from elemental mapping analysis.

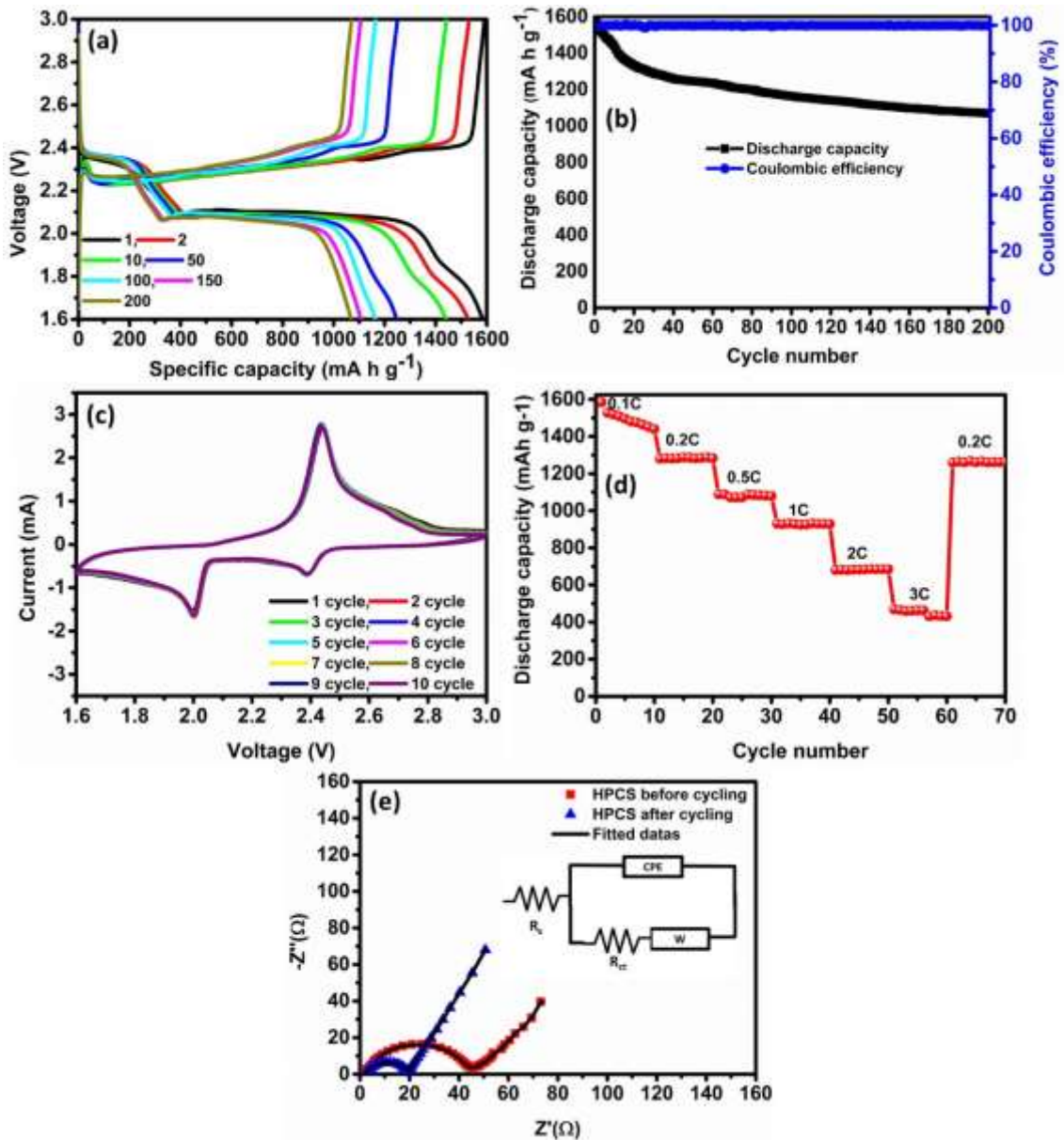


Figure 4.14. (a) GCD curves of HPCS (b) Cyclic stability performance and coulombic efficiency of HPCS (c) CV of the HPCS after 200 cycles (d) Rate capability studies of the HPC at various C-rate and (e) EIS analysis of the cell before discharge and after 200 cycles at the OCV [inset: equivalent circuit diagram]

The electrochemical properties of HPCS composite were evaluated by fabricating coin cells (section 2.2) with Li metal as anode and HPCS as a cathode.

Figure 4.14 (a) shows the GCD profile of HPCS at the 0.1C rate. It exhibits 1, 2, 25, 50, 100, 150 and 200th charge-discharge cycle between the voltage window 1.6-3V. The charge-discharge profile exhibits two discharge plateaus (~2.36 V and 2.01 V) and one charge plateau (2.39 V). It is obvious that the plateaus are due to the electrochemical reaction of sulphur. The first discharge plateau is from the reduction of sulphur to long chain lithium polysulphides and second discharge plateau is due to the further reduction to short chain lithium polysulphides. The charging plateau is due to oxidation of lithium polysulphides to sulphur. HPCS displays high initial discharge capacity 1584 mA h g⁻¹ compared to similar materials reported elsewhere (Arias et al., 2018; X. Fan et al., 2018). Due to the presence of N, O, FeS functionalities imparted multiple confinement effects on polysulphides during the charge-discharge process.

Figure 4.14 (b) shows the cycling performance and coulombic efficiency of HPCS at the 0.1C rate. HPCS exhibits ~99% coulombic efficiency in each cycle. HPCS shows 67.5% capacity retention after 200 cycles with 0.07% capacity decay rate. The electrochemical performance of the HPCS was further evaluated at a scan rate of 0.5 mV s⁻¹ after 200 cycles of GCD analysis in the same voltage window as in GCD analysis by cyclic voltammetry. Figure 4.14 (c) shows CV profile of the HPCS for 10 cycles with reduction peaks at 2.38 V and 2.01 V and an oxidation peak at 2.39 V. In the successive cycles the peak position, the peak current is overlapping with each other for 10 cycles, which indicates good electrode stability of the HPCS cathode material. It shows a stable electrode kinetics and reversibility in every cycle.

The electrochemical performances of the HPCS at different C rates are investigated in details. Figure 4.14 (d) shows the rate capability studies of HPCS between the C rates 0.1 to 3. The HPCS exhibited an initial discharge capacity of 1584 mA h g⁻¹, 1280 mA h g⁻¹, 1089 mA h g⁻¹, 935 mA h g⁻¹, 680 mA h g⁻¹ & 433 mA h g⁻¹ at 0.1C, 0.2C, 0.5C, 1C, 2C, 3C, respectively. When it returned to 0.2C rate, 1263 mA h g⁻¹ is obtained with 98.6% capacity retention. The rate capability studies demonstrate the robustness of the developed HPCS cathode material.

The electrochemical performance of HPCS is significantly greater than that of other biomass-derived carbon sulphur composite in terms of reversible capacity after cycling. Lu et al. reported shaddock peel derived carbon sulphur composite with a reversible capacity of 722.5 mA h g⁻¹ with 0.2 C rate after 100 cycles (S. Lu et al., 2016). Similarly, reported pomelo peel derived activated carbon developed by Zhang et al exhibited a final capacity of 750 mA h g⁻¹ after 100 cycles with 0.2C rate (J. Zhang et al., 2014). Yang et al studied apricot shell derived carbon sulphur composite and exhibited a stable discharge capacity of 710 mA h g⁻¹ after 200 cycles at 0.2C rate (K. Yang et al., 2015). Xu et al reported aspergillus flavus conidia as a carbon source for Li-S battery and obtained a reversible capacity of 940 mA h g⁻¹ after 120 cycles with 0.2C rate (M. Xu et al., 2016). This improved electrochemical performance of the HPCS is due to the presence of multiple confinement effects of PSs in the cathode side itself, which block the migration of PSs towards anode by physical and chemical interactions of N, O, porous carbon and FeS.

To further understand the improved electrochemical performance of HPCS composite, EIS was employed before and after 200 cycles at OCV with 10 mV amplitude (Figure 4.14 (e)) and inset shows the equivalent circuit. R_s refers the ohmic resistance of the electrolyte, the internal resistance of electrode materials, and contact resistances between electrodes and current collectors, R_{ct} refers the charge transfer resistance at the interface of the HPCS cathode and electrolyte. W indicates the Warburg impedance and CPE is the constant phase element, which is associated with the non-ideal capacitance. Table 4.9 gives the impedance parameters derived from the equivalent circuit model. The decrease in R_{ct} and ion diffusion resistance after 200 cycles may be due to the redistribution of sulphur in the HPC matrix and better lithium ion diffusion into the porous surface occupied by sulphur during charge discharge process (Y. Fu et al., 2012; Raghunandan et al., 2018; G. Ren et al., 2016).

Table 4.9: Impedance parameters obtained from the electrochemical equivalent circuit analysis of HPCS before and after cycling

Material description	R_s (Ω)	$CPE \times (10^{-6})$ (Ω^{-1})	R_{ct} (Ω)	Y_0 ($\Omega^{-1}s^{1/2}$)
HPCS before cycling	2.25	2.26	42.94	0.016
HPCS after cycling	2.3	1.76	17.41	0.086



Figure 4.15. (a) Lithium polysulphide solution (b) Lithium polysulphide mixed with PC after 10 minutes

The adsorption of PSs with HPCS was investigated by PS adsorption test. Digital photographs (Figure 4.15) show the changes in the colour of the PS solution after adding 20 mg of HPC to the PS solution after 10 minutes. HPC has the inherent capability to adsorb PSs (Chulliyote et al., 2017b).

SEM images of the HPCS cathode films before and after 200 cycles reveal the reason behind the superior electrochemical performance of the sulphur composite (Figure 4.16 (a and b)). Cathode film maintains its structural integrity after the charge-discharge process with minor morphological changes (Z. Liu et al., 2017; S. Wei et al., 2011; Ye et al., 2016). It is due to the presence of the porous carbon tube with heteroatom functionalities like N, O and Fe which alleviate the loss of active material during the charge-discharge process which is further supported by the XPS analysis of the HPCS cathode film after 200 charge-discharge cycles.

The survey scan analysis reveals C1s, O1s, N1s, S2s, S2p, Fe2p functionalities along with Al 2s, Al 2p and F1s (Figure 4.16 (c)). Al is from the current collector and fluorine is from the PVDF binder. The C1s peak is

comparatively weak, which could be due to the discharge products. High resolution Li 1s spectra (Figure 4.16 (d)) reveals the presence of Li-O (56.5 eV), Li-N (55.8 eV) along with Li-S (55.08 eV) attributed to the interaction of LPS with various functionalities (Aurbach et al., 2009; F. Chen et al., 2018; X. Fan et al., 2018; Xia Liand Sun, 2014; Seh et al., 2014; Son et al., 2015).

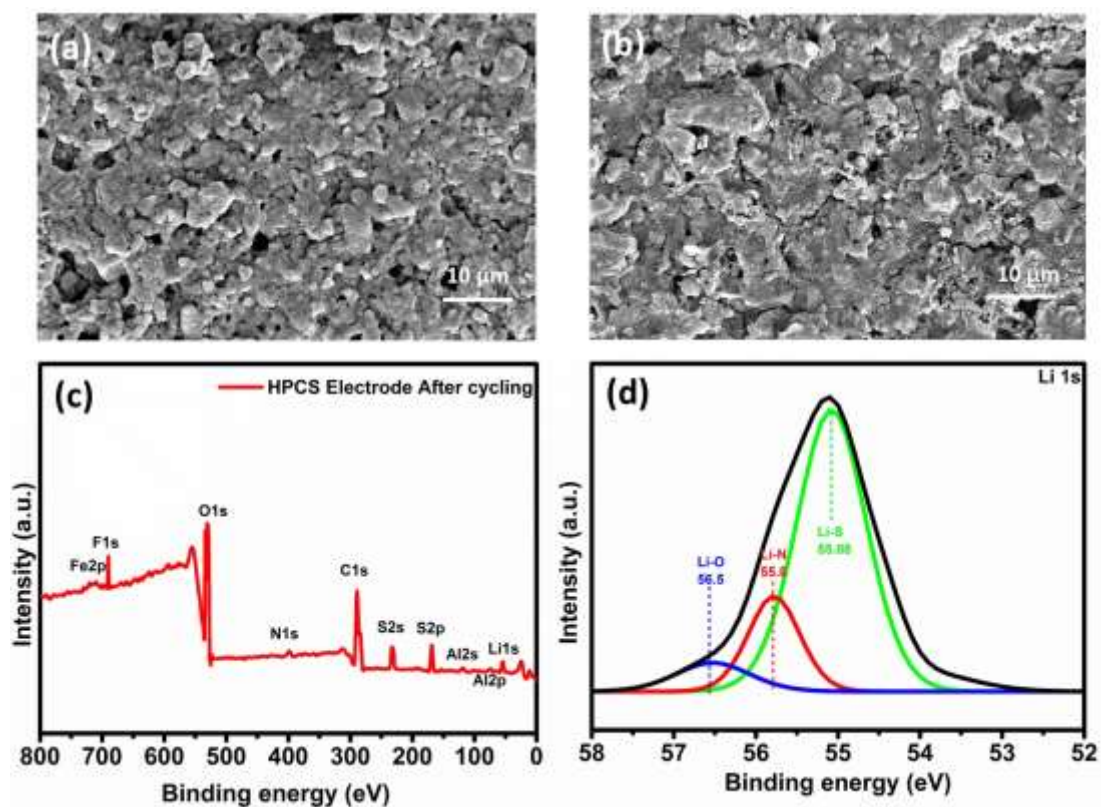


Figure 4.16. (a) HPCS cathode film before cycling (b) HPCS cathode film after 200 charge-discharge cycles (c) Survey scan and (d) High-resolution Li1s spectrum of HPCS after 200 cycles

4.4 Conclusion

High surface area carbon material inherently doped with N, O and Fe was derived from vetiver by a simple and scalable method. The hierarchical porous carbon tubes (HPC) obtained at 800 °C provided the highest BET surface area of 1879 m² g⁻¹ and total pore volume of 0.91 cm³ g⁻¹. The HPC-800 °C electrode displayed high specific capacitance of 296 F g⁻¹ at a current density of 0.8 A g⁻¹ with 1M Na₂SO₄ electrolyte. The symmetric supercapacitor is fabricated using 1M LiTFSI as the electrolyte exhibited a maximum energy density of 67.8 W h Kg⁻¹

and a maximum power of 15000 W Kg^{-1} . This result demonstrates that vertiver is a promising precursor for synthesizing heteroatoms doped porous carbon electrode materials for EDLC applications. The tubular like morphology of HPC decorated with pores of different sizes helps to adsorb more quantities of sulphur which in turn helps to enhance sulphur encapsulation and utilization during the charge-discharge process. The higher surface area and pore volume of HPC accommodate the volume changes of sulphur during the charge-discharge process and the appropriate chemical interactions of N and O with Li helps to retain PSs on the cathode surface. In addition to that, the presence of polar-polar interactions between LSPs and FeS restrict the movement of the PSs towards the anode surface. These multiple confinement effects such as higher surface area, pore volume, heteroatom functionalities and the presence of FeS leads to the superior electrochemical performance. The HPCS with 72% sulphur loading cathode delivers 1584 mA h g^{-1} as initial discharge capacity and sustains a reversible capacity of 1069 mA h g^{-1} after 200 cycles with a capacity retention of 67.48%. These results suggest that high surface area carbon with heteroatom doping and FeO is an effective host of sulphur for the future LSB applications.

CHAPTER 5

PINECONE DERIVED CARBON-SULPHUR COMPOSITE FOR LITHIUM-SULPHUR BATTERY

Hierarchically porous pinecone derived carbon (PC) with a high surface area of 2065 m² g⁻¹ and a pore volume of 1.5 cm³ g⁻¹ was prepared by the chemical activation of the pinecone with ZnCl₂. Pinecone carbon-sulphur composites (PCSCs) were prepared with 54, 68 & 73% sulphur loading and studied for its potential application as LSB cathode materials. Surface area and pore volume are reduced by almost 90% after sulphur loading onto porous carbon. Carbon with 54% sulphur loading displayed better performance among the three compositions and exhibited an initial discharge capacity of 1606 mA h g⁻¹ and final capacity of 1269 mA h g⁻¹ after 100 cycles with 79% capacity retention. The high cycling stability of PCSC (54%) is due to the better dispersion of sulphur in the pores and the high surface area, conductivity, large pore volume of the pinecone carbon to accommodate PS during shuttling process.

5.1 Introduction

Porous carbonaceous materials are widely used as a cathode material to hold the active material and to suppress the PS shuttling (D.-W. Wang et al., 2013). However, capacity fading is observed for long-term cycling due to the very weak interactions with polar PS. This demands host materials with functional groups exhibiting high adsorption/binding capacity for PS to confine the species physically/chemically onto the porous carbon architecture. Recently, there has been more interest to develop porous carbon materials capable of confining PSs physically/chemically (S. S. Zhang, 2015). In addition to the high surface area and good pore size distribution, binding groups in the porous carbon, improve its interaction with sulphur to reduce the loss of active materials. Most of the methods involved are sophisticated techniques which are economically unfavourable and also lack of consistency. Hence, it is essential to identify safe, low cost and environmentally benign material for large-scale applications of energy storage technologies such as electric and hybrid vehicles. A wide spectrum of porous carbons derived from plant and animal origin have been studied as cathode

materials for LSBs (Zan Gao et al., 2017; L. Yan et al., 2017). Doping of heteroatoms N/S/O/B/P in the carbon matrix reduces the charge transfer resistance, improves the electronic conductivity, and enhances the active sites to immobilize the sulphur/PSs (M. Chen et al., 2017; Jin et al., 2017; X. Yuan, Liu et al. 2017; G. Zhou et al., 2015). Co-doping is a more effective strategy to improve the physical adsorption and chemical bonding to trap LPSs (Pang et al., 2015). Co-doping of N and O intrinsically/extrinsically into the carbon framework has pyridinic N, pyrrolic N, graphitic N, C-O and C=O etc (Z. Wang, Y. Dong, H. Li, Z. Zhao, H. B. Wu, et al., 2014, Chulliyote et al., 2017b). These functional groups with a lone pair of electrons help to improve the electronic conductivity and wettability of the carbon matrices, which facilitate the confinement of PS. Thus, dual doping of N and O atoms with the high surface area is expected to enhance the performance of cathode material synergistically (Jin et al., 2017; Z. Wang et al., 2014; X. Yuan, Liu et al., 2017; G. Zhou et al., 2015). The porous structure of oxygen and nitrogen group species help to retain the active material and relieve the volumetric expansion during cycling (Pang et al., 2015). Most of the reported carbon materials with dopants were adopted tedious multistep procedures and chemicals for synthesis. Thus a simple, scalable and low-cost method is worth to consider for realizing LSBs.

In this chapter, pinecone is used as the carbon source to obtain high surface area carbon with heteroatoms (nitrogen and oxygen) for hosting sulphur due to the widespread occurrence of pinecone all over the world. Pinecone or activated carbon from pinecone is used to adsorb metal ions and organics from aqueous solution (Momčilović et al., 2011), CO₂ adsorption (K. Li et al., 2016) and an electrode material for SCs (Bello et al., 2016; Karthikeyan et al., 2014). However, pinecone derived porous carbon cathode material with nitrogen and oxygen functionalities will be promising for LSBs. It is demonstrated that the high surface area along with inherently doped N and O on hierarchically porous carbon matrix dramatically increases the performance of the cathode material. Also, the role of sulphur distribution within the porous structure for effective sulphur utilization and capacity retention during cycling was studied, with different sulphur compositions (54, 68 & 73%) at the cathode. The results show that the hierarchical porous carbon-sulphur

composite (PCSC) with 54% of sulphur exhibits a high specific capacity of 1606 mA h g⁻¹ with excellent capacity retention of 79% after 100 cycles with 0.29 % average fading per cycle at 0.1C rate and a good rate capability (923 mA h g⁻¹ at 2C) as a cathode material for LSB. The physical adsorption of PSs onto the porous carbon and chemical binding of PSs through O and N dopants increase the electrochemical performance and diminish the active material loss during the cycling process. The excellent electrochemical performance is due to the synergistic effect of the hierarchically porous features of the activated carbon with oxygen and nitrogen binding sites to immobilise the active PS species.

5.2 Materials and Methods

5.2.1 Materials

Pinecone (*Pinus roxburghii*) was obtained from Kodaikanal, India and all other chemicals were mentioned in section 2. 2.1.

5.2.2 Material synthesis

5.2.2.1 Preparation of porous carbon

The schematic representation of the preparation of porous carbon from pinecone is given in Figure 5.1. Pinecone petals were washed with distilled water followed by ethanol and dried. The powdered pinecone petals were used as the precursor for activated carbon. Chemical activation was carried out by mixing pinecone powder with zinc chloride of weight ratio 1:2. After drying it was heated at 800 °C in a tubular furnace for 1 h in an argon atmosphere at a heating rate of 5 °C min⁻¹. Then, it was washed with hydrochloric acid and distilled water until the filtrate became neutral. The pinecone derived carbon material (PC) was dried in an oven at 100 °C and stored in a desiccator.

5.2.2.2 Preparation of porous carbon-sulphur composite

Pinecone derived carbon-sulphur composites (PCSCs) were prepared by melt diffusion method with different weight ratios (1:1, 3:2, 7:3) of sulphur and PC as the procedure described in the section 2.2.2.2.

5.2.3 Material characterization

UV-Vis absorption spectra were performed using Varian Cary Bio 100 UV Spectrophotometer in the wavelength range of 200-800 nm at room temperature. All other characterizations were done by the techniques described in section 2.2.3 and 3.2.3.

5.2.4 Fabrication of coin cell and electrochemical measurements

The PCSC cathode was prepared and the electrochemical characterization was studied by the procedure described in the previous chapter 2, section 2.2.4 and 2.2.5 respectively. The mass loading of sulphur on the composite electrode is $\sim 2 \text{ mg cm}^{-2}$.

5.3 Results and Discussion

5.3.1 Material characterization

ZnCl_2 is used as an activation agent to prepare PC since it is comparatively less toxic and non-corrosive. The yield obtained by ZnCl_2 activation is more than that of KOH activation. It can promote the dehydration of the biomass precursor at low temperatures and aromatic condensation reactions at high temperatures.

The nitrogen adsorption-desorption isotherms and the corresponding DFT pore size distribution curves of PC are shown in Figure 5.2. According to IUPAC, the adsorption curve of PC is a type IV isotherm with adsorption hysteresis loop indicating the characteristic range of pores from meso to micropores. The rapid adsorption at low relative pressure suggests the existence of micropores and the hysteresis loop in Figure 5.2 (a) exemplify mesopores. The extension in the curve at a relative pressure greater than 0.9 is due to the existence of macropores (C. X. Guo and Li, 2011; Jiaqi Xu et al., 2016; M. Xu et al., 2016; K. Yang et al., 2015; S.

Zhao et al., 2013). This is evidenced in Figure 2.2 (b), which depicts the pore size distribution of PC and PCSCs. It has a small fraction of macropores along with mesopores and micropores distributed in the PC revealing a hierarchical porous structure.

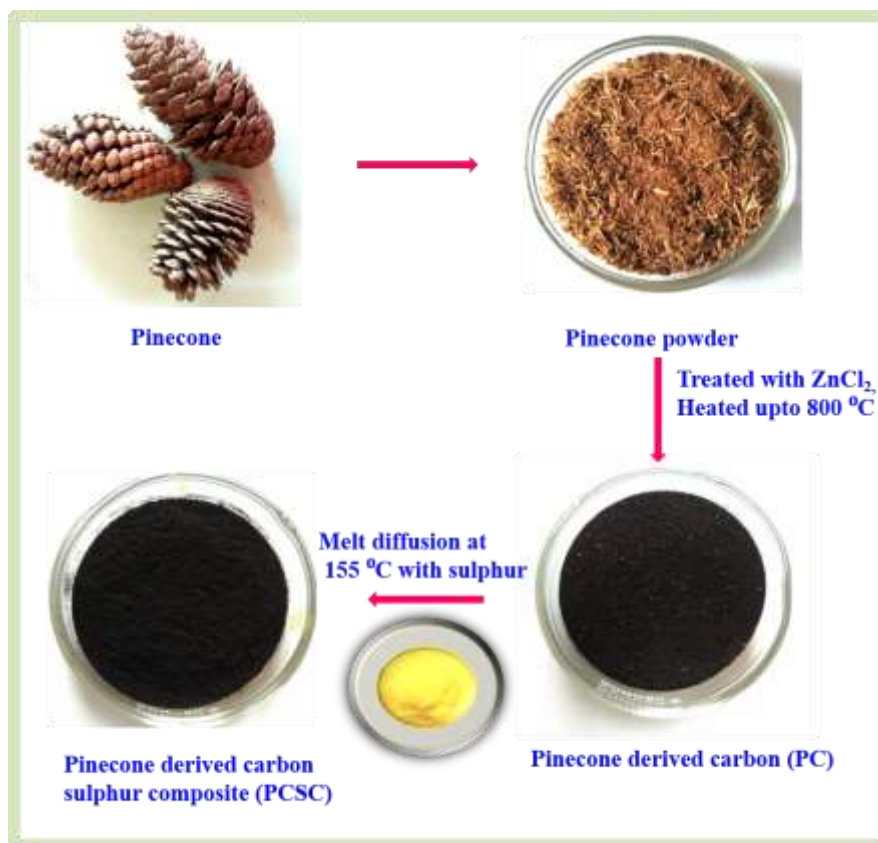


Figure 5.1. Schematic illustration of the preparation of PC and PCSC

The high surface area ($2065\text{ m}^2\text{ g}^{-1}$) and pore volume ($1.5\text{ cm}^3\text{ g}^{-1}$) affirms the well-developed porous structure. The BET surface area of PC, $2065\text{ m}^2\text{ g}^{-1}$ is reduced to $410\text{ m}^2\text{ g}^{-1}$ (54%), $100\text{ m}^2\text{ g}^{-1}$ (68%) and $10\text{ m}^2\text{ g}^{-1}$ (73%) after sulphur loading. The total pore volume of PC is $1.5\text{ cm}^3\text{ g}^{-1}$ and PCSCs are $0.406\text{ cm}^3\text{ g}^{-1}$ (54%), $0.154\text{ cm}^3\text{ g}^{-1}$ (68%) and $0.037\text{ cm}^3\text{ g}^{-1}$ (73%). It is observed that the surface area and pore volume are reduced significantly with increased sulphur content in the PC, which indicates that the pores are embedded with sulphur so that PC act as an ideal host for sulphur (Y. Tan et al., 2017). When the sulphur content is 54%, fraction of pores are either partially filled or unfilled in the composite which enhances the electrolyte accessibility, hence improved Li-ion transport during cycling.

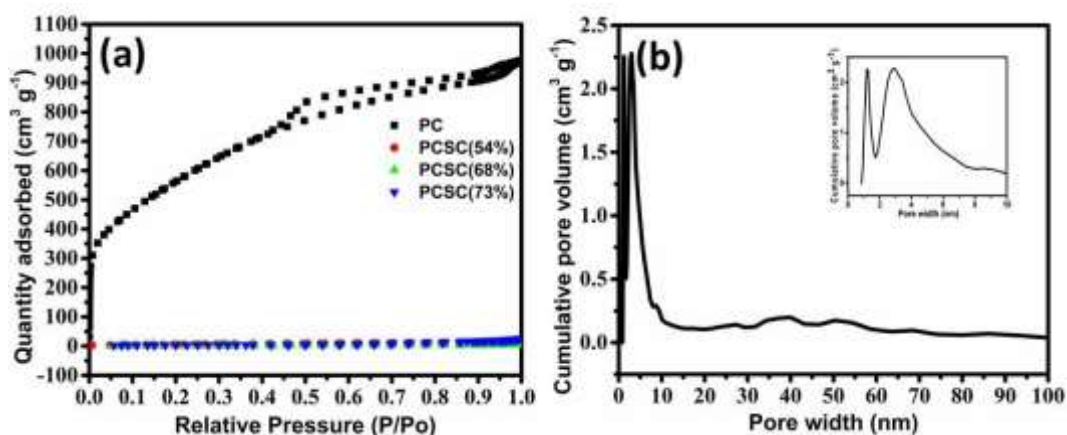


Figure 5.2. (a) N₂ adsorption/desorption isotherm and (b) Pore size distribution curve of PC [inset: enlarged at 0-10nm]

Table 5.1: Surface area and pore volume for PC and PCSCs

Description of properties	PC	PCSC (54%)	PCSC (68%)	PCSC (73%)
BET surface area (m ² g ⁻¹)	2065	439	105	10
Total pore volume (cm ³ g ⁻¹)	1.50	0.41	0.15	0.04

XRD patterns of PC and PCSCs at room temperature are shown in Figure 5.3 (a). The diffraction peaks for the elemental sulphur in the wide range of $2\theta = 15^\circ - 60^\circ$ match well with the characteristic diffraction peaks of orthorhombic sulphur (JCPDS no. 00-001-0478). The XRD pattern of PC exhibits two broad peaks at $2\theta = 26^\circ$ and 43° corresponding to (002) and (100) reflections of amorphous carbon and disordered graphitic structure, respectively (Gu et al., 2015; S. Zhang et al., 2014). During the preparation process of PCSCs, sulphur melts and diffuse into the pores of the carbon and is trapped inside the network due to the strong adsorbing capacity of PC. The PCSCs exhibits less intense diffraction peaks of crystalline sulphur indicating the presence of trace quantities of bulk crystalline sulphur on the surface, in addition to the well-adsorbed sulphur inside the porous network (Jinxin Guo et al., 2015; W. G. Wang et al., 2014; S. Zhao et al., 2013). The structure of the PC and PCSCs are further confirmed by the Raman spectrum as shown in Figure 5.3 (b). The peaks obtained at 1336 cm^{-1} (D band) and 1595 cm^{-1} (G band) in the Raman spectrum of PC and PCSCs are attributed to the disordered amorphous carbon and the crystalline graphite, respectively (Dresselhaus et al., 2007; Tao et al., 2014; Ward, 1968). The broadening and the intensity ratio I_D/I_G , provides evidence of the degree of defects present in carbon materials. Broadening

of peaks may be due to the deviation in the interplanar bond lengths and angles. The I_D/I_G ratio for PC is 0.808 which indicates the disordered crystalline carbon structure of the material. However, the I_D/I_G ratio of PCSCs is relatively more than that of PC which indicates that the defects get more pronounced with the increase in sulphur impregnation. Crystalline sulphur exhibits three peaks at 148 cm^{-1} , 214 cm^{-1} and 470 cm^{-1} (Inset of Figure 2.3 (b) (Ward, 1968)). The observed sulphur peaks in PCSCs indicates the effective incorporation of sulphur within the carbon matrix via melt diffusion process (Niu et al., 2015; Xuebing Yang et al., 2015).

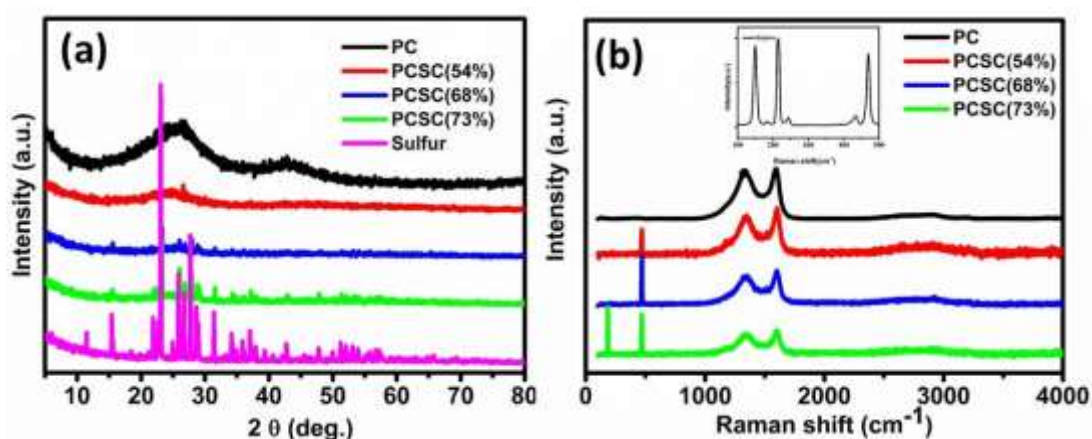


Figure 5.3. (a) X-ray diffractograms of sulphur, PC, and PCSCs (b) Raman spectra for PC and PCSCs [Inset: Raman spectrum of sulphur]

The fraction of sulphur present in PCSCs is measured using thermogravimetric analysis (Figure 5.4. (a)). TGA curve of PC is quite stable, decomposition below 100°C is due to the elimination of water during TGA analysis. TGA curves of PCSCs show major weight loss in the temperature range $200\text{--}400^\circ\text{C}$. The sulphur content is calculated as 54%, 68% and 73% based on the weight loss of sulphur from 100 to 400°C . The weight loss in PCSCs starts at a higher temperature than the elemental sulphur due to the well-dispersed sulphur within the micro and mesopores of PC. The weight loss in PCSCs (68% and 73%) commences at a lower temperature (166°C) than PCSC (54%), indicating the presence of sulphur at the surface of the porous carbon. The second weight loss ($\sim 250^\circ\text{C}$) is attributed to the confined sulphur within the porous network (Y. Fu et al., 2012; W. G. Wang et al., 2014). TGA results are well agreed with XRD and Raman analysis.

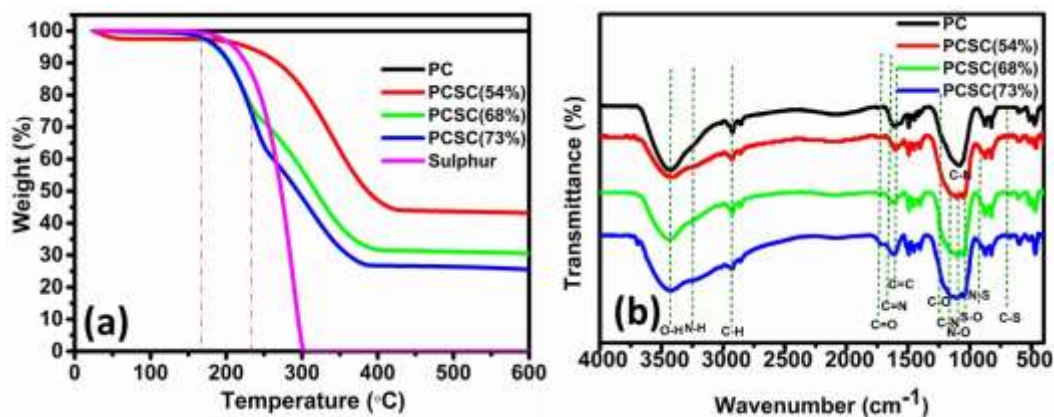


Figure 5.4. (a) TGA of sulphur, PC and PCSCs (b) FTIR spectrum of PC and PCSCs

The presence of functional groups on the surface of porous carbon and composites is determined by FTIR spectroscopy. Figure 5.4 (b) shows the IR spectrum of PC and PCSCs. The band at 3455 cm⁻¹ and 3267 cm⁻¹ is due to stretching vibrations of O-H and N-H bonds, respectively. The band at 2939 cm⁻¹ and 2854 cm⁻¹ are due to symmetric and asymmetric stretching vibrations of C-H bonds. The band at 1725 cm⁻¹ and 1648 cm⁻¹ are due to stretching vibrations of C=O and C=N in the PC and PCSCs. The band at 1247 cm⁻¹, 1148 cm⁻¹, 1042 cm⁻¹ is due to stretching vibrations of C-O, C-N and N-O stretching vibrations of the PC and PCSCs. These results prove that, the presence of oxygen and nitrogen functionalities on the surface of PC and PCSCs. After incorporation of sulphur into the PC, we have observed that the new peaks emerged at 1100 cm⁻¹, 918 cm⁻¹ and 618 cm⁻¹ is due to the stretching vibration of S-O, N-S and C-S bonds, respectively. Herein, we hypothesised that the heteroatoms with lone pairs may interact with PSs which further leads to the anchoring of PSs on cathode during the charge-discharge process (H. Ding et al., 2014; Y. Z. Zhang et al., 2014).

CHNS analysis demonstrated the presence of oxygen (14%) and nitrogen (2%) in the PC (Table 5.2). The nature of surface functional groups in the PC is investigated in detail by XPS analysis. The XPS survey scan (Figure 5.5) reveals the presence of C1s, N1s and O1s in the porous carbon at 283.7 eV, 400 eV and 533.1 eV, respectively. The nitrogen (2.22%) and oxygen (14.67%) content obtained from XPS analysis (Table 2.3) are very close to the CHNS results.

Table 5.2: Elemental content of PC and PCSCs obtained from CHNS Analysis

Sample	C (%)	H (%)	N (%)	S (%)	O (%)
PC	76	6.26	2	-	14
PCSC (54%)	32	1.07	2	53.80	11
PCSC 68%)	28	0.75	1.56	68	10
PCSC 73%)	24	0.62	1.43	73	9.67

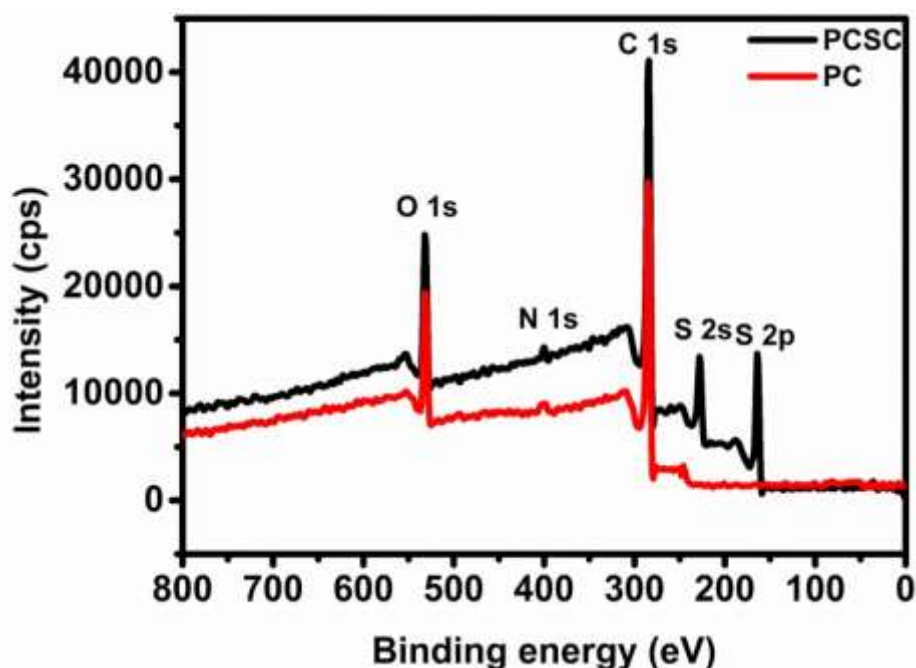


Figure 5.5. Survey scan of PC and PCSC (54%)

Table 5.3: Elemental composition of PC and PCSC (54%) obtained XPS Analysis

Sample	C (%)	N (%)	S (%)	O (%)
PC	83	2.22	-	14.67
PCSC (54%)	33	1.97	54	11

The high resolution C1s (Figure 5.6 (a)) peak is divided into 5 components, C-C bond (284.7 eV) of sp^2 , C-N (285.4), C-O bond (286.6 eV), C=N bond (287.3 eV) and C=O (288.6 eV). The high-resolution O1s spectrum (Figure 5.6 (b)) is deconvoluted into three components: N-O bond (530.5), C-O bond (531.7 eV), and C=O bond (533.1 eV). XPS results reveal the presence of ample oxygen functionalities in PC matrix, such as N-O (27 at.%), C-O (33 at.%) and C=O (40 at.%), which are believed to promote the chemical adsorption of sulphur. The N1s spectrum (Figure 5.6 (c)) contains 4 contributions at 398.2 eV, 400 eV, 401.7 eV and 403.7 eV assigned to the pyridinic, pyrrolic, graphitic and nitrogen oxide,

respectively, which includes 27 at.% pyridinic nitrogen, 34 at.% pyrrolic nitrogen, 25 at.% graphitic nitrogen and 14 at.% N-O species (Pang et al., 2015; Z. Wang et al., 2014; X. Yuan, Liu et al., 2017; G. Zhou et al., 2015; Jin et al., 2017; Shao et al., 2016). These functional groups are concordant with the FTIR results. Thus XPS results confirm the intrinsic doping of nitrogen and oxygen onto a porous carbon matrix during pyrolysis. A schematic representation of PC is exhibited in Figure 5.6 (d) based on the above observations (Y. Hao et al., 2015; Jing Xu et al., 2016).

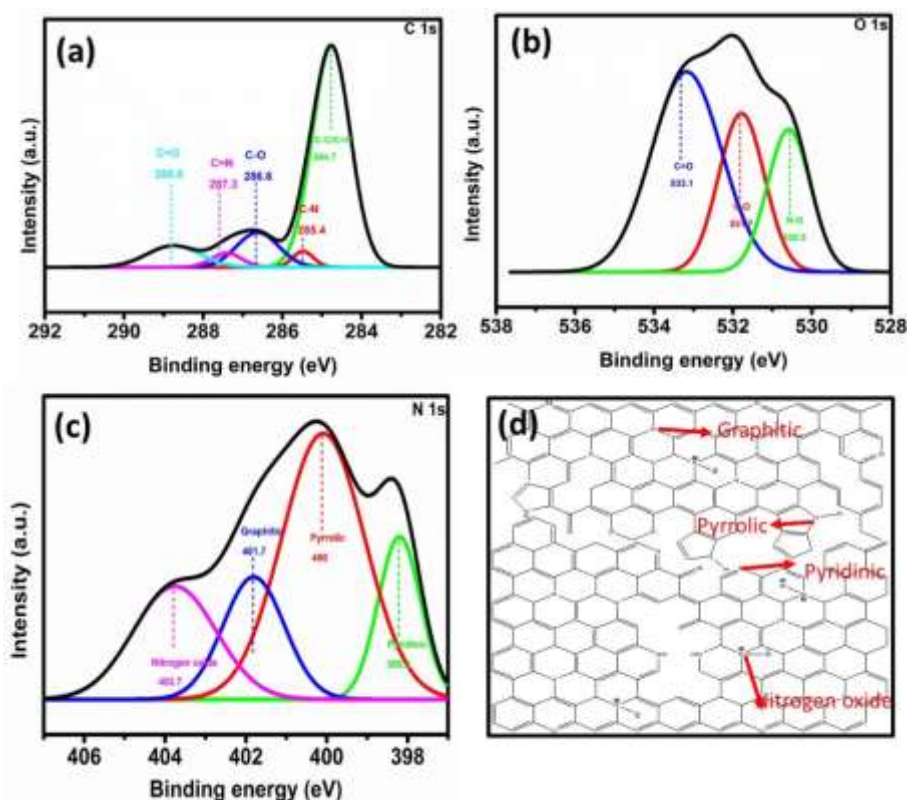


Figure 5.6. XPS for PC (a) C1s (b) O1s (c) N1s and (d) Schematic illustration of nitrogen and oxygen containing porous carbon.

XPS studies of PCSC (54%) was carried out to explore the surface chemistry of PC after sulphur incorporation and to study the interaction between heteroatoms and sulphur. The survey scans of the composite (Figure 5.5) reveal the presence of S2s and S2p in the composite at 240 eV and 163.4 eV, respectively. The C1s (Figure 5.7(a)) split into, C-C bond (284.7 eV) of sp^2 , C-N (285.4), C-O bond (286.6 eV), C=N bond (287.3 eV) and C=O (288.6 eV). Also, the existence of a new C-S bond at 285.2 eV reveals the effective doping of sulphur onto the carbon matrix (M. Chen et al., 2017; Jin et al., 2017; J. Yang et al., 2016). The high-

resolution O1s spectrum (Figure 5.7 (b)) is deconvoluted into four components: C-O bond (530.5 eV), N-O bond (530.5), C=O bond (533.1 eV) and a new S-O bond (530.2 eV), among which S-O contribute 17 at.%, 19 at.% by N-O, 24 at.% by C-O and 40 at.% by C=O. The N1s spectrum (Figure 5.7 (c)) consists of 5 contributions at 398.2 eV, 400 eV, 401.7 eV and 403.7 eV which are assigned to the pyridinic, pyrrolic, graphitic and nitrogen oxide, respectively and a new N-S at 402.7 eV. The at.% of pyridinic, pyrrolic, graphitic, N-S and pyridinic nitrogen oxide are 8, 34, 25, 21 and 10, respectively. New S-O and N-S bonds indicate that the nitrogen and oxygen groups interact with sulphur in the composite (M. Chen et al., 2017; Pang et al., 2015; Z. Wang et al., 2014; X. Yuan, Liu et al., 2017; G. Zhou et al., 2015). Figure 5.7 (d) displays the deconvoluted S2p spectrum of PCSC (54%), which contains two peaks corresponds to S2p_{3/2} and S2p_{1/2} with an energy separation of 1.2 eV and an intensity ratio of 2:1. Pristine sulphur shows S2p doublet with a binding energy of 164.3-165.5 eV (Demir-Cakan et al., 2011; Y. Hao et al., 2015). After impregnation of sulphur onto PC, S-S bond is slightly shifted to 163.6-164.8 eV from sulphur powder possibly due to the changes in the electronic distribution on the sulphur after melt diffusion which indicates the formation of C-S bond (L. Zhang et al., 2012; Niu et al., 2015; J. Yang et al., 2016). Further, sulphur is bonded to both nitrogen and oxygen [S-N (163.8-165) and S-O (164.1-165.3)] in the carbon matrix (J. Yang et al., 2016; L. Zhang et al., 2012). It is expected that the interaction of sulphur with carbon matrix through S-O and S-N bonds effectively confine PSs during the charge-discharge process (Niu et al., 2015; L. Zhang et al., 2012). These major changes in the XPS spectra before and after melt diffusion indicates the interaction of sulphur with heteroatoms and modifies the electronic distribution around atoms that is reflected in the binding energy shift. The heteroatoms with lone pairs act as Lewis base and it interacts with Li (Lewis acid) during charge-discharge process that helps to anchor PSs. The O and N functional groups synergically contribute to improving the performance of LSB along with the high surface area of the carbon material (G. Li et al., 2016).

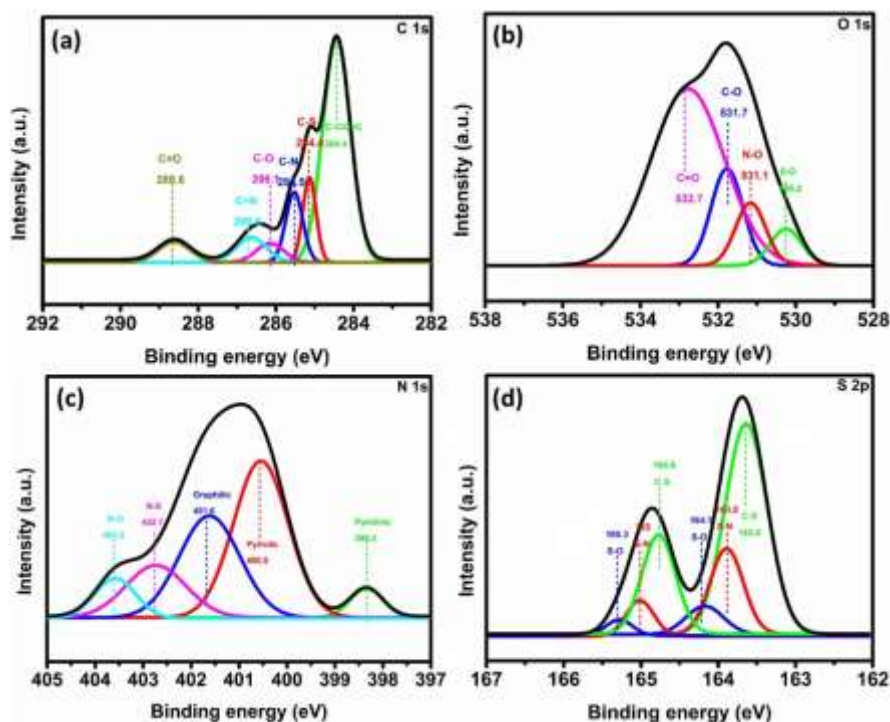


Figure 5.7. XPS for PCSC (54%) (a) C1s (b) O1s (c) N1s and (d) S2p

The morphology and microstructure of the PC and PCSCs were analysed in detail by SEM and TEM, which are presented in Figure 5.8 and 5.9, respectively. SEM of PC (Figure 5.8 (a-c)) reveals that the prepared carbon materials have a hierarchical morphology with interconnected pores. The TEM image of a PC (Figure 5.8 (d)) displays a large number of nanopores, which affirms high surface area and porosity of the material. SAED pattern (inset) exhibits the amorphous nature of the PC. The morphological changes after sulphur infiltration into the micro, meso and macropores of PC-suggest uniform diffusion of sulphur into the pores (Figure 5.9 (a-c)). Also, bulk crystalline sulphur is observed on the surface of PCSCs (68% and 73%) in addition to the diffused sulphur. These results corroborate with TGA and XRD analysis. TEM image (Figure 5.9 (d)) of PCSC (54%) shows no agglomerated sulphur particle onto the carbon matrix, SAED pattern (inset) displays the crystalline nature of the PCSCs which confirms the presence of sulphur in the system. The hierarchical porous structure of the carbon matrix is helpful to accommodate volume changes in LSBs. The presence of nitrogen and oxygen in the PC, as well as nitrogen, oxygen and sulphur in the PCSCs, are further confirmed by elemental mapping analysis (Figure 5.10).

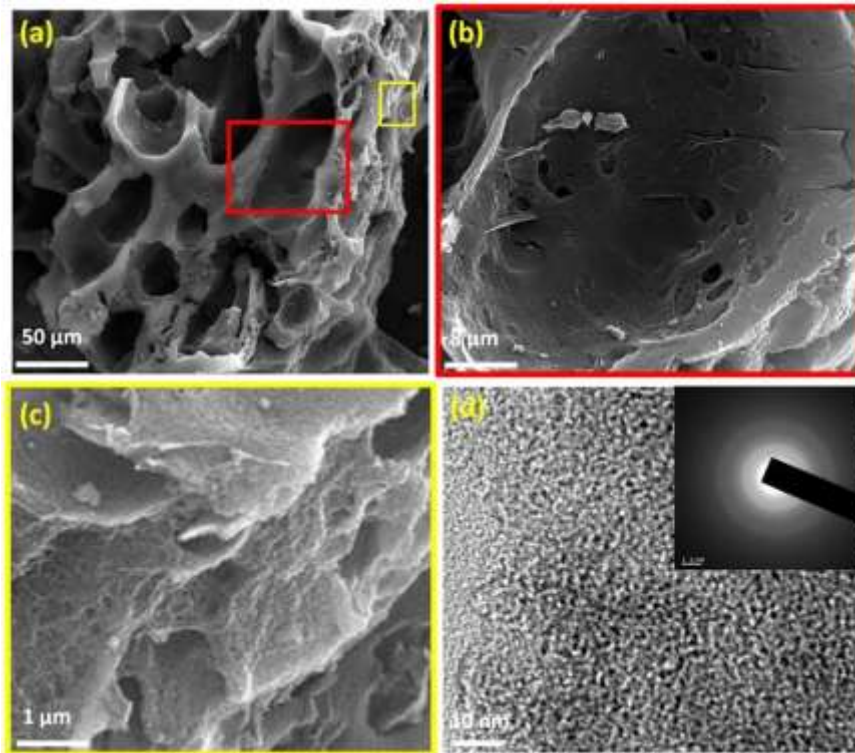


Figure 5.8. SEM of (a) PC (b) and (c) are enlarged portion of (a) and (d) TEM image of PC (inset: SAED pattern)

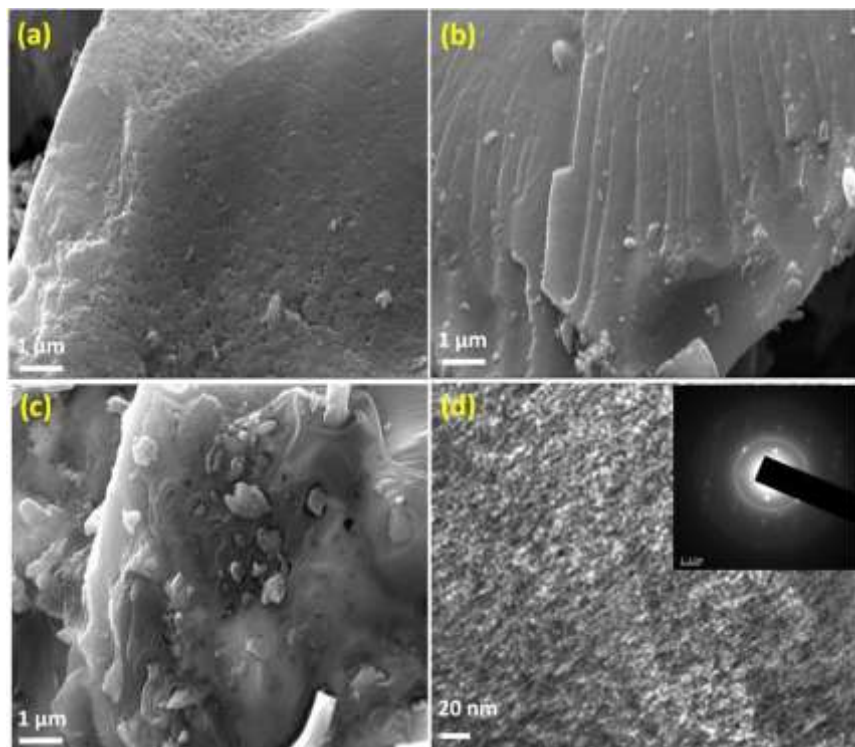


Figure 5.9. SEM of (a) PCSC (54%) (b) PCSC (68%) (c) PCSC (73%) and (d) TEM image of PCSC (54%) (Inset: SAED pattern)

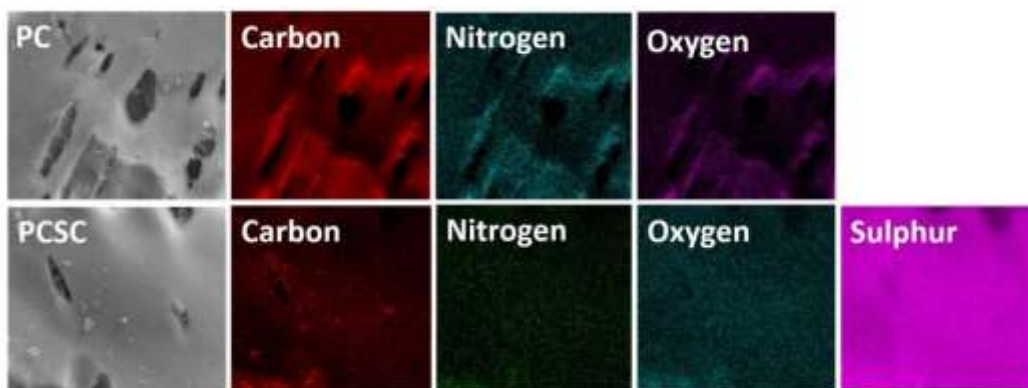


Figure 5.10. Elemental mapping of PC and PCSC (54%)

5.3.1 Electrochemical performance of the composite

The electrochemical properties of PCSCs have been evaluated by assembling CR2032 type coin cell with metallic lithium as anode. The cyclic voltammograms of PCSCs in a potential range of 1.6 to 3V at a scan rate 0.1mV s^{-1} are shown in Figure 5.11. The two reduction and one oxidation peaks are observed due to the multistep reaction between sulphur and lithium. In the cathodic scan process, the peak at 2.36V is due to the reduction of elemental sulphur to long chain LPSs (Li_2S_x , $4 \leq x \leq 8$). The second peak at 2.01 is due to the conversion of these long chain PSs to short chain PSs (Li_2S_x , $2 \leq x \leq 4$). In the subsequent anodic scan process, a peak at 2.39 V is observed, which corresponds to the conversion of these polysulphides to sulphur (Qu et al., 2015; Jiaqi Xu et al., 2016; M. Xu et al., 2016). In the successive cycles, the peak positions, the anodic and cathodic current are almost similar ascribing the reactive reversibility and cycling stability of the developed electrode material. The anodic and cathodic peak positions of PCSCs with 54, 68 & 73% sulphur content are same. However, a decrease in the current density is observed when the sulphur content in the composite increases (Figure 5.11 (b-c)). This may be due to the poor conductivity of sulphur crystals at the surface of PCSC 68% & 73% owing to the high sulphur content as indicated by N_2 adsorption studies and SEM.

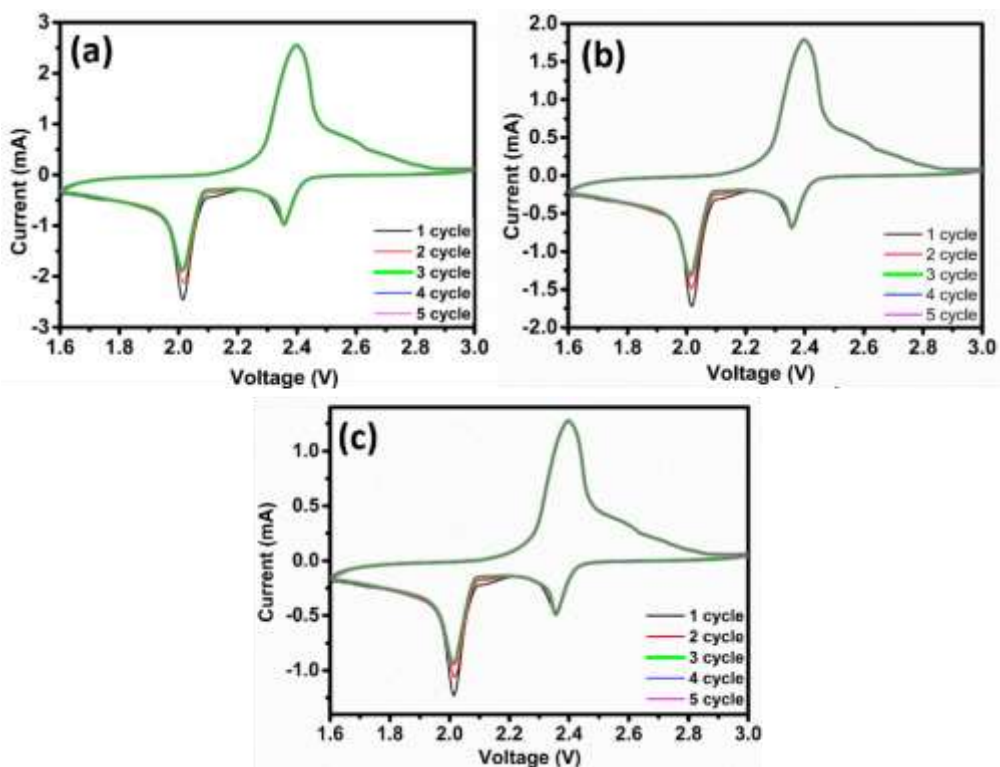


Figure 5.11. CV of the PCSCs (a) 54%, (b) 68% and (c) 73%

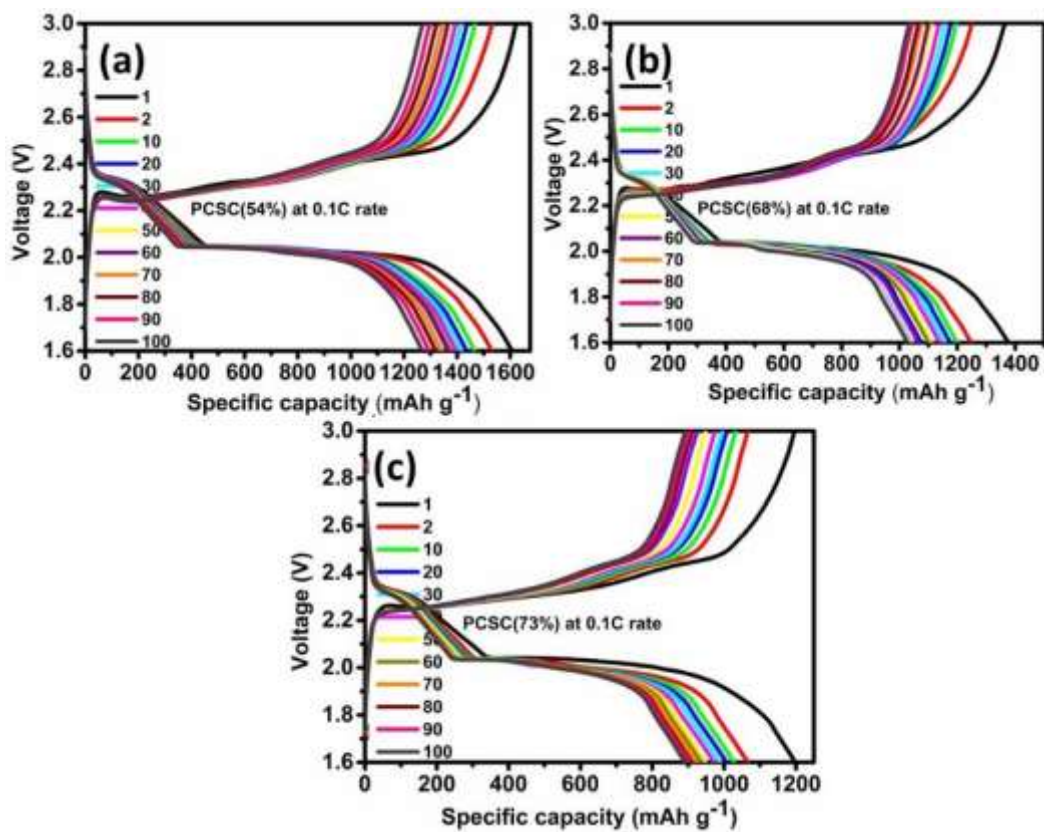


Figure 5.12. GCD curves of PCSCs (a) 54% (b) 68% and (c) 73%

The electrochemical performance of the sulphur-carbon composite is further tested by GCD experiments. Figure 5.12 shows the 1, 2, 10, 20, 30, upto 100th charge-discharge profiles of PCSCs at 0.1C rate. The charge-discharge profiles of PCSCs exhibit two plateaus (~2.36 V and 2.01 V) in the discharge curve and one plateau (2.39 V) at the charging curve aligning with the two reduction peaks and one oxidation peak of CV. The second plateau is due to the formation of short chain lithium sulphides, afterwards exhibiting stable voltage during cycling indicates better retention in the electrochemical performance. This may be ascribed to the N and O containing hierarchically porous carbon host with micro and mesopores, which further enhances the electronic and ionic transport at the cathode.

An impressive high discharge capacity of 1606 mA h g⁻¹ is observed for PCSC (54%) (Figure 5.12 (a)), compared to similar material reported elsewhere (Table 5.4). PCSC (68%) and PCSC (73%) display an initial discharge capacity of 1370 mA h g⁻¹ and 1198 mA h g⁻¹, respectively (Figure 5.12 (b-c)). The amount of active material utilization is decreased as the sulphur content increases. The sulphur utilization is 95.9%, 81.8 % and 71.5% for PCSC (54%), PCSC (68%) and PCSC (73%), respectively. The reason could be the uniform dispersion of sulphur within the pores is feasible in the PCSC (54%) which improves the ionic transport. In the second cycle its discharge capacities become 1531 mA h g⁻¹, 1370 mA h g⁻¹ and 1198 mA h g⁻¹ with 4.6%, 8.9% and 11.1% capacity degradation for PCSC (54%), PCSC (68%) and PCSC (73%), respectively. After 100 cycles, PCSC (54%) shows a reversible capacity of 1269 mA h g⁻¹ which is higher than that of sulphur rich PCSCs (1028 mA h g⁻¹ and 891 mA h g⁻¹) with 79% capacity retention compared to initial discharge capacity. These results are attributed to the heteroatoms induced chemical adsorption of PSs in the hierarchically porous carbon matrix. The specific capacity may decrease if the capacity was normalized by the weight of the whole electrode. Since the active material in the electrode is less as sulphur loading is decreased.

Table 5.4: Comparison of biomass derived carbon/sulphur hybrid materials for LSBs

Sl. No.	Cathode materials	% of sulphur	Initial capacity (mA h g ⁻¹)	Current rate	Cycles	Capacity retention (%)	References
1	Litchi	60	1105	0.12C	100	65	(S. Zhang et al., 2014)
2	Fish scale	58.8	1400	0.1C	20	78	(S. Zhao et al., 2013)
3	Pig bone	63	1265	0.24C	50	51	(S. Wei et al., 2011a)
4	Apricot	53.5	1277	0.2C	200	55	(K. Yang et al., 2015)
5	Corn cobs	44	1600	0.1C	50	35	(Jinxin Guo et al., 2015)
6	Bamboo Charcoal	57.7	685	0.5C	500	73	(J. J. Cheng et al., 2015)
7	Bamboo biochar	50	1295	160 mA g ⁻¹	150	62	(Gu et al., 2015)
8	Soyabean	80	1330	0.1C	150	78	(G. Ren et al., 2016)
9	Silk fibroid	73	1140	0.2C	60	71	(Jiawei Zhang et al., 2015)
10	Banana peel	65	1227	0.1C	100	71	(F. Li et al., 2017)
11	Sisal fibers	40	950	0.1C	-	-	(Raja et al., 2016)
12	Kapok fiber	93	549	670 mA g ⁻¹	90	95.4	(Tao et al., 2014a)
13	Cotton	80	1173	0.1C rate	100	67	(Chung et al., 2016)
14	Crab shell	65	1205	0.2C	100	71	(Yao et al., 2013)
15	Tree bark	48	1159	200 mA g ⁻¹	60	52	(Jiaqi Xu et al., 2016)
16	Aspergillus flavus Conidia	56.7	1625	0.2C	120	57	(M. Xu et al., 2016)
17	Olive stone	80	930	0.06C	50	72	(Moreno et al., 2014)
18	Pomeleo peel	60.1	1258	0.2C	100	49	(J. Zhang et al., 2014)
19	Gelatin	53.3	1209	1C	200	50	(Qu et al., 2015)
20	Shaddock peel	62	1189	0.1C	100	65	(S. Lu et al., 2016)
21	Pinecone	54	1608	0.1C	100	79	Our work

22	Pinecone	68	1370	0.1C	100	76	Our work
23	Pinecone	73	1145	0.1C	100	75	Our work

Cycling performance and coulombic efficiency of PCSCs at the 0.1C rate are shown in Figure 5.13(a). It exhibits good electrochemical performance and coulombic efficiency of more than 99% up to 100 cycles, due to the reduced shuttling effect. The rate capability of PCSCs at various current densities from 0.1C to 2C is shown in Figure 5.13(b). The discharge capacity of PCSC (54%, 68% and 73%) at various current densities of 0.1C, 0.2C, 0.5C, 1C and 2C are 1606 mA h g⁻¹, 1435 mA h g⁻¹, 1265 mA h g⁻¹, 1027 mA h g⁻¹ & 923 mA h g⁻¹ (54%), 1370 mA h g⁻¹, 1172 mA h g⁻¹, 1026 mA h g⁻¹, 819 mA h g⁻¹ & 730 mA h g⁻¹ (68%) and 1198 mA h g⁻¹, 1002 mA h g⁻¹, 840 mA h g⁻¹, 606 mA h g⁻¹ & 513 mA h g⁻¹ (73%), respectively. There is no specific capacity loss is observed while discharging at different current densities. When the current density, reduced back to 0.2C the discharge capacity is recovered, indicating an excellent rate performance of PCSC cathodes. These higher specific capacities at different current densities are appreciable to obtain high energy density and power density. The outstanding rate capabilities may be due to the good conductivity, surface area, and the pore volume of the carbon material and the heteroatoms with lone pairs which facilitate chemical adsorption of PSs and Li⁺ diffusion during charge-discharge processes.

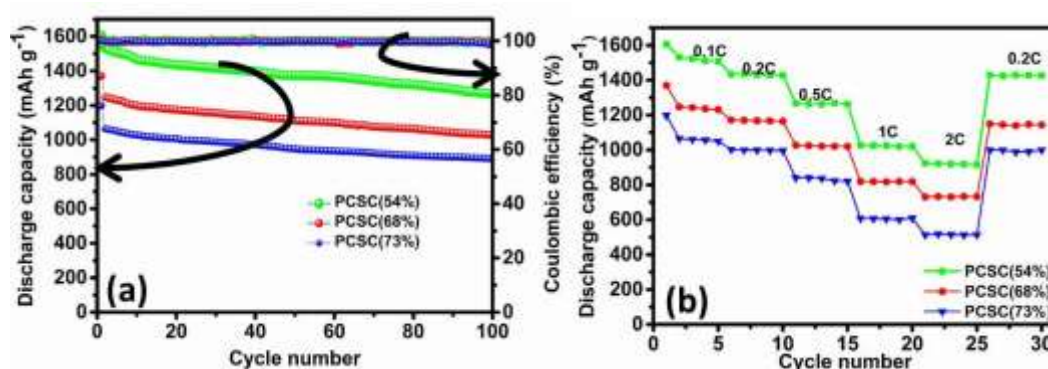


Figure 5.13. Cyclic stability performance and coulombic efficiency of PCSCs (a) and (b) Rate capability studies of PCSCs at different C-rate

The adsorption of PS by PC was investigated using the UV visible absorption spectra of PS solution with PC (Figure 5.14) using polysulphide

adsorption test discussed in section 4.2.2.3. The inset shows the digital photographs of the LPS solution and the variation in the colour of PS solution after adding PC. UV visible spectra show the broad absorption between 200-600 nm for various sulphide species in the case of control PS solution (a). Initially, it is a homogenous mixture of PC and PS solution (b), after 10 minutes the solution becomes colourless indicating a strong interaction between PC and PSs. A dramatic reduction in the peak intensity is observed in UV- visible spectra of the solution after 10 minutes demonstrate the excellent adsorption of lithium PSs onto PC (Jin et al., 2017; Y. Peng, Y. Zhang, J. Huang, et al., 2017; Xia et al., 2017). These results are in good agreement with excellent cycling stability and rate capability of the cathode material.

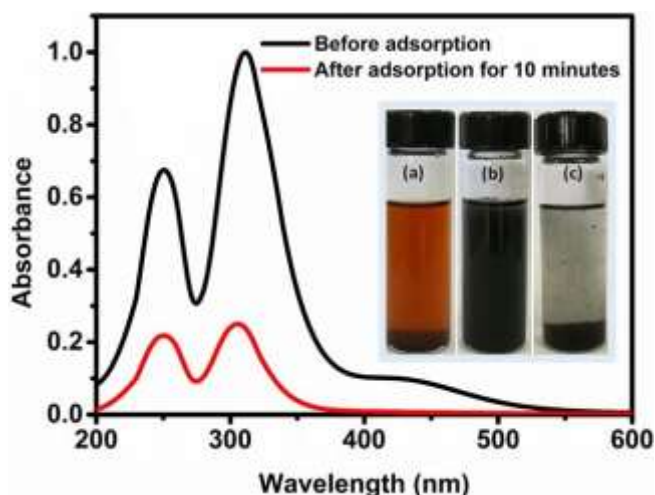


Figure 5.14. UV-vis absorption spectra of polysulphide solution with PC. Inset is the digital images of the polysulphide adsorption test [(a) Lithium polysulphide solution (b) Lithium polysulphide mixed with PC after 0 min. and (c) Lithium polysulphide mixed with PC after 10 min.]

EIS was carried out to understand the electrochemical reaction of lithium and sulphur when PCSCs are cathode materials in LSBs. EIS before and after 100 cycles at the OCV are shown in Figure 5.15 with the equivalent circuit (inset). The impedance spectra consist of depressed semicircle at high-frequency region and a sloping line in the low-frequency region. Semicircle in the high-frequency region relates to charge transfer resistance at electrode/electrolyte interface. A slope in the low-frequency region is called as Warburg impedance attributed to the Li^+ ion diffusion within the cathode. Nyquist impedance plot is evaluated by equivalent circuit model which is shown in the inset of Figure 5.15. Table 5.5 give the

impedance parameters obtained from the circuit model. The resistance of the electrolyte (R_s) determined from the intersection of the front end of the semicircle on the Z' axis, R_s is comparatively more for PCSCs with higher sulphur content which can be correlated to the less active material utilization due to the accumulation of sulphur on the surface of carbon matrix (Figure 5.15 (a and b)).

PCSCs (54%, 68% and 73%) exhibit two depressed semicircles at high and medium frequency region and a slope at the low-frequency region. It indicates two types of resistance offered by the system due to the charge transfer reaction at electrode-electrolyte interfaces of PCSCs (Y. Peng, Y. Zhang, J. Huang, et al., 2017; Y. Tan et al., 2017; W. Wang et al., 2014). The partial semi-circle at the high-frequency region is related to the resistance offered for the charge transfer between the porous carbon material and electrolyte i.e., electrical double layer resistance (R_{ct1}) (Meher et al., 2010). The semi-circle at the medium frequency region is related to the charge transfer resistance offered due to the interaction between sulphur and electrolyte (R_{ct2}); it is due to the faradaic process. The charge transfer and ion diffusion resistance are very small for PCSC (54%) compared to PCSC (68%) and PCSC (73%). It may be due to the low-density sulphur in the meso/micropores favour the diffusion of electrolyte hence the transportation of lithium ion. Figure 5.15(b) represents EIS analysis after 100 cycles. It is clear that R_{ct} and ion diffusion resistance decreased as a result of enhanced electronic conductivity upon cycling, may be due to the well-disseminated electrolyte in the cathode (Table 5.5) (Gu et al., 2015; Qin et al., 2014; W. G. Wang et al., 2014; S. Zhao et al., 2013). The disappearance of partial semicircle after 100 cycles attributed to the non-availability of free active carbon sites due to the physical/chemical adsorption of active material during the charge-discharge process. These results further confirm the ability of N and O containing porous network to confine PSs and enhance cycling performance of hierarchical porous carbon sulphur composites.

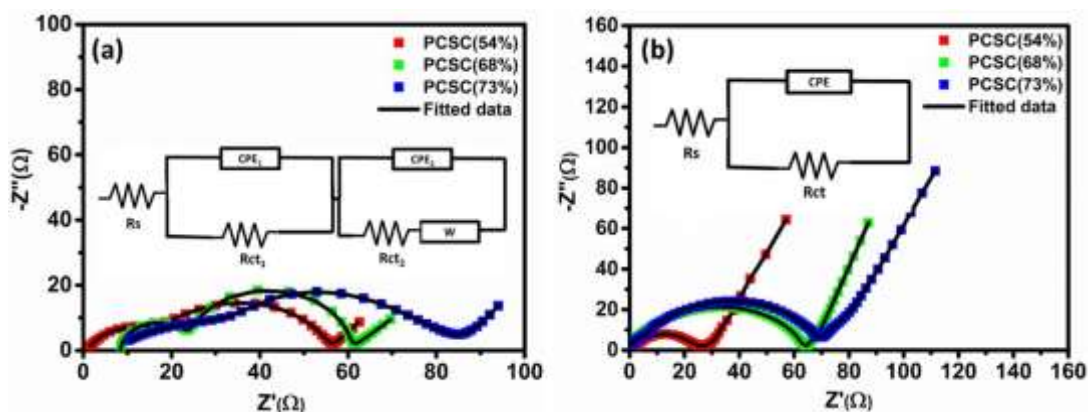


Figure 5.15. EIS analysis of the electrodes (a) Before discharge and (b) After 100 cycles at the OCV [inset: equivalent circuit diagram]

Table 5.5: Impedance parameters obtained from the equivalent circuit for the PCSCs before and after cycling

Material description	R_s (Ω)	$CPE_1 \times 10^{-5}$ ($\Omega^{-1} s^1$)	R_{ct1} (Ω)	$CPE_2 \times 10^{-7}$ ($\Omega^{-1} s^1$)	R_{ct2} (Ω)	Y_0 ($\Omega^{-1} s^{1/2}$)
PCSC (54%) before cycling	1.49	9.5	15.13	1.6	40.73	0.097
PCSC (68%) before cycling	8.59	1.1	15.73	0.98	45.95	0.046
PCSC (73%) before cycling	10.26	0.67	21.74	0.45	63.27	0.02
PCSC (54%) after cycling	1.74	-	-	1.5*	23.9**	0.139
PCSC (68%) after cycling	0.89	-	-	1.23*	64.6**	0.126
PCSC (73%) after cycling	0.89	-	-	0.87*	69.9**	0.109

*CPE **Rct

5.4 Conclusion

The hierarchically porous, N and O inherently co-doped carbon with high surface area have been explored from a renewable raw material of pincone, to develop a high-performance cathode material for LSBs. The cyclability and the specific capacity of the system are influenced by the sulphur content and distribution in the porous matrix with high surface area of $2065 \text{ m}^2 \text{ g}^{-1}$ and the dopants (N & O). PCSC (54%) cathode demonstrates 1606 mA h g^{-1} initial capacity and sustains a capacity of 1269 mA h g^{-1} after 100 cycles at 0.1C rate and a good rate capability (923 mA h g^{-1} at 2C). The physical adsorption of PSs onto the porous

carbon and chemical binding of PSs through O and N dopants increase the electrochemical performance and diminish the active material loss during the cycling process. The excellent electrochemical performance is due to the synergic effect of the hierarchically porous features of the activated carbon with oxygen and nitrogen binding sites to immobilise the active PS species. The sulphur utilization is decreased with the increase of sulphur content on PCSCs due to the accumulation of sulphur on the surface of the porous carbon matrix. PCSC (54%) displays 79% retention with 0.29% capacity fading per cycle. Furthermore, being a low cost, easily available and facile N and O co-doped hierarchically porous carbon is an ideal host for sulphur. Hence, PCSC is a promising cathode material for Li-S batteries.

CHAPTER 6

ORANGE PEEL DERIVED CARBON FOR LITHIUM-SULPHUR BATTERY

The shuttle effect associated with LSB deteriorate the battery performance and delay their practical applications. In this chapter, orange peel derived carbon-sulphur composite (OPCSC) is used as the cathode material. To improve its performance, heteroatom doped microporous carbon (HMC-1), with the surface area of $969 \text{ m}^2 \text{ g}^{-1}$ and pore volume of $0.43 \text{ cm}^3 \text{ g}^{-1}$ is used for the modification of separator. The HMC-1 coated on the surface of commercial PP separator by doctor blade method act as a LPS shuttle inhibitor. The LSB with HMC-1 coated separator shows an initial discharge capacity of 1213 mA h g^{-1} at 0.1C rate and excellent cycling performances with 85% capacity retention even after 100 cycles and deliver 845 mA h g^{-1} at 2C rate. The thin layer coating of HMC-1 on separator effectively blocks the migration of PSs towards the anode, thereby decreasing the capacity loss and improving the rate performance. This enhancement in the electrochemical performance is attributed to the synergistic effect of heteroatoms along with the high surface area of carbon materials which are used for the modification of the separator and sulphur host.

6.1 Introduction

Sulphur, which exhibits 2600 W h kg^{-1} specific energy, could be a better option to develop energy storage device with high energy density. Moreover, its availability, cost, and performance are additional advantages if it is possible to achieve high discharge capacity by reducing capacity fading and minimizing the insulating behaviour of sulphur (Manthiram et al., 2014; H.-J. Peng et al., 2017; Seh et al., 2016). The latter issue can be diminished by using different formats of conductive materials, most commonly, carbon-based materials (Z. Li, Y. Huang, et al., 2015; Z.-L. Xu et al., 2018). To attain the discharge capacity close to theoretical level and minimizing the capacity fading are the challenges that need to be solved through alleviating PS dissolution and the shuttling effect of PS (J. Wang et al., 2017). Previous chapters and recent studies demonstrate that surface functional groups and heteroatom doped porous carbon plays an important role to improve the electrochemical performance of the carbon-sulphur composite when used as cathode material in LSBs (L. Chen et al., 2017; Zan Gao et al., 2017). Biomass-

derived carbon is successfully converted into porous carbon and used as cathode supporter, separator modifications, etc., for LSBs (Zan Gao et al., 2017; X. Zhang et al., 2017). Orange peel (*Citrus Sinensis*) is a major biowaste. It is a widely available and cheapest material in all over the world (Pandiarajan et al., 2018). Orange peel is 44% of the orange fruit, consists of lignin, cellulose, pectin, hydroxyl, carboxyl, and amide functional groups. Orange peel biowaste is used for the adsorption of heavy metals (N. Feng et al., 2011; Guiza, 2017; S. Liang et al., 2009), polymer synthesis (Ranaweera, Ionescu, et al., 2017), pectin extraction (Prakash Maran et al., 2013), biofuel production (Martín et al., 2010; Santos et al., 2015), adsorption of dyes (Khaled et al., 2009), flavone extraction (Lachos-Perez et al., 2018), etc. Orange peel derived activated carbon is used as electrode material for supercapacitors (Arie et al., 2013; Dhelipan et al., 2017; Maharjan et al., 2017; Ranaweera, Kahol, et al., 2017; C. Wang et al., 2018), catalyst support for the oxygen-reduction reactions (Dhelipan et al., 2017), chemical adsorption (M. E. Fernandez et al., 2015; Gupta and Singh, 2018; Pandiarajan et al., 2018), dye adsorption (Maria Emilia Fernandez et al., 2014; Lam et al., 2017), anode for Li/Na ion batteries (J. Xiang et al., 2017; Z. Li, Y. Huang, et al., 2015; D.-W. Wang et al., 2013). In this chapter, orange peel derived microporous carbon (OPC) is prepared and evaluated as cathode materials in LSBs. The OPCSC shows 51% capacity retention after 100 cycles at 0.1C rate. The capacity degradation is mainly due to the loss of sulphur as PSs during the redox reactions shows the inefficiency to utilize sulphur. To block the PSs migration extensive efforts have been carried out like special cathode design, anode protection, and electrolyte modification and separator modifications (X. Zhang et al., 2017). The materials used to obstruct the voyage of the PSs is clearly emphasized in section 1.3.2. Shuttle effect occurs via PS passage through the separator and has a major impact on the performance of LSBs (Yibo He, Chang, et al., 2018; Ogoke et al., 2017). The separator is a porous membrane through which the PSs moves towards the anode side, deposit as Li_2S . It is not soluble in the electrolyte and leads to the degradation in the performance (Zhian Zhang et al., 2015). Blocking of PSs on the cathode side is an effective approach by modifying the separator to achieve good electrochemical performance (W. Lin et al., 2015). The carbon coated separator has a dual function as PSs

confinement and an upper current collector which helps to smooth transfer of electrons during the oxidation-reduction reaction. It has been reported that many carbon materials with the high surface area, lightweight and conducting nature such as MWCNT (Chung and Manthiram, 2014), rGO (W. Lin et al., 2015), GO (J.-Q. Huang et al., 2015), porous carbon (Balach et al., 2015; J. Zhu et al., 2016), carbon nanofiber (G. Chen et al., 2018), etc are coated on the separator. These non-polar carbon substrates have a weak physical interaction with the polar PSs, hence this material cannot ensure the long-term stability of the LSBs. The introduction of heteroatom on the surfaces of the porous carbon materials make them interact chemically with the PSs during the charge-discharge process (S. S. Zhang, 2015). It includes the N doped carbon nanowire (X. Zhou et al., 2016), N, S & O co-doped carbon (F. Ai et al., 2017), N doped porous carbon sphere (Zhian Zhang et al., 2015), N & P co-doped honeycomb-like carbon (P. Zeng, Huang, Zhang, Zhang, et al., 2018), B & N doped rGO (P. Han and Manthiram, 2017) is successfully used as a barrier between the separator and the cathode for trapping the PSs.

In the present study, OPC derived from orange peel with the high surface area is used to host sulphur and heteroatom doped microporous carbon (HMC-1) derived from DDS is used as a functional modifier of the separator based on the above consideration and motivation. A thin coating of HMC-1 on one side of the separator was placed towards the cathode to capture the PSs. Based on the literature, it is the first time to use the carbon from DDS for separator modification in LSBs. To understand PS blocking ability of HMC-1 coated separator in LSBs, electrochemical characterizations were carried out and made a comparative study with MWCNT coated separator for the same cathode film OPCSC (73%) in LSBs. HMC-1 coated separator exhibits an initial discharge capacity of 1213 mA h g⁻¹ and a stable capacity of 1033 mA h g⁻¹ after 100 cycles with 0.17% capacity decay per cycle at the 0.1C rate. The HMC-1 is microporous which allows only the movement of the Li⁺ ions and effectively block the PS diffusion. The high surface area carbon with pyridinic N, pyrrolic N and O functionalities aimed at physical and chemical adsorption for PSs during the charge-discharge process (Huangfu et al., 2018).

6.2 Materials and Methods

6.2.1 Materials

Orange peel biowaste was obtained from Kerala, Thiruvananthapuram. 4, 4'-diamino diphenyl sulphone (DDS, 99%, Merck), and all other chemicals were as mentioned in section 2.2.1.

6.2.2 Material synthesis

6.2.2.1 Preparation of porous carbon

Orange peel was washed, dried, crushed and ground into fine powders. The powder was washed with distilled water and ethanol and dried in an air oven at 100 °C for 24 hours. These powders were used as activated carbon precursors. Chemical activation was done by mixing 10 grams of orange peel powder with 20 grams of zinc chloride in 100 ml of distilled water. After drying it was heated at 600 °C in a tube furnace for 1 hour in an inert atmosphere. After that, it was washed with HCl, distilled water until it becomes neutral (Arie et al., 2013). The activated carbon was dried in an oven at 100 °C and stored in a desiccator, which is denoted as orange peel derived carbon (OPC) (Figure 6.1).

6.2.2.2 Preparation of carbon-sulphur composites

Orange peel derived carbon-sulphur composite (OPCSC) was prepared by melt diffusion method (Figure 7.1) as discussed in section 3.2.2.2.

6.2.3 Preparation of modified separator

The MWCNT obtained from the Sigma Aldrich is used as the separator coating without any further purification. A mixture of MWCNT and PVDF in a weight ratio of 9:1 is mixed with NMP as a solvent to form the slurry, which was then coated on one side of the polypropylene separator. Then the separator was dried under vacuum oven at 60 °C for 24 hours. HMC-1 was prepared by using the

procedure discussed in section 3.1. After that, it was coated on the separator with the procedure mentioned above by replacing MWCNT with HMC-1.

6.2.4 Material Characterization

The materials prepared above were characterized using the techniques described in section 2.2.3.

6.2.5 Fabrication of coin cell and electrochemical measurements

Coin cells were fabricated using OPCSC as a cathode material and the electrochemical characterization was studied by the procedure described in the section 2.2.4 and 2.2.5. The mass loading of the active material was $\sim 3.5 \text{ mg cm}^{-2}$.

6.3 Results and Discussion

6.3.1 Characterization of OPC and OPCSCs

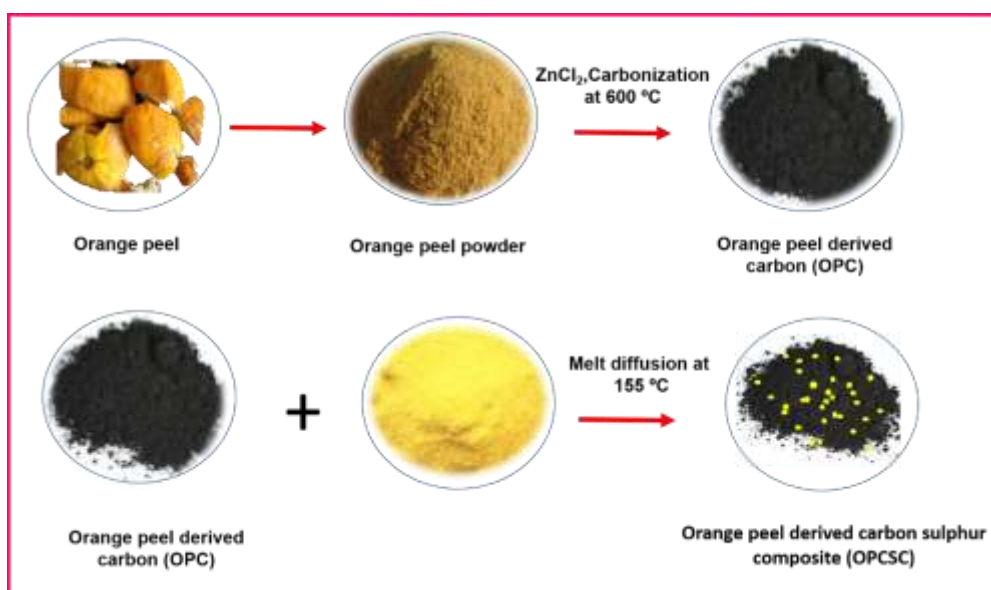


Figure 6.1. Schematic illustration of the preparation of OPC and OPCSCs

Figure 6.1 displays the scheme for the preparation of OPCSCs from the OPC. The nitrogen adsorption-desorption isotherms of the OPC and OPCSCs are shown in Figure 6.2 (a). Rapid adsorption at relatively low pressure indicates the presence of micropores. A very small hysteresis loop at relatively medium pressure

indicates the presence of mesopores. Pore size distribution curves confirm that the OPC has microporous morphology (Figure 6.2 (b)) (Gu et al., 2015). This material has a surface area of $1806 \text{ m}^2 \text{ g}^{-1}$ and pore volume of $0.93 \text{ cm}^3 \text{ g}^{-1}$. These results guarantee that OPC is an ideal host of sulphur for LSB applications (J. Liu et al., 2017; S. Zhang et al., 2014). Surface area and pore volume are drastically reduced after sulphur loading. Surface area reduced to $0.95 \text{ m}^2 \text{ g}^{-1}$ for OPCSC (61%) and $0.94 \text{ m}^2 \text{ g}^{-1}$ for OPCSC (73%). The pore volume is reduced to $0.00 \text{ cm}^3 \text{ g}^{-1}$ in both the cases suggests that the sulphur covers the surface of the carbon (Y. Tan et al., 2017). Table 6.1 represents the surface area and pore volume details of OPC and OPCSCs.

Table 6.1: Surface area and pore volume of OPC/OPCSCs

Description of properties	OPC	OPCSC (61%)	OPCSC (73%)
BET surface area ($\text{m}^2 \text{ g}^{-1}$)	1806	0.95	0.94
Total pore volume ($\text{cm}^3 \text{ g}^{-1}$)	0.94	0.00	0.00

The structural investigation of the OPC and OPCSCs were carried out by the XRD analysis. XRD patterns of the OPC shows two broad diffraction peaks centered at $2\theta=26^\circ$ and 43° is due to the presence of disordered porous structure with a low degree of graphitization (Gu et al., 2015; S. Xiao et al., 2015). XRD pattern for the sulphur shows the crystalline phases of the orthorhombic sulphur (JCPDS 00-008-0247). OPCSCs shows all the crystalline phases of sulphur indicate the presence of sulphur in the composite (Figure 6.2 (c)) (Gu et al., 2015; W. G. Wang et al., 2014). Further, structural investigation of OPC and OPCSCs is carried out by Raman spectrum (Figure 6.2 (d)). It is characterized by a band at 1336 cm^{-1} and another band at 1595 cm^{-1} called D (disordered) and G (graphitic) bands, respectively (Dresselhaus et al., 2007; Jiawei Zhang et al., 2015). The D band ascribed to the disordered amorphous carbon and G band is due to the presence of graphitized carbon. The I_D/I_G ratio for OPC is ~ 0.9 which indicates the amorphous structure of carbon material. The I_D/I_G ratio of OPCSCs is relatively higher than that of OPC which indicates the defects get pronounced in the composite. The inset showing the Raman spectra of crystalline sulphur, which exhibits three peaks at 148 cm^{-1} , 214 cm^{-1} and 470 cm^{-1} (Ward, 1968). OPCSCs shows the sulphur bands in a moderate intensity indicating the presence of sulphur in the surface of the carbon

matrix. The observed sulphur peaks in OPCSCs indicating that sulphur is incorporated into the carbon matrix successfully by melt diffusion process (Niu et al., 2015; Xuebing Yang et al., 2015).

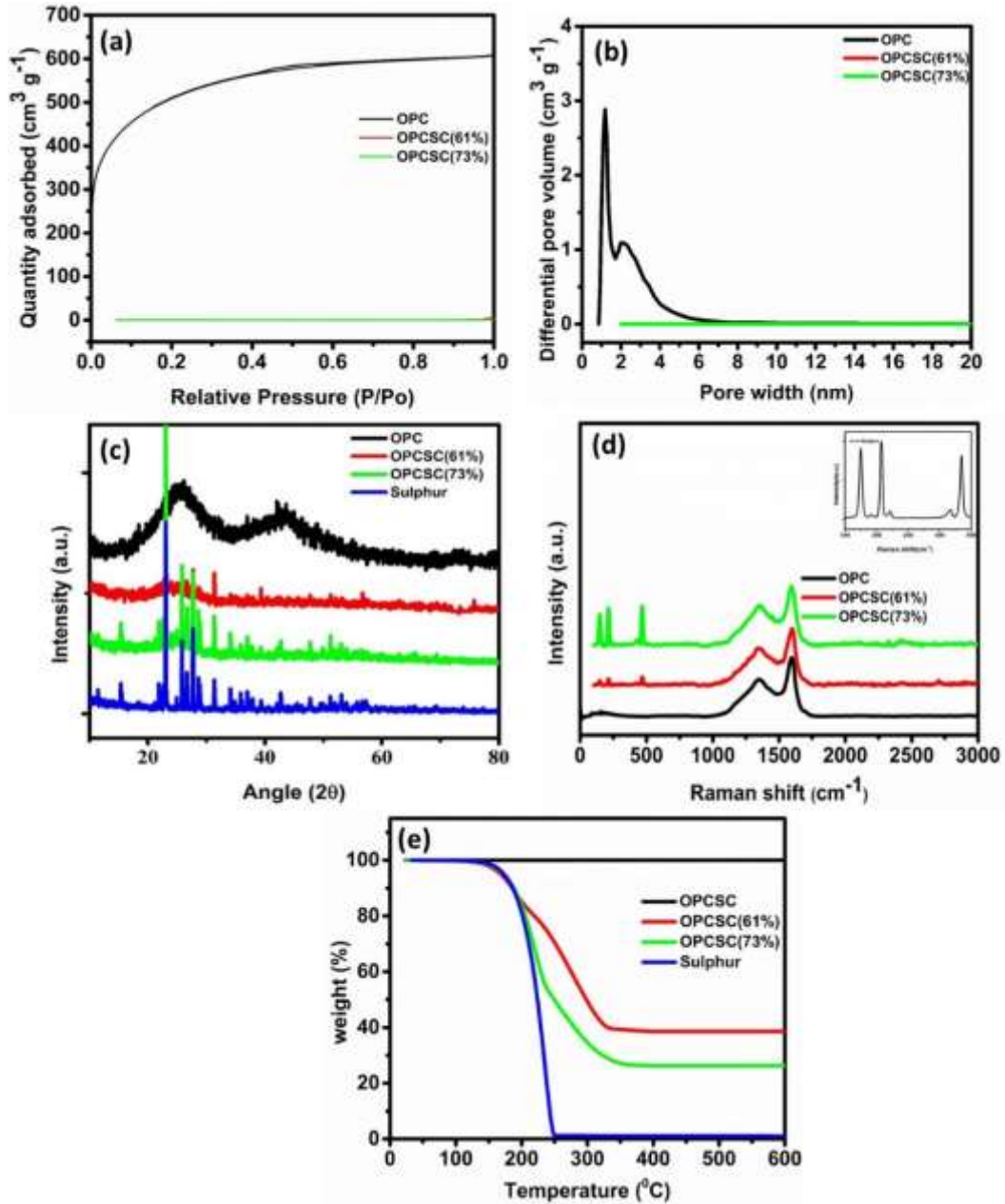


Figure 6.2. (a) N₂ adsorption/desorption isotherms of OPC and OPCSCs (b) Pore size distribution curves of OPC and OPCSCs (c) XRD pattern for sulphur and OPCSCs (d) Raman spectra of OPC, OPCSCs [inset: Raman spectrum of sulphur] and (e) TGA of OPC, OPCSCs and sulphur

The amount of sulphur in the OPCSCs and the thermal stability of OPC are determined using TGA. Figure 6.2 (e) shows the TGA of the sulphur, OPC and OPCSCs. TGA of OPC indicates the thermal stability of the prepared carbon

material. The sulphur completely evaporated at a temperature of 250 °C, however, OPCSC (61%) and OPCSC (73%) shows complete weight loss at 320 °C and 360 °C, respectively attributed to the removal sulphur infused from the micropores. TGA curves of OPCSCs show major weight loss in the temperature range 116 °C–350 °C (Y. Fu et al., 2012; W. G. Wang et al., 2014). The amount of sulphur calculated in the OPCSCs with reference to sulphur is 61% and 73%.

The presence of functional groups and chemical states of the elements in the OPC and OPCSCs are characterized using the XPS measurements. From the survey scan analysis of OPC, it can be observed that the presence of C1s, N1s, O1s at 283.7 eV, 400 eV and 533.1 eV, respectively (Figure 6.3 (a)). The deconvoluted C1s spectrum (Figure 6.3 (b)) has 5 components, C-C/C=C (284.6 eV) of sp^2 , C-N (285.6 eV), C-O bond (286.4 eV), C=N bond (287.2 eV) and C=O (288.6 eV). The deconvoluted N1s spectrum (Figure 6.3 (c)) contains pyridinic (398.1 eV), pyrrolic (400 eV), and graphitic (401.7 eV). The deconvoluted O1s spectrum (Figure 6.3 (d)) has two components: C-O bond (531.9 eV), and C=O bond (533.1 eV) (Jin et al., 2017; Shao et al., 2016; X. Yuan, Liu et al., 2017; G. Zhou et al., 2015; S. Jiang et al., 2019).

Figure 6.4 shows the XPS analysis of the OPCSC (73%). The survey scan analysis (Figure 6.4 (a)) reveals the presence of C1s, O1s, N1s, S2s and S2p functionalities. The deconvoluted C1s spectra (Figure 6.4 (b)) is attributed to C-C (284.3 eV), C-S (284.9 eV), C-N (285.3 eV), C-O (286.4 eV), C=N (287eV) and C=O (288.4 eV) from OPCSC composite (M. Chen et al., 2017; Jin et al., 2017; Jing Xu et al., 2016).

The deconvoluted N1s spectrum (Figure 6.4 (c)) contains pyridinic (398.3 eV), pyrrolic (400.3 eV), graphitic (401.7 eV), N-S (402.6 eV), etc. The high-resolution O1s spectrum (Figure 6.4 (d)) is deconvoluted into S-O bond (530.7 eV), C-O bond (531.8 eV) and C=O bond (532.4 eV). The high-resolution S2p (Figure 6.4 (e)) contains two $S2p_{3/2}$ and $S2p_{1/2}$ (Niu et al., 2015). It is observed that $S2p_{3/2}$ (163.7, 164 and 164.2 eV) and $S2p_{1/2}$ (164.9, 165.2 and 165.4eV) with an energy separation of 1.2 eV corresponds to the C-S, S-N and S-O bonds in the OPCSC

(Niu et al., 2015; Jing Xu et al., 2016; L. Zhang et al., 2012; Pang et al., 2015; Z. Wang et al., 2014; X. Yuan, Liu et al., 2017; G. Zhou et al., 2015; Jin et al., 2017).

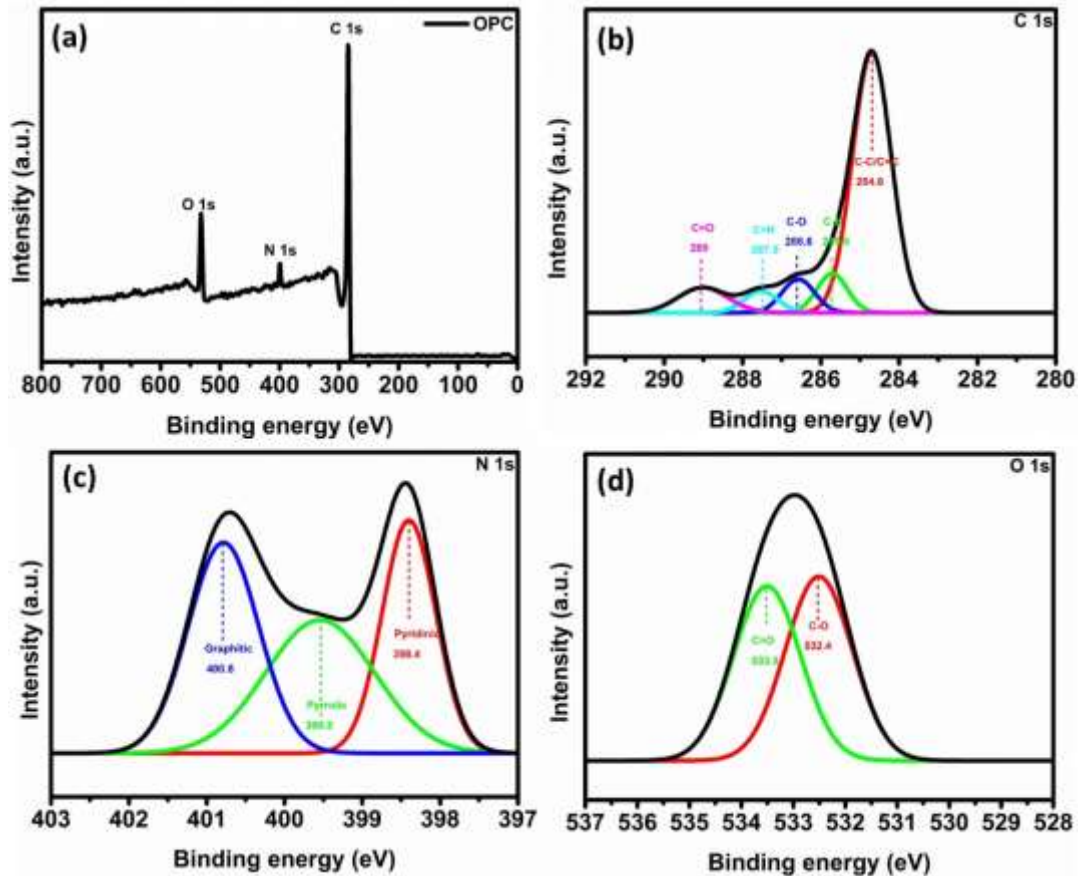


Figure 6.3. XPS analysis of OPC (a) survey scan (b) C1s (c) N1s and (d) O1s

Figure 6.5 shows the SEM images of OPC and OPCSC (73%). SEM images of OPC (Figure 7.5(a-c)) is composed of numerous micropores with a slight amount of mesopores which is highly useful for the absorption of sulphur during melt diffusion. Morphological change is observed in the SEM images of the OPCSC due to infused sulphur into pores and the surface of the carbon matrix (Figure.7.5 (d-f)).

Figure 6.6 (a and c) shows the TEM images of the OPC and OPCSC (73%) which confirms the presence of nanopores. The inset shows the SAED pattern of the OPC and OPCSC reveals the amorphous nature of the carbon material and crystalline nature of the composite, due to the presence of sulphur in the composite.

TEM-EDS analysis reveals the information about the presence of hetero elements N, O in the OPC (Figure 6.6 (b)) and N, O, S in the OPCSC (Figure 6.6 (d)).

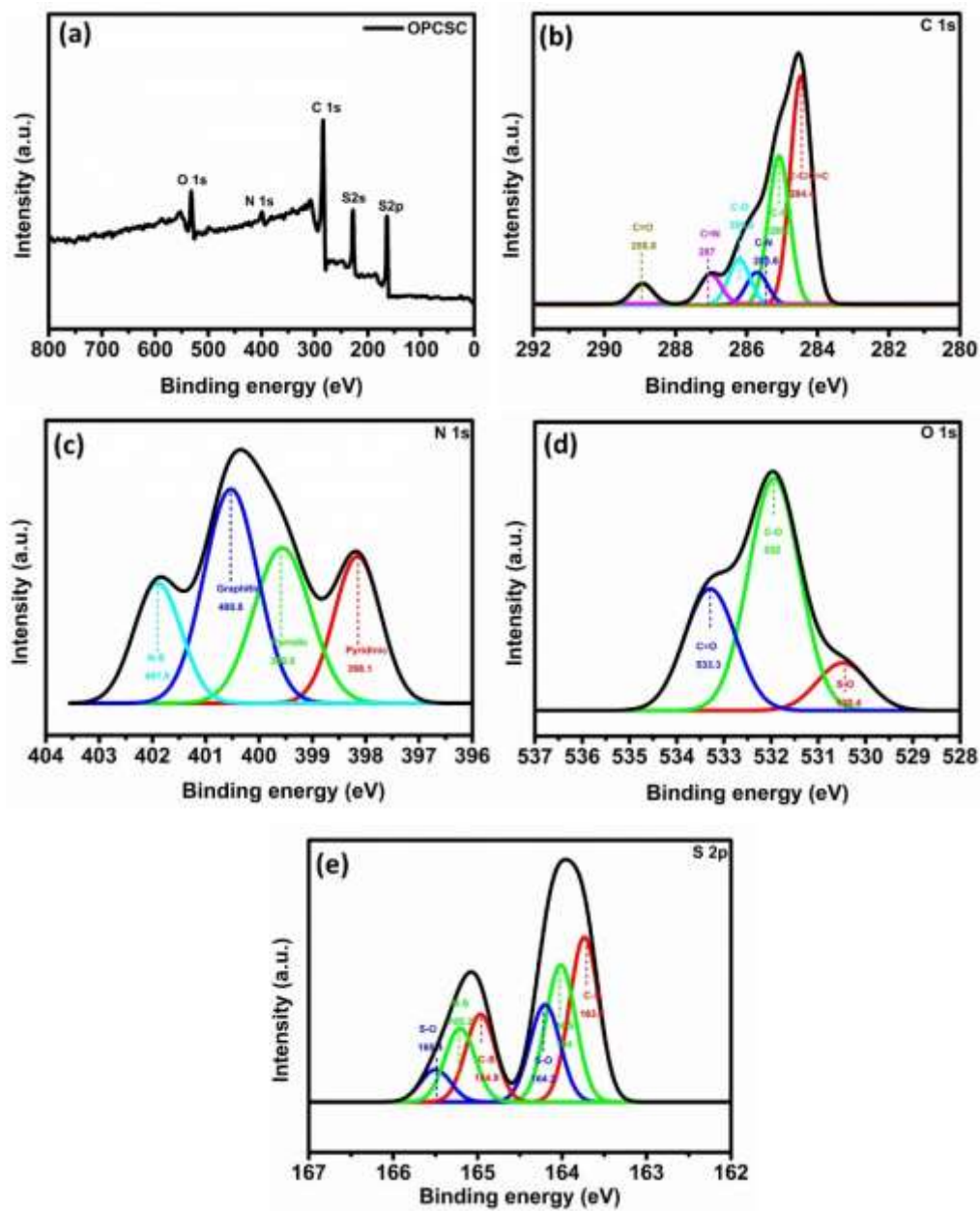


Figure 6.4. XPS analysis of OPCSC (73%) (a) survey scan (b) C1s (c) N1s (d) O1s and (e) S2p

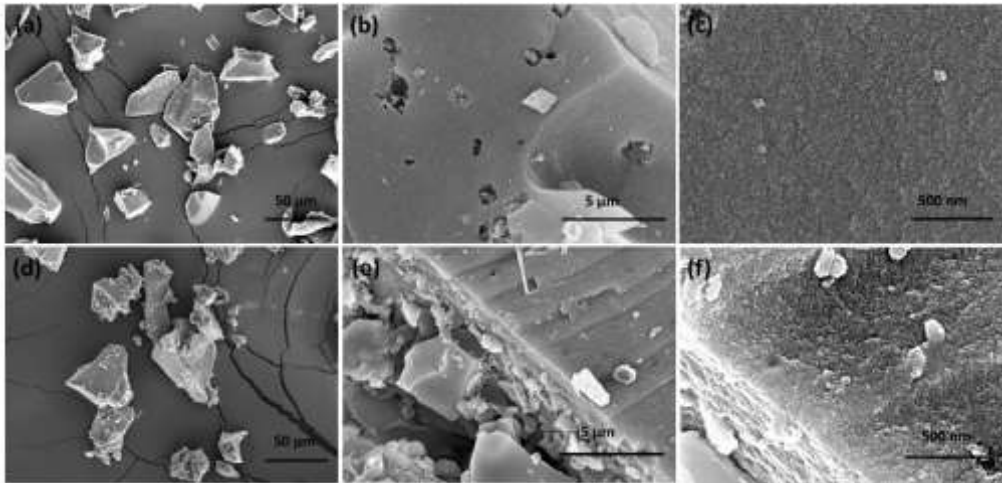


Figure 6.5. SEM images (a-c) OPC and (d-f) OPCSC (73%)

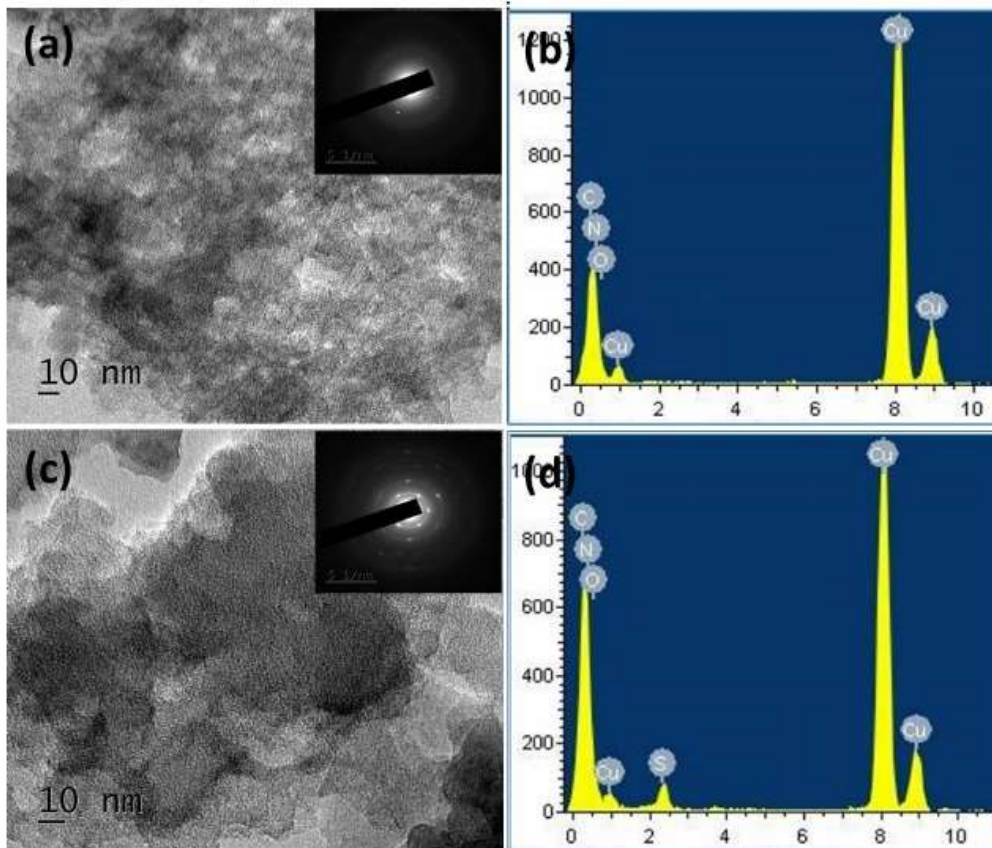


Figure 6.6. Images of (a) TEM (b) EDS analysis of OPC and (c) TEM (d) EDS analysis of OPCSC (73%) [Inset showing the corresponding SAED pattern]

6.3.2 Electrochemical performance of the composite

6.3.2.1 OPCSC as cathode material for Li-S batteries

To understand the electrochemical performance of OPCSC as a cathode material, a series of electrochemical tests were carried out. Figure 6.7 (a-b) shows

the CV curves of OPCSC in a potential range of 1.6-3 V at 0.1 mV s⁻¹ scan rate. During the cathodic scanning, two reduction peaks at 2.39 V and 2.01 V are observed. The peak at 2.39 V is due to the reduction of elemental sulphur to long chain lithium polysulphides (Li₂S_x, 4 ≤ x ≤ 8). The second peak at 2.01V is due to the conversion of these long chain polysulphides to short chain polysulphides (Li₂S_x, 2 ≤ x ≤ 4). In the subsequent anodic scan process, a peak of 2.43 V is observed, which corresponds to the conversion of these polysulphides to sulphur (Jing Xu et al., 2016; K. Yang et al., 2015). In the subsequent scan process, the oxidation and reduction peak potentials are not changed, indicating the reactive reversibility. Both OPCSCs maintain same oxidation and reduction peak positions, an increase in current density is observed in the higher sulphur content composite due to the increase in the amount of active material utilization. In the successive cycles, the current density is decreased for both the composite may be due to the loss of active material (S. Zhang et al., 2014; J. Yang et al., 2015). The cathodic peaks are slightly shifted to higher oxidation potential and the anodic peaks are slightly shifted to lower potentials indicate that the active material is rearranged from their original position to get more energetic stable position in the successive scan and to obtain lower polarization (Zhengjiao Liu et al., 2018). The initial discharge capacity of OPCSC (73%) and OPCSC (61%) are 1099 mA h g⁻¹ and 1019 mA h g⁻¹, respectively (Figure 6.7(c-d)). The second discharge capacity is 777 mA h g⁻¹ (61%) and 796 mA h g⁻¹ (73%) exhibits a capacity degradation at 23% and 27%, respectively with respect to the first discharge capacity. When the cycle number turns to 100, both the composite display 51% capacity retention with respect to the initial discharge capacity. This notorious capacity degradation is mainly due to the loss of sulphur during the redox reactions (Ogoke et al., 2017). Figure 6.7 (e) shows the cycle performances and coulombic efficiency of OPCSCs at 0.1C rate, with a 0.66% capacity decay rate for OPCSC (61%) and 0.73% for OPCSC (73%) with the coulombic efficiency ~99% (Gu et al., 2015).

To investigate the charge-discharge behaviour of OPCSCs at various current densities, rate performance tests were conducted. As shown in Figure 6.7 (f) OPCSC (73%) delivers the discharge capacity of 1099, 672, 492 and 400 mA h g⁻¹ at 0.1C, 0.2C, 1C and 2C, respectively. When the current density is decreased

to 0.2C, it exhibits a discharge capacity of 654 mA h g⁻¹ with 2.7 % capacity degradation. While the OPCSC (61%) delivers the discharge capacity of 1019, 620, 455 and 384 mA h g⁻¹ at the same rates and obtained 3% capacity degradation when returned back to the 0.2C rate. OPCSC (73%) is chosen for further evaluations due to the high sulphur content when compared with OPCSC (61%).

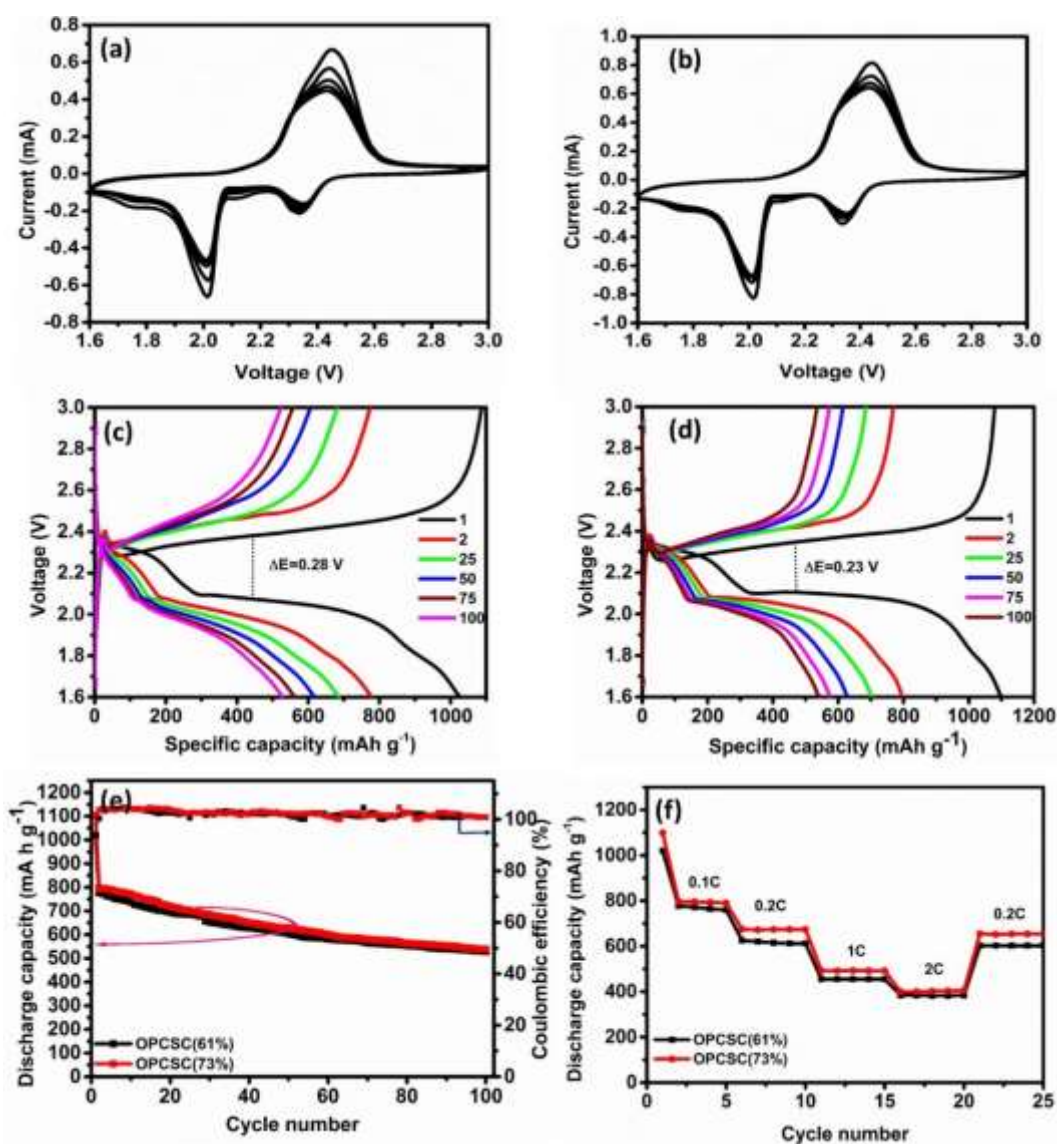


Figure 6.7. CV of the OPCSCs (a) 61% and (b) 73%, GCD curves of OPCSCs (c) 61% (d) 73% (e) Cyclic stability performances and coulombic efficiency and (f) Rate capability studies at different C-rate

6.3.2.2 Structural and electrochemical evaluation of LSB with modified separator

A separator between the two electrodes is made from a porous electrically insulating material used to prevent contact and short-circuiting between the electrodes, and also provides pathways for electrolyte ions and is made up of polyethylene, polypropylene or their composite. The SEM images of the pristine separator (Figure 6.8) consists of abundant pores on its surface, through which PSs can easily pass through and react with Li metal, it causes corrosion of the anode.

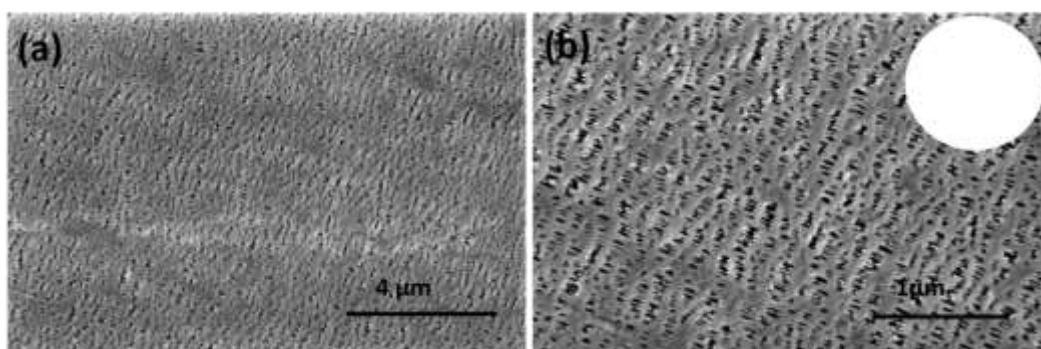


Figure 6.8. SEM Images of PP (a) Lower magnification and (b) Higher magnification [inset showing digital photograph]

One side of the separator is modified and placed towards the cathode side to capture PSs within the cathodic compartment. From the schematic illustration (Figure 6.9), it is evident that the battery with common PP separator is prone to shuttle effect, however, the modified separator restrict PS as in the cathode side by physical/chemical adsorption. HMC-1, a heteroatom doped microporous carbon and MWCNT is used for the separator modification its electrochemical performance is compared with a bare separator. The modified cell configuration facilitates to improve the active material utilization, hence the specific capacity of the cell.

The carbon material MWCNT and HMC-1 are characterized by surface area analysis, XRD, Raman and XPS analysis. Figure 6.10 (a) shows the N_2 adsorption-desorption isotherms of MWCNT and HMC-1. MWCNT shows a type V isotherm and BET surface area is $218 \text{ m}^2 \text{ g}^{-1}$ with a pore volume of $1.8 \text{ cm}^3 \text{ g}^{-1}$. DFT pore size distribution analysis of MWCNT clearly shows that the most of the

pores are in the meso and macroporous region (Figure 6.10 (b)) (Peigney et al., 2001; L. Wang et al., 2011; Hua Yue Zhu et al., 2013).

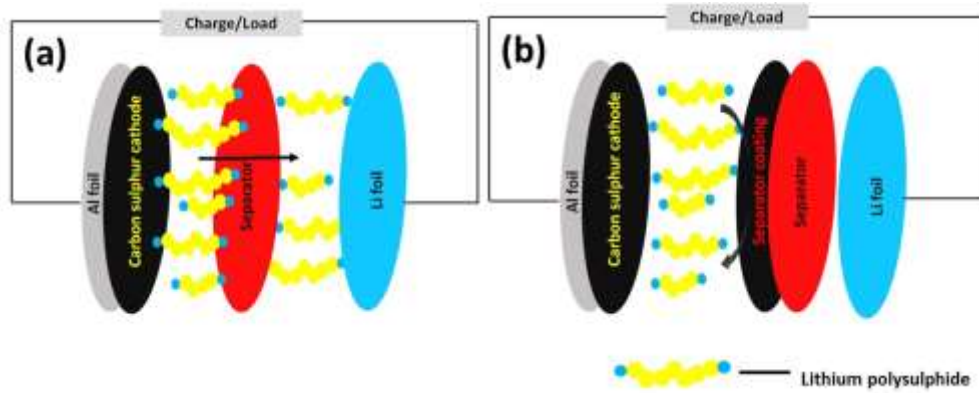


Figure 6.9. Schematic illustration of LSB and polysulphide shuttling (a) With bare separator and (b) With separator coating

The XRD pattern of MWCNT (Figure 6.10 (c)) shows the broadband at $2\theta=24.6^\circ$, is due to the reflection of (002), another diffraction peak at $2\theta = 44^\circ$ corresponding to the reflection of (100) plane, indicating amorphous structure with low graphitic nature. Raman spectra of MWCNT show D band at 1336 cm^{-1} and G band at 1595 cm^{-1} (Figure 6.10 (d)). The I_D/I_G ratio is 1.5 indicates the MWCNT is a disordered amorphous carbon material. A trace amount of oxygen is observed in the XPS survey scan analysis of MWCNT (Figure 6.10 (e)) (Varga et al., 2017; L. Wang et al., 2011; Zhiteng Zhang et al., 2014). The presence of oxygen is due to atmospheric oxidation when MWCNT is exposed to air. HMC-1 is an amorphous carbon with N and O functionalities and was well characterized in chapter 4. The BET specific surface area is $969\text{ m}^2\text{ g}^{-1}$ and the pores are in the microporous region. The specific surface area and suitable micropore size distribution are highly advantageous for the PS adsorption along with N and O functionalities which will anchor the PSs on the cathode side itself.

The material used for coating the separator was further characterized by the SEM and TEM analysis. SEM analysis of MWCNT reveals the tubular morphology and the entangled bundles of tubes with macro, meso and micropores (Figure 6.11 (a)) (Faramarzi et al., 2011). HMC-1 reveals the sheet-like morphology with numerous micropores (Figure 6.11 (d)). Figure 6.11(b and e) shows the TEM images of MWCNT and HMC-1. Nano pores in HMC-1 ease Li-ion transport and

blocks the PS anions. TEM-EDS analysis reveals the presence of carbon in the MWCNT (Figure 6.11 (c)) and C, N and O in the HMC-1 (Figure 6.11 (f)). A trace amount of O in MWCNT may be due to oxidation in air.

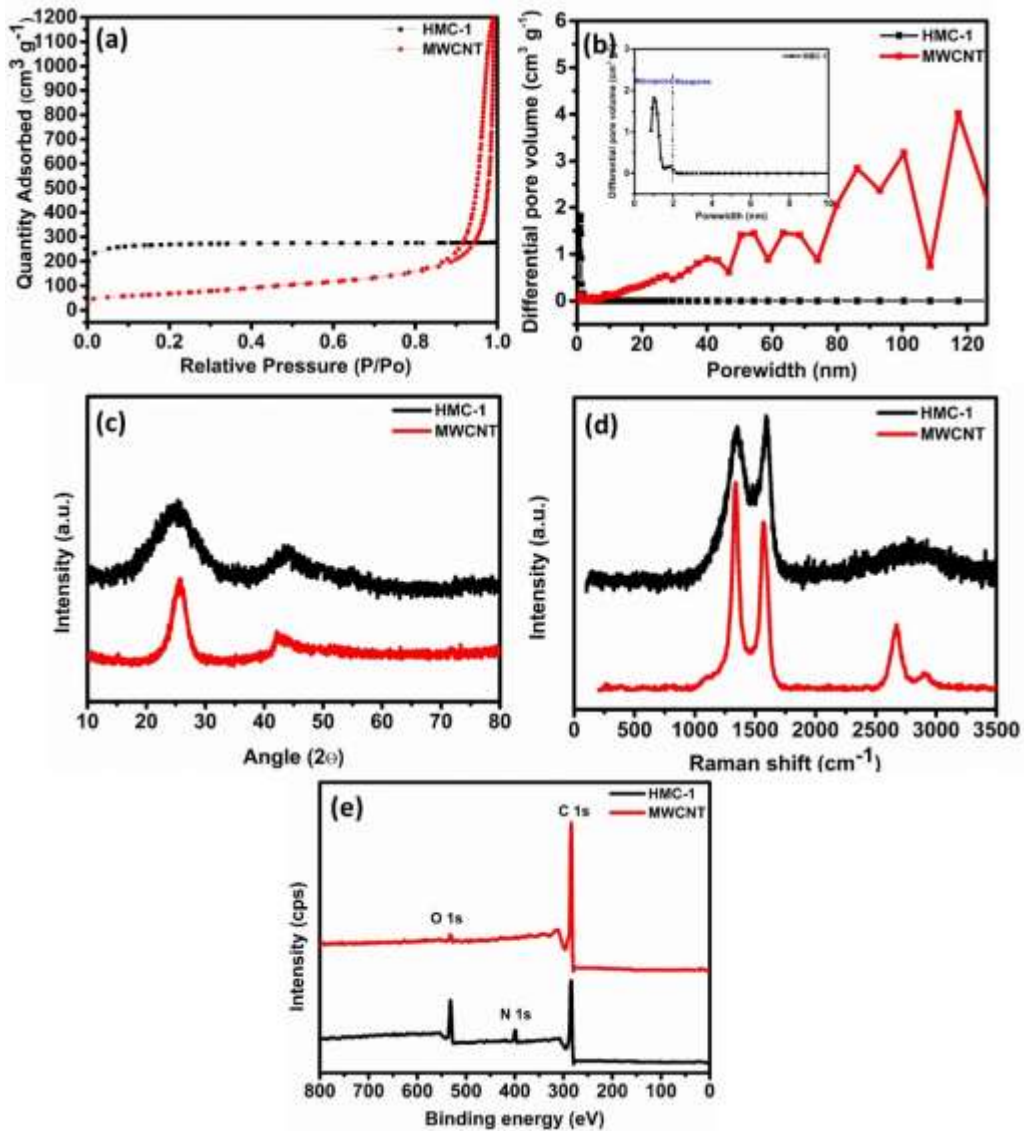


Figure 6.10. Characterization of MWCNT and HMC-1 (a) N₂ adsorption/desorption isotherms (b) Pore size distribution curves [inset: enlarged portion of pore size distribution of HMC-1] (c) XRD pattern (d) Raman spectra and (e) XPS survey scan analysis

Table 6.2. Porosity details of MWCNT and HMC-1

Sample	MWCNT	HMC-1
BET surface area (m ² g ⁻¹)	218	969
Total pore volume (cm ³ g ⁻¹)	1.8	0.43

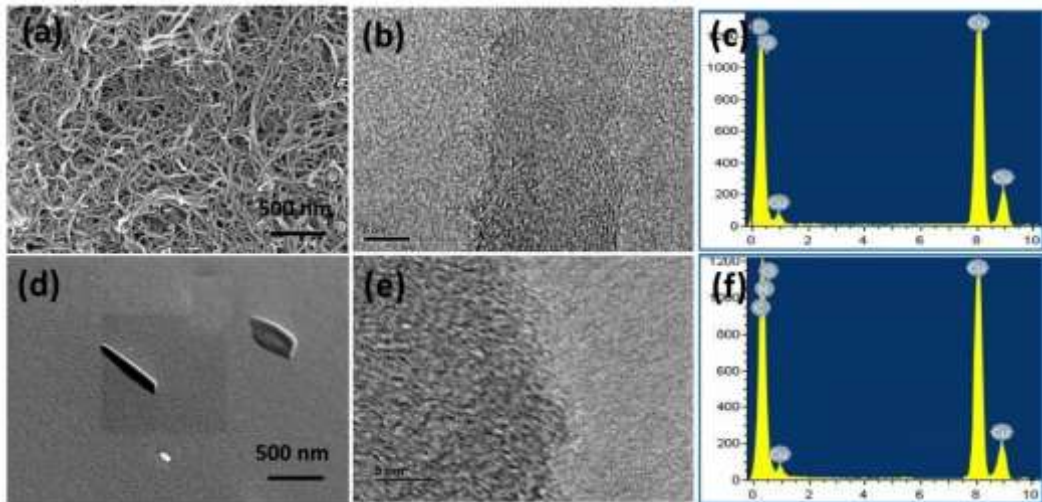


Figure 6.11. Images of (a) SEM, (b) TEM (c) EDS analysis of MWCNT and (d) SEM, (e) TEM (f) EDS analysis of HMC-1

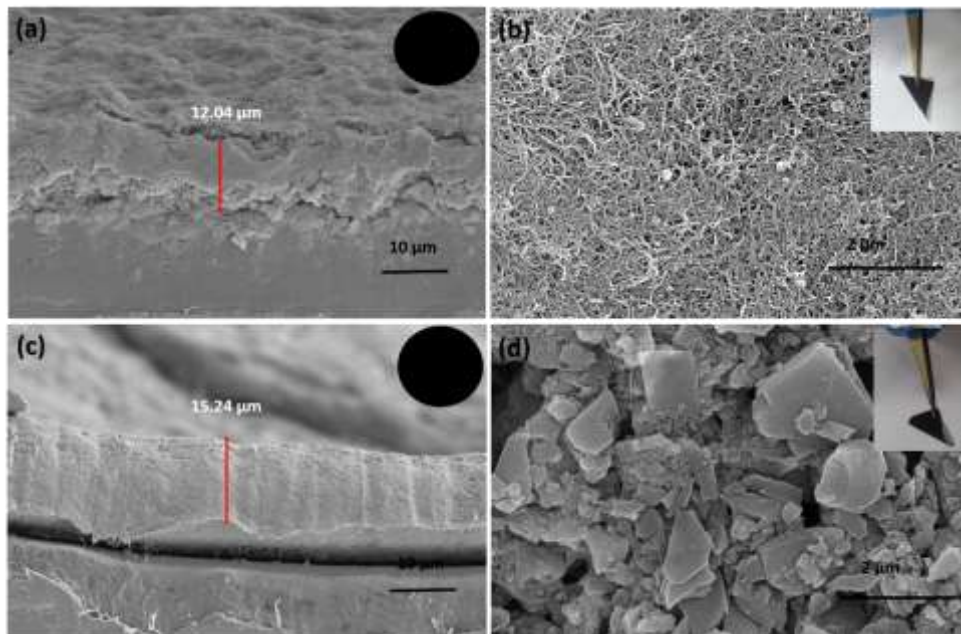


Figure 6.12. Cross sectional Images of SEM images (a-b) MWCNT and (c-d) HMC-1[inset a and c shows the digital photographs of the modified separator] [inset b and d demonstration of flexibility and mechanical strength]

The cross-sectional views and surface morphology of the modified separator were characterized by the SEM analysis (Figure 6.12). The SEM images show the both MWCNT and HMC-1 are uniformly coated on the PP separator. The cross-sectional images of the two types of the modified separator are shown in Figure 6.12 (a and c) for MWCNT and HMC-1, respectively. It is observed that the slurries are well stacked on the surface of PP separator. The average thickness is $\sim 12 \mu\text{m}$ and $\sim 15 \mu\text{m}$ for the separator modified by MWCNT and HMC-1,

respectively. The weight of the coating is $\sim 0.79 \text{ mg cm}^{-2}$ and 1.02 mg cm^{-2} for MWCNT and HMC-1, respectively. Top view SEM images are shown in the Figure 7.12 (b and f). The coated separators have good mechanical strength, it is robust during the cell assembly (inset of Figure 6.12 (b and d)).

Electrochemical studies were carried out to know the impact of separator coating on the performance of LSB. Figure 6.13 (a and b) shows the CV profile for OPCSC cathode with MWCNT and HMC-1 coated separators at the scan rate of 0.1 mV s^{-1} in the voltage window of 1.6-3V. Two reduction peaks and one oxidation peak is observed similar to that of the cell with a bare separator (Figure 6.7 (b)). The reduction peaks at $\sim 2.34 \text{ V}$ and $\sim 2.36 \text{ V}$ for the MWCNT and HMC-1 are due to the conversion of sulphur to higher order lithium polysulphides (Li_2S_x , $4 \leq x \leq 8$). The second reduction peak at $\sim 2.01 \text{ V}$ and $\sim 2.02 \text{ V}$ is due to the conversion of higher order polysulphides to lower order polysulphides (Li_2S_x , $4 \leq x \leq 2$) for the MWCNT and HMC-1, respectively. The broad oxidation peak at $\sim 2.34 \text{ V}$ & $\sim 2.30 \text{ V}$ is due to conversion of higher order polysulphides to lower order polysulphides (I peak) and $\sim 2.41 \text{ V}$ & $\sim 2.40 \text{ V}$ is due to the conversion of lower order polysulphides to sulphur (II peak) for the MWCNT and HMC-1, respectively (Zhaoxia Cao et al., 2016; Su et al., 2012a). Oxidation and reduction peak position shows the slight difference from the OPCSC cathode films with a bare separator. Oxidation peak shift to lower potential and reduction peaks shift to higher potential indicates the enhanced electrochemical kinetics of the reactions which indicates separator coating has a positive impact towards the LSB performance (Y. Peng, Y. Zhang, Y. Wang, et al., 2017; Yunbo et al., 2015). The oxidation and reduction peak positions are nearly the same in the succeeding scan processes indicating the enhanced cycling stability and reactive reversibility of the cathode material. It is observed an increase in current density when HMC-1 as separator coating, attributed to more active material utilization than MWCNT coating. In addition the coating act as a second current collector and improves the electrochemical performance (Shao et al., 2016).

Figure 6.13 (c and d) represents the GCD experiments of OPCSC cathode at a 0.1C rate with MWCNT and HMC-1 coated separators. GCD profile of 1, 2,

25, 50, 75 and 100th charge-discharge curves with two reductions and one oxidation plateau is displayed. An improved initial capacity is observed compared to the cells with bare separator, 1203 mA h g⁻¹ and 1213 mA h g⁻¹ for MWCNT and HMC-1 coated separator cells, respectively. The coating acts as a second current collector and enhances the active material utilization which reflects in the initial discharge capacity (Yibo He, Qiao, et al., 2018). MWCNT coated separator gives 13.2% capacity degradation in the second cycle whereas only 5.2% for HMC-1. It is due to the higher surface area of the HMC-1 which can adsorb more quantity of PSs during the charge-discharge process and restrict the movement towards the anode. When the cycle number turns to 100, the discharge capacity becomes 900 mA h g⁻¹ displaying 74.8% capacity retention with respect to the initial discharge capacity for MWCNT coated separator. While the HMC-1 coated separator depicts a reversible capacity of 1033 mA h g⁻¹ demonstrating 85% capacity retention with respect to initial discharge capacity. Better (10.2%) capacity retention in the HMC-1 modified separator compared to MWCNT modified separator is due to the microporous structure along with N, O doping, effectively restricts the movement of PSs towards the anode side and allows the transportation of Li⁺ ion. The overlapped charge-discharge plateaus in all 100 cycles, indicates the extremely high electrochemical stability of the HMC-1 coated separator. The HMC-1 coated separator exhibits lower voltage separation ($\Delta E=0.17$ V) than MWCNT coated ($\Delta E=0.19$ V) suggesting lower polarization and enhanced reaction kinetics during the charge-discharge process (Shao et al., 2018). The better electrochemical performances and capacity retention are due to the lone pairs of pyridinic N and pyrrolic N which helps to interact with LPSs during the discharge process and retard the movements of the PSs in HMC-1. Similarly, lone pairs of O in the C-O bonds also bonded to the LSPs, such type of interactions are absent in the case of MWCNT. In addition to this, the high surface area of the HMC-1 helps to adsorb more quantity of PS during the cycling process.

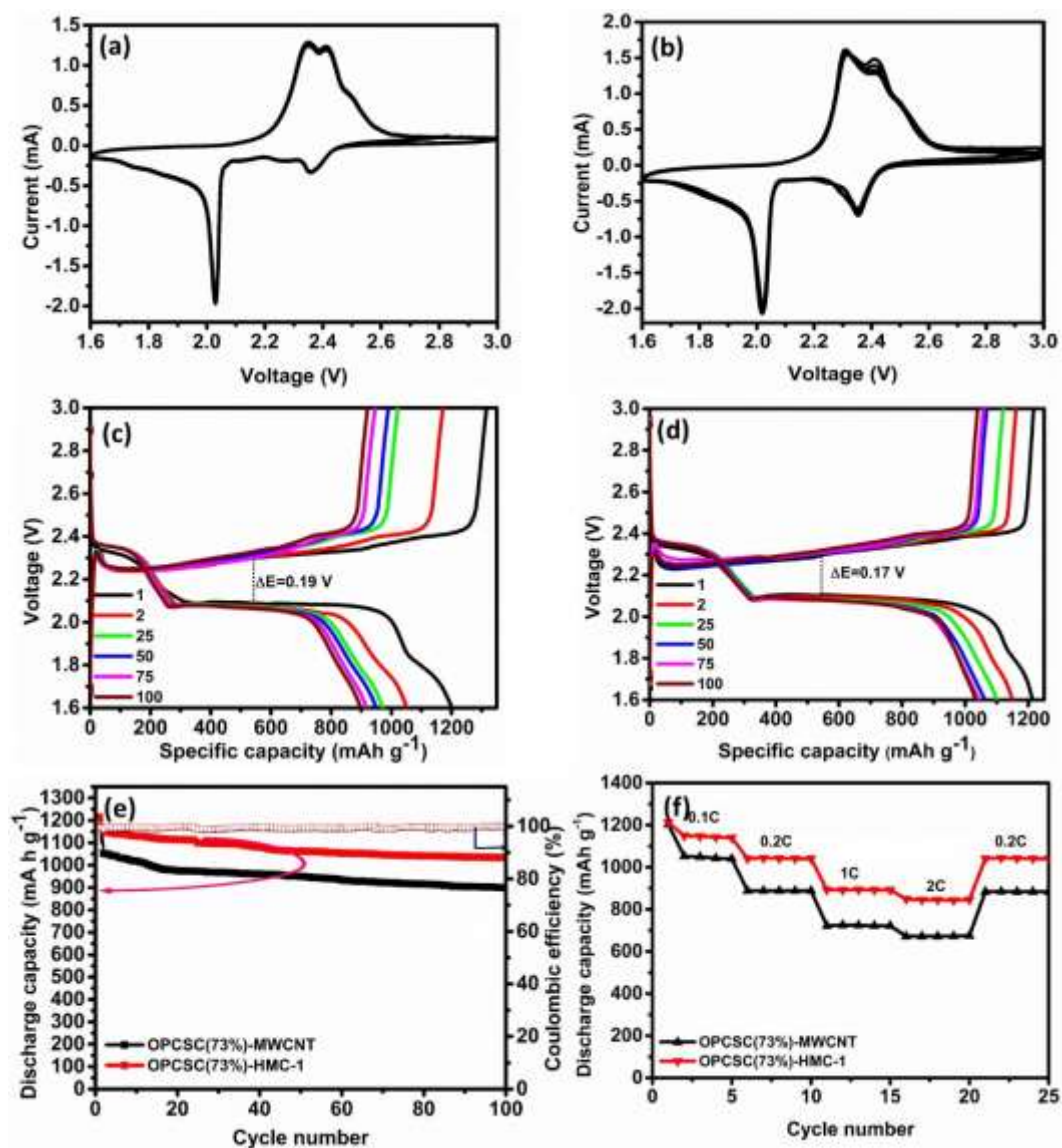


Figure 6.13. CV of the OPCSC-73% with separator coating (a) MWCNT (b) HMC-1 GCD curves of OPCSC-73% with separator coating (c) MWCNT (d) HMC-1 (e) Cyclic stability performances and coulombic efficiency and (f) Rate capability studies at different C-rate

Figure 6.13 (e) shows the cycle performance of the OPCSC cathode using MWCNT and HMC-1 coated separators at the 0.1C rate. A capacity decay of 0.66% per cycle and less than 100% coulombic efficiency is observed for cells with MWCNT coated separator due to imperfect charging cycle. The sp^2 carbon network help to transport Li^+ ion in a faster rate in MWCNT coated separator, but PSs detach easily during the discharge process (Chang et al., 2015). However, HMC-1 coated separator displays a capacity decay of 0.17 % with $\sim 99\%$ coulombic efficiency. The rate capability studies of MWCNT and HMC-1 coated separator with OPCSC

cathode film at various current densities are shown in Figure 6.13 (f). MWCNT coated separator with OPCSC cathode delivers the discharge capacity of 1202, 888, 722 and 678 mA h g⁻¹ at 0.1C, 0.2C, 1C and 2C, respectively. When the current density is decreased to 0.2C, it exhibits a discharge capacity of 884 mA h g⁻¹ with 99.5 % capacity retention. While the cell with HMC-1 coated separator gives 1213, 1041, 893 and 849 mA h g⁻¹ at the current densities of 0.1C, 0.2C, 1C and 2C, respectively. It delivers the discharge capacity of 1040 mA h g⁻¹ when the current density returned back to 0.2C rate and 99.9% capacity retention indicating better dynamic electrochemical stability. The capacity retention of the OPCSC cathode film with MWCNT/HMC-1 modified separator are very close to the literature reported previously. Table 6.3 gives the comparison of the capacity and cyclic performance of the HMC-1 modified separator and other heteroatom modified separators.

To better understand the enhanced electrochemical performance of the cell with HMC-1 coated separator, EIS was employed. Figure 6.14 (a) shows the EIS of the OPCSC cathode films with/without separator modifications before 100 cycles and Figure 6.14 (b) gives the equivalent circuit. Figure 6.14 (c) gives EIS analysis of OPCSC cathode films after 100 cycles at OCV voltage and its inset showing the corresponding equivalent circuit. The R_{ct} and ion diffusion resistance for OPCSC (61%) and OPCSC (73%) with bare separator are higher than that of the modified separator with OPCSC (73%) cathode film before and after cycling, indicates the better reaction kinetics during the electrochemical process (Table 6.4). The significant decrease in impedance in the cell with HMC-1 coated separator than the MWCNT coated separator attributing to the heteroatom doped porous structure and sp² conductive skeleton which facilitates charge transfer (Chang et al., 2015). The decrease in charge transfer resistance and diffusion resistance after cycling attributed to the fact that the redistribution of sulphur onto the porous carbon, which helps to mitigate PS species and effective diffusion of ions throughout the cathode (Raghuveer et al., 2018; G. Ren et al., 2016).

Table 6.3: Comparison of capacity retention of LSB with heteroatom-doped carbon modified separator

Sl. no	Material	Initial discharge capacity (mA h g ⁻¹)	Final discharge capacity (mA h g ⁻¹)	Cycles	C Rate	Capacity retention (%)	References
1	Functionalized carbon nanotube	1057	570	400	0.5	54	(Ponraj et al., 2017)
2	N doped carbon sphere	1656	542	500	1	33	(Zhian Zhang et al., 2015)
3	N/S/O tri-doped tuna bone derived carbon	1397	1044	100	0.2	75	(F. Ai et al., 2017)
4	rGO	733	519	100	1	71	(P. Zhu et al., 2018)
5	rGO	1067	878	100	0.2	82	(W. Lin et al., 2015)
6	GO	920	700	100	0.1	76	(J.-Q. Huang et al., 2015)
7	N/P co-doped carbon	1387	930	200	0.2	67	(P.Zeng, Huang, Zhang, Zhang, et al., 2018)
8	Fe/N co-doped carbon nanofiber and graphene	994.6	601.9	500	0.5	60	(X. Song et al., 2018)
9	O doped carbon/rGO	922.5	601.8	600	1	65	(Linlin Zhang et al., 2018)
10	Co/N co-doped carbon nanofiber	865	616	500	0.5	71	(G. Chen et al., 2018)
11	B doped rGO	902	367	400	0.1	41	(P. Han and Manthiram, 2017)
12	N doped rGO	856	435	400	0.2	80	(P. Han and Manthiram, 2017)
13	N/S co-doped carbon	1049	690	500	1	66	(K. Yang et al., 2018)
14	B/N/S tri doped activated carbon nanofiber	1166	881	700	0.3	75	(M. Chen et al., 2018)
15	N doped hierarchical graphene	1415	1092	100	0.3	77	(Q.Li et al., 2018)
16	Sulphonated carbon black	1262	955	100	0.1	75	(F. Zeng et al., 2016)
17	N doped carbon from crab shell	1301	971	100	0.1	75	(Shao et al., 2017)
18	S doped microporous carbon	1544	976.6	200	0.2	63	(J. Yang et al., 2016)

19	B-rGO	1227.8	663.6	300	0.1	54	(F. Wu et al., 2016)
20	S/N Co-doped graphene	770	612	250	2	79	(L. Wang et al., 2016)
21	N doped microporous carbon	1051	591.6	500	0.5	56	(Xiangyang Zhou et al., 2017)
22	N/S hierarchical porous biomass carbon	1549	947	100	0.1	61	(S. Jiang et al., 2019)
23	N/S mesoporous carbon using egg shell	1125	653	100	0.1	58	(X. Yuan, Wu, et al., 2017)
24	Carbon nitride	990	829	200	0.2	84	(Huangfu et al., 2018)
25	N rich hierarchical carbon sponge	1525	1128	100	0.5	74	(Zhen et al., 2018)
26	N doped porous carbon	1426	866	200	0.2	61	(Q. Wang et al., 2018)
27	MWCNT	1203	900	100	0.1	74.8	Our work
28	HMC-1	1213	1033	100	0.1	85	Our work

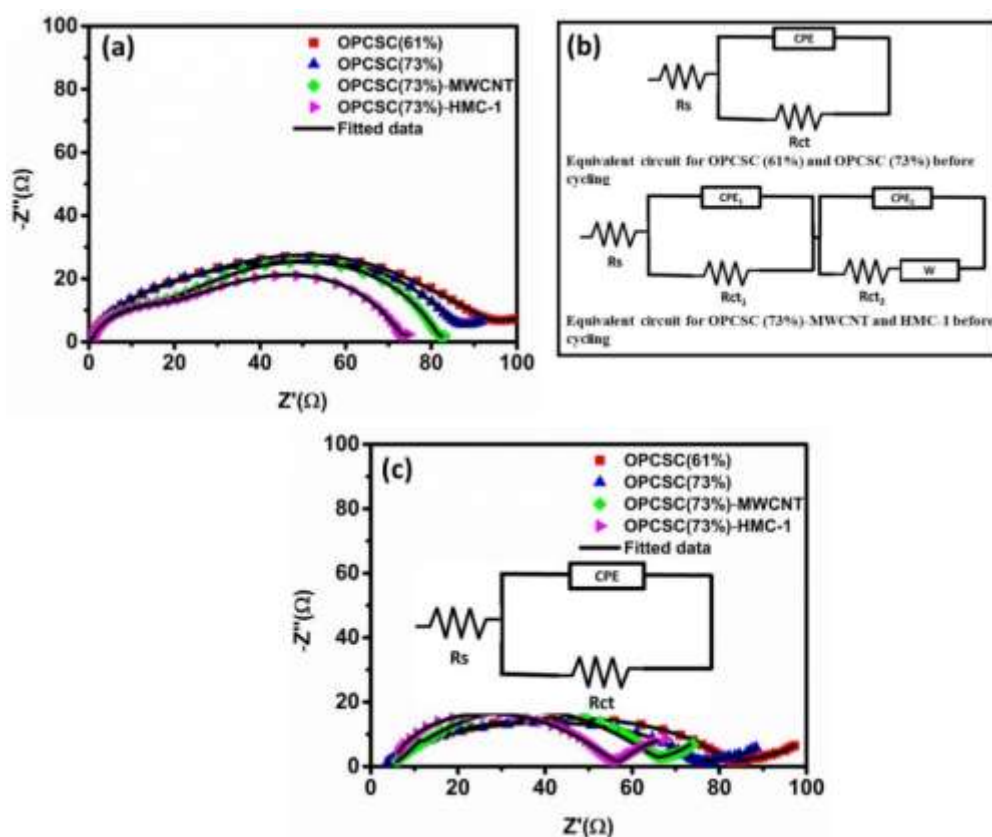


Figure 6.14. Electrochemical performances of OPCSCs, MWCNT, HMC-1 separator coating (a) EIS analysis of the electrodes before discharge (b) fitted equivalent circuit for before cycling (c) EIS analysis of the electrodes after 100 cycles at the OCV [inset: equivalent circuit]

In the case of cells with coated separator (before cycling) it can be seen a semi-circle in the middle frequency region is due to the charge transfer resistance (R_{ct1}) at the carbon and the electrolyte (Figure 6.14 (a and b)) (Y. Peng, Y. Zhang, J. Huang, et al., 2017; Y. Tan et al., 2017). After cycling, the small semicircle at the high frequency region is vanished, due to the non-availability of free active carbon sites, owing to the physical /chemical adsorption of active material during the charge-discharge process. So it is confident to say that HMC-1/MWCNT coated separators adsorb the PSs in addition to enhancing the interfacial charge transfer. It is further confirmed by the low ion diffusion resistance after charge discharge process due to the accessibility of electrolyte onto the carbon network.

After 100th charge-discharge cycle, the cell was disassembled in the Ar-filled glove box. The morphology of the OPCSC cathode film was characterized by SEM analysis. Figure 6.15 shows the SEM images of fresh cathode surface of OPCSC film and cycled cathode films. Remarkable differences can be seen between cycled OPCSC cathode film by using the bare separator (Figure 6.15 (b)) and fresh cathode surfaces (Figure 6.15 (a)). After 100 charge-discharge cycles, normal cathode shows dense solid layer on the surface. The solid layer is due to gradual aggregation of insulated Li_2S on the surfaces of the cathode during the prolonged cycles which could be the reason for the lowest electrochemical performance of the OPCSC cathode film with a bare separator. But there is no thick solid layer is observed in the OPCSC cathode surfaces with MWCNT/HMC-1 coated separator (Figure 6.15 (c and d)). Here the separator coating effectively block the dissolution of PS into the electrolyte and thereby reduces the irreversible deposition of Li_2S in the OPCSC cathode surfaces. It can be seen that very small morphological differences between the OPCSC cathode film of MWCNT and HMC-1 coated separator cases (S. Wei et al., 2011; Miao et al., 2013; Z. Liu et al., 2017). It is because, the HMC-1 have higher surface area and micro pore size distribution than the MWCNT, which effectively adsorb more PS and thereby prevent its dissolution than MWCNT coated cases. In addition to that the presence of N, O heteroatoms anchor the LPSs and enhances the electrochemical performance which maintain its structural integrity with fresh OPCSC cathode film.

Table 6.4: Equivalent circuit for the OPCSC-73% cathodes with MWCNT and HMC-1 coated separator before and cycling

Material description	R_s (Ω)	$CPE_1 \times 10^{-5}$ (Ω^{-1})	R_{ct1} (Ω)	$CPE_2 \times 10^{-6}$ (Ω^{-1})	R_{ct2} (Ω)	Y_0 ($\Omega^{-1}s^{1/2}$)
OPCSC (61%) before cycling	0.45	-	-	3.02*	93.7**	0.0017
OPCSC (73%) before cycling	0.70	-	-	6.29*	87.1**	0.0018
OPCSC (73%) - MWCNT before cycling	0.30	8.10	18.06	8.24*	63.6**	0.10
OPCSC (73%) - HMC-1 after cycling	0.30	6.52	17.43	5.9	56.05	0.13
OPCSC (61%) after cycling	4.27	-	-	1.36*	7.73**	0.184
OPCSC (73%) after cycling	4.4	-	-	1.08*	0.6**	0.193
OPCSC (73%) - MWCNT after cycling	6.39	-	-	2.6*	58.2**	0.263
OPCSC (73%) - HMC-1 after cycling	6.12	-	-	3.5*	50.2**	0.259

*CPE **Rct

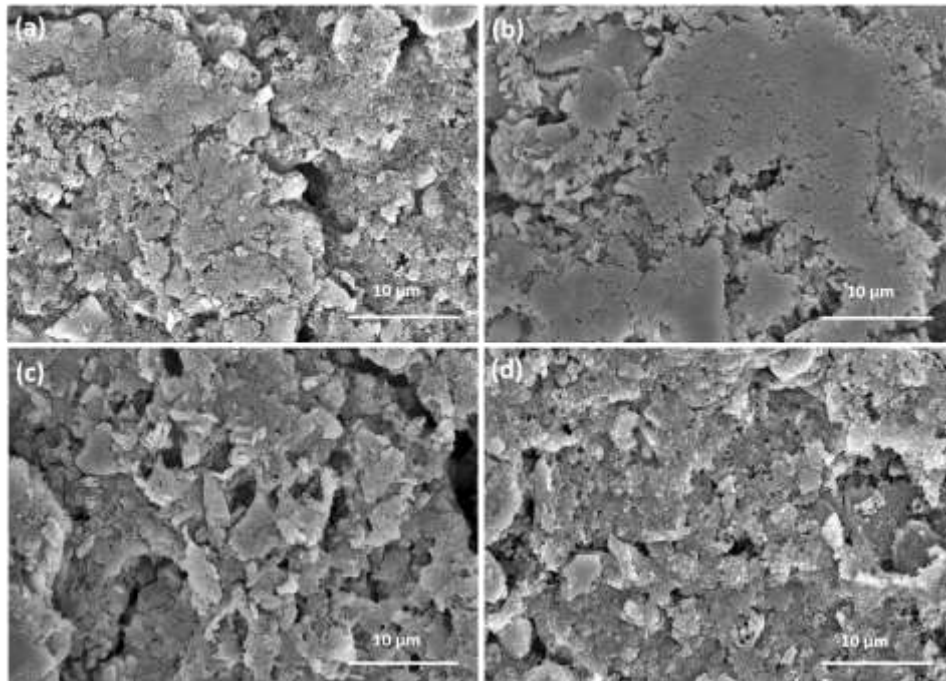


Figure 6.15. SEM of OPCSC (73%) cathode film (a) before cycling (b) With bare separator after 100 cycles (c) With MWCNT modified separator after 100 cycles and (d) With HMC-1 modified separator after 100 cycles

To estimate the interaction between carbon materials and LPS, adsorption tests were carried out using the procedure described in chapter 4 and section 4.2.2.3 (Figure 6.16). The yellow coloured LPS solution was taken in bottle A (Figure 6.16 (a)). An equal amount of LPS solution is taken in bottle B, C and added an equal amount (20 mg) of MWCNT and HMC-1, respectively. When HMC-1 added to the bottle C, the coloured solution became completely transparent in 15 min, shown in Figure 6.16 (c). While the bottle B displays a pale yellow colour (Fig 6.16 (b)). This point out better adsorption capability of HMC-1 compared to MWCNT (Jin et al., 2017; Y. Peng, Y. Zhang, J. Huang, et al., 2017; Xia et al., 2017).

The improved electrochemical performance of the HMC-1 over MWCNT is due to the (1) morphology of the HMC-1 facilitate the PS adsorption (2) higher surface area and lower pore volume, surface area helps to adsorb more quantity of sulphur (3) Micro pore size distribution: retards the movement of PSs and allows for Li-ion (4) N and O functionalities doped on porous carbon network. As a result, HMC-1 modified separator display stable cyclability by confining PSs.



Figure 6.16. Digital images of the polysulphide adsorption test (a) Lithium polysulphide solution (b) Lithium polysulphide mixed with MWCNT after 15 min and (c) Lithium polysulphide mixed with HMC after 15 min

The excellent electrochemical performance of the HMC-1 is further evidenced by the XPS analysis of the coated separator before and after 100 charge-discharge cycles (Figure 6.17). Before analysis, XPS survey scan reveals the presence of C1s, N1s, and O1s from HMC-1. F1s from PVDF is observed. The emergence of new Li1s, S2s and S2p with high intensity after the 100 cycles display

the evidence for the adsorption of PS on the HMC-1 via Li-N and Li-O bonds (Aurbach et al., 2009; X. Fan et al., 2018; Seh et al., 2014). Figure 6.17 (b) shows the high-resolution Li1s spectrum which can be fitted by three components Li-S (55.2 eV), Li-N (56.2 eV) and Li-O (56.6 eV) (X. Fan et al., 2018; Xia Li and Sun, 2014; Aurbach et al., 2009; F. Chen et al., 2018; X. Fan et al., 2018; Son et al., 2015). These results suggest that N and O functionalities of HMC-1 contribute to mitigate PS shuttle by chemical interaction which enhances the overall electrochemical performance of the Li-S cell.

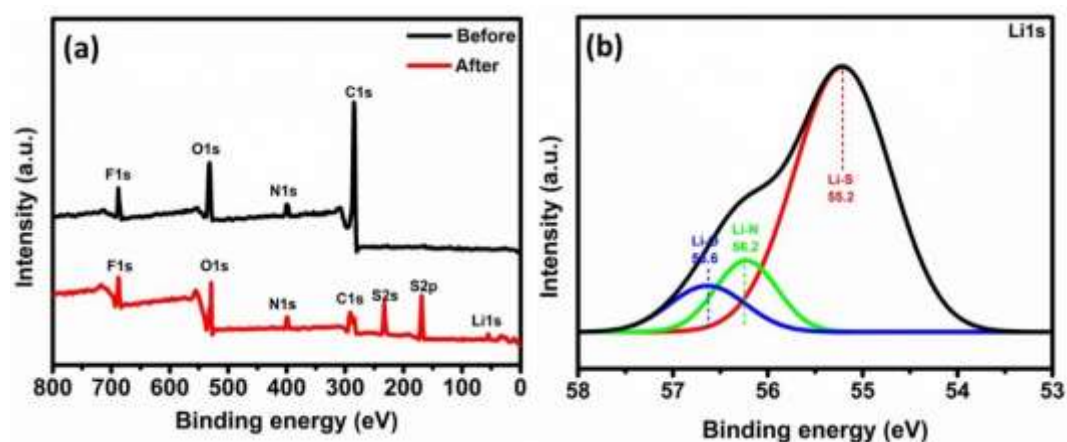


Figure 6.17. (a) Survey scan analysis of HMC-1 coated separator before and after 100 charge-discharge cycles and (b) High-resolution Li1s spectrum of coated separator after 100 cycles

6.4 Conclusion

A facile method was developed to improve the electrochemical performance by coating heteroatom-doped carbon material slurry on the cathodic side of the separator by doctor blading. The Li-S cells with HMC-1 coated separator exhibit better rate capability and cycle stability than the MWCNT coated separator. This coating facilitates Li-ion transport due to its microporous structure and serves as upper current collector also. The surface area of HMC-1 ($969 \text{ m}^2 \text{ g}^{-1}$) provides more active adsorption sites for PS adsorption along with pyridinic N, pyrrolic N and O functionalities. OPCSC (73%) with HMC-1 coated separator exhibits an initial capacity of 1213 mA h g^{-1} and sustains a capacity of 1033 mA h g^{-1} with 85% capacity retention at the 0.1C rate. The thin layer coating of HMC-1 (1.2 mg cm^{-2} and $15 \text{ }\mu\text{m}$) alleviate the migration of PSs towards the anode and enhances the

capacity retention. Therefore, employing HMC-1 modified separator is a promising way to improve the performance of LSB.

CHAPTER 7

HONEYCOMB DERIVED CARBON FOR LITHIUM–SULPHUR BATTERY

LSB received global attention due to its high theoretical capacity of sulphur 1675 mA h g⁻¹. However, these low electrical conductivity of sulphur, dissolution of PSs in the electrolyte and PS shuttle towards Li anode restricted its reach to the market. The carbon-based interlayer between the sulphur cathode and the separator have been demonstrated to be a simple but powerful means to promote the electrochemical performances of the LSBs. In this chapter, honeycomb derived carbon (HC) is used as conductive host for sulphur (HCS). HCS (80%) gives a high reversible capacity of 1101 mA h g⁻¹ after 200 cycles at 0.1C rate with 82% capacity retention. A thin coating of HC onto the cathode film (HCS (80%)) yield 92% capacity retention. Here, sulphur is sandwiched between the two conductive hosts. Therefore, the HCS (80%) composite electrode with interlayer (HCS (80%)-HC) exhibits great progress in both cycling performance and rate capability as compared to bare cathode with HCS even though the sulphur content of the HCS composite is as high as 80%. Thus HCS (80%)-HC would be a potential combination for high performance LSB.

7.1 Introduction

LSBs have potential applications in high energy density devices due to the low cost and abundance of sulphur. Extensive research has been carried out to make it commercially viable by restricting the movement of PSs and its migration across the separator during the charge-discharge process (Chi-Hao et al., 2016; Yibo He, Chang, et al., 2018; Song et al., 2013). Various approaches observed in the literature for the protection of lithium metal anode, preparation of new cathode materials, modification of cathodes using additives and interlayers, electrolyte modifications, optimisation and modification of separators (N. Deng et al., 2016; X. Fan et al., 2018; Z.-L. Xu et al., 2018; H. Zhao et al., 2018). One of the common approach to enhance the electrochemical kinetics of the cathode is the use of porous carbon as sulphur host (Schuster et al., 2012). The electron transport is facilitated by the interconnected carbon network and the porosity of the carbon material to restrain the PSs during the presence of cycling through physical interactions (Z.-L. Xu et al., 2018). However, the weak physical interactions of non-polar carbon with polar

PSs cannot restrict the movement of PSs toward the separator and to the anode effectively which is one of the reason for the corrosion of Li metal anode and degradation in the battery performances (H. Zhao et al., 2018). Hence, the introduction of heteroatom into the carbon matrix leads to chemical interactions with the PSs and restrict the movement within the cathode region. Thus introduction of heteroatoms like N, O and the polar metal oxides into the carbon substrate, implies cooperative effect on the LPSs (S. S. Zhang, 2015).

In this chapter, honeycomb is chosen as carbon source which is inherently doped with N, O and silica (SiO_2) in the carbon network. SiO_2 is a widely studied material for energy storage applications. Few systems investigated for LSB applications are Si/ SiO_2 /carbon sphere, SiO_2 /rGO, SiO_2 /activated carbon nanofiber, SBA-15/porous carbon, ternary graphene/ SiO_2 , mesoporous graphene/ SiO_2 , hierarchical porous graphene/carbon/ SiO_2 , porous carbon/ thin layer of SiO_2 coating (Campbell et al., 2015; Ji et al., 2011; Jörg et al., 2012; K. H. Kim et al., 2014; J. Li et al., 2018; Rehman et al., 2016; P. Wei, Fan, Chen, Chen, et al., 2016).

To enhance the performance of cathode further, modification in the cell configuration is another strategy adopted in the research reports (Niu, Lv, et al., 2016). Even though heteroatom doped porous carbon reduces the shuttling effect, due to the presence of concentration gradient during cycling, PS diffusion from the cathode is unavoidable. Recently an additional interlayer has been introduced in between the sulphur cathode and separator to capture the PS and to avoid the direct contact between the cathode and the bulk electrolyte. The interlayer includes microporous carbon paper (Su and Manthiram, 2012b), free-standing MWCNT (Su and Manthiram, 2012c), mesoporous carbon layers (Balach et al., 2015) and rGO film (X. Wang et al., 2013) which effectively block the PS migration only through a physical adsorption of LPSs (Xi et al., 2015). However, the heteroatom-doped carbon material, heteroatom-containing polymer and metal oxides/metal sulphides can effectively capture the LPSs through chemical bonds (Zhengjiao Liu et al., 2018; Y. Peng, Y. Zhang, Y. Wang, et al., 2017). TiO_2 /graphene, V_2O_5 modified carbon nanofiber and MnO_2 anchored carbon nanofiber (M. Liu et al., 2017; Zhengjiao Liu et al., 2018; Z. Xiao et al., 2015) reported as a functional interlayer

for LSBs. An ideal protection layer have the following functions (1) can effectively block the migration of LPS (2) the thin layer of coating able to transport of Li-ion and (3) a conductive layer can act as an upper current collector (Niu, Lv, et al., 2016). An interlayer composed of heteroatom and metal oxides/metal sulphide like polar materials doped carbon is an effective approach to address the PS issues. Hence, in this chapter a multi-functional coating on the HCS cathode is adopted, to prevent the loss of active material. SiO₂ along with N, O heteroatoms doped activated honeycomb derived carbon material (HC), is used as an interlayer for the HCS cathode. The coated layer (interlayer) acts as an upper current collector, PS warehouse, allow the transport of the Li⁺ ion and avoid the direct contact between the cathode and the electrolyte. In effect, sulphur is sandwiched between two conductive hosts and offer better electrochemical performance compared to HCS cathode.

7.2 Materials and Methods

7.2.1 Materials

Raw honeycomb material was obtained from IIST campus, Thiruvananthapuram, Kerala, and all other chemicals used as procured (section 2.2.1 and 4.2.1)

7.2.2 Material synthesis

7.2.2.1 Preparation of porous carbon

Honeycomb was dried, crushed and ground into powder. Then the powder was dried at 100 °C for 24 hours. This powder was used as activated carbon precursor. Chemical activation was done by mixing precursor with zinc chloride of 1:2 ratio in 100 ml of distilled water. After drying it was heated at different temperatures starting from 500 °C to 700 °C for 1 hour in a tubular furnace under Ar atmosphere. After that, it was washed with HCl followed by distilled water until the filtrate becomes neutral. The activated carbon from the honeycomb (HC) was dried in a vacuum oven at 70 °C and stored in a desiccator.

7.2.2.2 Preparation of carbon-sulphur composites

Honeycomb derived carbon-sulphur composites (HCS) were prepared by melt diffusion method as discussed in section 2.2.2.2. Two HCS combination are prepared. Figure 7.1 is the schematic illustration of the preparation of the HC and HCS.

7.2.2.3 Preparation of HC coated cathode

HC is used for the cathode surface coating (interlayer) without any further purification. A mixture of HC and PVDF in a weight ratio of 9:1 is mixed with NMP as a solvent to form the slurry, which was then coated on the cathode film and was dried under vacuum at 70 °C for 24 hours.

7.2.3 Material characterization

The materials prepared were characterized as described in section 2.2.3. The electrochemical evaluation of the electrode was carried out by fabricating coin cells as mentioned in sections 2.2.4 and 2.2.5. The areal mass loading on the composite electrode was $\sim 2.8 \text{ mg cm}^{-2}$.

7.3 Results and Discussion

7.3.1 Material characterization

Porous carbon was prepared at high temperatures of 500, 600 and 700°C in an inert atmosphere with precursor and the ZnCl_2 in the ratio of 1:2. The nitrogen adsorption-desorption isotherms of the activated carbons prepared at various carbonization temperatures are shown in Figure 7.2 (a). HCs exhibit Type I and Type IV N_2 adsorption-desorption isotherms. The rapid increase in the uptake of N_2 at relatively low pressure followed by nearly horizontal plateau at higher relative pressures indicate type I isotherm which is associated with microporous structure (HC-500 °C). A small hysteresis loop at intermediate and high relative pressure associated with a monolayer–multilayer adsorption followed by capillary condensation in narrow slit-like pores indicates mesoporosity in the material (HC-

600 °C & HC-700 °C) which is a type IV isotherm according to IUPAC nomenclature. It is observed that N₂ uptake increases for HC-600 °C compared to HC-500 °C due to the gradual development of pores when the carbonization temperature increases, as a result surface area and pore volume increases. After that, the surface area and pore volume are reduced when the temperature is raised to HC-700 °C due to the deterioration of the porous structure (S. Wei et al., 2011; S. Zhang et al., 2014). DFT analysis confirms the well-developed hierarchical porous nature of HC-600 °C & HC-700 °C (Figure 7.2 (b)). BET surface area of HCs increases from 817 m² g⁻¹ to 931 m² g⁻¹ and pore volume is also increased from 0.45 cm³ g⁻¹ to 0.64 cm³ g⁻¹ when activation temperature increases from 500 °C to 600 °C. Surface area and pore volume reduced to 806 m² g⁻¹ and 0.63 cm³ g⁻¹ when temperature was further increased to 700 °C (Table 5.1). The highest surface area carbon with hierarchical porosity (HC-600 °C) is used for sulphur loading and in the following investigations, which is termed as HC instead of HC-600 °C. HC-sulphur composites (HCS) of 70% and 80% were prepared. The surface area and pore volume reduced to 6.66 m² g⁻¹ and 0.029 cm³ g⁻¹ for HCS (70%) and HCS (80%) exhibits a surface area of 5.02 m² g⁻¹ and 0.021 cm³ g⁻¹ (Y. Tan et al., 2017) (Figure 7.2 (a)).



Figure 7.1. Schematic illustration of the preparation of HC and HCS

Table 7.1: Surface area and pore volume of HCs/HCSs

Sample	BET surface area (m ² g ⁻¹)	Total pore volume (cm ³ g ⁻¹)
HC-500 °C	817	0.45
HC-600 °C	931	0.64
HC-700 °C	806	0.63
HCS (70%)	6.66	0.03
HCS (80%)	5.02	0.02

XRD patterns of the HC are shown in Figure 7.2 (c), where sulphur and HC served as the reference. Broad diffraction peak is observed in the case of HC, due to the presence of amorphous nature of carbon and silica (K. et al., 2014; Y. Liang et al., 2012; Singh et al., 2014). HCSs show sharp diffraction peaks of sulphur indicating that sulphur is successfully incorporated into the carbon matrix during the melt diffusion process. The crystalline phases are well matched with the orthorhombic sulphur (JCPDS 00-008-0247). It is obvious that the intensity of sulphur diffraction peaks are less in HCS (70%) than HCS (80%) (Gu et al., 2015; W. G. Wang et al., 2014).

Raman spectra of HC and HCSs (Figure 7.2 d) consists of D band at 1336 cm⁻¹ and G band at 1595 cm⁻¹. The D band ascribed to the disordered amorphous carbon and G band is due to the presence of graphitized carbon. A distinct amorphous silicon oxide broad band can be seen at 780 cm⁻¹ which indicates the presence of silica along with the carbon. I_D/I_G ratio for HC is 0.9 which indicates the disordered amorphous carbon structure of the material (Dresselhaus et al., 2007). In the case of HCSs, the I_D/I_G ratio is increased due to the enhancement of a defect in the carbon structure when sulphur loading increases. The inset shows the Raman spectra of crystalline sulphur, exhibits three peaks at 148 cm⁻¹, 214 cm⁻¹ and 470 cm⁻¹ (Ward, 1968). The intensity variations in the sulphur bands between HCS (70%) and HCS (80%) indicate the presence of sulphur on the surface in addition to the infused sulphur into the porous network. The observed sulphur peaks in HCSs indicate the successful incorporation of sulphur in the carbon matrix (Niu et al., 2015; Xuebing Yang et al., 2015).

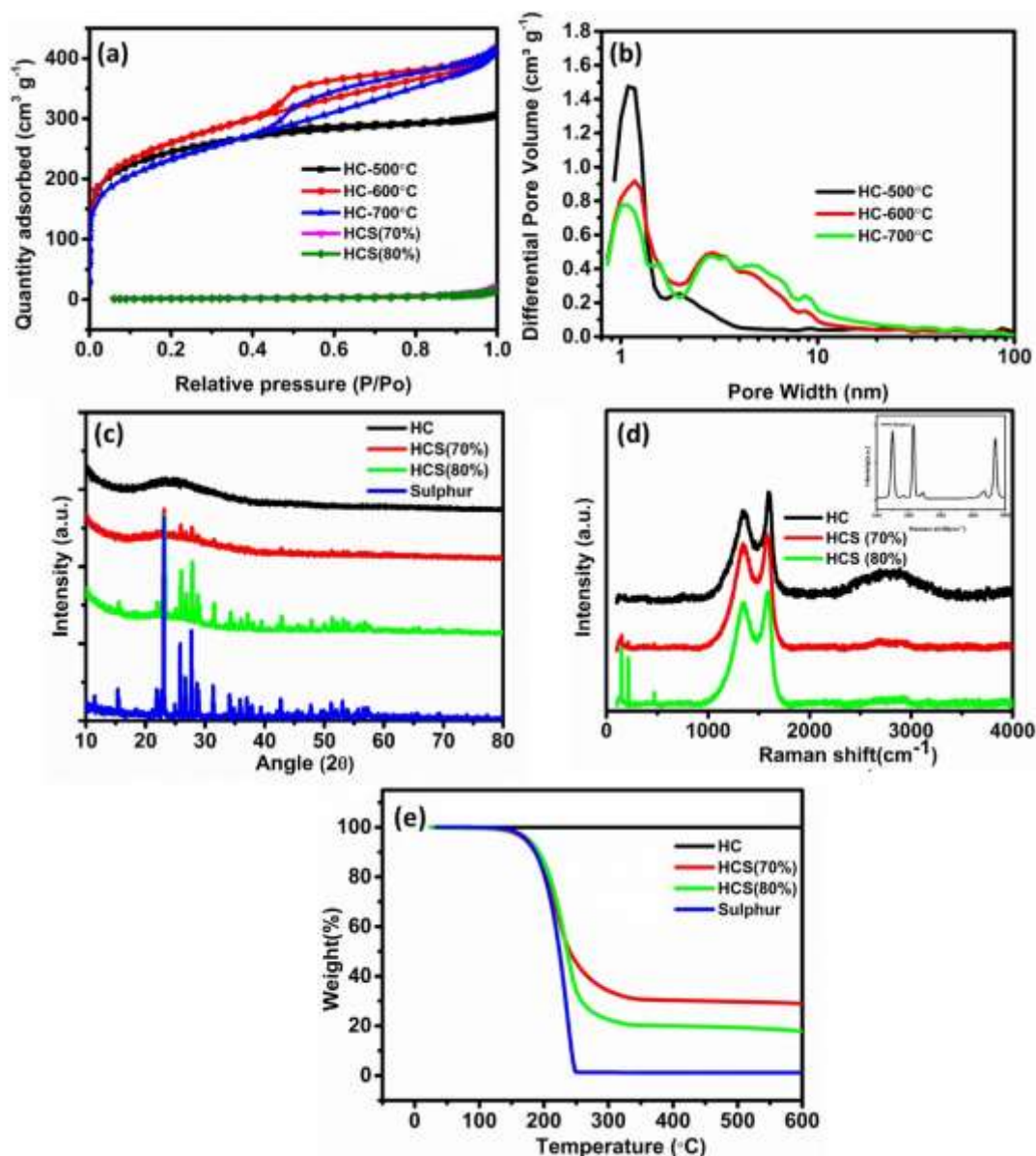


Figure 7.2. (a) N_2 adsorption/desorption isotherms of HC and HCSs (b) Pore size distribution curves of HC (c) XRD pattern for sulphur and HCSs (d) Raman spectra of HC, HCSs [inset: Raman spectrum of sulphur] and (e) TGA of HC, HCSs and sulphur

TGA is used to determine the amount of sulphur in the HC and the thermal stability of the HC (Figure 7.2 (e)). TGA of HC is quite stable up to 600 °C. The weight loss in the TGA curves of HCSs is observed in the temperature range 116 °C–350 °C. The amount of sulphur in the HC is calculated to be 70% and 80% with respect to the elemental sulphur. The complete evaporation of elemental sulphur occurs at a lower temperature compared to HCSs, due to the well-dispersed sulphur within the porous network (Y. Fu et al., 2012; L. Wang et al., 2013; W. G. Wang et al., 2014).

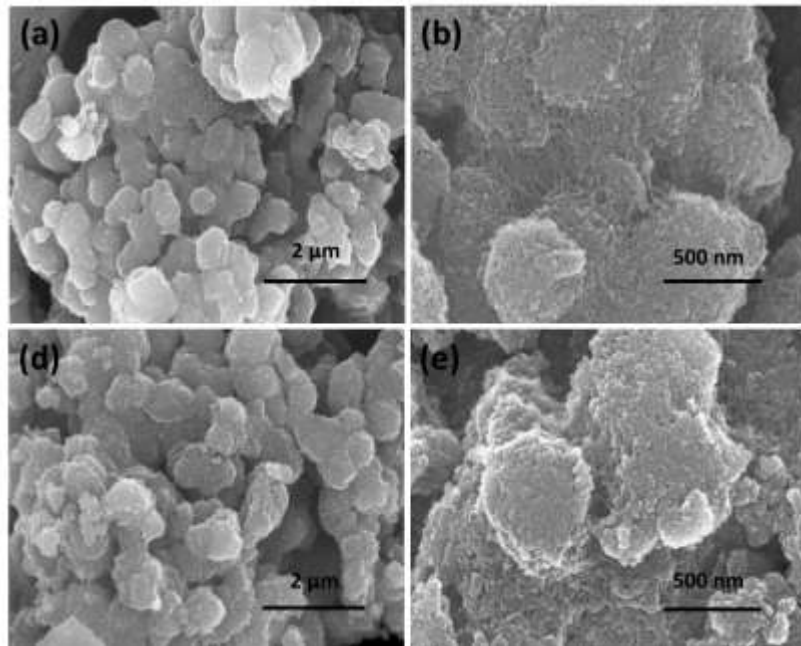


Figure 7.3. SEM Images of (a-b) HC and (c-d) HCS (80%)

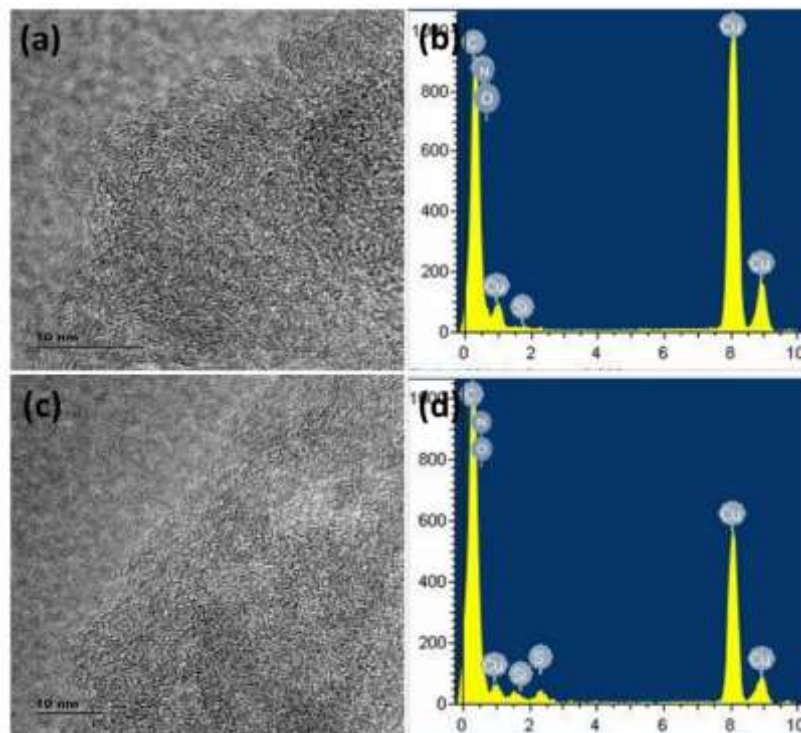


Figure 7.4. TEM Images of (a) HC and (b) EDS analysis of HC (c) HCS (80%) and EDS analysis

The surface morphology of the HC and HCS (80%) composite were characterized by FESEM (Figure 7.3). SEM of HC shows porous particles aggregated morphology (Figure 7.3 (a-b)). Figure 7.3 (c-d) shows the SEM images

of HCS (80%). It can be seen that particle aggregated morphology still maintained after sulphur loading. It is due to the uniform distribution of sulphur throughout the carbon network.

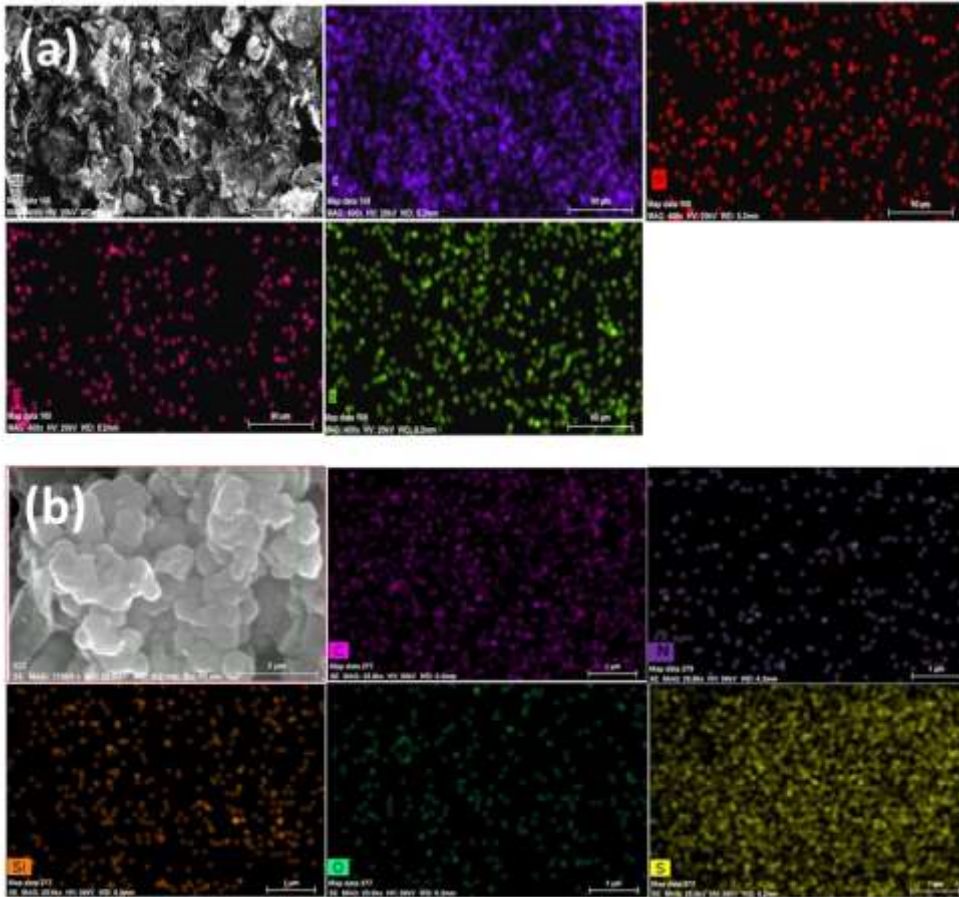


Figure 7.5. Elemental mapping of (a) HC and (b) HCS (80%)

TEM images of the HC (Figure 7.4 (a)) reveals a large number of interconnected pores in the carbon lattice. These morphological characteristics of the HC reveals that the HC has hierarchical porous structure, which corroborate with the DFT pore size distribution analysis.

TEM-EDS confirms the presence of N, O and Si in the carbon material. (Figure 7.4 (b)). Figure 7.4 (c) shows the TEM of HCS (80%) and gives the same microstructure as that of the HC, which indicates the uniform distribution of sulphur in the porous network and it is highly beneficial for the active material utilization of sulphur during the cycling process. TEM-EDS confirms the presence of S, N, O and Si in the HCS network (Figure 7.4 (d)).

Figure 7.5 shows the elemental mapping analysis of HC and HCS (80%), which confirms the presence and distribution of N, O, Si in the HC (Figure 7.5 (a)) and N, O, Si, S in the HCS (Figure 7.5 (b)).

CHNS analysis represents the presence of nitrogen 5.89 % in HC and nitrogen (2.47 %), sulphur (80 %) in HCS (Table 7.2).

Table 7.2: CHNS analysis of HC and HCS

Sample	C (%)	H (%)	N (%)	S (%)	O + Si (calculated) (%)
HC	70	6.26	5.89	-	17.85
HCS (80%)	8.39	0.75	2.47	80	8.39

XPS measurements were carried out by core spectrum analysis followed by high-resolution spectral analysis. The XPS survey scan (Figure 7.6 (a)) reveals the presence of Si2p, Si2s, C1s, N1s and O1s in the HC at 101 eV, 152.4 eV, 283.7 eV, 399 eV and 532.3 eV, respectively. The high-resolution C1s spectrum contains 5 components of peaks (Figure 7.6 (b)), they are C-C bond (284.6 eV) of sp², C-N (285.5 eV), C-O bond (286.2 eV), C=N bond (287 eV) and C=O (289 eV) (X. Yuan, Liu et al., 2017; G. Zhou et al., 2015). The bonding nature of N is well characterized by the high-resolution N1s spectrum. It is separated into 4 peaks at 398.2 eV, 399.9 eV, 400.9 eV and 402.7 eV for pyridine-like N, pyrrole like N, graphitic N and pyridinic nitrogen oxide, respectively (Figure 7.6 (c)) (X. Yuan, Liu et al., 2017; G. Zhou et al., 2015). The high-resolution O1s spectrum (Figure 7.6 (d)) deconvoluted into 4 components: N-O bond (530.3 eV), C-O bond (532.1 eV), C=O bond (532.7 eV) and silicon oxide bond (533.3 eV) (Weinhold and West, 2011; X. Yuan, Liu et al., 2017). In the case of HC, there is overlapping of Si2p_{3/2} and Si2p_{1/2} components providing an asymmetric shape (higher pass energy). The high resolution Si2p spectrum is deconvoluted into two components 101.8 eV (Si-O) and 103 eV (Si=O) (A. Huang et al., 2018; Weinhold and West, 2011) (Figure 7.6 (e)). XPS observations confirm that the HC matrix is enriched with nitrogen, oxygen and silicon functionalities.

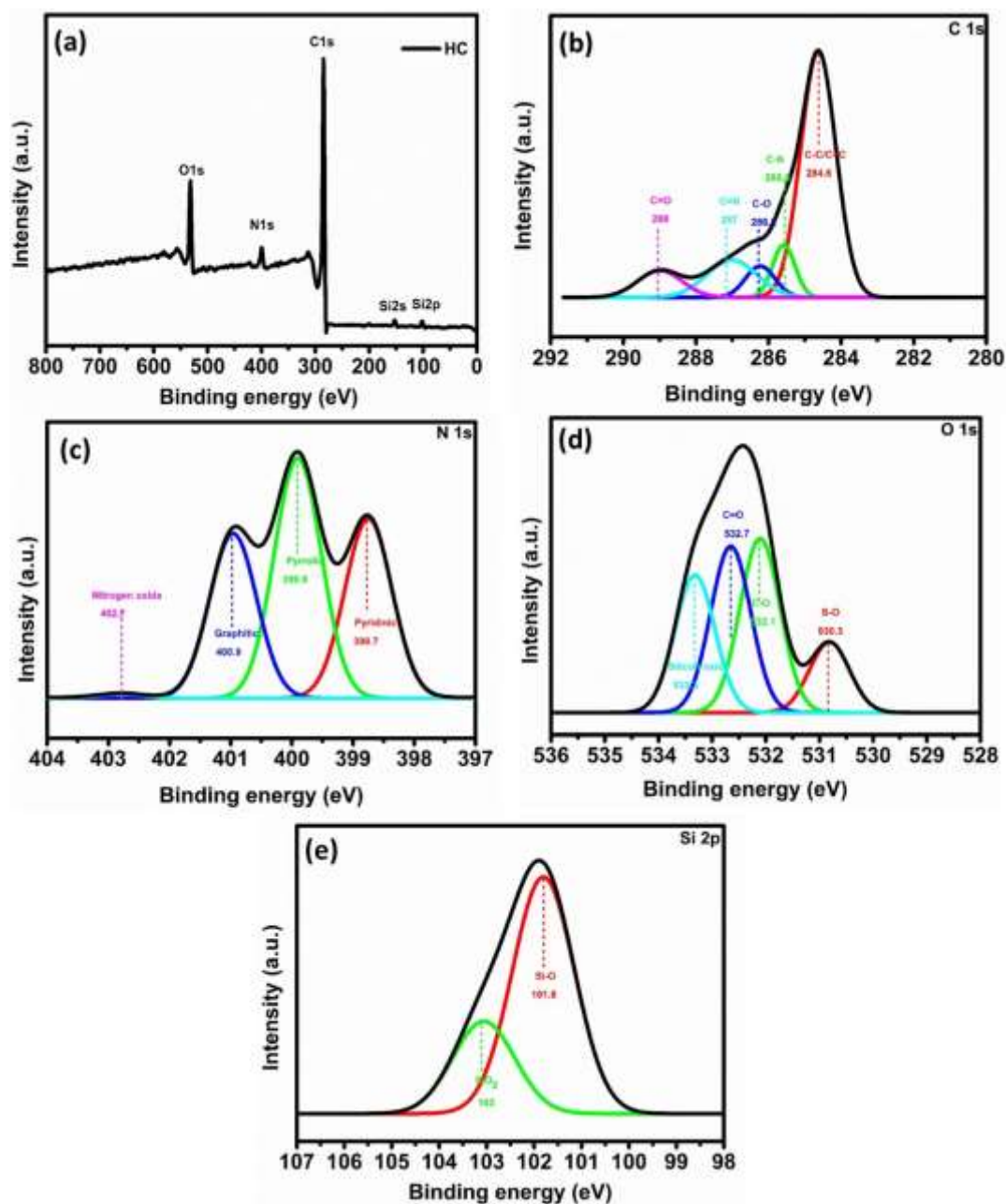


Figure 7.6. XPS analysis of HC (a) Survey scan (b) C1s (c) N1s (d) O1s and (e) Si 2p

Pang et al reviewed the studies that explore the nature and strength of the interaction of functionally modified surfaces, metal oxides and carbide materials with PSs and its effect on cycle life and capacity fading. It is discussed that polar functional groups and metal oxides interact more efficiently compared to non-polar carbon matrix (Pang et al., 2015). Hence, the interaction of oxygen, nitrogen and metal oxide was investigated in detail using XPS analysis of HC after melt diffusion of sulphur (Figure 7.7). The survey scan analysis of HCS (80%) reveals 7 peaks

centred at 103 eV, 163 eV, 163.4 eV, 240 eV 283.7 eV, 400 eV and 533.1 eV for Si2p and Si2s S2p, S2s, C1s, N1s and O1s, respectively (Figure 7.7 (a)). Figure 7.7 (b-f) shows the high-resolution spectra of C1s, N1s, O1s, Si2p and S2p. In the C1s spectra, emergence of new C-S bond is observed in addition to the C-C, C-N, C-O, C=N and C=O bonds in HC, represents the incorporation of sulphur into the carbon matrix (M. Chen et al., 2017; Jing Xu et al., 2016). The high resolution O1s spectra reveals the presence of S-O bond and N1s shows the S-N bonds, which confirms the presence of S and its bonding nature with N and O (Pang et al., 2015; X. Yuan, Liu et al., 2017; L. Zhang et al., 2012). After the sulphur impregnation into the HC matrix, the silicon bonds are slightly shifted (Figure 7.7 (e)), due to the changes in the electronic distribution of Si (Si-O to 162.1 eV and Si=O to 163.3 eV). These changes may be due to the bonding of sulphur with silicon (Hassan et al., 2015; Morgan and Van Wazer, 1973).

The bonding nature of sulphur is further confirmed from the high-resolution spectrum of S2p (Figure 7.7 (f)). It consists of S2p_{3/2} and S2p_{1/2} at 164.9 and 165.1, respectively with an energy separation of 1.2 eV. Each peak is contains three components each, C-S bond (163.7-164.9), S-N (164-165.2) and S-O (164.3-165.5) (Chulliyote et al., 2017a; Y. Hao et al., 2015; Niu et al., 2015; L. Zhang et al., 2012). The existence of C-N, C-O bonds facilitate interatomic interaction between the heteroatoms and PSs, the further movement towards anode surface. The presence of silicon bonds help to restrain the PSs through Si-S bonds or S-O bonds from silicon oxides (X. Fan et al., 2018) S-O (O1s component), S-N (N1s component) and S-O & Si-S (Si2p) can effectively confine the PS movements during the shuttling process. These major changes in the XPS spectra before and after melt diffusion indicates the interaction of sulphur with heteroatoms and modifies the electronic distribution of heteroatoms that is reflected in the binding energy shift (L. Zhang et al., 2012).

The heteroatoms with lone pairs act as Lewis base and it interacts with Li (Lewis acid) during charge-discharge process that helps to anchor PSs (L. Zhang et al., 2012). The O and N functional groups along with silicon oxide additives synergically contribute to enhance the performance of the LSB along with the high

surface area of the carbon material. The elemental composition obtained from the XPS analysis (Table 7.3) is very close to the CHNS analysis.

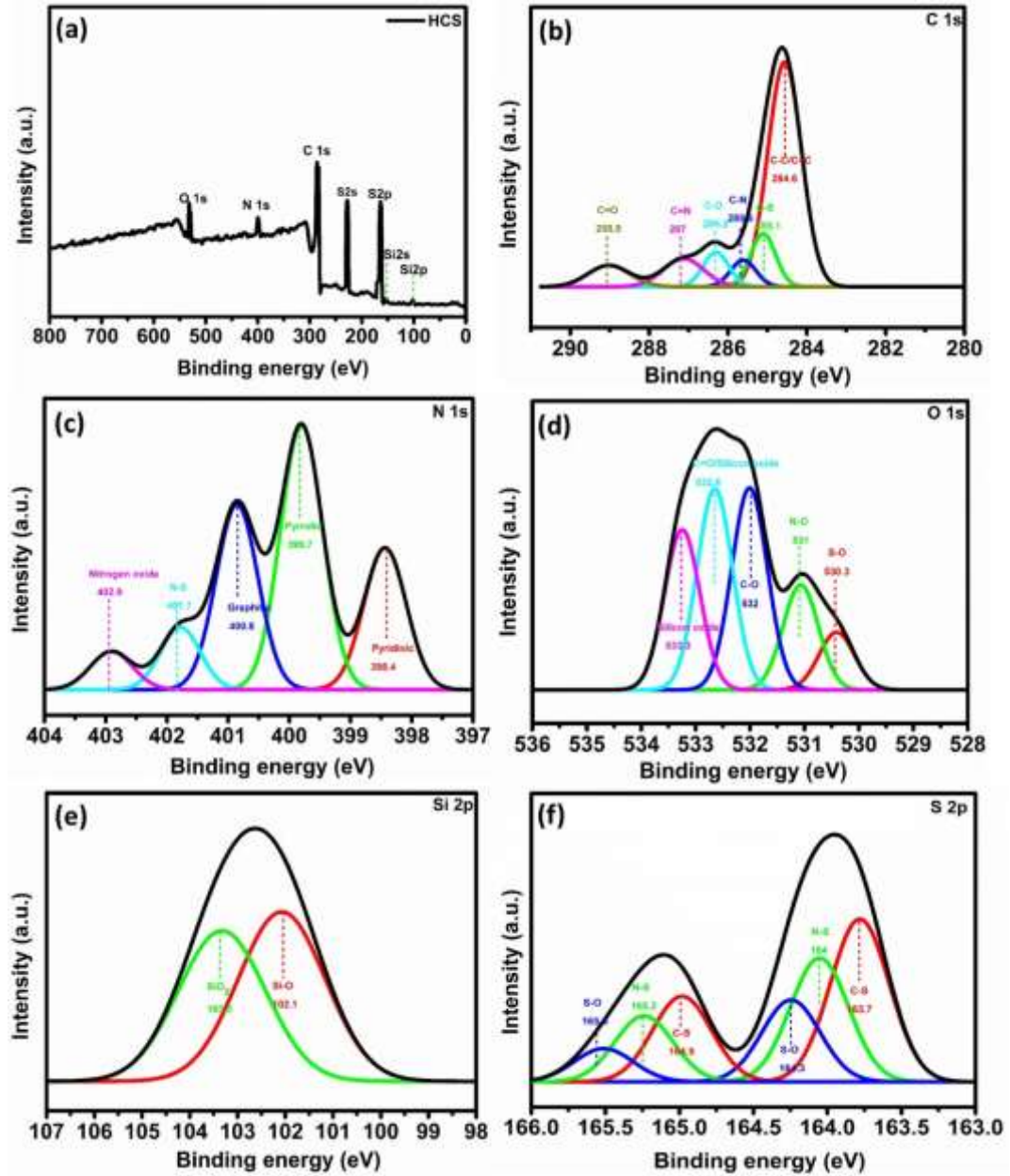


Figure 7.7. XPS analysis of HCS (80%) (a) Survey scan (b) C1s (c) N1s (d) O1s (e) Si 2p and (f) S 2p

Table 7.3: Elemental composition from XPS Analysis

Sample	C (%)	N (%)	S (%)	Si (%)	O (%)
HC	76.7	6.3	-	4	13
HCS (80%)	8.39	2.58	80	2.6	6.43

7.3.2 Electrochemical performance of the composite

7.3.2.1 HCS as cathode material for Li-S batteries

Li-S cells were fabricated to estimate the electrochemical performance of HCS composite in which HCS (70%) and HCS (80%) as cathode and lithium as a counter/reference electrode with 0.07M LiNO₃ added in the electrolyte to passivate the lithium anode. Figure 7.8 (a-b) shows the GCD profile for HCS (70%) and HCS (80%), contains 1, 2, 25, 50, 100, 125, 150, 175 and 200th discharge-charge profiles of HCSs at 0.1C rate. The charge-discharge profiles are characterized by two discharge plateaus (~2.36 V and 2.01 V) and one charge plateau (2.39 V) as a result of the multistep reaction between the HCS cathode films and lithium. There is no voltage plateau shift observed in HCS (70%) and HCS (80%) indicate good retention in the performance. The discharge plateaus at 2.36 V are due to the reduction of elemental sulphur to long chain lithium polysulphides (Li₂S_x, 4 ≤ x ≤ 8). The plateaus at 2.01 are due to the conversion of these long chain polysulphides to short chain polysulphides (Li₂S_x, 2 ≤ x ≤ 4). In the subsequent charging process, the plateau at 2.39 corresponds to the conversion of polysulphides to sulphur. An impressive high discharge capacity of 1341 mA h g⁻¹ was observed in the case of HCS (80%). In comparison, HCS (70%) exhibited an initial discharge capacity of 1226 mA h g⁻¹ and 9% reduction with respect to the initial discharge capacity of HCS (80%). The amount of active material utilization is more in HCS (80%) (Gu et al., 2015). In the second cycle, discharge capacities of HCS (80%) become 1317 mA h g⁻¹ with 10% capacity degradation, and 3% capacity degradation was observed for HCS (70%) (1187 mA h g⁻¹), which attributed to loss of sulphur at the surface of HCs. After 200 cycles the discharge capacity of the HCS (80%) is 1101 mA h g⁻¹ with 82% capacity retention when compared with initial discharge capacity and the HCS (70%) shows the 78% capacity retention.

The Li-S cell after 200 charge-discharge cycles is evaluated by cyclic voltammetry in a potential range of 1.6 - 3 V at a scan rate 0.5 mV s⁻¹ (Figure 7.8 (c and d)). In the cathodic scan process, the peak at ~ 2.36 V is due to the reduction of elemental sulphur to long chain lithium polysulphides (Li₂S_x, 4 ≤ x ≤ 8). The

second peak at 2.01 V is due to the conversion of these long chain polysulphides to short chain polysulphides (Li_2S_x , $2 \leq x \leq 4$). In the subsequent anodic scan process, a peak of 2.39 V is observed, which corresponds to the conversion of these polysulphides to sulphur. In the successive cycles, the voltage and current of reduction and oxidation peaks are almost similar ascribing the reactive reversibility and cycling stability of the developed electrode material (G. Ren et al., 2016). HCS (80%) exhibits increase in current density attributing to the increase in utilization of active material facilitated by the conductive carbon network. It is understood that HCSs have good electrochemical stability and the silicon dioxide containing hierarchically porous carbon network along with N and O functionalities are good for hosting sulphur, thereby decreasing the loss of active material into the electrolyte (Ogoke et al., 2017).

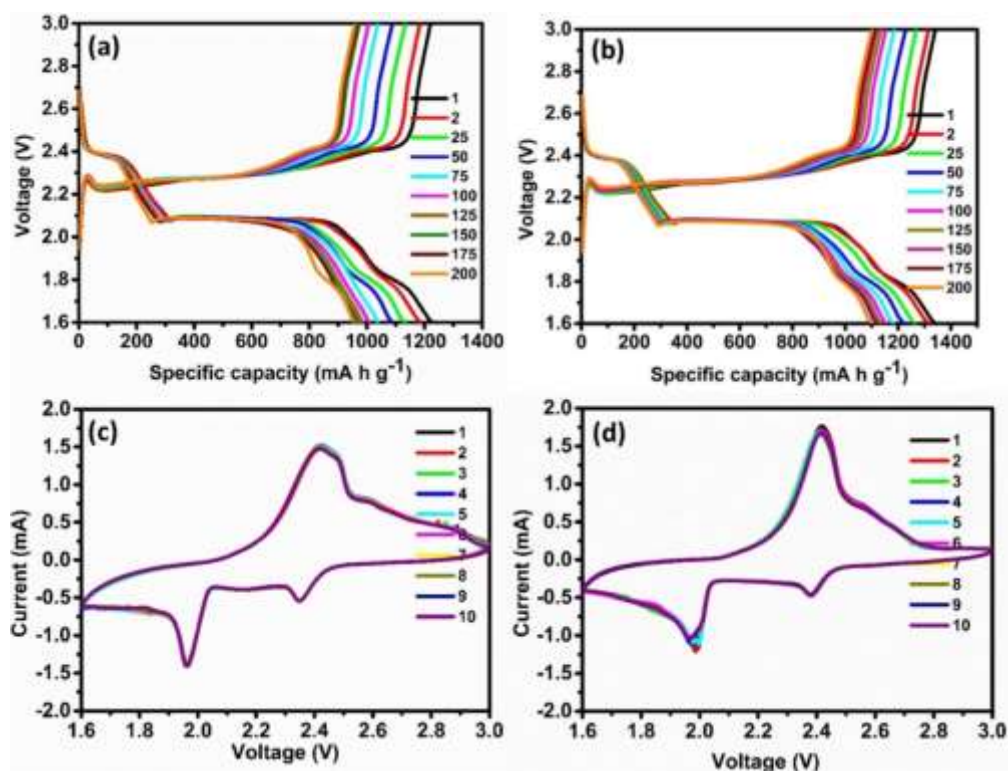


Figure 7.8. GCD curves of HCSs (a) 70% (b) 80% and CV of the HCSs (c) 70% (d) 80%

The capacity retention of HCS (70%) and HCS (80%) is comparatively better than the literature reports. Rehman et al reported Si/SiO₂/hierarchical porous carbon spheres as sulphur host for 69.6% sulphur exhibited an initial discharge capacity of 1215 mA h g^{-1} and a reversible capacity of $\sim 900 \text{ mA h g}^{-1}$ after 100

cycles at 0.2 C rate with 74% capacity retention (Rehman et al., 2016). Campbell et al informed SiO₂ coated sulphur particles with rGO as cathode material (90% sulphur), displayed an initial discharge capacity of 1400 mA h g⁻¹ and final capacity of 700 mA h g⁻¹ after 50 cycles at 0.1 C rate with 72.5% capacity retention. (Campbell et al., 2015). Wei et al described graphene and SiO₂ as sulphur host for 92% sulphur delivered an initial discharge capacity of 696 mA h g⁻¹ and a stable capacity of 629 mA h g⁻¹ after 120 cycles at 0.1C rate with 90% capacity retention (P. Wei, Fan, Chen, Chen, et al., 2016). Li et al reported hollow nano SiO₂/carbon nanofiber as host for sulphur and exhibited an initial discharge capacity of 806 mA h g⁻¹ and final capacity of 584 mA h g⁻¹ after 300 cycles at 0.5C rate with 72.5% capacity retention. It contains 70% sulphur loading (J. Li et al., 2018). Ji et al added SiO₂ as additive to the porous carbon-sulphur composite with 59.85% sulphur and displayed a final capacity of 650 mA h g⁻¹ after 40 cycles with 65% capacity retention at 0.2C rate (Ji et al., 2011). Wu et al reported hierarchical porous graphene/carbon/ SiO₂ as sulphur host (63.3% sulphur) and exhibits an initial discharge capacity of 786 mA h g⁻¹ and final capacity of 626 mA h g⁻¹ after 100 cycles at 0.1C rate with 79.6% capacity retention (Huali Wu et al., 2017). Kim et al reported mesoporous graphene and SiO₂ with 60% sulphur as PS reservoir which exhibits an initial discharge capacity of ~1200 mA h g⁻¹ and a reversible capacity of ~600 mA h g⁻¹ after 40 cycles at 0.1C rate with ~50% capacity retention (K. H. Kim et al., 2014). Schuster et al reported a thin layer of SiO₂ on the surfaces of spherical ordered mesoporous carbon nanoparticles with 70% sulphur that improved the performance of the cell (Jörg et al., 2012).

Cycle performance and coulombic efficiency studies of HCSs at the 0.1C rate are shown in Figure 7.9 (a). HCS (70%) shows 78% capacity retention and HCS (80%) shows 82% capacity retention. HCS (80%) exhibits comparatively better electrochemical performance with 99% coulombic efficiency in each cycle.

The electrochemical performance of the HCSs cathodes were further evaluated by rate capability studies at different current densities (Figure 7.9 (b)). The HCS (80%) shows a discharge capacity of 1351 mA h g⁻¹ at a 0.1C rate and 1230 mA h g⁻¹ for HCS (70%). The cathodes (HCS (70 & 80)) exhibit the reversible

capacities of 1112 mA h g⁻¹, 1028 mA h g⁻¹, 739 mA h g⁻¹ & 410 mA h g⁻¹ (70%), 1252 mA h g⁻¹, 1170 mA h g⁻¹, 938 mA h g⁻¹ & 584 mA h g⁻¹ (80%) for the current densities of 0.2C, 0.5C, 1C & 2C, respectively. When current rates were reduced to 0.2C rate, HCS (70%) exhibits 1080 mA h g⁻¹ with 97% capacity retention and HCS (80%) exhibits 1241 mA h g⁻¹ with 99% capacity retention. These high specific capacities at different current densities are appreciable to obtain high energy density and power density. The outstanding rate capabilities may be due to the good conductivity, surface area, and pore volume of HC and the presence of heteroatoms with lone pairs and the presence of silicon compounds which facilitate chemical adsorption of PSs and Li diffusion during charge-discharge processes (X. Fan et al., 2018).

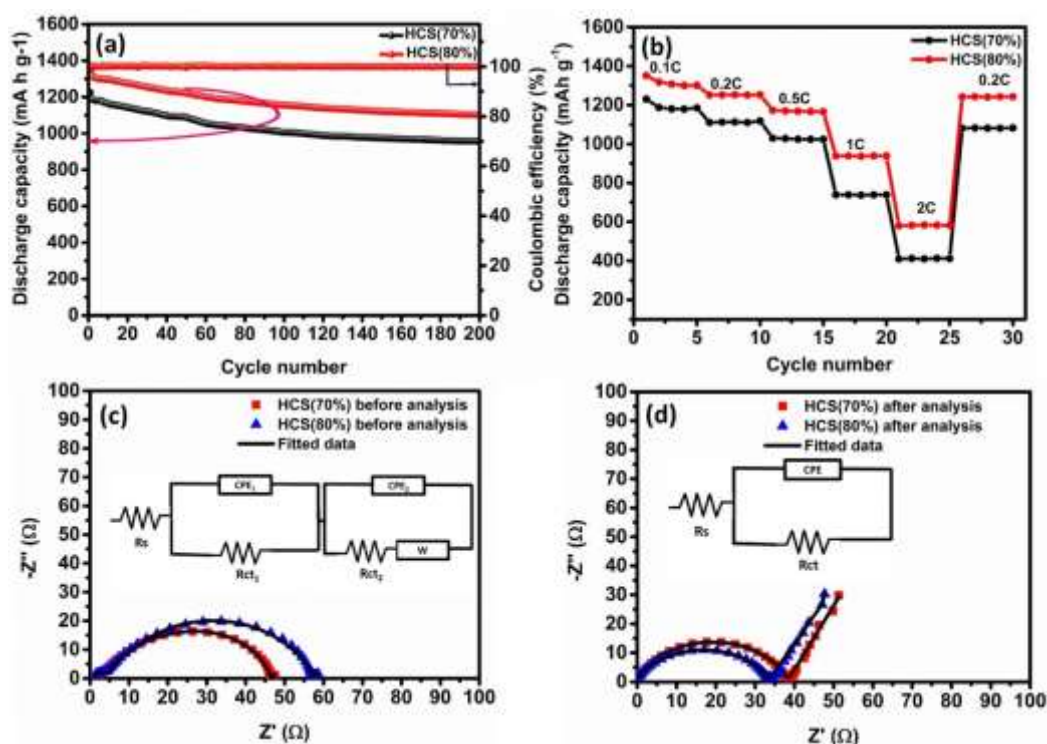


Figure 7.9. (a) Cyclic stability performance and coulombic efficiency (b) Rate capability studies at different C-rate, (c) EIS analysis of the electrodes at the OCV of HCSs before cycling [inset: equivalent circuit model] and (d) EIS analysis of the electrodes at the OCV of HCSs after cycling [inset: equivalent circuit model]

To investigate the charge transfer kinetics of the composites, EIS was carried out. Figure 7.9 (c) and (d) shows a typical Nyquist plot before and after charge-discharge cycling at OCV with the equivalent circuit (inset). The small semicircle in the high-frequency region related to the charge transfer resistance at

the interface of the high surface area porous carbon material (free carbon) and electrolyte, ie, electrical double layer resistance (R_{ct1}) (Meher et al., 2010). The large semicircle is the charge transfer resistance at HCS composite cathode film and electrolyte interface (R_{ct2}). HCS (80%) displays higher charge transfer and ion diffusion resistance than HCS (70%) before cycling due to the high sulphur content in the HCS (80%) composite, which resists diffusion of the electrolyte at the electrode surface (W. G. Wang et al., 2014) (Table 7.4). From the impedance plot, it is very clear that the R_{ct} and ion diffusion resistance decreased after 200 cycles which is due to the redistribution of sulphur in the porous carbon network, through which charges can transfer more easily (Raghuhandanan et al., 2018; G. Ren et al., 2016; Gu et al., 2015) (Table 7.4). The small semicircle in the high-frequency region is disappeared after cycling, due to non-availability of free space after continuous charge-discharge cycles (Chulliyote et al., 2017b).

Table 7.4: Impedance parameters obtained from the equivalent circuit for the HCSs cathodes before and cycling

Material description	R_s (Ω)	CPE_1 ($\Omega^{-1} \times 10^{-6}$)	R_{ct1} (Ω)	CPE_2 ($\Omega^{-1} \times 10^{-6}$)	R_{ct2} (Ω)	Y_0 ($\Omega^{-1} s^{1/2}$)
HCS(70%) before cycling	1.39	3.02	2.28	4.45	44.25	0.025
HCS(80%) before cycling	1.45	7.32	2.75	4.9	54.72	0.028
HCS(70%) after cycling	0.28	-	-	8.26*	38.39**	0.25
HCS(80%) after cycling	0	-	-	2.5*	33.9**	0.29

*CPE ** R_{ct}

7.3.2.2 Impact of HC interlayer on HCS cathode material

HCS (80%) exhibited better electrochemical performance compared to HCS (70%). To improve the electrochemical performance further, we modified the HCS (80%) cathode film with a thin layer of HC coating (interlayer). Figure 7.10 shows the schematic illustration of the working mechanism of the HCS cathode film and HC particles coated HCS cathode film.

Figure 7.11 shows the cross sectional SEM images of the HCS (80%) cathode film and HCS (80%)-HC coated cathode film. The mixture of HCS (80%) composite along with carbon black and PVDF is coated on the Al foil and the thickness is $\sim 17 \mu\text{m}$ (Figure 7.11 (a)). As shown in Figure 7.11(b) the HCS (80%) cathode film is completely coated with HC and the coating thickness is $\sim 23 \mu\text{m}$ with weight of the HC material of $\sim 3.3 \text{ mg cm}^{-2}$.

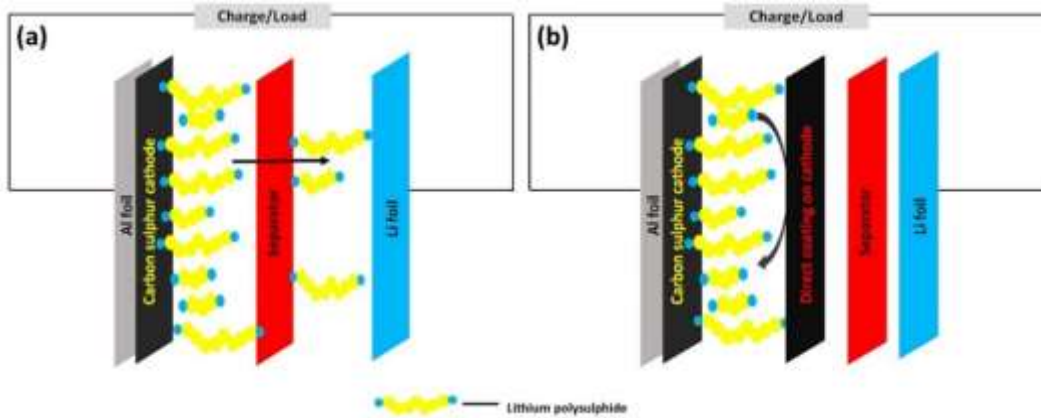


Figure 7.10. Schematic illustration of a working mechanism (a) Cathode film and (b) With interlayer on the cathode

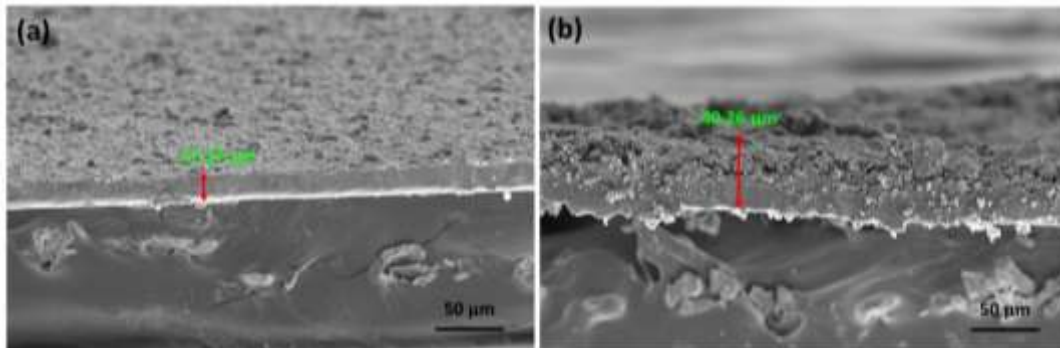


Figure 7.11. Cross sectional image of (a) HCS (80%) cathode film and (b) HCS (80%)-HC (interlayer) cathode film

The effect of HC coating on HCS (80%) cathode is evaluated by using GCD at a 0.1C rate in between the voltage window 1.6-3 V. Figure 7.12 (a) shows the HCS (80%)-HC coated GCD profile which displays 1, 2, 25, 50, 100, 125, 150, 175 and 200th discharge-charge cycles. It contains two discharge plateaus ($\sim 2.39 \text{ V}$ and 2.01 V) and one charge plateau (2.37 V) as same as bare HCS (80%) electrode (P. Zeng, Huang, Zhang, Zhang, et al., 2018). There is no voltage drop in the charge-discharge plateau during the continuous charge-discharge cycles after the HC coating, indicating good compatibility with the HCS cathode (Shao et al.,

2017). The initial discharge capacity is 1353 mA h g^{-1} , the second discharge capacity is 1330 mA h g^{-1} with 98.3% capacity retention. At the 200th cycle, its discharge capacity becomes 1252 mA h g^{-1} and exhibits 92% capacity retention with 0.04% capacity decay per cycle. It was further evaluated by CV after 200 GCD cycles at the same voltage window as HCS cathodes at a scan rate of 0.5 mV s^{-1} (Figure 7.12 (b)). Two reduction and one oxidation peaks are observed in the CV profile. In the cathodic scan process, the peak at 2.36 V is due to the reduction of elemental sulphur to long chain lithium polysulphides (Li_2S_x , $4 \leq x \leq 8$). The second peak at 2.01 is due to the conversion of these long chain polysulphides to short chain polysulphides (Li_2S_x , $2 \leq x \leq 4$). It can be seen that oxidation peak slightly shifted to lower voltage and reduction peaks slightly shifted to higher voltage in comparison with HCS (80%) CV profile, indicating better kinetics and lower polarizations (Y. Peng, Y. Zhang, Y. Wang, et al., 2017). In addition the area under the CV curve is not changed for HCS (80%)-HC coated cell, compared to HCS (80%) indicating the good capacity retention. It is due to the HC interlayer facilitating adsorption of the LPSs and effective utilization of the active material in the prolonged cycles (W. Fan et al., 2018).

Cycle performance and coulombic efficiency of HCS (80%)-HC cathode at 0.1C rate is shown in Figure 7.12 (c). Excellent cycling performance is observed with 100% coulombic efficiency. The HCS (80%)-HC coated shows a discharge capacity of 1353 mA h g^{-1} at the 0.1C rate. The cathode exhibits the reversible capacities of 1297 mA h g^{-1} , 1253 mA h g^{-1} , 1130 mA h g^{-1} & 1009 mA h g^{-1} for the current densities of 0.2C, 0.5C, 1C & 2C, respectively (Figure 7.12 (d)). When current rate reduced back to 0.2C rate, it exhibits 1288 mA h g^{-1} with 99% capacity retention. There is no specific capacity loss observed while discharging at different current densities. The excellent electrochemical performance is due to the effective coating of HC on HCS cathode film, which blocks the migration of PSs from the cathode to anode surface (Yibo He, Qiao, et al., 2018). Here sulphur is sandwiched in between the conductive carbon made up of N, O hetero atom, SiO_2 which retards the dissolution of PSs into the electrolytes (C. Wang et al., 2013). Besides, the higher surface area and pore volume of carbon helps to adsorb more quantities of LPSs. Here sulphur is placed in between two carbon matrices with multiple

functionalities helps to improve the electrochemical performance (Ogoke et al., 2017).

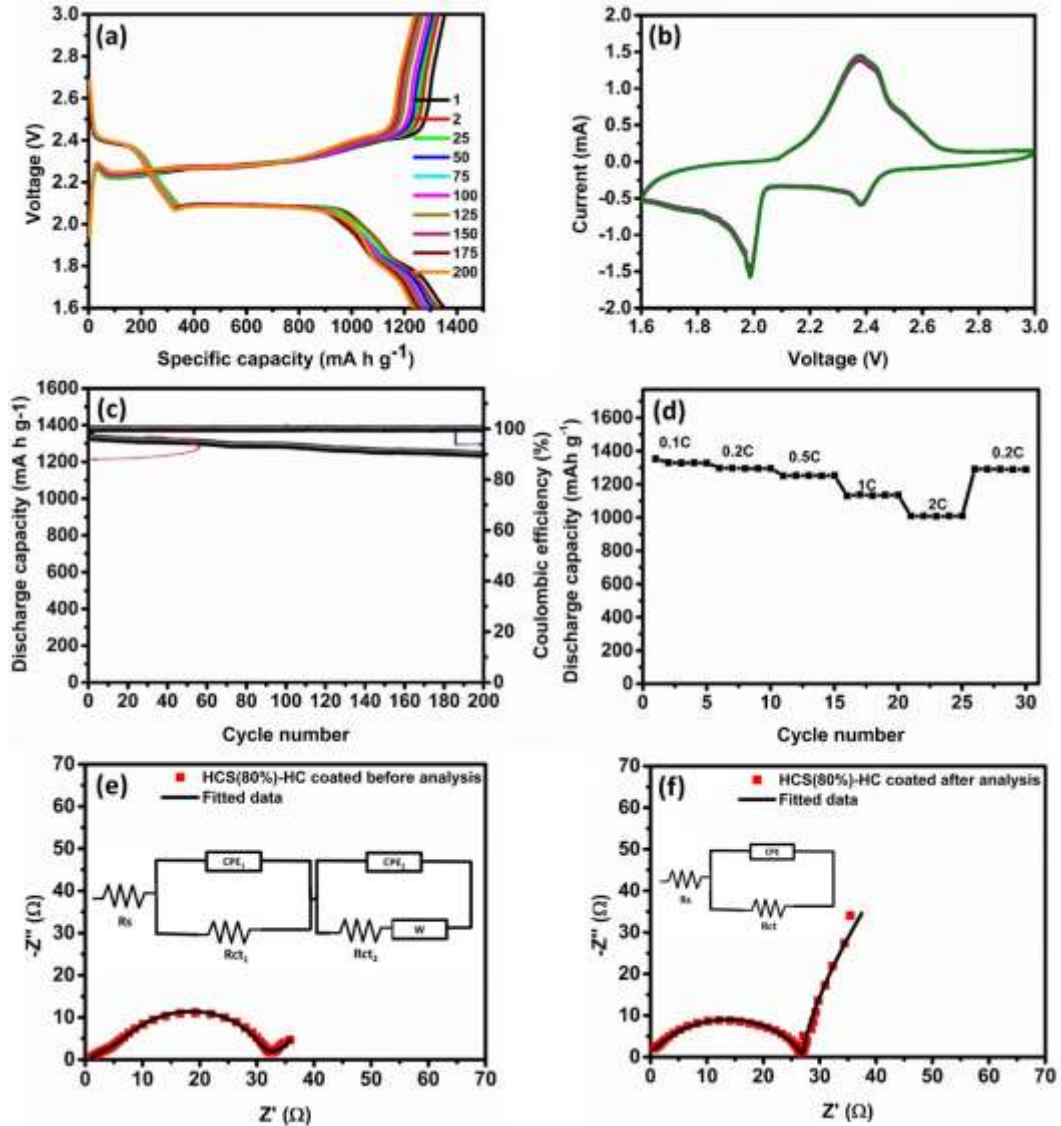


Figure 7.12. (a) GCD curves at 0.1C rate (b) CV (c) Cyclic stability performance and coulombic efficiency (d) Rate capability studies at different C-rate (e) EIS analysis of the electrodes at the OCV of HCS (80%)-HC coated cathode before cycle and EIS analysis of the electrodes at the OCV of HCS (80%)-HC coated cathode after cycles [inset: equivalent circuit]

Figure 7.12 (e and f) represents the Nyquist plot of HCS (80%)-HC before and after 200 cycles with equivalent circuit (inset). It is observed that a small semicircle at the high frequency region, due to the charge transfer resistance offered by the HC coated carbon with the electrolyte (R_{ct1}). The large semicircle in the middle frequency region attributed to the charge transfer resistance at HCS (80%)-HC composite cathode film and electrolyte interface (R_{ct2}). HCS (80%)-HC

exhibits better ion diffusion and charge transfer than the bare HCS (80%) (Table 7.5). The coating of HC on the cathode film with porous structure, facilitates the permeation of the electrolyte ions and the movement of Li⁺ ion (W. G. Wang et al., 2014). After 200 cycles the Rct and ionic diffusion resistance decreased compared to the bare HCS cathode films, indicating that the inherently doped porous carbon network maintains its structural integrity during cycling (Chulliyote et al., 2017a; Su and Manthiram, 2012a) (Table 7.5). The small semicircle in the high-frequency region is disappeared after cycling, due to physical and chemical confinement of PSs during the cycling process.

Table 7.5: Impedance parameters obtained from the equivalent circuit for the HCS (80) %-HC cathodes before and after cycling

Material description	Rs (Ω)	CPE ₁ (Ω^{-1})	Rct ₁ (Ω)	CPE ₂ (Ω^{-1})	Rct ₂ (Ω)	W ($\Omega^{-1} s^{1/2}$)
HCS(80%)-HC before cycling	1.01	0.37	3.46	0.0008	29.01	0.13
HCS(80%)-HC after cycling	0.55	-	-	2.45*	25.98**	0.29

*CPE ** Rct

The adsorption capability of HC was characterized by PS adsorption test as described in section 4.2.2.3 (Figure 7.13). Digital photographs show the changes in the colour of the PS solution after adding HC within 10 minute, which indicates the inherent adsorption capability of HC materials.

The excellent electrochemical performance are due to the higher surface area and hierarchical porosity of the HC carbon, which helps to access the electrolyte ion into the carbon matrices. Sulphur is uniformly distributed in the HC due to its identical morphology and higher pore volume. The HC interlayer blocks the migration of the LPSs into the electrolyte and acts as a barrier for the PS movement. This interlayer act as upper current collector also and supports to improve the electrochemical performance. It adsorbs the LPSs and helps to reutilize the active material. Polar SiO₂, N and O help to confine through chemical bonds along with the physical confinement of high surface area carbon. These confinements are acting from both sides, since sulphur is sandwiched between the multifunctional carbons.

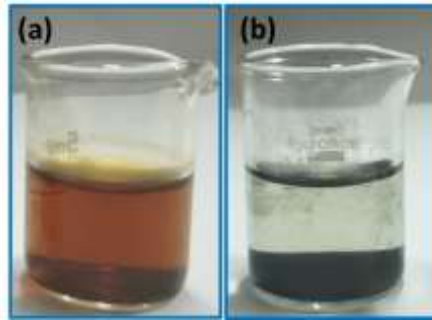


Figure 7.13. Digital images of the polysulphide adsorption test (a) Lithium polysulphide solution and (b) Lithium polysulphide mixed with HC after 10 minutes (in Ar filled glove box)

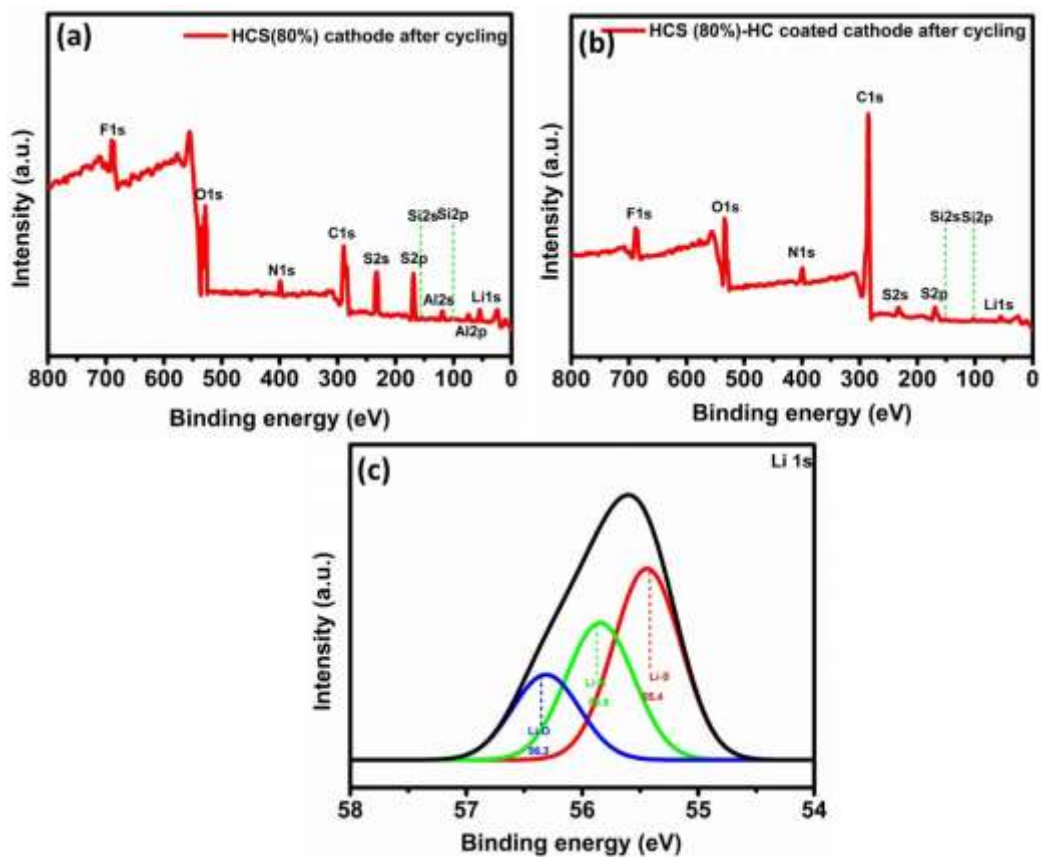


Figure 7.14. XPS survey scan analysis of cathode film after 200 cycles (a) HCS (80%) (b) HCS (80%)-HC coated (c) high resolution Li 1s

To further investigate the significance of HC coating on HCS cathode film to block the PS intermediate, the cells with and without coating were disassembled after 200 cycles and XPS analysis were carried out (Figure 7.14). The survey scan analysis reveals C1s, N1s, O1s, S2s, S2p, Si2s, Si2p functionalities along with Al 2s, Al 2p and F1s. The presence of Al is from the current collector and F is from the PVDF binder. It is observed an intensity variation in the sulphur peak between HCS (80%) and HCS (80%)-HC after 200 cycles (Figure 7.14 (a and b)). The

sulphur species are within the interlayer evidencing the excellent performance of the HCS (80%)-HC over bare HCS (80%) cathode films. In HCS (80%) cathode there is a direct contact between the cathode film and electrolyte, the discharge product is on the surfaces of the HC carbon although there is a physical confinement effect of carbon, heteroatom and silica confinement. So more quantities of PSs on the cathode films after cycling when compared with the HCS (80%)-HC cathode. In addition, high-resolution Li 1s spectra (Figure 7.14 (c)) reveal the presence of Li-O (56.5 eV), Li-N (55.8 eV) along with Li-S (55.08 eV) attributed to the interaction of sulphides of lithium with various functionalities (Aurbach et al., 2009; F. Chen et al., 2018; X. Fan et al., 2018; Xia Liand Sun, 2014; Son et al., 2015).

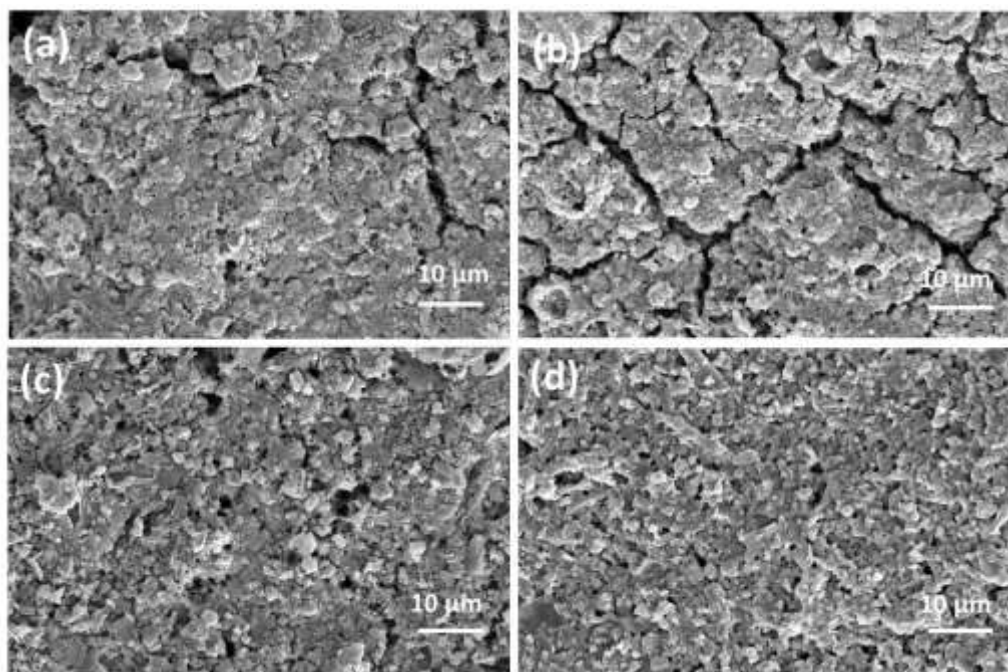


Figure 7.15. Cathode surfaces of (a) HCS (80%) film before cycling (b) HCS(80%) film after 200 cycling (c) HCS (80%)–HC interlayer cathode films before cycling and (d) HCS (80%)–HC interlayer cathode films after 200 cycling

Figure 7.15 shows the SEM images of HCS and HCS (80%)-HC coated cathode films before and after 200 cycles. It is observed that the visible cracks and agglomerated particles in HCS cathode cause structural failure and capacity fading (Figure 7.15 (a and b)). There is no obvious morphological differences noted and the structural integrity is maintained in HCS (80%)-HC cathode films before and after cycling (Figure 7.15 (c and d)) (Miao et al., 2013; S. Wei et al., 2011; Ye et

al., 2016). This observation indicates interlayer on the cathode surface highly beneficial for structural protection of the sulphur cathode, which leads to excellent cycling stability.

7.4 Conclusion

In summary, we developed a high surface area porous carbon from a low cost and green carbon source, honeycomb by zinc chloride activation method. The porous carbon acts as an ideal host of elemental sulphur and as an interlayer to mitigate shuttle effect by interacting with PS. The HCS (80%)–HC (with interlayer) provides better rate performance, improved active material utilization and better cyclability. It exhibits high initial discharge capacity of 1353 mA h g^{-1} with excellent capacity retention of 92% after 200 cycles with 0.04 % average fading per cycle at 0.1C rate and a good rate capability (1006 mA h g^{-1} at 2C) as a cathode material for LSB. This porous HC coating provides excellent electrolyte access, and act as second current collector. It anchors the PSs on the cathode side by multiple confinement effects like N, O heteroatom, SiO_2 , higher surface area, porosity. HCS (80%)–HC electrode provides excellent long-term stability with high coulombic efficiencies of almost 100% for 200 cycles. From these interesting results, the HCS (80%)–HC interlayer configuration becomes a promising cathode material for the next generation rechargeable batteries.

CHAPTER 8

CONCLUSIONS AND FUTURE PERSPECTIVES

8.1 Conclusions

Porous carbon materials are one of the interesting class of carbon, due to its excellent properties such as low cost, biocompatibility, low toxicity, high conductivity, higher surface area, pore volume, tunable morphologies, etc. Porous carbon materials are easy to synthesize with the desired properties for a wide variety of applications such as energy storage, CO₂ adsorption, separation/removal of contaminants, EMI shielding, thermal protection system, biological and chemical sensors, photocatalysis, etc. There is a variety of synthetic sources for the preparation of these materials. Out of this bioderived carbon received special attention due to its low cost and ease of availability. The depletion of fossil fuel, environmental issues and ever increasing energy demand force to develop renewable and sustainable energy conversion and storage devices. LSB and supercapacitors are more attractive due to its special features. LSBs paid more attention due to its high theoretical capacity and energy density. Here the sulphur is used as a cathode which is a low cost easily available material. Its merits and demerits were discussed in the thesis at many places. Importantly, low electrical conductivity, volume changes of sulphur during the charge-discharge process, PS dissolution into the electrolytes are the issues at the cathode side. To address the drawbacks associated with the sulphur cathode, functionalized porous carbon was used as a host for the sulphur. The developed porous carbon-based materials tested for EDLC application too. The objective of this thesis was to cut down the shortcomings on the cathodic side of LSB and to improve the specific capacity and cycle performance. The carbon materials investigated in various chapters were MWCNT, 4,4-diamino diphenyl sulphone derived carbon, pinecone derived carbon, vetiver derived carbon, orange peel derived carbon, honeycomb derived carbon, etc. The strategies adopted to improve the electrochemical performance are modification of cathode and separator. To solve the insulating problem of sulphur

and to minimise the PSs dissolution heteroatom/metal oxide doped porous carbon–sulphur composite, MWCNT-sulphur-conducting polymer ternary composite, functionalised porous carbon modified separator and a thin porous carbon coating onto cathode film (interlayer) are prepared and investigated in detail.

A detailed literature survey on the strategies adopted to improve the performance of LSBs is described in chapter 1. In addition, the importance and an overview of carbon-based supercapacitors are emphasised.

A cathode material to solve the insulating problem of sulphur was developed using MWCNT/S/PIN as a dual core-shell type ternary nanocomposite in chapter 2. Here PIN and MWCNT are used for wrapping the sulphur. The ternary composite shows an initial discharge capacity of 1490 mA h g⁻¹ and a stable capacity of 1043 mA h g⁻¹ after 100 cycles at 0.1C with 70% capacity retention. The enhanced electrochemical performance of MWCNT/S/PIN is due to the encapsulation of sulphur between functionalized MWCNT and PIN, which simultaneously help to restrict the movement of PSs.

Heteroatom doped microporous carbon (HMC) with a high surface area is prepared from 4, 4'-diamino-diphenyl sulphone in chapter 4. It is prepared by single step carbonization without adding any additive through varying carbonization time 1-3 h. The highest BET surface area of 1766 m² g⁻¹ and pore volume of 0.87 cm³ g⁻¹ is obtained at the carbonization time of 2 h (HMC-2). HMC-1 and HMC-2 materials were investigated for both SC and LSB applications. The carbon material is used as a sulphur host (~74% sulphur) and provides a stable capacity of 790 mA h g⁻¹ after 100 cycles at 0.1C rate with 79% capacity retention (HMC-2S). HMC-2 displays a maximum specific capacitance of 431 F g⁻¹ at a current density of 0.8 A g⁻¹ using 6M KOH as an electrolyte with three electrode system. A symmetrical supercapacitor is fabricated by PVA+ Na₂SO₄ as gel electrolyte, exhibits an energy density of 35 W h kg⁻¹ at a power of 529 W kg⁻¹ and this device is stable for 5000 cycles with 91.07% capacity retention at a current density of 0.6 A g⁻¹.

High surface area hierarchical porous carbon which contains Fe functionalities in addition to N, O heteroatoms derived from vetiver was used as

sulphur host in chapter 4. The sulphur-carbon composite with 72% sulphur content exhibits a reversible capacity of 1069 mA h g⁻¹ with 67% retention capacity after 200 cycles at 0.1C rate. It is due to the synergistic effect of the tubular porous nature of the derived carbon, with the N, O and Fe functionalities which help to retain the PSs in the carbon matrix. In addition, this carbon is tested for supercapacitor application in both aqueous and organic electrolytes. Highest discharge time is obtained for the supercapacitor electrode of the HPC-800 °C and the specific capacitance value is 296 F g⁻¹ using 1M Na₂SO₄ as an electrolyte with the three electrode system at a current density of 0.8 A g⁻¹. A maximum energy density of 67.8 W h kg⁻¹ at a power density of 749 W kg⁻¹ for the current density of 0.5A g⁻¹ with is obtained ~ 88% capacity retention after 10,000 cycles by using 1M LiTFSI as the organic electrolyte.

N and O co-doped hierarchically porous carbon derived from pinecone is demonstrated as a host for the active material sulphur in chapter 5. It has a high BET surface area of 2065 m² g⁻¹ and a pore volume of 1.5 cm³ g⁻¹. The specific capacity and cycling stability are highly influenced by the surface area, pore volume, sulphur content and the distribution of sulphur in the porous carbon. Three carbon-sulphur composites with 54, 68 and 73% of sulphur were electrochemically evaluated to find out the best cathode material for LSB. The electrochemical performance decreased when increasing the sulphur content, due to the presence of non-conducting sulphur on the surface of the porous carbon. 54% sulphur loaded composite exhibited better performance with an initial discharge capacity of 1606 mA h g⁻¹ and a reversible capacity of 1269 mAh g⁻¹ after 100 cycles at the 0.1C rate. It is due to the uniform distribution of sulphur into the pores of carbon and it can accommodate the volume changes of sulphur during the charge-discharge process. It delivers a high specific capacity of 923 mA h g⁻¹ at the 2C rate.

Chapter 6 investigates on the sulphur host derived from orange peel. To reduce the capacity fading of OPCSC a thin layer coating of the N, O heteroatoms doped high surface area carbon onto separator on the cathodic side allows the Li⁺ transport and effectively blocks the migration of the PSs, In addition, the high surface area of HMC-1 provides more active adsorption sites for PSs in LSBs. 85%

capacity retention at a 0.1C rate is obtained with a specific capacity of 845 mA h g⁻¹ at the 2C rate.

Chapter 7 discusses the sulphur host, derived from the honeycomb. The carbon material contains N, O and SiO₂, which helps to retain the PS on the cathode surface. A thin layer of the same carbon material is used to coat on carbon-sulphur composite cathode film to act as a barrier to restrict PS migration and exhibited 92% capacity retention after 200 cycles at 0.1C rate. It delivers a specific capacity of 1006 mA h g⁻¹ at the 2C rate. The excellent electrochemical performance is due to the multiple confinement effects of N, O and SiO₂ exerted on sulphur. Here, sulphur is sandwiched between the two HC, PS dissolution to the electrolytes is restricted.

Table 8.1 lists the electrochemical performance of the developed cathode materials for LSBs. Among these HCS (80%) with HC coating displays an initial discharge capacity of 1354 mA h g⁻¹ and a stable capacity of 1284 mA h g⁻¹ after 200 cycles at a 0.1C rate with 0.002% capacity decay per cycle. The PCSC (54%) exhibits 79% capacity retention after 100 cycles and shows better performances than the 4, 4' diamino diphenyl sulphone derived carbon-sulphur composites. It was due to the uniform distribution of sulphur in the inner layer of the carbon. It is believed that these methods have practical significance for the realization of high-performance LSBs indicating a major progress in energy storage devices.

Table 8.1: Comparison of electrochemical performance of the developed material

Sl no	Cathode	Heteroatoms	Surface area (m ² g ⁻¹)	Sulphur (%)	Separator	Initial capacity (mA h g ⁻¹)	Cycles	Final capacity (mAh g ⁻¹)	Capacity retention (%)
1	MWCNT/S			83	PP	1267	100	760	61
2	MWCNT/S/PIN	N		79	PP	1490	100	1043	70
3	HMC-1S	N, O	931	74	PP	792	100	536	76
4	HMC-2S		1766	74	PP	997	100	730	80
5	PCSC	N, O	2065	54	PP	1608	100	1269	79
6				68	PP	1370	100	1028	75
7				73	PP	1145	100	891	74
8	OPCSC	N, O	1806	61	PP	1019	100	528	51
9				61	PP	1054	100	562	51
10				73	PP-MWCNT	1203	100	900	75
11				73	PP-HMC	1213	100	1033	85
12	HPCS	N, O, FeS	1879	72	PP	1584	200	996	63
13	HCS	N, O, SiO ₂	931	70	PP	1226	200	957	78
14				80	PP	1341	200	1101	82
15				HCS-HC	80	PP	1354	200	1284

8.2 Future Perspectives

This doctoral thesis work has focused on cathode materials, its design and preparation to reduce shuttle effect and to achieve good cyclability. Even though the structure-property relationship of the carbon-sulphur composites were evaluated electrochemically, more challenges are still unresolved to make this battery commercially viable. LSBs have great potential to compete with the existing technologies, it will become the spotlight in the near future. To achieve this, further optimisation and improvement in the fabrication of other components are required. In this direction, the following are the future outlook on Li-S system for further studies.

- The pore characteristics of the carbon and the interaction of sulphur need to be explored. Studies should be done by decreasing the particle size of sulphur and to improve the intimate contact with carbon.
- Electrodes with the high mass loading of active material $\sim 10 \text{ mg cm}^{-2}$ is being studied to overcome the present battery technologies. The markets of portable electronic devices required prolonged cycle stability of 5000 cycles without capacity fading.
- Studies to understand more about the impact of heteroatom doped porous carbon for the formation of a solid electrolyte interface (SEI) layer is required.
- Further studies may be carried out to develop Li-metal free cell, using the Li_2S loaded functionalized carbon and silicon/tin/germanium as electrode materials for LSBs.
- A suitable electrolyte may be developed to solve the shuttling problems.
- LSBs contains more additives (conductive carbons and binders) which do not make any contribution to the discharge capacity. Studies need to be carried out to reduce the additives contained in the cathode film.
- Alternative methods can be explored to increase the rate of sulphur reduction, hence the PS dissolution may be controlled

To develop flexible SCs using hybrid materials with an energy density close to that of rechargeable batteries (supercapattery) along with high power density and long cycle life. New electrolytes with a voltage window more than 3V and new materials/electrode configuration with low resistance are being developed.

REFERENCES

1. Abdul Razzaq, A., Yao, Y., Shah, R., Qi, P., Miao, L., Chen, M., et al. (2019). High-Performance Lithium Sulfur Batteries Enabled by a Synergy Between Sulfur and Carbon Nanotubes. *Energy Storage Materials*, 16: 194-202.
2. Agostini, M., Aihara, Y., Yamada, T., Scrosati, B., and Hassoun, J. (2013). A Lithium–Sulfur Battery Using a Solid, Glass-type P2S5–Li2S Electrolyte. *Solid State Ionics*, 244: 48-51.
3. Ahmed, S., Ahmed, A., and Rafat, M. (2018). Supercapacitor Performance of Activated Carbon Derived from Rotten Carrot in Aqueous, Organic and Ionic Liquid Based Electrolytes. *Journal of Saudi Chemical Society*.
4. Ai, F., Liu, N., Wang, W., Wang, A., Wang, F., Zhang, H., et al. (2017). Heteroatoms-Doped Porous Carbon Derived from Tuna Bone for High Performance Li-S Batteries. *Electrochimica Acta*, 258: 80-89.
5. Ai, W., Li, J., Du, Z., Zou, C., Du, H., Xu, X., et al. (2018). Dual Confinement of Polysulfides in Boron-Doped Porous Carbon Sphere/Graphene Hybrid for Advanced Li-S Batteries. *Nano Research*, 11: 4562-4573.
6. An, S., Abdiryim, T., Ding, Y., and Nurulla, I. (2008). A Comparative Study of the Microemulsion and Interfacial Polymerization for Polyindole. *Materials Letters*, 62(6–7): 935-938.
7. An, Y., Li, Z., Yang, Y., Guo, B., Zhang, Z., Wu, H., et al. (2017). Synthesis of Hierarchically Porous Nitrogen-Doped Carbon Nanosheets from Agaric for High-Performance Symmetric Supercapacitors. *Advanced Materials Interfaces*, 4(12): 1700033-1700043.
8. Angulakshmi, N., and Stephan, A. M. (2015). Efficient Electrolytes for Lithium–Sulfur Batteries. *Frontiers in Energy Research*, 3(17).
9. Arias, A. N., Tesio, A. Y., and Flexer, V. (2018). Review—Non-Carbonaceous Materials as Cathodes for Lithium-Sulfur Batteries. *Journal of The Electrochemical Society*, 165(1): A6119-A6135.
10. Aricò, A. S., Bruce, P., Scrosati, B., Tarascon, J.-M., and van Schalkwijk, W. (2005). Nanostructured Materials for Advanced Energy Conversion and Storage Devices. *Nature Materials*, 4: 366-377.

11. Arie, A. A., Kristianto, H., and Lee, J. K. (2013). Activated Carbons from Orange Peel Waste as Supercapacitor Electrodes. *ECS Transactions*, 53(31): 9-13.
12. Aurbach, D., Pollak, E., Elazari, R., Salitra, G., Kelley, C. S., and Affinito, J. (2009). On the Surface Chemical Aspects of Very High Energy Density, Rechargeable Li–Sulfur Batteries. *Journal of The Electrochemical Society*, 156(8): A694-A702.
13. Bai, S., Tan, G., Li, X., Zhao, Q., Meng, Y., Wang, Y., et al. (2016). Pumpkin-Derived Porous Carbon for Supercapacitors with High Performance. *Chemistry – An Asian Journal*, 11(12): 1828-1836.
14. Balach, J., Jaumann, T., Klose, M., Oswald, S., Eckert, J., and Giebeler, L. (2015). Functional Mesoporous Carbon-Coated Separator for Long-life, High-Energy Lithium–Sulfur Batteries. *Advanced Functional Materials*, 25(33): 5285-5291.
15. Bello, A., Manyala, N., Barzegar, F., Khaleed, A. A., Momodu, D. Y., and Dangbegnon, J. K. (2016). Renewable Pine cone Biomass Derived Carbon Materials for Supercapacitor Application. *RSC Advances*, 6(3): 1800-1809.
16. Bhattacharjya, D., and Yu, J.-S. (2014). Activated Carbon made from Cow Dung as Electrode Material for Electrochemical Double Layer Capacitor. *Journal of Power Sources*, 262: 224-231.
17. Biswal, M., Banerjee, A., Deo, M., and Ogale, S. (2013). From Dead Leaves to High Energy Density Supercapacitors. *Energy & Environmental Science*, 6(4): 1249-1259.
18. Borenstein, A., Hanna, O., Attias, R., Luski, S., Brousse, T., and Aurbach, D. (2017). Carbon-Based Composite Materials for Supercapacitor Electrodes: A Review. *Journal of Materials Chemistry A*, 5(25): 12653-12672.
19. Bose, S., Kuila, T., Mishra, A. K., Rajasekar, R., Kim, N. H., and Lee, J. H. (2012). Carbon-Based Nanostructured Materials and their Composites as Supercapacitor Electrodes. *Journal of Materials Chemistry*, 22(3): 767-784.
20. Bouchelta, C., Medjram, M. S., Bertrand, O., and Bellat, J.-P. (2008). Preparation and Characterization of Activated Carbon from Date Stones by Physical Activation with Steam. *Journal of Analytical and Applied Pyrolysis*, 82(1): 70-77.
21. Brett, C. (2009). Fundamentals of Electrochemistry. *Piezoelectric transducers and applications* (pp. 223-239).

22. Bruce, P. G., Freunberger, S. A., Hardwick, L. J., and Tarascon, J.-M. (2012). Li–O₂ and Li–S Batteries with High Energy Storage. *Nature materials*, 11(1), 19-29.
23. Cai, J., Wu, C., Yang, S., Zhu, Y., Shen, P. K., and Zhang, K. (2017). Templated and Catalytic Fabrication of N-Doped Hierarchical Porous Carbon–Carbon Nanotube Hybrids as Host for Lithium–Sulfur Batteries. *ACS Applied Materials & Interfaces*, 9(39): 33876-33886.
24. Cai, Y., Luo, Y., Xiao, Y., Zhao, X., Liang, Y., Hu, H., et al. (2016). Facile Synthesis of Three-Dimensional Heteroatom-Doped and Hierarchical Egg-box-like Carbons Derived from Moringa Oleifera Branches for High-Performance Supercapacitors. *ACS Applied Materials & Interfaces*, 8(48): 33060-33071.
25. Campbell, B., Bell, J., Hosseini Bay, H., Favors, Z., Ionescu, R., Ozkan, C. S., et al. (2015). SiO₂-Coated Sulfur Particles with Mildly Reduced Graphene Oxide as a Cathode Material for Lithium–Sulfur Batteries. *Nanoscale*, 7(16): 7051-7055.
26. Cao, Z., Wang, C., and Chen, J. (2018). Novel Mesoporous Carbon Nanofibers Prepared via Electrospinning Method as Host Materials for Li–S Battery. *Materials Letters*, 225: 157-160.
27. Cao, Z., Zhang, J., Ding, Y., Li, Y., Shi, M., Yue, H., et al. (2016). In situ Synthesis of Flexible Elastic N-Doped Carbon Foam as a Carbon Current Collector and Interlayer for High-Performance Lithium Sulfur Batteries. *Journal of Materials Chemistry A*, 4(22): 8636-8644.
28. Carbone, L., Greenbaum, S. G., and Hassoun, J. (2017). Lithium Sulfur and Lithium Oxygen Batteries: New Frontiers of Sustainable Energy Storage. *Sustainable Energy & Fuels*, 1(2): 228-247.
29. Chang, C.-H., Chung, S.-H., and Manthiram, A. (2015). Ultra-Lightweight PANiNF/MWCNT-Functionalized Separators with Synergistic Suppression of Polysulfide Migration for Li–S Batteries with Pure Sulfur Cathodes. *Journal of Materials Chemistry A*, 3(37): 18829-18834.
30. Chaofeng, Z., Bin, W. H., Changzhou, Y., Zaiping, G., and Wen, L. X. (2012). Confining Sulfur in Double-Shelled Hollow Carbon Spheres for Lithium–Sulfur Batteries. *Angewandte Chemie*, 124(38): 9730-9733.
31. Chen, F., Ma, L., Ren, J., Luo, X., Liu, B., and Zhou, X. (2018). Sandwich-type Nitrogen and Sulfur Codoped Graphene-backed Porous Carbon Coated Separator for High Performance Lithium-Sulfur Batteries. *Nanomaterials*, 8(4): 191-208.

32. Chen, G., Song, X., Wang, S., Wang, Y., Gao, T., Ding, L.-X., et al. (2018). A Multifunctional Separator Modified with Cobalt and Nitrogen Co-doped Porous Carbon Nanofibers for Li–S Batteries. *Journal of Membrane Science*, 548: 247-253.
33. Chen, H., Dong, W., Ge, J., Wang, C., Wu, X., Lu, W., et al. (2013). Ultrafine Sulfur Nanoparticles in Conducting Polymer Shell as Cathode Materials for High Performance Lithium/Sulfur Batteries. *Scientific Reports*, 3: 1910-1916.
34. Chen, H., Shen, Y., Wang, C., Hu, C., Lu, W., Wu, X., et al. (2018). Review—From Nano Size Effect to In situ Wrapping: Rational Design of Cathode Structure for High Performance Lithium–Sulfur Batteries. *Journal of The Electrochemical Society*, 165(1): A6034-A6042.
35. Chen, H., Wang, C., Dai, Y., Qiu, S., Yang, J., Lu, W., et al. (2015). Rational Design of Cathode Structure for High Rate Performance Lithium–Sulfur Batteries. *Nano Letters*, 15(8): 5443-5448.
36. Chen, H., Wei, Y., Wang, J., Qiao, W., Ling, L., and Long, D. (2015). Controllable Nitrogen Doping of High-Surface-Area Microporous Carbons Synthesized from an Organic–Inorganic Sol–Gel Approach for Li–S Cathodes. *ACS Applied Materials & Interfaces*, 7(38): 21188-21197.
37. Chen, J.-z., Wu, F., Chen, R.-j., Li, L., and Chen, S. (2014). Preparation of Multi-wall Carbon Nanotube/S Composites as Cathodes for Lithium/Sulfur Batteries. *Carbon*, 70: 320.
38. Chen, L., Feng, J., Zhou, H., Fu, C., Wang, G., Yang, L., et al. (2017). Hydrothermal Preparation of Nitrogen, Boron Co-doped Curved Graphene Nanoribbons with High Dopant Amounts for High-Performance Lithium Sulfur Battery Cathodes. *Journal of Materials Chemistry A*, 5(16): 7403-7415.
39. Chen, M., Jiang, S., Huang, C., Wang, X., Cai, S., Xiang, K., et al. (2017). Honeycomb-like Nitrogen and Sulfur Dual-Doped Hierarchical Porous Biomass-Derived Carbon for Lithium–Sulfur Batteries. *ChemSusChem*, 10(8): 1803-1812.
40. Chen, M., Zhao, S., Jiang, S., Huang, C., Wang, X., Yang, Z., et al. (2018). Suppressing the Polysulfide Shuttle Effect by Heteroatom-Doping for High-Performance Lithium–Sulfur Batteries. *ACS Sustainable Chemistry & Engineering*, 6(6): 7545-7557.
41. Chen, R., Zhao, T., and Wu, F. (2015). From a Historic Review to Horizons Beyond: Lithium-Sulphur Batteries Run on the Wheels. *Chemical Communications*, 51(1) 18-33.

42. Chen, S.-R., Zhai, Y.-P., Xu, G.-L., Jiang, Y.-X., Zhao, D.-Y., Li, J.-T., et al. (2011). Ordered Mesoporous Carbon/Sulfur Nanocomposite of High Performances as Cathode for Lithium–Sulfur Battery. *Electrochimica Acta*, 56(26): 9549-9555.
43. Chen, Y., Liu, N., Shao, H., Wang, W., Gao, M., Li, C., et al. (2015). Chitosan as a Functional Additive for High-Performance Lithium–Sulfur Batteries. *Journal of Materials Chemistry A*, 3(29): 15235-15240.
44. Chen, Z.-H., Du, X.-L., He, J.-B., Li, F., Wang, Y., Li, Y.-L., et al. (2017). Porous Coconut Shell Carbon Offering High Retention and Deep Lithiation of Sulfur for Lithium–Sulfur Batteries. *ACS Applied Materials & Interfaces*, 9(39): 33855-33862.
45. Cheng, H., and Wang, S. (2014). Recent Progress in Polymer/Sulphur Composites as Cathodes for Rechargeable Lithium-Sulphur Batteries. *Journal of Materials Chemistry A*, 2(34): 13783-13794.
46. Cheng, J. J., Pan, Y., Pan, J. A., Song, H. J., and Ma, Z. S. (2015). Sulfur/Bamboo Charcoal Composites Cathode for Lithium-Sulfur Batteries. *RSC Advances*, 5(1): 68-74.
47. Cheng, Y., Ji, S., Xu, X., and Liu, J. (2015). Wheat Straw Carbon Matrix Wrapped Sulfur Composites as a Superior Cathode for Li-S Batteries. *RSC Advances*, 5(121): 100089-100096.
48. Chi-Hao, C., Sheng-Heng, C., and Arumugam, M. (2016). Effective Stabilization of a High-Loading Sulfur Cathode and a Lithium-Metal Anode in Li-S Batteries Utilizing SWCNT-Modulated Separators. *Small*, 12(2): 174-179.
49. Choudhury, S., Zeiger, M., Massuti-Ballester, P., Fleischmann, S., Formanek, P., Borchardt, L., et al. (2017). Carbon Onion-Sulfur Hybrid Cathodes for Lithium-Sulfur Batteries. *Sustainable Energy & Fuels*, 1(1): 84-94.
50. Chulliyote, R., Hareendrakrishnakumar, H., Raja, M., Gladis, J. M., and Stephan, A. M. (2017a). Enhanced Cyclability Using a Polyindole Modified Cathode Material for Lithium Sulphur Batteries. *Sustainable Energy & Fuels*, 1(8): 1774-1781.
51. Chulliyote, R., Hareendrakrishnakumar, H., Raja, M., Gladis, J. M., and Stephan, A. M. (2017b). Sulfur-Immobilized Nitrogen and Oxygen Co-doped Hierarchically Porous Biomass Carbon for Lithium-Sulfur Batteries: Influence of Sulfur Content and Distribution on its Performance. *Chemistry Select*, 2(32): 10484-10495.

52. Chung, S.-H., Chang, C.-H., and Manthiram, A. (2016). A Carbon-Cotton Cathode with Ultrahigh-Loading Capability for Statically and Dynamically Stable Lithium–Sulfur Batteries. *ACS Nano*, 10(11): 10462-10470.
53. Chung, S.-H., and Manthiram, A. (2014). High-Performance Li–S Batteries with an Ultra-Lightweight MWCNT-Coated Separator. *The Journal of Physical Chemistry Letters*, 5(11): 1978-1983.
54. Conder, J., Urbonaite, S., Streich, D., Novák, P., and Gubler, L. (2015). Taming the Polysulphide Shuttle in Li–S Batteries by Plasma-Induced Asymmetric Functionalisation of the Separator. *RSC Advances*, 5(97): 79654-79660.
55. Contreras, M. S., Páez, C. A., Zubizarreta, L., Léonard, A., Blacher, S., Olivera-Fuentes, C. G., et al. (2010). A Comparison of Physical Activation of Carbon Xerogels with Carbon Dioxide with Chemical Activation Using Hydroxides. *Carbon*, 48(11): 3157-3168.
56. Conway, B., and Pell, W. (2003). Double-Layer and Pseudocapacitance Types of Electrochemical Capacitors and their Applications to the Development of Hybrid Devices. *Journal of Solid State Electrochemistry*, 7(9): 637-644.
57. Datsyuk, V., Kalyva, M., Papagelis, K., Parthenios, J., Tasis, D., Siokou, A., et al. (2008). Chemical Oxidation of Multiwalled Carbon Nanotubes. *Carbon*, 46(6): 833-840.
58. Daud, W. M. A. W., Ali, W. S. W., and Sulaiman, M. Z. (2001). Effect of Carbonization Temperature on the Yield and Porosity of Char Produced from Palm Shell. *Journal of Chemical Technology & Biotechnology*, 76(12): 1281-1285.
59. Dawei, S., Michael, C., and Guoxiu, W. (2017). Fabrication of N-Doped Graphene–Carbon Nanotube Hybrids from Prussian Blue for Lithium–Sulfur Batteries. *Advanced Energy Materials*, 7(8): 1602014-1602026.
60. Demir-Cakan, R., Morcrette, M., Nouar, F., Davoisne, C., Devic, T., Gonbeau, D., et al. (2011). Cathode Composites for Li–S Batteries via the Use of Oxygenated Porous Architectures. *Journal of the American Chemical Society*, 133(40): 16154-16160.
61. Demiral, H., Demiral, İ., Karabacakoğlu, B., and Tımsek, F. (2011). Production of Activated Carbon from Olive Bagasse by Physical Activation. *Chemical Engineering Research and Design*, 89(2): 206-213.
62. Deng, N., Kang, W., Liu, Y., Ju, J., Wu, D., Li, L., et al. (2016). A Review on Separators for Lithium-Sulfur Battery: Progress and Prospects. *Journal of Power Sources*, 331: 132-155.

63. Deng, W., Zhou, X., Fang, Q., and Liu, Z. (2017). A Bifunctional Hierarchical Porous Carbon Network Integrated with an In situ formed Ultrathin Graphene Shell for Stable Lithium–Sulfur Batteries. *Journal of Materials Chemistry A*, 5(26): 13674-13682.
64. Deng, Y., Xie, Y., Zou, K., and Ji, X. (2016). Review on Recent Advances in Nitrogen-Doped Carbons: Preparations and Applications in Supercapacitors. *Journal of Materials Chemistry A*, 4(4): 1144-1173.
65. Deng, Y., Xu, H., Bai, Z., Huang, B., Su, J., and Chen, G. (2015). Durable Polydopamine-Coated Porous Sulfur Core–Shell Cathode for High Performance Lithium–Sulfur Batteries. *Journal of Power Sources*, 300: 386-394.
66. Dhelipan, M., Arunchander, A., Sahu, A. K., and Kalpana, D. (2017). Activated Carbon from Orange Peels as Supercapacitor Electrode and Catalyst Support for Oxygen Reduction Reaction in Proton Exchange Membrane Fuel Cell. *Journal of Saudi Chemical Society*, 21(4): 487-494.
67. Ding, B., Chang, Z., Wang, J., Dou, H., and Zhang, X. (2016). An In situ Confinement Strategy to Porous Poly(3,4-ethylenedioxythiophene)/Sulfur Composites for Lithium-Sulfur Batteries. *RSC Advances*, 6(53): 47858-47863.
68. Ding, H., Wei, J.-S., and Xiong, H.-M. (2014). Nitrogen and Sulfur Co-doped Carbon Dots with Strong Blue Luminescence. *Nanoscale*, 6(22): 13817-13823.
69. Dirlam, P. T., Glass, R. S., Char, K., and Pyun, J. (2017). The Use of Polymers in Li-S Batteries: A Review. *Journal of Polymer Science Part A: Polymer Chemistry*, 55(10): 1635-1668.
70. Dong, Y., He, R.-T., and Fan, L.-Z. (2017). Graphene and polydopamine Double-Wrapped Porous Carbon-Sulfur Cathode Materials for Lithium-Sulfur Batteries with High Capacity and Cycling Stability. *Ionics*, 23(12): 3329-3337.
71. Dong, Z., Zhang, J., Zhao, X., Tu, J., Su, Q., and Du, G. (2013). Sulfur@Hollow Polypyrrole Sphere Nanocomposites for Rechargeable Li-S Batteries. *RSC Advances*, 3(47): 24914-24917.
72. Donghai, L., Chen, Z., Guangmin, Z., Wei, L., Guowei, L., Linjie, Z., et al. (2018). Catalytic Effects in Lithium–Sulfur Batteries: Promoted Sulfur Transformation and Reduced Shuttle Effect. *Advanced Science*, 5(1): 1700270-1700282.

73. Dresselhaus, M. S., Dresselhaus, G., and Jorio, A. (2007). Raman Spectroscopy of Carbon Nanotubes in 1997 and 2007. *The Journal of Physical Chemistry C*, 111(48): 17887-17893.
74. Dubal, D. P., Chodankar, N. R., Kim, D.-H., and Gomez-Romero, P. (2018). Towards Flexible Solid-State Supercapacitors for Smart and Wearable Electronics. *Chemical Society Reviews*, 47(6): 2065-2129.
75. Dunn, B., Kamath, H., and Tarascon, J.-M. (2011). Electrical Energy Storage for the Grid: A Battery of Choices. *Science*, 334(6058): 928-935.
76. Eftekhari, A., and Kim, D.-W. (2017). Cathode Materials for Lithium–Sulfur Batteries: A Practical Perspective. *Journal of Materials Chemistry A*, 5(34): 17734-17776.
77. Elizabeth, A. O., Tonya, M. A., Dustin, A. G., Susan, M. K., Kai, L., and Angelique, Y. L. (2012). Rapid Microwave-Assisted Synthesis of Dextran-Coated Iron oxide Nanoparticles for Magnetic Resonance Imaging. *Nanotechnology*, 23(21), 215602-215611.
78. Enock, T. K., Kingondu, C. K., Pogrebnoi, A., and Jande, Y. A. C. (2017). Status of Biomass Derived Carbon Materials for Supercapacitor Application. *International Journal of Electrochemistry*, 2017, 14.
79. Falco, C., Sieben, J. M., Brun, N., Sevilla, M., van der Maelen, T., Morallón, E., et al. (2013). Hydrothermal Carbons from Hemicellulose-Derived Aqueous Hydrolysis Products as Electrode Materials for Supercapacitors. *ChemSusChem*, 6(2): 374-382.
80. Fan, C.-Y., Liu, S.-Y., Li, H.-H., Shi, Y.-H., Wang, H.-C., Wang, H.-F., et al. (2017). Synergistic Mediation of Sulfur Conversion in Lithium–Sulfur Batteries by a Gerber Tree-like Interlayer with Multiple Components. *Journal of Materials Chemistry A*, 5(22): 11255-11262.
81. Fan, H., Niu, R., Duan, J., Liu, W., and Shen, W. (2016). Fe₃O₄@Carbon Nanosheets for All-Solidstate Supercapacitor Electrodes. *ACS Applied Materials & Interfaces*, 8(30): 19475-19483.
82. Fan, M., An, Y., Yin, H., Li, W., Sun, W., and Lin, Z. (2018). Self-Assembled Reduced Graphene Oxide/Sulfur Composite Encapsulated by Polyaniline for Enhanced Electrochemistry Performance. *Journal of Solid State Electrochemistry*, 22(3): 667-675.
83. Fan, Q., Liu, W., Weng, Z., Sun, Y., and Wang, H. (2015). Ternary Hybrid Material for High-Performance Lithium–Sulfur Battery. *Journal of the American Chemical Society*, 137(40): 12946-12953.

84. Fan, W., Zhang, L., and Liu, T. (2018). Multifunctional Second Barrier Layers for Lithium–Sulfur Batteries. *Materials Chemistry Frontiers*, 2(2): 235-252.
85. Fan, X., Sun, W., Meng, F., Xing, A., and Liu, J. (2018). Advanced Chemical Strategies for Lithium–Sulfur Batteries: A Review. *Green Energy & Environment*, 3(1): 2-19.
86. Fei, P., Taihua, A., Jun, Z., Xiaojing, Z., Xiaoliang, F., Minseng, Z., et al. (2016). From Hollow Carbon Spheres to N-Doped Hollow Porous Carbon Bowls: Rational Design of Hollow Carbon Host for Li-S Batteries. *Advanced Energy Materials*, 6(8): 1502539-1502547.
87. Feifei, Z., Yunhui, D., Yun, H., Gang, H., Xinbo, Z., and Limin, W. (2012). Preparation and Performance of a Sulfur/Graphene Composite for Rechargeable Lithium-Sulfur Battery. *Journal of Physics: Conference Series*, 339(1): 012003-012008.
88. Feng, H., Zheng, M., Dong, H., Xiao, Y., Hu, H., Sun, Z., et al. (2015). Three-Dimensional Honeycomb-like Hierarchically Structured Carbon for High-Performance Supercapacitors Derived from High-Ash-Content Sewage Sludge. *Journal of Materials Chemistry A*, 3(29): 15225-15234.
89. Feng, J., Qin, X., Ma, Z., Yang, J., Yang, W., and Shao, G. (2016). A Novel Acetylene Black/Sulfur@Graphene Composite Cathode with Unique Three-Dimensional Sandwich Structure for Lithium-Sulfur Batteries. *Electrochimica Acta*, 190: 426-433.
90. Feng, N., Guo, X., Liang, S., Zhu, Y., and Liu, J. (2011). Biosorption of Heavy Metals from Aqueous Solutions by Chemically Modified Orange Peel. *Journal of Hazardous Materials*, 185(1): 49-54.
91. Feng, S., Song, J., Fu, S., Zhu, C., Shi, Q., Song, M.-K., et al. (2017). One-Step Synthesis of Carbon Nanosheet-Decorated Carbon Nanofibers as a 3D Interconnected Porous Carbon Scaffold for Lithium–Sulfur Batteries. *Journal of Materials Chemistry A*, 5(45): 23737-23743.
92. Fernandez, M. E., Ledesma, B., Román, S., Bonelli, P. R., and Cukierman, A. L. (2015). Development and Characterization of Activated Hydrochars from Orange Peels as Potential Adsorbents for Emerging Organic Contaminants. *Bioresource Technology*, 183: 221-228.
93. Fernandez, M. E., Nunell, G. V., Bonelli, P. R., and Cukierman, A. L. (2014). Activated Carbon Developed from Orange Peels: Batch and Dynamic Competitive Adsorption of Basic Dyes. *Industrial Crops and Products*, 62: 437-445.

94. François, B., Volker, P., Andrea, B., and Elzbieta, F. (2014). Carbons and Electrolytes for Advanced Supercapacitors. *Advanced Materials*, 26(14): 2219-2251.
95. Fu, K., Li, Y., Dirican, M., Chen, C., Lu, Y., Zhu, J., et al. (2014). Sulfur Gradient-Distributed CNF Composite: A Self-Inhibiting Cathode for Binder-Free Lithium-Sulfur Batteries. *Chemical Communications*, 50(71): 10277-10280.
96. Fu, Y., and Manthiram, A. (2012a). Core-Shell Structured Sulfur-Polypyrrole Composite Cathodes for Lithium-Sulfur Batteries. *RSC Advances*, 2(14): 5927-5929.
97. Fu, Y., and Manthiram, A. (2012b). Enhanced Cyclability of Lithium-Sulfur Batteries by a Polymer Acid-Doped Polypyrrole Mixed Ionic-Electronic Conductor. *Chemistry of Materials*, 24(15): 3081-3087.
98. Fu, Y., and Manthiram, A. (2012c). Orthorhombic Bipyramidal Sulfur Coated with Polypyrrole Nanolayers as a Cathode Material for Lithium-Sulfur Batteries. *The Journal of Physical Chemistry C*, 116(16): 8910-8915.
99. Fu, Y., Su, Y.-S., and Manthiram, A. (2012). Sulfur-Carbon Nanocomposite Cathodes Improved by an Amphiphilic Block Copolymer for High-Rate Lithium-Sulfur Batteries. *ACS Applied Materials & Interfaces*, 4(11): 6046-6052.
100. Fuertes, A. B., and Sevilla, M. (2015). Hierarchical Microporous/Mesoporous Carbon Nanosheets for High-Performance Supercapacitors. *ACS Applied Materials & Interfaces*, 7(7): 4344-4353.
101. Gao, Z., Sun, H., Fu, L., Ye, F., Zhang, Y., Luo, W., et al. (2018). Promises, Challenges, and Recent Progress of Inorganic Solid-State Electrolytes for All-Solid-State Lithium Batteries. *Advanced Materials*, 30(17): 1705702.
102. Gao, Z., Zhang, Y., Song, N., and Li, X. (2017). Biomass-Derived Renewable Carbon Materials for Electrochemical Energy Storage. *Materials Research Letters*, 5(2): 69-88.
103. Gong, Y., Fu, C., Zhang, G., Zhou, H., and Kuang, Y. (2017). Three-Dimensional Porous C₃N₄ Nanosheets@Reduced Graphene Oxide Network as Sulfur Hosts for High Performance Lithium-Sulfur Batteries. *Electrochimica Acta*, 256: 1-9.
104. Goodenough, J. B., and Park, K.-S. (2013). The Li-ion Rechargeable Battery: A Perspective. *Journal of the American Chemical Society*, 135(4): 1167-1176.

105. Gopalakrishnan, R., Goutam, S., Miguel Oliveira, L., Timmermans, J.-M., Omar, N., Messagie, M., et al. (2017). A Comprehensive Study on Rechargeable Energy Storage Technologies. *Journal of Electrochemical Energy Conversion and Storage*, 13(4): 040801-040825.
106. Gu, X., and Lai, C. (2018). Recent Development of Metal Compound Applications in Lithium–Sulphur Batteries. *Journal of Materials Research*, 33(1): 16-31.
107. Gu, X., Wang, Y., Lai, C., Qiu, J., Li, S., Hou, Y., et al. (2015). Microporous Bamboo Biochar for Lithium-Sulfur Batteries. *Nano Research*, 8(1): 129-139.
108. Guiza, S. (2017). Biosorption of Heavy Metal from Aqueous Solution Using Cellulosic Waste Orange Peel. *Ecological Engineering*, 99: 134-140.
109. Gulzar, U., Li, T., Bai, X., Colombo, M., Ansaldo, A., Marras, S., et al. (2018). Nitrogen-Doped Single-Walled Carbon Nanohorns as a Cost-Effective Carbon Host Toward High-Performance Lithium–Sulfur Batteries. *ACS Applied Materials & Interfaces*, 10(6): 5551-5559.
110. Guo, C. X., and Li, C. M. (2011). A Self-Assembled Hierarchical Nanostructure Comprising Carbon Spheres and Graphene Nanosheets for Enhanced Supercapacitor Performance. *Energy & Environmental Science*, 4(11): 4504-4507.
111. Guo, J., Xu, Y., and Wang, C. (2011). Sulfur-Impregnated Disordered Carbon Nanotubes Cathode for Lithium–Sulfur Batteries. *Nano Letters*, 11(10): 4288-4294.
112. Guo, J., Zhang, J., Jiang, F., Zhao, S., Su, Q., and Du, G. (2015). Microporous Carbon Nanosheets Derived from Corncobs for Lithium–Sulfur Batteries. *Electrochimica Acta*, 176: 853-860.
113. Guo, X., Zheng, S., Zhang, G., Xiao, X., Li, X., Xu, Y., et al. (2017). Nanostructured Graphene-Based Materials for Flexible Energy Storage. *Energy Storage Materials*, 9: 150-169.
114. Gupta, H., and Singh, S. (2018). Kinetics and Thermodynamics of Phenanthrene Adsorption from Water on Orange Rind Activated Carbon. *Environmental Technology & Innovation*, 10: 208-214.
115. Hagen, M., Dörfler, S., Althues, H., Tübke, J., Hoffmann, M. J., Kaskel, S., et al. (2012). Lithium–Sulphur Batteries – Binder Free Carbon Nanotubes Electrode Examined with Various Electrolytes. *Journal of Power Sources*, 213: 239-248.

116. Hagen, M., Dörfler, S., Fanz, P., Berger, T., Speck, R., Tübke, J., et al. (2013). Development and Costs Calculation of Lithium–Sulfur Cells with High Sulfur Load and Binder Free Electrodes. *Journal of Power Sources*, 224: 260-268.
117. Han, J., Li, Y., Li, S., Long, P., Cao, C., Cao, Y., et al. (2018). A Low Cost Ultra-Microporous Carbon Scaffold with Confined Chain-Like Sulfur Molecules as a Superior Cathode for Lithium-Sulfur Batteries. *Sustainable Energy & Fuels*. 2(10): 2187-2196
118. Han, P., and Manthiram, A. (2017). Boron- and Nitrogen-Doped Reduced Graphene Oxide Coated Separators for High-Performance Li-S Batteries. *Journal of Power Sources*, 369: 87-94.
119. Hanesch, M. (2009). Raman Spectroscopy of Iron Oxides and (Oxy)hydroxides at Low Laser Power and Possible Applications in Environmental Magnetic Studies. *Geophysical Journal International*, 177(3): 941-948.
120. Hao, Y., Shi, Z., Wang, J., and Xu, Q. (2015). One Step Production of In situ Nitrogen Doped Mesoporous Carbon Confined Sulfur for Lithium–Sulfur Batteries. *RSC Advances*, 5(40): 31629-31636.
121. Hao, Z., Zeng, R., Yuan, L., Bing, Q., Liu, J., Xiang, J., et al. (2017). Perovskite La_{0.6}Sr_{0.4}CoO_{3-δ} as a New Polysulfide Immobilizer for High-Energy Lithium-Sulfur Batteries. *Nano Energy*, 40: 360-368.
122. Hasegawa, G., Deguchi, T., Kanamori, K., Kobayashi, Y., Kageyama, H., Abe, T., et al. (2015). High-Level Doping of Nitrogen, Phosphorus, and Sulfur into Activated Carbon Monoliths and their Electrochemical Capacitances. *Chemistry of Materials*, 27(13): 4703-4712.
123. Hassan, F. M., Batmaz, R., Li, J., Wang, X., Xiao, X., Yu, A., et al. (2015). Evidence of Covalent Synergy in Silicon–Sulfur–Graphene Yielding Highly Efficient and Long-Life Lithium-ion Batteries. *Nature Communications*, 6: 8597-8608.
124. Hayashi, A., Ohtsubo, R., Ohtomo, T., Mizuno, F., and Tatsumisago, M. (2008). All-Solid-State Rechargeable Lithium Batteries with Li₂S as a Positive Electrode Material. *Journal of Power Sources*, 183(1), 422-426.
125. Hayashi, J. i., Kazehaya, A., Muroyama, K., and Watkinson, A. P. (2000). Preparation of Activated Carbon from Lignin by Chemical Activation. *Carbon*, 38(13), 1873-1878.
126. He, G., Ji, X., and Nazar, L. (2011). High "C" Rate Li-S cathodes: Sulfur Imbibed Bimodal Porous Carbons. *Energy & Environmental Science*, 4(8), 2878-2883.

127. He, J., Chen, Y., Li, P., Fu, F., Wang, Z., and Zhang, W. (2015). Three-Dimensional CNT/Graphene-Sulfur Hybrid Sponges with High Sulfur Loading as Superior-Capacity Cathodes for Lithium-Sulfur Batteries. *Journal of Materials Chemistry A*, 3(36): 18605-18610.
128. He, Y., Chang, Z., Wu, S., and Zhou, H. (2018). Effective Strategies for Long-Cycle Life Lithium-Sulfur Batteries. *Journal of Materials Chemistry A*, 6(15): 6155-6182.
129. He, Y., Han, X., Du, Y., Zhang, B., and Xu, P. (2016). Heteroatom-Doped Carbon Nanostructures Derived from Conjugated Polymers for Energy Applications. *Polymers*, 8(10): 366-384.
130. He, Y., Qiao, Y., and Zhou, H. (2018). Recent Advances in Functional Modification of Separators in Lithium-Sulfur Batteries. *Dalton Transactions*, 47(20): 6881-6887.
131. Hernández-Rentero, C., Córdoba, R., Moreno, N., Caballero, A., Morales, J., Olivares-Marín, M., et al. (2018). Low-Cost Disordered Carbons for Li/S Batteries: A High-Performance Carbon with Dual Porosity Derived from Cherry Pits. *Nano Research*, 11(1): 89-100.
132. Hnedkovsky, L., Wood, R. H., and Balashov, V. N. (2005). Electrical Conductances of Aqueous Na₂SO₄, H₂SO₄, and their Mixtures: Limiting Equivalent Ion Conductances, Dissociation constants, and Speciation to 673 K and 28 MPa. *The Journal of Physical Chemistry B*, 109(18): 9034-9046.
133. Hou, Y., Xiao, J., Guo, Y., Qi, M., Jiang, A., and Li, Y. (2017). Gaseous-Phase, Silica-Coated Sulfur Particles as a Cathode Material for High-Performance Lithium/Sulfur Batteries. *Journal of Materials Science: Materials in Electronics*, 28(12): 8901-8907.
134. Housseinou, B., Wei, W., Sergey, P., Thierry, R., Walid, B., Lam, N.-D., et al. (2018). Biosourced Foam-like Activated Carbon Materials as High-Performance Supercapacitors. *Advanced Sustainable Systems*, 2(2): 1700123-1700135.
135. Hu, C., Chen, H., Shen, Y., Lu, D., Zhao, Y., Lu, A.-H., et al. (2017). In situ Wrapping of the Cathode Material in Lithium-Sulfur Batteries. *Nature Communications*, 8: 479-488.
136. Hu, F., Wang, J., Hu, S., Li, L., Wang, G., Qiu, J., et al. (2016). Inherent N,O-Containing Carbon Frameworks as Electrode Materials for High-Performance Supercapacitors. *Nanoscale*, 8(36): 16323-16331.

137. Huang, A., Chen, L.-H., Chen, C.-H., Tsai, H.-Y., and Tung, K.-L. (2018). Carbon dioxide Capture Using an Omniphobic Membrane for a Gas-Liquid Contacting Process. *Journal of Membrane Science*, 556: 227-237.
138. Huang, J.-Q., Zhang, Q., Peng, H.-J., Liu, X.-Y., Qian, W.-Z., and Wei, F. (2014). Ionic Shield for Polysulfides Towards Highly-Stable Lithium-Sulfur Batteries. *Energy & Environmental Science*, 7(1): 347-353.
139. Huang, J.-Q., Zhuang, T.-Z., Zhang, Q., Peng, H.-J., Chen, C.-M., and Wei, F. (2015). Permselective Graphene Oxide Membrane for Highly Stable and Anti-Self-Discharge Lithium-Sulfur Batteries. *ACS Nano*, 9(3): 3002-3011.
140. Huang, S., Zhang, L., Wang, J., Zhu, J., and Shen, P. K. (2018). In situ Carbon Nanotube Clusters Grown from Three-Dimensional Porous Graphene Networks as Efficient Sulfur Hosts for High-Rate Ultra-Stable Li-S Batteries. *Nano Research*, 11(3): 1731-1743.
141. Huang, X., Sun, B., Li, K., Chen, S., and Wang, G. (2013). Mesoporous Graphene Paper Immobilised Sulfur as a Flexible Electrode for Lithium-Sulfur Batteries. *Journal of Materials Chemistry A*, 1(43): 13484-13489.
142. Huangfu, Y., Zheng, T., Zhang, K., She, X., Xu, H., Fang, Z., et al. (2018). Facile Fabrication of Permselective g-C₃N₄ Separator for Improved Lithium-Sulfur batteries. *Electrochimica Acta*, 272: 60-67.
143. Hui, Z., Wenqi, Z., Mingchu, Z., Yunsong, W., Yijun, C., Lu, X., et al. (2018). 3D, Mutually Embedded MOF@Carbon Nanotube Hybrid Networks for High-Performance Lithium-Sulfur Batteries. *Advanced Energy Materials*, 8(19): 1800013-1800024.
144. Hui, Z., Xiaolei, W., Xuexia, L., and Xiurong, Y. (2012). Integrated Synthesis of Poly(o-phenylenediamine)-Derived Carbon Materials for High Performance Supercapacitors. *Advanced Materials*, 24(48): 6524-6529.
145. Imtiaz, S., Zhang, J., Zafar, Z. A., Ji, S., Huang, T., Anderson, J. A., et al. (2016). Biomass-Derived Nanostructured Porous Carbons for Lithium-Sulfur Batteries. *Science China Materials*, 59(5): 389-407.
146. Ji, X., Evers, S., Black, R., and Nazar, L. F. (2011). Stabilizing Lithium-Sulphur Cathodes Using Polysulphide Reservoirs. *Nature Communications*, 2: 325-332.
147. Ji, X., Lee, K. T., and Nazar, L. F. (2009). A Highly Ordered Nanostructured Carbon-Sulphur Cathode for Lithium-Sulphur Batteries. *Nature Materials*, 8: 500-506.

148. Jiang, J., Zhu, J., Ai, W., Wang, X., Wang, Y., Zou, C., et al. (2015). Encapsulation of Sulfur with Thin-Layered Nickel-Based Hydroxides for Long-Cyclic Lithium–Sulfur Cells. *Nature Communications*, 6: 8622-8631.
149. Jiang, K., Gao, S., Wang, R., Jiang, M., Han, J., Gu, T., et al. (2018). Lithium Sulfonate/Carboxylate-Anchored Polyvinyl Alcohol Separators for Lithium Sulfur Batteries. *ACS Applied Materials & Interfaces*, 10(21): 18310-18315.
150. Jiang, S., Chen, M., Wang, X., Zhang, Y., Huang, C., Zhang, Y., et al. (2019). Honeycomb-Like Nitrogen and Sulfur Dual-Doped Hierarchical Porous Biomass Carbon Bifunctional Interlayer for Advanced Lithium-Sulfur Batteries. *Chemical Engineering Journal*, 355: 478-486.
151. Jin, C., Zhang, W., Zhuang, Z., Wang, J., Huang, H., Gan, Y., et al. (2017). Enhanced Sulfide Chemisorption Using Boron and Oxygen Dually Doped Multi-Walled Carbon Nanotubes for Advanced Lithium-Sulfur Batteries. *Journal of Materials Chemistry A*, 5(2), 632-640.
152. Jin, J., Wen, Z., Ma, G., Lu, Y., Cui, Y., Wu, M., et al. (2013). Flexible Self-Supporting Graphene-Sulfur Paper for Lithium Sulfur Batteries. *RSC Advances*, 3(8): 2558-2560.
153. Jin, Z., Xie, K., and Hong, X. (2013). Electrochemical Performance of Lithium/Sulfur Batteries Using Perfluorinated Ionomer Electrolyte with Lithium Sulfonyl Dicyanomethide Functional Groups as Functional Separator. *RSC Advances*, 3(23): 8889-8898.
154. Jörg, S., Guang, H., Benjamin, M., Taeun, Y., Tae, L. K., Thomas, B., et al. (2012). Spherical Ordered Mesoporous Carbon Nanoparticles with High Porosity for Lithium–Sulfur Batteries. *Angewandte Chemie International Edition*, 51(15), 3591-3595.
155. Juan, B., Tony, J., Markus, K., Steffen, O., Jürgen, E., and Lars, G. (2015). Functional Mesoporous Carbon-Coated Separator for Long-Life, High-Energy Lithium–Sulfur Batteries. *Advanced Functional Materials*, 25(33): 5285-5291.
156. Judez, X., Zhang, H., Li, C., Eshetu, G. G., González-Marcos, J. A., Armand, M., et al. (2018). Review—Solid Electrolytes for Safe and High Energy Density Lithium-Sulfur Batteries: Promises and Challenges. *Journal of The Electrochemical Society*, 165(1): A6008-A6016.
157. Judez, X., Zhang, H., Li, C., Eshetu, G. G., Zhang, Y., González-Marcos, J. A., et al. (2017). Polymer-Rich Composite Electrolytes for All-Solid-State Li–S Cells. *The Journal of Physical Chemistry Letters*, 8(15): 3473-3477.

158. K., S. V., Erkin, C. M., Xuwen, L., Leena-Sisko, J., Yanling, G., and Simo-Pekka, H. (2014). Tuning the Mechanical and Adsorption Properties of Silica with Graphene Oxide. *ChemPlusChem*, 79(10): 1512-1522.
159. Kai, Y., Qiuming, G., Yanli, T., Weiqian, T., Weiwei, Q., Lihua, Z., et al. (2016). Biomass-Derived Porous Carbon with Micropores and Small Mesopores for High-Performance Lithium–Sulfur Batteries. *Chemistry – European Journal*, 22(10): 3239-3244.
160. Kalpana, D., Cho, S. H., Lee, S. B., Lee, Y. S., Misra, R., and Renganathan, N. G. (2009). Recycled Waste Paper—A New Source of Raw Material for Electric Double-Layer Capacitors. *Journal of Power Sources*, 190(2): 587-591.
161. Kang, W., Fan, L., Deng, N., Zhao, H., Li, Q., Naebe, M., et al. (2018). Sulfur-Embedded Porous Carbon Nanofiber Composites for High Stability Lithium-Sulfur Batteries. *Chemical Engineering Journal*, 333: 185-190.
162. Kang, X., Zhu, H., Wang, C., Sun, K., and Yin, J. (2018). Biomass Derived Hierarchically Porous and Heteroatom-Doped Carbons for Supercapacitors. *Journal of Colloid and Interface Science*, 509(Supplement C): 369-383.
163. Karthikeyan, K., Amaresh, S., Lee, S. N., Sun, X., Aravindan, V., Lee, Y.-G., et al. (2014). Construction of High-Energy-Density Supercapacitors from Pine-cone-Derived High-Surface-Area Carbons. *ChemSusChem*, 7(5): 1435-1442.
164. Ke, C., Zhenhua, S., Ruopian, F., Ying, S., Hui-Ming, C., and Feng, L. (2018). Metal–Organic Frameworks (MOFs)-Derived Nitrogen-Doped Porous Carbon Anchored on Graphene with Multifunctional Effects for Lithium–Sulfur Batteries. *Advanced Functional Materials*, 28(38): 1707592-1707600.
165. Khaled, A., Nemr, A. E., El-Sikaily, A., and Abdelwahab, O. (2009). Removal of Direct N Blue-106 from Artificial Textile Dye Effluent Using Activated Carbon from Orange Peel: Adsorption Isotherm and Kinetic Studies. *Journal of Hazardous Materials*, 165(1): 100-110.
166. Kim, C. H., Lee, D.-K., and Pinnavaia, T. J. (2004). Graphitic Mesostructured Carbon Prepared from Aromatic Precursors. *Langmuir*, 20(13): 5157-5159.
167. Kim, E. T., Park, J., Kim, C., Simmonds, A. G., Sung, Y.-E., Pyun, J., et al. (2016). Conformal Polymeric Multilayer Coatings on Sulfur Cathodes Via the Layer-By-Layer Deposition for High Capacity Retention in Li–S Batteries. *ACS Macro Letters*, 5(4): 471-475.

168. Kim, K. H., Jun, Y.-S., Gerbec, J. A., See, K. A., Stucky, G. D., and Jung, H.-T. (2014). Sulfur Infiltrated Mesoporous Graphene–Silica Composite as a Polysulfide Retaining Cathode Material for Lithium–Sulfur Batteries. *Carbon*, 69: 543-551.
169. Kobayashi, T., Imade, Y., Shishihara, D., Homma, K., Nagao, M., Watanabe, R., et al. (2008). All Solid-State Battery with Sulfur Electrode and Thio-LISICON Electrolyte. *Journal of Power Sources*, 182(2): 621-625.
170. Koiry, S. P., Saxena, V., Sutar, D., Bhattacharya, S., Aswal, D. K., Gupta, S. K., et al. (2007). Interfacial Synthesis of Long Polyindole Fibers. *Journal of Applied Polymer Science*, 103(1): 595-599.
171. Konnola, R., Joji, J., Parameswaranpillai, J., and Joseph, K. (2015). Structure and Thermo-Mechanical Properties of CTBN-grafted-GO Modified Epoxy/DDS Composites. *RSC Advances*, 5(76): 61775-61786.
172. Krüner, B., Schreiber, A., Tolosa, A., Quade, A., Badaczewski, F., Pfaff, T., et al. (2018). Nitrogen-Containing Novolac-Derived Carbon Beads as Electrode Material for Supercapacitors. *Carbon*, 132: 220-231.
173. Kumar, R., Liu, J., Hwang, J.-Y., and Sun, Y.-K. (2018). Recent Research Trends in Li–S Batteries. *Journal of Materials Chemistry A*, 6(25): 11582-11605.
174. Kwiatkowski, M., and Broniek, E. (2017). An Analysis of the Porous Structure of Activated Carbons Obtained from Hazelnut Shells by Various Physical and Chemical Methods of Activation. *Colloids and Surfaces A: Physicochemical and Engineering Aspects*, 529: 443-453.
175. Lachos-Perez, D., Baseggio, A. M., Mayanga-Torres, P. C., Maróstica, M. R., Rostagno, M. A., Martínez, J., et al. (2018). Subcritical Water Extraction of Flavanones from Defatted Orange Peel. *The Journal of Supercritical Fluids*, 138: 7-16.
176. Lai, Y., Wang, P., Qin, F., Xu, M., Li, J., Zhang, K., et al. (2017). A Carbon Nanofiber@Mesoporous δ -MnO₂ Nanosheet-Coated Separator for High-Performance Lithium-Sulfur Batteries. *Energy Storage Materials*, 9: 179-187.
177. Lam, S. S., Liew, R. K., Wong, Y. M., Yek, P. N. Y., Ma, N. L., Lee, C. L., et al. (2017). Microwave-Assisted Pyrolysis with Chemical Activation, an Innovative Method to Convert Orange Peel into Activated Carbon with Improved Properties as Dye Adsorbent. *Journal of Cleaner Production*, 162: 1376-1387.

178. Lee, C. L., H'ng, P., Paridah, T., Chin, K. L., Khoo, P., Nazrin, R. A. R., et al. (2017). Effect of Reaction Time and Temperature on the Properties of Carbon Black made from Palm Kernel and Coconut Shell. *Asian Journal of Scientific Research*, 10: 24-33.
179. Lee, H.-Y., Jung, Y., and Kim, S. (2016). Conducting Polymer Coated Graphene Oxide Electrode for Rechargeable Lithium-Sulfur Batteries. *Journal of Nanoscience and Nanotechnology*, 16(3): 2692-2695.
180. Lee, J., Hwang, T., Lee, Y., Lee, J. K., and Choi, W. (2015). Coating of Sulfur Particles with Manganese Oxide Nanowires as a Cathode Material in Lithium-Sulfur Batteries. *Materials Letters*, 158: 132-135.
181. Lee, J. S., and Manthiram, A. (2017). Hydroxylated N-Doped Carbon Nanotube-Sulfur Composites as Cathodes for High-Performance Lithium-Sulfur Batteries. *Journal of Power Sources*, 343: 54-59.
182. Lei, H., Yue, L., Xiaona, L., Jianwen, L., Tao, H., Yongchun, Z., et al. (2017). Optimization of Microporous Carbon Structures for Lithium-Sulfur Battery Applications in Carbonate-Based Electrolyte. *Small*, 13(11): 1603533.
183. Li, B., Xiao, Q., and Luo, Y. (2017). A polymer Enhanced Sulfur/Graphene Aerogel as a No-Slurry Cathode for Lithium-Sulfur Batteries. *RSC Advances*, 7(86): 54453-54459.
184. Li, C., Zou, Y., Duan, J., Wang, Y., Qi, Z., and Li, Z. (2018). Polythiophene Lamella Wrapped Sulfur as Cathode for Rechargeable Lithium Sulfur Batteries. *Materials Letters*, 218: 142-145.
185. Li, D., Han, F., Wang, S., Cheng, F., Sun, Q., and Li, W.-C. (2013). High Sulfur Loading Cathodes Fabricated Using Peapod like, Large Pore Volume Mesoporous Carbon for Lithium-Sulfur Battery. *ACS Applied Materials & Interfaces*, 5(6): 2208-2213.
186. Li, F., Qin, F., Zhang, K., Fang, J., Lai, Y., and Li, J. (2017). Hierarchically Porous Carbon Derived from Banana Peel for Lithium Sulfur Battery with High Areal and Gravimetric Sulfur Loading. *Journal of Power Sources*, 362: 160-167.
187. Li, G., Sun, J., Hou, W., Jiang, S., Huang, Y., and Geng, J. (2016). Three-Dimensional Porous Carbon Composites Containing High Sulfur Nanoparticle Content for High-Performance Lithium-Sulfur Batteries. *Nature Communications*, 7: 10601-10611.
188. Li, G. C., Jing, H. K., Su, Z., Lai, C., Chen, L., Yuan, C. C., et al. (2015). A hydrophilic Separator for High Performance Lithium Sulfur Batteries. *Journal of Materials Chemistry A*, 3(20): 11014-11020.

189. Li, H., Yang, X., Wang, X., He, Y.-S., Ye, F., Liu, M., et al. (2016). A Dual-Spatially-Confined Reservoir by Packing Micropores Within Dense Graphene for Long-Life Lithium/Sulfur Batteries. *Nanoscale*, 8(4): 2395-2402.
190. Li, J., Guo, Y., Wen, P., Zhu, J., Liu, Z., and Qiu, Y. (2018). Zinc acetate Activation-Enhanced Performance of Hollow Nano silica/Carbon Composite Nanofibers for Lithium-Sulfur Batteries. *Journal of Electroanalytical Chemistry*, 823: 287-295.
191. Li, J., Ma, S., Cheng, L., and Wu, Q. (2015). Egg Yolk-Derived Three-Dimensional Porous Carbon for Stable Electrochemical Supercapacitors. *Materials Letters*, 139: 429-432.
192. Li, J., Qin, F., Zhang, L., Zhang, K., Li, Q., Lai, Y., et al. (2014). Mesoporous Carbon from Biomass: One-Pot Synthesis and Application for Li-S Batteries. *Journal of Materials Chemistry A*, 2(34): 13916-13922.
193. Li, J., Zan, G., and Wu, Q. (2016). Nitrogen and Sulfur Self-Doped Porous Carbon from Brussel Sprouts as Electrode Materials for High Stable Supercapacitors. *RSC Advances*, 6(62): 57464-57472.
194. Li, K., Tian, S., Jiang, J., Wang, J., Chen, X., and Yan, F. (2016). Pine cone Shell-Based Activated Carbon Used for CO₂ Adsorption. *Journal of Materials Chemistry A*, 4(14): 5223-5234.
195. Li, L., Liu, X., Zhu, K., Tian, J., Liu, X., Yang, K., et al. (2015). PEO-Coated Sulfur-Carbon Composite for High-Performance Lithium-Sulfur Batteries. *Journal of Solid State Electrochemistry*, 19(11): 3373-3379.
196. Li, N., Zheng, M., Lu, H., Hu, Z., Shen, C., Chang, X., et al. (2012). High-Rate Lithium-Sulfur Batteries Promoted by Reduced Graphene Oxide Coating. *Chemical Communications*, 48(34): 4106-4108.
197. Li, Q., Song, Y., Xu, R., Zhang, L., Gao, J., Xia, Z., et al. (2018). Biotemplating Growth of Nepenthes-like N-Doped Graphene as a Bifunctional Polysulfide Scavenger for Li-S Batteries. *ACS Nano*.
198. Li, Q., Zhang, Z., Zhang, K., Fang, J., Lai, Y., and Li, J. (2014). A Simple Synthesis of Hollow Carbon Nanofiber-Sulfur Composite Via Mixed-Solvent Process for Lithium-Sulfur Batteries. *Journal of Power Sources*, 256: 137-144.
199. Li, W., Hicks-Garner, J., Wang, J., Liu, J., Gross, A. F., Sherman, E., et al. (2014). V₂O₅ Polysulfide Anion Barrier for Long-Lived Li-S Batteries. *Chemistry of Materials*, 26(11): 3403-3410.

200. Li, X., Cheng, X., Gao, M., Ren, D., Liu, Y., Guo, Z., et al. (2017). Amylose-Derived Macrohollow Core and Microporous Shell Carbon Spheres as Sulfur Host for Superior Lithium–Sulfur Battery Cathodes. *ACS Applied Materials & Interfaces*, 9(12): 10717-10729.
201. Li, X., Rao, M., Chen, D., Lin, H., Liu, Y., Liao, Y., et al. (2015). Sulfur Supported by Carbon Nanotubes and Coated with Polyaniline: Preparation and Performance as Cathode of Lithium-Sulfur Cell. *Electrochimica Acta*, 166: 93-99.
202. Li, X., and Sun, X. (2014). Nitrogen-Doped Carbons in Li–S Batteries: Materials Design and Electrochemical Mechanism. *Frontiers in Energy Research*, 2(49): 1-9.
203. Li, X., Xing, W., Zhuo, S., Zhou, J., Li, F., Qiao, S.-Z., et al. (2011). Preparation of Capacitor's Electrode from Sunflower Seed Shell. *Bioresource Technology*, 102(2): 1118-1123.
204. Li, Y.-T., Pi, Y.-T., Lu, L.-M., Xu, S.-H., and Ren, T.-Z. (2015). Hierarchical Porous Active Carbon from Fallen Leaves by Synergy of K_2CO_3 and their Supercapacitor Performance. *Journal of Power Sources*, 299: 519-528.
205. Li, Y., Wang, G., Wei, T., Fan, Z., and Yan, P. (2016). Nitrogen and Sulfur Co-doped Porous Carbon Nanosheets Derived from Willow Catkin for Supercapacitors. *Nano Energy*, 19(Supplement C): 165-175.
206. Li, Y., Wang, L., Gao, B., Li, X., Cai, Q., Li, Q., et al. (2017). Hierarchical Porous Carbon Materials Derived from Self-Template Bamboo Leaves for Lithium–Sulfur Batteries. *Electrochimica Acta*, 229: 352-360.
207. Li, Y., Xu, X., He, Y., Jiang, Y., and Lin, K. (2017). Nitrogen Doped Macroporous Carbon as Electrode Materials for High Capacity of Supercapacitor. *Polymers*, 9(1): 2.
208. Li, Y., Ye, D., Liu, W., Shi, B., Guo, R., Zhao, H., et al. (2016). A MnO₂/Graphene Oxide/Multi-Walled Carbon Nanotubes-Sulfur Composite with Dual-Efficient Polysulfide Adsorption for Improving Lithium-Sulfur Batteries. *ACS Applied Materials & Interfaces*, 8(42): 28566-28573.
209. Li, Z., Huang, Y., Yuan, L., Hao, Z., and Huang, Y. (2015). Status and Prospects in Sulfur–Carbon Composites as Cathode Materials for Rechargeable Lithium–Sulfur Batteries. *Carbon*, 92: 41-63.
210. Li, Z., Jiang, Q., Ma, Z., Liu, Q., Wu, Z., and Wang, S. (2015). Oxygen Plasma Modified Separator for Lithium Sulfur Battery. *RSC Advances*, 5(97): 79473-79478.

211. Li, Z., and Yin, L. (2015). Nitrogen-Doped MOF-Derived Micropores Carbon as Immobilizer for Small Sulfur Molecules as a Cathode for Lithium Sulfur Batteries with Excellent Electrochemical Performance. *ACS Applied Materials & Interfaces*, 7(7): 4029-4038.
212. Liang, C., Dudney, N. J., and Howe, J. Y. (2009). Hierarchically Structured Sulfur/Carbon Nanocomposite Material for High-Energy Lithium Battery. *Chemistry of Materials*, 21(19): 4724-4730.
213. Liang, J., Sun, Z.-H., Li, F., and Cheng, H.-M. (2016). Carbon Materials for Li-S Batteries: Functional Evolution and Performance Improvement. *Energy Storage Materials*, 2: 76-106.
214. Liang, S., Guo, X., Feng, N., and Tian, Q. (2009). Application of Orange Peel Xanthate for the Adsorption of Pb²⁺ from Aqueous Solutions. *Journal of Hazardous Materials*, 170(1): 425-429.
215. Liang, X., Wen, Z., Liu, Y., Zhang, H., Jin, J., Wu, M., et al. (2012). A Composite of Sulfur and Polypyrrole–Multi Walled Carbon Combinatorial Nanotube as Cathode for Li/S Battery. *Journal of Power Sources*, 206: 409-413.
216. Liang, X., Zhang, M., Kaiser, M. R., Gao, X., Konstantinov, K., Tandiono, R., et al. (2015). Split-Half-Tubular Polypyrrole@Sulfur@Polypyrrole Composite with a Novel Three-Layer-3D Structure as Cathode for Lithium/Sulfur Batteries. *Nano Energy*, 11: 587-599.
217. Liang, Y., Deng, N., Ju, J., Zhou, X., Yan, J., Zhong, C., et al. (2018). Facilitation of Lithium Polysulfides Adsorption by Nitrogen Doped Carbon Nanofibers with 3D Interconnected Pore Structures for High-Stable Lithium-Sulfur Batteries. *Electrochimica Acta*. 281: 257-265.
218. Liang, Y., Ouyang, J., Wang, H., Wang, W., Chui, P., and Sun, K. (2012). Synthesis and Characterization of Core–Shell Structured SiO₂@YVO₄:Yb³⁺,Er³⁺ Microspheres. *Applied Surface Science*, 258(8): 3689-3694.
219. Liao, H., Zhang, H., Hong, H., Li, Z., and Lin, Y. (2017). Novel Flower-like Hierarchical Carbon Sphere with Multi-Scale Pores Coated on PP Separator for High-Performance Lithium-Sulfur Batteries. *Electrochimica Acta*, 257: 210-216.
220. Lifan, X., Yuliang, C., Jie, X., Birgit, S., H., E. M., V., S. L., et al. (2012). A Soft Approach to Encapsulate Sulfur: Polyaniline Nanotubes for Lithium-Sulfur Batteries with Long Cycle life. *Advanced Materials*, 24(9): 1176-1181.

221. Lim, A. C., Jadhav, H. S., and Seo, J. G. (2018). Electron Transport Shuttle Mechanism Via an Fe-N-C Bond Derived from a Conjugated Microporous Polymer for a Supercapacitor. *Dalton Transactions*, 47(3): 852-858.
222. Lim, S., Lilly Thankamony, R., Yim, T., Chu, H., Kim, Y.-J., Mun, J., et al. (2015). Surface Modification of Sulfur Electrodes by Chemically Anchored Cross-Linked Polymer Coating for Lithium–Sulfur Batteries. *ACS Applied Materials & Interfaces*, 7(3): 1401-1405.
223. Lin, D., Zhao, J., Sun, J., Yao, H., Liu, Y., Yan, K., et al. (2017). Three-Dimensional Stable Lithium Metal Anode with Nanoscale Lithium Islands Embedded in Ionically Conductive Solid Matrix. *Proceedings of the National Academy of Sciences*. 114(18): 4613-4618.
224. Lin, W., Chen, Y., Li, P., He, J., Zhao, Y., Wang, Z., et al. (2015). Enhanced Performance of Lithium Sulfur Battery with a Reduced Graphene Oxide Coating Separator. *Journal of The Electrochemical Society*, 162(8): A1624-A1629.
225. Liu, B., Zhou, X., Chen, H., Liu, Y., and Li, H. (2016). Promising Porous Carbons Derived from Lotus Seedpods with Outstanding Supercapacitance Performance. *Electrochimica Acta*, 208: 55-63.
226. Liu, C., Yin, Z. J., Deng, H., Liu, C., Zhao, J., Lan, Q., et al. (2017). Nitrogen-Doped Porous Carbon as High-Performance Cathode Material for Lithium-Sulfur Battery. *ChemistrySelect*, 2(34): 11030-11034.
227. Liu, J., Liu, B., Wang, C., Huang, Z., Hu, L., Ke, X., et al. (2017). Walnut Shell – Derived Activated Carbon: Synthesis and its Application in the Sulfur Cathode for Lithium–Sulfur Batteries. *Journal of Alloys and Compounds*, 718: 373-378.
228. Liu, M., Chen, Y., Chen, K., Zhang, N., Zhao, X., Zhao, F., et al. (2014). Biomass-Derived Activated Carbon for Rechargeable Lithium-Sulfur Batteries. *BioResources*, 10(1): 155-168.
229. Liu, M., Li, Q., Qin, X., Liang, G., Han, W., Zhou, D., et al. (2017). Suppressing Self-Discharge and Shuttle Effect of Lithium–Sulfur Batteries with V₂O₅-Decorated Carbon Nanofiber Interlayer. *Small*, 13(12): 1602539-1602546.
230. Liu, M., Zhou, D., He, Y.-B., Fu, Y., Qin, X., Miao, C., et al. (2016). Novel Gel Polymer Electrolyte for High-Performance Lithium–Sulfur Batteries. *Nano Energy*, 22: 278-289.
231. Liu, S., Hong, X., Wang, D., Li, Y., Xu, J., Zheng, C., et al. (2018). Hollow Carbon Spheres with Nanoporous Shells and Tailored Chemical Interfaces

as Sulfur Host for Long Cycle Life of Lithium Sulfur Batteries. *Electrochimica Acta*, 279: 10-18.

232. Liu, S., Li, Y., Hong, X., Xu, J., Zheng, C., and Xie, K. (2016). Reduced Graphene Oxide-Hollow Carbon Sphere Nanostructure Cathode Material with Ultra-High Sulfur Content for High Performance Lithium-Sulfur Batteries. *Electrochimica Acta*, 188: 516-522.
233. Liu, S., Xie, K., Li, Y., Chen, Z., Hong, X., Zhou, L., et al. (2015). Graphene Oxide Wrapped Hierarchical Porous Carbon-Sulfur Composite Cathode with Enhanced Cycling and Rate Performance for Lithium Sulfur Batteries. *RSC Advances*, 5(8): 5516-5522.
234. Liu, X., Men, C., Gao, P., Zhuang, S., Tang, H., and Bao, Z. (2016). Improved Cycling Performance of Sulfur Nanoparticles with a Mussel Inspired Polydopamine Coating. *RSC Advances*, 6(3): 1902-1906.
235. Liu, Y., Yan, W., An, X., Du, X., Wang, Z., Fan, H., et al. (2018). A Polypyrrole Hollow Nanosphere with Ultra-Thin Wrinkled Shell: Synergistic Trapping of Sulfur in Lithium-Sulfur Batteries with Excellent Elasticity and Buffer Capability. *Electrochimica Acta*, 271: 67-76.
236. Liu, Z., Li, J., Xiang, J., Cheng, S., Wu, H., Zhang, N., et al. (2017). Hierarchical Nitrogen-Doped Porous Graphene/Reduced Fluorographene/Sulfur Hybrids for High-Performance Lithium-Sulfur Batteries. *Physical Chemistry Chemical Physics*, 19(3): 2567-2573.
237. Liu, Z., Liu, B., Guo, P., Shang, X., Lv, M., Liu, D., et al. (2018). Enhanced Electrochemical Kinetics in Lithium-Sulfur Batteries by Using Carbon Nanofibers/Manganese dioxide Composite as a Bifunctional Coating on Sulfur Cathode. *Electrochimica Acta*, 269: 180-187.
238. Liu, Z., Zhou, L., Ge, Q., Chen, R., Ni, M., Utetiwabo, W., et al. (2018). Atomic Iron Catalysis of Polysulfide Conversion in Lithium-Sulfur Batteries. *ACS Applied Materials & Interfaces*, 10(23): 19311-19317.
239. Long, C., Chen, X., Jiang, L., Zhi, L., and Fan, Z. (2015). Porous Layer-Stacking Carbon Derived from In-built Template in Biomass for High Volumetric Performance Supercapacitors. *Nano Energy*, 12: 141-151.
240. Lopes, M., Antunes, C., and Martins, N. (2012). Energy Behaviours as Promoters of Energy Efficiency: A 21st Century Review. *Renewable and Sustainable Energy Reviews*, 16(6): 4095-4104.
241. Lu, Q., Gao, H., Yao, Y., Liu, N., Wang, X., and Wang, F. (2015). One-Step Synthesis of an Urchin-like Sulfur/Polyaniline Nano-Composite as a Promising Cathode Material for High-Capacity Rechargeable Lithium-Sulfur Batteries. *RSC Advances*, 5(113): 92918-92922.

242. Lu, S., Chen, Y., Zhou, J., Wang, Z., Wu, X., Gu, J., et al. (2016). A Sheet-like Carbon Matrix Hosted Sulfur as Cathode for High-Performance Lithium-Sulfur Batteries. *Scientific Reports*, 6, 20445.
243. Lu, Y., Zhang, S., Yin, J., Bai, C., Zhang, J., Li, Y., et al. (2017). Mesoporous Activated Carbon Materials with Ultrahigh Mesopore Volume and Effective Specific Surface Area for High Performance Supercapacitors. *Carbon*, 124(Supplement C): 64-71.
244. Ma, G., Wen, Z., Jin, J., Lu, Y., Rui, K., Wu, X., et al. (2014). Enhanced Performance of Lithium Sulfur Battery with Polypyrrole Warped Mesoporous Carbon/Sulfur Composite. *Journal of Power Sources*, 254: 353-359.
245. Ma, G., Wen, Z., Jin, J., Lu, Y., Wu, X., Wu, M., et al. (2014). Hollow Polyaniline Sphere@Sulfur Composites for Prolonged Cycling Stability of Lithium-Sulfur Batteries. *Journal of Materials Chemistry A*, 2(27): 10350-10354.
246. Ma, G., Wen, Z., Jin, J., Wu, M., Wu, X., and Zhang, J. (2014). Enhanced Cycle Performance of Li-S Battery with a Polypyrrole Functional Interlayer. *Journal of Power Sources*, 267: 542-546.
247. Ma, J., Dong, Y.-z., Wang, L., Yu, P., Yan, H.-j., Tian, C.-g., et al. (2016). In-situ Molten salt Template Strategy for Hierarchical 3D Porous Carbon from Palm Shells as Advanced Electrochemical Supercapacitors. *ChemistrySelect*, 1(10): 2167-2173.
248. Ma, X., Ning, G., Wang, Y., Song, X., Xiao, Z., Hou, L., et al. (2018). S-Doped Mesoporous Graphene Microspheres: A High Performance Reservoir Material for LiS Batteries. *Electrochimica Acta*, 269: 83-92.
249. Ma, Z., Tao, L., Liu, D., Li, Z., Zhang, Y., Liu, Z., et al. (2017). Ultrafine Nano-Sulfur Particles Anchored on In situ Exfoliated Graphene for Lithium-Sulfur Batteries. *Journal of Materials Chemistry A*, 5(19): 9412-9417.
250. Maharjan, M., Ulaganathan, M., Aravindan, V., Sreejith, S., Yan, Q., Madhavi, S., et al. (2017). Fabrication of High Energy Li-Ion Capacitors from Orange Peel Derived Porous Carbon. *ChemistrySelect*, 2(18): 5051-5058.
251. Manthiram, A., Fu, Y., Chung, S.-H., Zu, C., and Su, Y.-S. (2014). Rechargeable Lithium-Sulfur Batteries. *Chemical Reviews*, 114(23): 11751-11787.

252. Manthiram, A., Fu, Y., and Su, Y.-S. (2013). Challenges and Prospects of Lithium–Sulfur Batteries. *Accounts of Chemical Research*, 46(5): 1125-1134.
253. Martín, M. A., Siles, J. A., Chica, A. F., and Martín, A. (2010). Biomethanization of Orange Peel Waste. *Bioresource Technology*, 101(23): 8993-8999.
254. McDonough, J. K., and Gogotsi, Y. (2013). Carbon Onions: Synthesis and Electrochemical Applications. *The Electrochemical Society Interface*, 22(3): 61-66.
255. Meher, S. K., Justin, P., and Rao, G. R. (2010). Pine-cone Morphology and Pseudocapacitive Behavior of Nanoporous Nickel oxide. *Electrochimica Acta*, 55(28): 8388-8396.
256. Mendes, T. C., Xiao, C., Zhou, F., Li, H., Knowles, G. P., Hilder, M., et al. (2016). In-Situ-Activated N-Doped Mesoporous Carbon from a Protic Salt and its Performance in Supercapacitors. *ACS Applied Materials & Interfaces*, 8(51): 35243-35252.
257. Mi, L., Xiao, W., Cui, S., Hou, H., and Chen, W. (2016). An N-Doped Three Dimensional Flexible Carbon/Sulfur Cathode for Lithium Sulfur Battery Design. *Dalton Transactions*, 45(8): 3305-3309.
258. Miao, L.-X., Wang, W.-K., Wang, A.-B., Yuan, K.-G., and Yang, Y.-S. (2013). A high Sulfur Content Composite with Core–Shell Structure as Cathode Material for Li–S Batteries. *Journal of Materials Chemistry A*, 1(38): 11659-11664.
259. Mikhaylik, Y. V., Kovalev, I., Schock, R., Kumaresan, K., Xu, J., and Affinito, J. (2010). High Energy Rechargeable Li-S Cells for EV Application: Status, Remaining Problems and Solutions. *ECS Transactions*, 25(35): 23-34.
260. Mo, R.-J., Zhao, Y., Wu, M., Xiao, H.-M., Kuga, S., Huang, Y., et al. (2016). Activated Carbon from Nitrogen Rich Watermelon Rind for High-Performance Supercapacitors. *RSC Advances*, 6(64): 59333-59342.
261. Momčilović, M., Purenović, M., Bojić, A., Zarubica, A., and Randelović, M. (2011). Removal of Lead (II) ions from Aqueous Solutions by Adsorption onto Pine cone Activated Carbon. *Desalination*, 276(1-3): 53-59.
262. Mondal, K., Lorethova, H., Hippo, E., Wiltowski, T., and Lalvani, S. (2004). Reduction of Iron Oxide in Carbon monoxide Atmosphere—Reaction Controlled Kinetics. *Fuel Processing Technology*, 86(1): 33-47.

263. Moreno, N., Caballero, A., Hernán, L., and Morales, J. (2014). Lithium–Sulfur Batteries with Activated Carbons Derived from Olive Stones. *Carbon*, 70: 241-248.
264. Morgan, W. E., and Van Wazer, J. R. (1973). Binding Energy Shifts in the X-Ray Photoelectron Spectra of a Series of Related Group IVa Compounds. *The Journal of Physical Chemistry*, 77(7): 964-969.
265. Nagao, M., Suzuki, K., Imade, Y., Tateishi, M., Watanabe, R., Yokoi, T., et al. (2016). All-Solid-State Lithium–Sulfur Batteries with Three-Dimensional Mesoporous Electrode Structures. *Journal of Power Sources*, 330: 120-126.
266. Nishimoto, A., Agehara, K., Furuya, N., Watanabe, T., and Watanabe, M. (1999). High Ionic Conductivity of Polyether-Based Network Polymer Electrolytes with Hyperbranched Side Chains. *Macromolecules*, 32(5): 1541-1548.
267. Nitze, F., Agostini, M., Lundin, F., Palmqvist, A. E. C., and Matic, A. (2016). A Binder-Free Sulfur/Reduced Graphene Oxide Aerogel as High Performance Electrode Materials for Lithium Sulfur Batteries. *Scientific Reports*, 6: 39615.
268. Niu, S., Lv, W., Zhang, C., Shi, Y., Zhao, J., Li, B., et al. (2015). One-Pot Self-Assembly of Graphene/Carbon nanotube/Sulfur Hybrid with Three Dimensionally Interconnected Structure for Lithium–Sulfur Batteries. *Journal of Power Sources*, 295: 182-189.
269. Niu, S., Lv, W., Zhou, G., Shi, H., Qin, X., Zheng, C., et al. (2016). Electrostatic-Spraying an Ultrathin, Multifunctional and Compact Coating onto a Cathode for a Long-Life and High-Rate Lithium-Sulfur Battery. *Nano Energy*, 30: 138-145.
270. Niu, S., Zhou, G., Lv, W., Shi, H., Luo, C., He, Y., et al. (2016). Sulfur Confined in Nitrogen-Doped Microporous Carbon Used in a Carbonate-Based Electrolyte for Long-Life, Safe Lithium-Sulfur Batteries. *Carbon*, 109: 1-6.
271. Ogoke, O., Wu, G., Wang, X., Casimir, A., Ma, L., Wu, T., et al. (2017). Effective Strategies for Stabilizing Sulfur for Advanced Lithium-Sulfur Batteries. *Journal of Materials Chemistry A*, 5(2): 448-469.
272. Olivares-Marín, M., Fernández, J. A., Lázaro, M. J., Fernández-González, C., Macías-García, A., Gómez-Serrano, V., et al. (2009). Cherry Stones as Precursor of Activated Carbons for Supercapacitors. *Materials Chemistry and Physics*, 114(1): 323-327.

273. Ould Ely, T., Kamzabek, D., Chakraborty, D., and Doherty, M. F. (2018). Lithium–Sulfur Batteries: State of the Art and Future Directions. *ACS Applied Energy Materials*, 1(5): 1783-1814.
274. Pan, J., Wu, C., Cheng, J., Pan, Y., Ma, Z., Xie, S., et al. (2015). Sepiolite-Sulfur as a High-Capacity, High-Rate Performance, and Low-Cost Cathode Material for Lithium–Sulfur Batteries. *Journal of Power Sources*, 293: 527-532.
275. Pandiarajan, A., Kamaraj, R., Vasudevan, S., and Vasudevan, S. (2018). OPAC (Orange Peel Activated Carbon) Derived from Waste Orange Peel for the Adsorption of Chlorophenoxyacetic Acid Herbicides from Water: Adsorption Isotherm, Kinetic Modelling and Thermodynamic Studies. *Bioresource Technology*, 261: 329-341.
276. Pang, Q., Liang, X., Kwok, C., and Nazar, L. F. (2015). The Importance of Chemical Interactions Between Sulfur Host Materials and Lithium Polysulfides for Advanced Lithium-Sulfur Batteries. *Journal of The Electrochemical Society*, 162(14): A2567-A2576.
277. Paraknowitsch, J. P., and Thomas, A. (2013). Doping Carbons Beyond Nitrogen: An Overview of Advanced Heteroatom Doped Carbons with Boron, Sulphur and Phosphorus for Energy Applications. *Energy & Environmental Science*, 6(10): 2839-2855.
278. Pei, F., Lin, L., Ou, D., Zheng, Z., Mo, S., Fang, X., et al. (2017). Self-Supporting Sulfur Cathodes Enabled by Two-Dimensional Carbon Yolk-Shell Nanosheets for High-Energy-Density Lithium-Sulfur Batteries. *Nature Communications*, 8(1), 482.
279. Peigney, A., Laurent, C., Flahaut, E., Bacsa, R., and Rousset, A. (2001). Specific Surface Area of Carbon Nanotubes and Bundles of Carbon Nanotubes. *Carbon*, 39(4): 507-514.
280. Peitao, X., Fanxing, B., Guanhui, Y., Yu, Z., and Yuxi, X. (2017). Integration of Graphene, Nano sulfur, and Conducting Polymer into Compact, Flexible Lithium–Sulfur Battery Cathodes with Ultrahigh Volumetric Capacity and Superior Cycling Stability for Foldable Devices. *Advanced Materials*, 29(40): 1703324-1703332.
281. Peng, H.-J., Huang, J.-Q., Cheng, X.-B., and Zhang, Q. (2017). Review on High-Loading and High-Energy Lithium–Sulfur Batteries. *Advanced Energy Materials*, 7(24): 1700260-1700314.
282. Peng, H., Wang, X., Zhao, Y., Tan, T., Bakenov, Z., and Zhang, Y. (2018). Synthesis of a Flexible Freestanding Sulfur/Polyacrylonitrile/Graphene Oxide as the Cathode for Lithium/Sulfur Batteries. *Polymers*, 10(4): 399.

283. Peng, Y., Zhang, Y., Huang, J., Wang, Y., Li, H., Hwang, B. J., et al. (2017). Nitrogen and Oxygen Dual-Doped Hollow Carbon Nanospheres Derived from Catechol/Polyamine as Sulfur Hosts for Advanced Lithium Sulfur Batteries. *Carbon*, 124: 23-33.
284. Peng, Y., Zhang, Y., Wang, Y., Shen, X., Wang, F., Li, H., et al. (2017). Directly Coating a Multifunctional Interlayer on the Cathode Via Electrospinning for Advanced Lithium–Sulfur Batteries. *ACS Applied Materials & Interfaces*, 9(35): 29804-29811.
285. Ping, Z., XiaoJing, L., Anye, R., and Peng, G. (2016). Preparation of a Novel Porous Gel Electrolyte and its Application in Micro Supercapacitor. *Journal of Electroanalytical Chemistry*, 782(Supplement C): 154-160.
286. Pólrolniczak, P., Nowicki, P., Wasíński, K., Pietrzak, R., and Walkowiak, M. (2016). Biomass-Derived Hierarchical Carbon as Sulfur Cathode Stabilizing Agent for Lithium-Sulfur Batteries. *Solid State Ionics*, 297: 59-63.
287. Ponraj, R., Kannan, A. G., Ahn, J. H., Lee, J. H., Kang, J., Han, B., et al. (2017). Effective Trapping of Lithium Polysulfides Using a Functionalized Carbon Nanotube-Coated Separator for Lithium–Sulfur Cells with Enhanced Cycling Stability. *ACS Applied Materials & Interfaces*, 9(44): 38445-38454.
288. Prakash Maran, J., Sivakumar, V., Thirugnanasambandham, K., and Sridhar, R. (2013). Optimization of Microwave Assisted Extraction of Pectin from Orange Peel. *Carbohydrate Polymers*, 97(2): 703-709.
289. Praveen, W., Sujith, V., and Prabhakaran, K. (2017). Nitrogen Doped Microporous Carbon by ZnCl₂ Activation of Protein. *Materials Research Express*, 4(9): 095602-0956016.
290. Puthusseri, D., Aravindan, V., Madhavi, S., and Ogale, S. (2014). 3D Micro-Porous Conducting Carbon Beehive by Single Step Polymer Carbonization for High Performance Supercapacitors: The Magic of In Situ Porogen Formation.. *Energy & Environmental Science*, 7(2): 728-735.
291. Qian, W., Gao, Q., Zhang, H., Tian, W., Li, Z., and Tan, Y. (2017). Crosslinked Polypyrrole Grafted Reduced Graphene Oxide-Sulfur Nanocomposite Cathode for High Performance Li-S Battery. *Electrochimica Acta*, 235: 32-41.
292. Qian, W., Sun, F., Xu, Y., Qiu, L., Liu, C., Wang, S., et al. (2014). Human Hair-Derived Carbon Flakes for Electrochemical Supercapacitors. *Energy & Environmental Science*, 7(1): 379-386.

293. Qian, X., Jin, L., Wang, S., Yao, S., Rao, D., Shen, X., et al. (2016). Zn-MOF Derived Micro/Meso Porous Carbon Nanorod for High Performance Lithium-Sulfur Battery. *RSC Advances*, 6(97): 94629-94635.
294. Qian, X., Zhao, D., Jin, L., Shen, X., Yao, S., Rao, D., et al. (2017). Hollow Spherical Lanthanum oxide Coated Separator for High Electrochemical Performance Lithium-Sulfur Batteries. *Materials Research Bulletin*, 94: 104-112.
295. Qin, F., Zhang, K., Fang, J., Lai, Y., Li, Q., Zhang, Z., et al. (2014). High Performance Lithium Sulfur Batteries with a Cassava-Derived Carbon Sheet as a Polysulfides Inhibitor. *New Journal of Chemistry*, 38(9): 4549-4554.
296. Qiuhong, Y., Yang, L., Tao, P., Xiaoyi, H., Rongjie, L., Yange, W., et al. (2017). Construction of Tubular Polypyrrole-Wrapped Biomass-Derived Carbon Nanospheres as Cathode Materials for Lithium-Sulfur Batteries. *Journal of Physics D: Applied Physics*, 50(11): 115002-115011.
297. Qu, Y., Zhang, Z., Zhang, X., Ren, G., Lai, Y., Liu, Y., et al. (2015). Highly Ordered Nitrogen-Rich Mesoporous Carbon Derived from Biomass Waste for High-Performance Lithium-Sulfur Batteries. *Carbon*, 84: 399-408.
298. Raghunandanan, A., Mani, U., and Pitchai, R. (2018). Low Cost Bio-Derived Carbon-Sprinkled Manganese dioxide as an Efficient Sulfur Host for Lithium-Sulfur Batteries. *RSC Advances*, 8(43): 24261-24267.
299. Raj, R. P., Ragupathy, P., and Mohan, S. (2015). Remarkable Capacitive Behavior of a Co₃O₄-Polyindole Composite as Electrode Material for Supercapacitor Applications. *Journal of Materials Chemistry A*, 3(48): 24338-24348.
300. Raja, M., Angulakshmi, N., and Stephan, A. M. (2016). Sisal-Derived Activated Carbons for Cost-Effective Lithium-Sulfur Batteries. *RSC Advances*, 6(17): 13772-13779.
301. Ranaweera, C. K., Ionescu, M., Bilic, N., Wan, X., Kahol, P. K., and Gupta, R. K. (2017). Biobased Polyols Using Thiol-ene Chemistry for Rigid Polyurethane Foams with Enhanced Flame-Retardant Properties. *Journal of Renewable Materials*, 5(1): 1-12.
302. Ranaweera, C. K., Kahol, P. K., Ghimire, M., Mishra, S. R., and Gupta, R. K. (2017). Orange-Peel-Derived Carbon: Designing Sustainable and High-Performance Supercapacitor Electrodes. *C Journal of carbon research*, 3(3): 25.
303. Ranjith, T., Karthikeyan, K., Vignesh, R. H., Xueliang, S., and Yun-Sung, L. (2017). Engineering the Pores of Biomass-Derived Carbon: Insights for

- Achieving Ultrahigh Stability at High Power in High-Energy Supercapacitors. *ChemSusChem*, 10(13): 2805-2815.
304. Razmjooei, F., Singh, K. P., Yang, D.-S., Cui, W., Jang, Y. H., and Yu, J.-S. (2017). Fe-Treated Heteroatom (S/N/B/P)-Doped Graphene Electrocatalysts for Water Oxidation. *ACS Catalysis*, 7(4): 2381-2391.
305. Rehman, S., Guo, S., and Hou, Y. (2016). Rational Design of Si/SiO₂@Hierarchical Porous Carbon Spheres as Efficient Polysulfide Reservoirs for High-Performance Li-S Battery. *Advanced Materials*, 28(16): 3167-3172.
306. Rehman, S., Khan, K., Zhao, Y., and Hou, Y. (2017). Nanostructured Cathode Materials for Lithium-Sulfur Batteries: Progress, Challenges and Perspectives.. *Journal of Materials Chemistry A*, 5(7): 3014-3038.
307. Ren, G., Li, S., Fan, Z.-X., Warzywoda, J., and Fan, Z. (2016). Soybean-Derived Hierarchical Porous Carbon with Large Sulfur Loading and Sulfur Content for High-Performance Lithium-Sulfur Batteries. *Journal of Materials Chemistry A*, 4(42): 16507-16515.
308. Ren, J., Zhou, Y., Wu, H., Xie, F., Xu, C., and Lin, D. (2018). Sulfur-Encapsulated in Heteroatom-Doped Hierarchical Porous Carbon Derived from Goat Hair for High Performance Lithium-Sulfur Batteries. *Journal of Energy Chemistry*.
309. Reshma, C., and Mary Gladis, J. (2015). Synthesis and Characterisation of Ternary Nanocomposites as Cathode Material for Lithium-Sulphur Batteries. *Materials Science Forum*, 830-831: 604-607.
310. Roy, S., Das, T., Ming, Y., Chen, X., Yue, C. Y., and Hu, X. (2014). Specific Functionalization and Polymer Grafting on Multiwalled Carbon Nanotubes to Fabricate Advanced Nylon 12 Composites. *Journal of Materials Chemistry A*, 2(11): 3961-3970.
311. Rybarczyk, M. K., Peng, H.-J., Tang, C., Lieder, M., Zhang, Q., and Titirici, M.-M. (2016). Porous Carbon Derived from Rice Husks as Sustainable Bioresources: Insights into the Role of Micro-/Mesoporous Hierarchy in Hosting Active Species for Lithium-Sulphur Batteries.. *Green Chemistry*, 18(19): 5169-5179.
312. Ryu, K. S., and Kim, K. M. (2008). Electrochemical Performance of Chemically Synthesized Oligo-Indole as a Positive Electrode for Lithium Rechargeable Batteries. *Journal of Applied Electrochemistry*, 38(4): 477-482.

313. Santos, C. M., Dweck, J., Viotto, R. S., Rosa, A. H., and de Morais, L. C. (2015). Application of Orange Peel Waste in the Production of Solid Biofuels and Biosorbents. *Bioresource Technology*, 196: 469-479.
314. Sarish, R., Shaojun, G., and Yanglong, H. (2016). Rational Design of Si/SiO₂@Hierarchical Porous Carbon Spheres as Efficient Polysulfide Reservoirs for High-Performance Li–S battery. *Advanced Materials*, 28(16): 3167-3172.
315. Scheers, J., Fantini, S., and Johansson, P. (2014). A Review of Electrolytes for Lithium–Sulphur Batteries. *Journal of Power Sources*, 255: 204-218.
316. Schuster, J., He, G., Mandlmeier, B., Yim, T., Lee, K. T., Bein, T., et al. (2012). Spherical Ordered Mesoporous Carbon Nanoparticles with High Porosity for Lithium–Sulfur Batteries. *Angewandte Chemie International Edition*, 51(15): 3591-3595.
317. Scrosati, B. (1992). Lithium Rocking Chair Batteries: An Old Concept? *Journal of The Electrochemical Society*, 139(10): 2776-2781.
318. Seh, Z. W., Sun, Y., Zhang, Q., and Cui, Y. (2016). Designing High-Energy Lithium-Sulfur Batteries. *Chemical Society Reviews*, 45(20): 5605-5634.
319. Seh, Z. W., Wang, H., Hsu, P.-C., Zhang, Q., Li, W., Zheng, G., et al. (2014). Facile Synthesis of Li₂S–Polypyrrole Composite Structures for High-Performance Li₂S Cathodes. *Energy & Environmental Science*, 7(2): 672-676.
320. Service, R. F. (2006). Materials science. New Supercapacitor Promises to Pack more Electrical Punch. *Science*, 313(5789): 902.
321. Sevilla, M., Gu, W., Falco, C., Titirici, M.-M., Fuertes, A., and Yushin, G. (2014). Hydrothermal Synthesis of Microalgae-Derived Microporous Carbons for Electrochemical Capacitors. *Journal of Power Sources*, 267: 26-32.
322. Sevilla, M., and Mokaya, R. (2014). Energy Storage Applications of Activated Carbons: Supercapacitors and Hydrogen Storage. *Energy & Environmental Science*, 7(4): 1250-1280.
323. Shaaban, A., Se, S.-M., Dimin, M. F., Juoi, J. M., Mohd Husin, M. H., and Mitan, N. M. M. (2014). Influence of Heating Temperature and Holding Time on Biochars Derived from Rubber Wood Sawdust Via Slow Pyrolysis. *Journal of Analytical and Applied Pyrolysis*, 107(Supplement C): 31-39.
324. Shaibani, M., Hollenkamp, A. F., Hill, M. R., and Majumder, M. (2017). Permselective Membranes in Lithium–Sulfur Batteries. *Current Opinion in Chemical Engineering*, 16: 31-38.

325. Shao-Zhong, Z., Yuechao, Y., Lin, H., Hongliang, W., Biaolin, P., Qi, Z., et al. (2018). Facile Synthesis of Ultrahigh-Surface-Area Hollow Carbon Nanospheres and their Application in Lithium-Sulfur Batteries. *Chemistry – A European Journal*, 24(8): 1988-1997.
326. Shao, H., Ai, F., Wang, W., Zhang, H., Wang, A., Feng, W., et al. (2017). Crab Shell-Derived Nitrogen-Doped Micro-/Mesoporous Carbon as an Effective Separator Coating for High Energy Lithium–Sulfur Batteries. *Journal of Materials Chemistry A*, 5(37): 19892-19900.
327. Shao, H., Huang, B., Liu, N., Wang, W., Zhang, H., Wang, A., et al. (2016). Modified Separators Coated with a Ca(OH)₂-Carbon Framework Derived from Crab Shells for Lithium–Sulfur Batteries. *Journal of Materials Chemistry A*, 4(42): 16627-16634.
328. Shao, H., Wang, W., Zhang, H., Wang, A., Chen, X., and Huang, Y. (2018). Nano-TiO₂ Decorated Carbon Coating on the Separator to Physically and Chemically Suppress the Shuttle Effect for Lithium-Sulfur Battery. *Journal of Power Sources*, 378: 537-545.
329. Sheng-Heng, C., and Arumugam, M. (2014). Bifunctional Separator with a Light-Weight Carbon-Coating for Dynamically and Statically stable Lithium-Sulfur Batteries. *Advanced Functional Materials*, 24(33): 5299-5306.
330. Sheng-Heng, C., Pauline, H., Richa, S., Vibha, K., and Arumugam, M. (2015). Electrochemically Stable Rechargeable Lithium–Sulfur Batteries with a Microporous Carbon Nanofiber Filter for Polysulfide. *Advanced Energy Materials*, 5(18): 1500738.
331. Sheng, H., Wei, M., D’Aloia, A., and Wu, G. (2016). Heteroatom Polymer-Derived 3D High-Surface-Area and Mesoporous Graphene Sheet-like Carbon for Supercapacitors. *ACS Applied Materials & Interfaces*, 8(44): 30212-30224.
332. Shengnan, J., Sumair, I., Dan, S., Ying, X., Qian, L., Taizhong, H., et al. (2017). Coralline-like N-Doped Hierarchically Porous Carbon Derived from Enteromorpha as a Host Matrix for Lithium-Sulfur Battery. *Chemistry – A European Journal*, 23(72): 18208-18215.
333. Shi, L., Zeng, F., Cheng, X., Lam, K. H., Wang, W., Wang, A., et al. (2018). Enhanced Performance of Lithium-Sulfur Batteries with High Sulfur Loading Utilizing Ion Selective MWCNT/SPANI Modified Separator. *Chemical Engineering Journal*, 334: 305-312.
334. Shiguo, Z., Ai, I., Kazuhide, U., Zhengjian, C., Kaoru, D., and Masayoshi, W. (2015). Protic-Salt-Derived Nitrogen/Sulfur-Codoped Mesoporous

- Carbon for the Oxygen Reduction Reaction and Supercapacitors. *ChemSusChem*, 8(9): 1608-1617.
335. Singh, V. K., Cura, M. E., Liu, X., Johansson, L.-S., Ge, Y., and Hannula, S.-P. (2014). Tuning the Mechanical and Adsorption Properties of Silica with Graphene Oxide. *ChemPlusChem*, 79(10): 1512-1522.
336. Singhal, R., Chung, S.-H., Manthiram, A., and Kalra, V. (2015). A Free-Standing Carbon Nanofiber Interlayer for High-Performance Lithium-Sulfur Batteries. *Journal of Materials Chemistry A*, 3(8): 4530-4538.
337. Son, Y., Lee, J. S., Son, Y., Jang, J. H., and Cho, J. (2015). Recent Advances in Lithium Sulfide Cathode Materials and their Use in Lithium Sulfur Batteries. *Advanced Energy Materials*, 5(16): 1500110-1500124.
338. Song, M.-K., Cairns, E. J., and Zhang, Y. (2013). Lithium/Sulfur Batteries with High Specific Energy: Old Challenges and New Opportunities. *Nanoscale*, 5(6): 2186-2204.
339. Song, S., Shi, L., Lu, S., Pang, Y., Wang, Y., Zhu, M., et al. (2018). A New Polysulfide Blocker - Poly(acrylic acid) Modified Separator for Improved Performance of Lithium-Sulfur Battery. *Journal of Membrane Science*, 563: 277-283.
340. Song, X., Wang, S., Chen, G., Gao, T., Bao, Y., Ding, L.-X., et al. (2018). Fe-N-Doped Carbon Nanofiber and Graphene Modified Separator for Lithium-Sulfur Batteries. *Chemical Engineering Journal*, 333: 564-571.
341. Sridhar, V., Lee, I., Chun, H.-H., and Park, H. (2015). Microwave Synthesis of Nitrogen-Doped Carbon Nanotubes Anchored on Graphene Substrates. *Carbon*, 87: 186-192.
342. Srivastava, G., Das, C. K., Das, A., Singh, S. K., Roy, M., Kim, H., et al. (2014). Seed Treatment with Iron pyrite (FeS₂) Nanoparticles Increases the Production of Spinach. *RSC Advances*, 4(102): 58495-58504.
343. Stein, A., Wang, Z., and Fierke, M. A. (2009). Functionalization of Porous Carbon Materials with Designed Pore Architecture. *Advanced Materials*, 21(3): 265-293.
344. Strubel, P., Althues, H., and Kaskel, S. (2016). Zinc-Salt Templating of Hierarchical Porous Carbons for Low Electrolyte High Energy Lithium-Sulfur Batteries (LE-LiS). *Carbon*, 107: 705-710.
345. Su, Y.-S., Fu, Y., Cochell, T., and Manthiram, A. (2013). A Strategic Approach to Recharging Lithium-Sulphur Batteries for Long Cycle Life. *Nature Communications*, 4: 2985-2993.

346. Su, Y.-S., Fu, Y., and Manthiram, A. (2012). Self-Weaving Sulfur-Carbon Composite Cathodes for High Rate Lithium-Sulfur Batteries. *Physical Chemistry Chemical Physics*, 14(42): 14495-14499.
347. Su, Y.-S., and Manthiram, A. (2012a). A Facile In Situ Sulfur Deposition Route to Obtain Carbon-Wrapped Sulfur Composite Cathodes for Lithium-Sulfur Batteries. *Electrochimica Acta*, 77: 272-278.
348. Su, Y.-S., and Manthiram, A. (2012b). Lithium-Sulphur Batteries with a Microporous Carbon Paper as a Bifunctional Interlayer. *Nature Communications*, 3: 1166-1172.
349. Su, Y.-S., and Manthiram, A. (2012c). A New Approach to Improve Cycle Performance of Rechargeable Lithium-Sulfur Batteries by Inserting a Free-Standing MWCNT Interlayer. *Chemical Communications*, 48(70): 8817-8819.
350. Sultan, A., Ahsan, A., and Rafat, M. (2018). Nitrogen Doped Activated Carbon from Pea Skin for High Performance Supercapacitor. *Materials Research Express*, 5(4): 045508-045518.
351. Sultan, A., Parvaz, M., Rahul, J., and Rafat, M. (2018). Studies on Activated Carbon Derived from Neem (*azadirachta indica*) Bio-waste, and its Application as Supercapacitor Electrode. *Materials Research Express*, 5(4): 045601-045613.
352. Sun, K., Cama, C. A., DeMayo, R. A., Bock, D. C., Tong, X., Su, D., et al. (2017). Interaction of FeS₂ and Sulfur in Li-S Battery System. *Journal of The Electrochemical Society*, 164(1): A6039-A6046.
353. Sun, L., Kong, W., Jiang, Y., Wu, H., Jiang, K., Wang, J., et al. (2015). Super-Aligned Carbon Nanotube/Graphene Hybrid Materials as a Framework for Sulfur Cathodes in High Performance Lithium Sulfur Batteries. *Journal of Materials Chemistry A*, 3(10): 5305-5312.
354. Sun, M.-H., Huang, S.-Z., Chen, L.-H., Li, Y., Yang, X.-Y., Yuan, Z.-Y., et al. (2016). Applications of Hierarchically Structured Porous Materials from Energy Storage and Conversion, Catalysis, Photocatalysis, Adsorption, Separation, and Sensing to Biomedicine. *Chemical Society Reviews*, 45(12): 3479-3563.
355. Sun, M., Zhang, S., Jiang, T., Zhang, L., and Yu, J. (2008). Nano-Wire Networks of Sulfur-Polypyrrole Composite Cathode Materials for Rechargeable Lithium Batteries. *Electrochemistry Communications*, 10(12): 1819-1822.

356. Sun, Y.-Z., Huang, J.-Q., Zhao, C.-Z., and Zhang, Q. (2017). A Review of Solid Electrolytes for Safe Lithium-Sulfur Batteries. *Science China Chemistry*, 60(12): 1508-1526.
357. Suo, L., Hu, Y.-S., Li, H., Armand, M., and Chen, L. (2013). A New Class of Solvent-in-Salt Electrolyte for High-Energy Rechargeable Metallic Lithium Batteries. *Nature Communications*, 4: 1481-1490.
358. Tan, L., Li, X., Wang, Z., Guo, H., and Wang, J. (2018). Lightweight Reduced Graphene Oxide@MoS₂ Interlayer as Polysulfide Barrier for High-Performance Lithium-Sulfur Batteries. *ACS Applied Materials & Interfaces*, 10(4): 3707-3713.
359. Tan, Y., Zheng, Z., Huang, S., Wang, Y., Cui, Z., Liu, J., et al. (2017). Immobilization of Sulfur by Constructing Three-Dimensional Nitrogen Rich Carbons for Long Life Lithium-Sulfur Batteries. *Journal of Materials Chemistry A*, 5(18): 8360-8366.
360. Tang, C., Liu, Y., Yang, D., Yang, M., and Li, H. (2017). Oxygen and Nitrogen Co-doped Porous Carbons with Finely-Layered Schistose Structure for High-Rate-Performance Supercapacitors. *Carbon*, 122(Supplement C): 538-546.
361. Tang, X.-n., Sun, Z.-h., Zhuo, S.-p., and Li, F. (2018). Nitrogen-Doped CMK-3@Graphene Hybrids as a Sulfur Host Material for Use in Lithium-Sulfur Batteries. *Carbon*, 130: 847.
362. Tao, X., Zhang, J., Xia, Y., Huang, H., Du, J., Xiao, H., et al. (2014). Bio-Inspired Fabrication of Carbon Nanotiles for High Performance Cathode of Li-S Batteries. *Journal of Materials Chemistry A*, 2(7): 2290-2296.
363. Tian, N., Tian, X., Liu, X., Zhou, Z., Yang, C., Ma, L., et al. (2016). Facile Synthesis of Hierarchical Dendrite-like Structure Iron Layered Double Hydroxide Nanohybrids for Effective Arsenic Removal. *Chemical Communications*, 52(80): 11955-11958.
364. Tian, Q., Wang, X., Xu, X., Zhang, M., Wang, L., Zhao, X., et al. (2018). A Novel Porous Carbon Material Made from Wild Rice Stem and its Application in Supercapacitors. *Materials Chemistry and Physics*, 213: 267-276.
365. Tian, W., Gao, Q., Tan, Y., Yang, K., Zhu, L., Yang, C., et al. (2015). Bio-Inspired Beehive-like Hierarchical Nanoporous Carbon Derived from Bamboo-Based Industrial By-Product as a High Performance Supercapacitor Electrode Material. *Journal of Materials Chemistry A*, 3(10): 5656-5664.

366. Tian, X., Ma, H., Li, Z., Yan, S., Ma, L., Yu, F., et al. (2017). Flute Type Micropores Activated Carbon from Cotton Stalk for High Performance Supercapacitors. *Journal of Power Sources*, 359(Supplement C): 88-96.
367. Truong, P., and Hart, B. (2001). *Vetiver System for Wastewater Treatment*: Office of the Royal Development Projects Board.
368. Tzeng, S.-S., and Chr, Y.-G. (2002). Evolution of Microstructure and Properties of Phenolic Resin-Based Carbon/Carbon Composites During Pyrolysis. *Materials Chemistry and Physics*, 73(2): 162-169.
369. Varga, M., Izak, T., Vretenar, V., Kozak, H., Holovsky, J., Artemenko, A., et al. (2017). Diamond/Carbon Nanotube Composites: Raman, FTIR and XPS Spectroscopic Studies. *Carbon*, 111: 54-61.
370. Wang, C., Chen, H., Dong, W., Ge, J., Lu, W., Wu, X., et al. (2014). Sulfur–Amine Chemistry-Based Synthesis of Multi-Walled Carbon Nanotube–Sulfur Composites for High Performance Li–S Batteries.. *Chemical Communications*, 50(10): 1202-1204.
371. Wang, C., Wan, W., Chen, J.-T., Zhou, H.-H., Zhang, X.-X., Yuan, L.-X., et al. (2013). Dual Core-Shell Structured Sulfur Cathode Composite Synthesized by a One-Pot Route for Lithium Sulfur Batteries.. *Journal of Materials Chemistry A*, 1(5): 1716-1723.
372. Wang, C., Xiong, Y., Wang, H., and Sun, Q. (2018). All-Round Utilization of Biomass Derived All-Solid-State Asymmetric Carbon-Based Supercapacitor. *Journal of Colloid and Interface Science*, 528: 349-359.
373. Wang, D.-W., Zeng, Q., Zhou, G., Yin, L., Li, F., Cheng, H.-M., et al. (2013). Carbon-Sulfur Composites for Li-S Batteries: Status and Prospects. *Journal of Materials Chemistry A*, 1(33): 9382-9394.
374. Wang, D., Xu, L., Wang, Y., and Xu, W. (2018). Rational Synthesis of Porous Carbon Nanocages and their Potential Application in High Rate Supercapacitors. *Journal of Electroanalytical Chemistry*, 815: 166-174.
375. Wang, F., Wu, X., Yuan, X., Liu, Z., Zhang, Y., Fu, L., et al. (2017). Latest Advances in Supercapacitors: From New Electrode Materials to Novel Device Designs. *Chemical Society Reviews*, 46(22): 6816-6854.
376. Wang, G., Lai, Y., Zhang, Z., Li, J., and Zhang, Z. (2015). Enhanced Rate Capability and Cycle Stability of Lithium–Sulfur Batteries with a Bifunctional MCNT@PEG-Modified Separator. *Journal of Materials Chemistry A*, 3(13): 7139-7144.

377. Wang, H., Xu, Z., Kohandehghan, A., Li, Z., Cui, K., Tan, X., et al. (2013). Interconnected Carbon Nanosheets Derived from Hemp for Ultrafast Supercapacitors with High Energy. *ACS Nano*, 7(6): 5131-5141.
378. Wang, H., Yang, Y., Liang, Y., Robinson, J. T., Li, Y., Jackson, A., et al. (2011). Graphene-Wrapped Sulfur Particles as a Rechargeable Lithium–Sulfur Battery Cathode Material with High Capacity and Cycling Stability. *Nano Letters*, 11(7): 2644-2647.
379. Wang, J.-Z., Lu, L., Choucair, M., Stride, J. A., Xu, X., and Liu, H.-K. (2011). Sulfur-Graphene Composite for Rechargeable Lithium Batteries. *Journal of Power Sources*, 196(16): 7030-7034.
380. Wang, J., and Liu, Q. (2014). An Efficient One-Step Condensation and Activation Strategy to Synthesize Porous Carbons with Optimal Micropore Sizes for Highly Selective CO₂ Adsorption. *Nanoscale*, 6(8): 4148-4156.
381. Wang, J., Nie, P., Ding, B., Dong, S., Hao, X., Dou, H., et al. (2017). Biomass Derived Carbon for Energy Storage Devices.. *Journal of Materials Chemistry A*, 5(6): 2411-2428.
382. Wang, L., Mu, G., Tian, C., Sun, L., Zhou, W., Yu, P., et al. (2013). Porous Graphitic Carbon Nanosheets Derived from Cornstalk Biomass for Advanced Supercapacitors. *ChemSusChem*, 6(5): 880-889.
383. Wang, L., Wang, M., Huang, Z.-H., Cui, T., Gui, X., Kang, F., et al. (2011). Capacitive Deionization of NaCl Solutions Using Carbon nanotube Sponge Electrodes. *Journal of Materials Chemistry*, 21(45): 18295-18299.
384. Wang, L., Yang, Z., Nie, H., Gu, C., Hua, W., Xu, X., et al. (2016). A Lightweight Multifunctional Interlayer of Sulfur–Nitrogen Dual-Doped Graphene for Ultrafast, Long-life Lithium–Sulfur Batteries. *Journal of Materials Chemistry A*, 4(40): 15343-15352.
385. Wang, M., Zhang, H., Wang, Q., Qu, C., Li, X., and Zhang, H. (2015). Steam-Etched Spherical Carbon/Sulfur Composite with High Sulfur Capacity and Long Cycle Life for Li/S Battery Application. *ACS Applied Materials & Interfaces*, 7(6): 3590-3599.
386. Wang, Q., Cao, Q., Wang, X., Jing, B., Kuang, H., and Zhou, L. (2013). A High-Capacity Carbon Prepared from Renewable Chicken Feather Biopolymer for Supercapacitors. *Journal of Power Sources*, 225: 101-107.
387. Wang, Q., Zhong, H., Jiang, M., Liao, Q., Yang, J., Zhou, X., et al. (2018). Recycling Antibiotic Bacterial Residues for Application in High-Performance Lithium–Sulfur Batteries. *ChemElectroChem*, 5(16): 2235-2241.

388. Wang, R., Wang, P., Yan, X., Lang, J., Peng, C., and Xue, Q. (2012). Promising Porous Carbon Derived from Celtuce Leaves with Outstanding Supercapacitance and CO₂ Capture Performance. *ACS Applied Materials & Interfaces*, 4(11): 5800-5806.
389. Wang, W., Wang, X., Tian, L., Wang, Y., and Ye, S. (2014). In situ Sulfur Deposition Route to Obtain Sulfur–Carbon Composite Cathodes for Lithium–Sulfur Batteries. *Journal of Materials Chemistry A*, 2(12): 4316-4323.
390. Wang, X., Wang, Z., and Chen, L. (2013). Reduced Graphene Oxide Film as a Shuttle-Inhibiting Interlayer in a Lithium–Sulfur Battery. *Journal of Power Sources*, 242: 65-69.
391. Wang, Y.-X., Chou, S.-L., Liu, H.-K., and Dou, S.-X. (2013). The Electrochemical Properties of High-Capacity Sulfur/Reduced Graphene Oxide with Different Electrolyte Systems. *Journal of Power Sources*, 244: 240-245.
392. Wang, Y.-Y., Hou, B.-H., Lü, H.-Y., Lü, C.-L., and Wu, X.-L. (2016). Hierarchically Porous N-Doped Carbon Nanosheets Derived from Grapefruit Peels for High-Performance Supercapacitors. *ChemistrySelect*, 1(7): 1441-1447.
393. Wang, Y., Song, Y., and Xia, Y. (2016). Electrochemical Capacitors: Mechanism, Materials, Systems, Characterization and Applications. *Chemical Society Reviews*, 45(21): 5925-5950.
394. Wang, Z., Dong, Y., Li, H., Zhao, Z., Bin Wu, H., Hao, C., et al. (2014). Enhancing Lithium–Sulphur Battery Performance by Strongly Binding the Discharge Products on Amino-Functionalized Reduced Graphene Oxide. 5: 5002-5010.
395. Ward, A. T. (1968). Raman Spectroscopy of Sulfur, Sulfur-Selenium, and Sulfur-Arsenic Mixtures. *The Journal of Physical Chemistry*, 72(12): 4133-4139.
396. Wei, H., Ma, J., Li, B., Zuo, Y., and Xia, D. (2014). Enhanced Cycle Performance of Lithium–Sulfur Batteries Using a Separator Modified with a PVDF-C Layer. *ACS Applied Materials & Interfaces*, 6(22): 20276-20281.
397. Wei, L., Sevilla, M., Fuertes, A. B., Mokaya, R., and Yushin, G. (2011). Hydrothermal Carbonization of Abundant Renewable Natural Organic Chemicals for High-Performance Supercapacitor Electrodes. *Advanced Energy Materials*, 1(3): 356-361.

398. Wei, L., Sevilla, M., Fuertes, A. B., Mokaya, R., and Yushin, G. (2012). Polypyrrole-Derived Activated Carbons for High-Performance Electrical Double-Layer Capacitors with Ionic Liquid Electrolyte. *Advanced Functional Materials*, 22(4): 827-834.
399. Wei, P., Fan, M., Chen, H., Chen, D., Li, C., Shu, K., et al. (2016). Ternary Graphene/Sulfur/SiO₂ Composite as Stable Cathode for High Performance Lithium/Sulfur Battery. *International Journal of Hydrogen Energy*, 41(3): 1819-1827.
400. Wei, P., Fan, M. Q., Chen, H. C., Yang, X. R., Wu, H. M., Chen, J., et al. (2016). Enhanced Cycle Performance of Hollow Polyaniline Sphere/Sulfur Composite in Comparison with Pure Sulfur for Lithium–Sulfur Batteries. *Renewable Energy*, 86: 148-153.
401. Wei, S., Zhang, H., Huang, Y., Wang, W., Xia, Y., and Yu, Z. (2011). Pig Bone Derived Hierarchical Porous Carbon and its Enhanced Cycling Performance of Lithium-Sulfur Batteries. *Energy & Environmental Science*, 4(3): 736-740.
402. Weinhold, F., and West, R. (2011). The Nature of the Silicon–Oxygen Bond. *organometallics*, 30(21): 5815-5824.
403. Wild, M., O'Neill, L., Zhang, T., Purkayastha, R., Minton, G., Marinescu, M., et al. (2015). Lithium Sulfur Batteries, a Mechanistic Review. *Energy & Environmental Science*, 8(12): 3477-3494.
404. Winter, M., and Brodd, R. J. (2004). What are Batteries, Fuel cells, and Supercapacitors? *Chemical Reviews*, 104(10): 4245-4270.
405. Wu, C., Yang, S., Cai, J., Zhang, Q., Zhu, Y., and Zhang, K. (2016). Activated Microporous Carbon Derived from Almond Shells for High Energy Density Asymmetric Supercapacitors. *ACS Applied Materials & Interfaces*, 8(24): 15288-15296.
406. Wu, F., Chen, J., Chen, R., Wu, S., Li, L., Chen, S., et al. (2011). Sulfur/Polythiophene with a Core/Shell Structure: Synthesis and Electrochemical Properties of the Cathode for Rechargeable Lithium Batteries. *The Journal of Physical Chemistry C*, 115(13): 6057-6063.
407. Wu, F., Chen, J., Li, L., Zhao, T., and Chen, R. (2011). Improvement of Rate and Cycle Performance by Rapid Polyaniline Coating of a MWCNT/Sulfur Cathode. *The Journal of Physical Chemistry C*, 115(49): 24411-24417.
408. Wu, F., Li, J., Tian, Y., Su, Y., Wang, J., Yang, W., et al. (2015). 3D Coral-like Nitrogen-Sulfur Co-doped Carbon-Sulfur composite for High Performance Lithium-Sulfur Batteries. *Scientific Reports*, 5: 13340-13350.

409. Wu, F., Qian, J., Chen, R., Ye, Y., Sun, Z., Xing, Y., et al. (2016). Light-Weight Functional Layer on a Separator as a Polysulfide Immobilizer to Enhance Cycling Stability for Lithium–Sulfur Batteries. *Journal of Materials Chemistry A*, 4(43): 17033-17041.
410. Wu, H., Huang, Y., Zhang, W., Sun, X., Yang, Y., Wang, L., et al. (2017). Lock of Sulfur with Carbon Black and a Three-Dimensional Graphene@Carbon Nanotubes Coated Separator for Lithium-Sulfur Batteries. *Journal of Alloys and Compounds*, 708: 743-750.
411. Wu, H., Mou, J., Zhou, L., Zheng, Q., Jiang, N., and Lin, D. (2016). Cloud Cap-like, Hierarchically Porous Carbon Derived from Mushroom as an Excellent Host Cathode for High Performance Lithium-Sulfur Batteries. *Electrochimica Acta*, 212: 1021-1030.
412. Wu, H., Tang, Q., Fan, H., Liu, Z., Hu, A., Zhang, S., et al. (2017). Dual-Confined and Hierarchical-Porous Graphene/C/SiO₂ Hollow Microspheres Through Spray Drying Approach for Lithium-Sulfur Batteries. *Electrochimica Acta*, 255: 179-186.
413. Wu, H., Xia, L., Ren, J., Zheng, Q., Xie, F., Jie, W., et al. (2018). A Multidimensional and Nitrogen-Doped Graphene/Hierarchical Porous Carbon as a Sulfur Scaffold for High Performance Lithium Sulfur Batteries. *Electrochimica Acta*, 278: 83-92.
414. Wu, K., Gao, B., Su, J., Peng, X., Zhang, X., Fu, J., et al. (2016). Large and Porous Carbon Sheets Derived from Water Hyacinth for High-Performance Supercapacitors. *RSC Advances*, 6(36): 29996-30003.
415. Wu, R., Chen, S., Deng, J., Huang, X., Song, Y., Gan, R., et al. (2018). Hierarchically Porous Nitrogen-Doped Carbon as Cathode for Lithium–Sulfur Batteries. *Journal of Energy Chemistry*.
416. Wu, X., Fan, L., Wang, M., Cheng, J., Wu, H., Guan, B., et al. (2017). Long-Life Lithium–Sulfur Battery Derived from Nori-Based Nitrogen and Oxygen Dual-Doped 3D Hierarchical Biochar. *ACS Applied Materials & Interfaces*, 9(22): 18889-18896.
417. Wu, Y., Gao, M., Li, X., Liu, Y., and Pan, H. (2014). Preparation of Mesohollow and Microporous Carbon Nanofiber and its Application in Cathode Material for Lithium–Sulfur Batteries. *Journal of Alloys and Compounds*, 608: 220-228.
418. Xi, K., Cao, S., Peng, X., Ducati, C., Vasant Kumar, R., and Cheetham, A. K. (2013). Carbon with Hierarchical Pores from Carbonized Metal-Organic Frameworks for Lithium Sulphur Batteries. *Chemical Communications*, 49(22): 2192-2194.

419. Xi, K., Chen, B., Li, H., Xie, R., Gao, C., Zhang, C., et al. (2015). Soluble Polysulphide Sorption Using Carbon Nanotube Forest for Enhancing Cycle Performance in a Lithium–Sulphur Battery. *Nano Energy*, 12: 538-546.
420. Xi, K., Kidambi, P. R., Chen, R., Gao, C., Peng, X., Ducati, C., et al. (2014). Binder Free Three-Dimensional Sulphur/Few-Layer Graphene Foam Cathode with Enhanced High-Rate Capability for Rechargeable Lithium Sulphur Batteries. *Nanoscale*, 6(11): 5746-5753.
421. Xia, Y., Fang, R., Xiao, Z., Huang, H., Gan, Y., Yan, R., et al. (2017). Confining Sulfur in N-Doped Porous Carbon Microspheres Derived from Microalgae for Advanced Lithium–Sulfur Batteries. *ACS Applied Materials & Interfaces*, 9(28): 23782-23791.
422. Xiang, J., Lv, W., Mu, C., Zhao, J., and Wang, B. (2017). Activated Hard Carbon from orange Peel for Lithium/Sodium Ion Battery Anode with Long Cycle Life. *Journal of Alloys and Compounds*, 701: 870-874.
423. Xiang, M., Wang, Y., Wu, J., Guo, Y., Wu, H., Zhang, Y., et al. (2017). Natural Silk Cocoon Derived Nitrogen-Doped Porous Carbon Nanosheets for High Performance Lithium-Sulfur Batteries. *Electrochimica Acta*, 227: 7-16.
424. Xiao, L., Yuen, K. C., Fernanda, L.-M., Quan, P., Marine, C., He, H., et al. (2016). Tuning Transition Metal Oxide–Sulfur Interactions for Long Life Lithium Sulfur Batteries: The “Goldilocks” Principle. *Advanced Energy Materials*, 6(6): 1501636-1501645.
425. Xiao, M., Huang, M., Zeng, S., Han, D., Wang, S., Sun, L., et al. (2013). Sulfur@Graphene Oxide Core-Shell Particles as a Rechargeable Lithium-Sulfur Battery Cathode Material with High Cycling Stability and Capacity. *RSC Advances*, 3(15): 4914-4916.
426. Xiao, S., Liu, S., Zhang, J., and Wang, Y. (2015). Polyurethane-Derived N-Doped Porous Carbon with Interconnected Sheet-like Structure as Polysulfide Reservoir for Lithium–Sulfur Batteries. *Journal of Power Sources*, 293: 119-126.
427. Xiao, Z., Yang, Z., Wang, L., Nie, H., Zhong, M. e., Lai, Q., et al. (2015). A Lightweight TiO₂/Graphene Interlayer, Applied as a Highly Effective Polysulfide Absorbent for Fast, Long-Life Lithium–Sulfur Batteries. *Advanced Materials*, 27(18): 2891-2898.
428. Xie, L., Sun, G., Su, F., Guo, X., Kong, Q., Li, X., et al. (2016). Hierarchical Porous Carbon Microtubes Derived from Willow Catkins for Supercapacitor Applications. *Journal of Materials Chemistry A*, 4(5): 1637-1646.

429. Xie, Y.-P., Cheng, H.-W., Chai, W., Yue, H., Zhang, X., Fang, J.-H., et al. (2017). Natural Nitrogen-Doped Multiporous Carbon from Biological Cells as Sulfur Stabilizers for Lithium–Sulfur Batteries. *Chinese Chemical Letters*, 28(4): 738-742.
430. Xie, Y., Zhao, H., Cheng, H., Hu, C., Fang, W., Fang, J., et al. (2016). Facile Large-Scale Synthesis of Core–Shell Structured Sulfur@Polypyrrole Aomposite and its application in Lithium–Sulfur Batteries with High Energy Density. *Applied Energy*, 175: 522-528.
431. Xin, S., Guo, Y.-G., and Wan, L.-J. (2012). Nanocarbon Networks for Advanced Rechargeable Lithium Batteries. *Accounts of Chemical Research*, 45(10): 1759-1769.
432. Xu, C., Xu, B., Gu, Y., Xiong, Z., Sun, J., and Zhao, X. S. (2013). Graphene-Based Electrodes for Electrochemical Energy Storage. *Energy & Environmental Science*, 6(5): 1388-1414.
433. Xu, G.-L., Xu, Y.-F., Fang, J.-C., Peng, X.-X., Fu, F., Huang, L., et al. (2013). Porous Graphitic Carbon Loading Ultra High Sulfur as High-Performance Cathode of Rechargeable Lithium–Sulfur Batteries. *ACS Applied Materials & Interfaces*, 5(21): 10782-10793.
434. Xu, G., Ding, B., Nie, P., Shen, L., Dou, H., and Zhang, X. (2014). Hierarchically Porous Carbon Encapsulating Sulfur as a Superior Cathode Material for High Performance Lithium–Sulfur Batteries. *ACS Applied Materials & Interfaces*, 6(1): 194-199.
435. Xu, G., Ding, B., Pan, J., Nie, P., Shen, L., and Zhang, X. (2014). High Performance Lithium-Sulfur Batteries: Advances and Challenges. *Journal of Materials Chemistry A*, 2(32): 12662-12676.
436. Xu, G., Ding, B., Shen, L., Nie, P., Han, J., and Zhang, X. (2013). Sulfur Embedded in Metal Organic Framework-Derived Hierarchically Porous Carbon Nanoplates for High Performance Lithium-Sulfur Battery. *Journal of Materials Chemistry A*, 1(14): 4490-4496.
437. Xu, J., Fan, H., Su, D., and Wang, G. (2018). Nitrogen Doped Yolk-Shell Carbon Spheres as Cathode Host for Lithium-Sulfur Battery. *Journal of Alloys and Compounds*, 747: 283-292.
438. Xu, J., Shui, J., Wang, J., Wang, M., Liu, H.-K., Dou, S. X., et al. (2014). Sulfur–Graphene Nanostructured Vathodes via Ball-Milling for High-Performance Lithium–Sulfur Batteries. *ACS Nano*, 8(10): 10920-10930.
439. Xu, J., Su, D., Zhang, W., Bao, W., and Wang, G. (2016). A Nitrogen-Sulfur Co-Doped Porous Graphene Matrix as a Sulfur Immobilizer for High

- Performance Lithium-Sulfur Batteries. *Journal of Materials Chemistry A*, 4(44): 17381-17393.
440. Xu, J., Zhou, K., Chen, F., Chen, W., Wei, X., Liu, X.-W., et al. (2016). Natural Integrated Carbon Architecture for Rechargeable Lithium–Sulfur Batteries. *ACS Sustainable Chemistry & Engineering*, 4(3): 666-670.
441. Xu, M., Jia, M., Mao, C., Liu, S., Bao, S., Jiang, J., et al. (2016). Aspergillus Flavus Conidia-Derived Carbon/Sulfur Composite as a Cathode Material for High Performance Lithium–Sulfur Battery. *Scientific Reports*, 6: 18739-18748.
442. Xu, M., Li, D., Yan, Y., Guo, T., Pang, H., and Xue, H. (2017). Porous High Specific Surface Area-Activated Carbon with Co-doping N, S and P for High-Performance Supercapacitors. *RSC Advances*, 7(69): 43780-43788.
443. Xu, R., Sun, Y., Wang, Y., Huang, J., and Zhang, Q. (2017). Two-Dimensional Vermiculite Separator for Lithium Sulfur Batteries. *Chinese Chemical Letters*, 28(12): 2235-2238.
444. Xu, Z.-L., Kim, J.-K., and Kang, K. (2018). Carbon Nanomaterials for Advanced Lithium Sulfur Batteries. *Nano Today*, 19: 84-107.
445. Xue, L., Jia-Qi, H., Qiang, Z., and Liqiang, M. (2017). Nanostructured Metal Oxides and Sulfides for Lithium–Sulfur Batteries. *Advanced Materials*, 29(20): 1601759-1601784.
446. Xue, M., Chen, C., Tan, Y., Ren, Z., Li, B., and Zhang, C. (2018). Mangosteen Peel-Derived Porous Carbon: Synthesis and its Application in the Sulfur Cathode for Lithium Sulfur Battery. *Journal of Materials Science*, 53(15): 11062-11077.
447. Yan, K., Lu, Z., Lee, H.-W., Xiong, F., Hsu, P.-C., Li, Y., et al. (2016). Selective Deposition and Stable Encapsulation of Lithium Through Heterogeneous Seeded Growth. *Nature Energy*, 1: 16010-16018.
448. Yan, L., Yu, J., Houston, J., Flores, N., and Luo, H. (2017). Biomass Derived Porous Nitrogen Doped Carbon for Electrochemical Devices. *Green Energy & Environment*, 2(2): 84-99.
449. Yan, N., zhang, W., Shi, J., Liu, Y., and Cui, H. (2018). Nano Potassium Phosphotungstate Spheres/Sulfur Composites as Cathode for Li-S Batteries. *Materials Letters*, 229: 198-201.
450. Yan, S., Lin, J., Liu, P., Zhao, Z., Lian, J., Chang, W., et al. (2018). Preparation of Nitrogen-Doped Porous Carbons for High-Performance Supercapacitor Using Biomass of Waste Lotus Stems. *RSC Advances*, 8(13): 6806-6813.

451. Yang, J., Chen, F., Li, C., Bai, T., Long, B., and Zhou, X. (2016). A Free-Standing Sulfur-Doped Microporous Carbon Interlayer Derived from Luffa Sponge for High Performance Lithium-Sulfur Batteries. *Journal of Materials Chemistry A*, 4(37): 14324-14333.
452. Yang, J., Wang, S., Ma, Z., Du, Z., Li, C., Song, J., et al. (2015). Novel Nitrogen-Doped Hierarchically Porous Coraloid Carbon Materials as Host Matrixes for Lithium-Sulfur Batteries. *Electrochimica Acta*, 159: 8-15.
453. Yang, J., Xie, J., Zhou, X., Zou, Y., Tang, J., Wang, S., et al. (2014). Functionalized N-Doped Porous Carbon Nanofiber Webs for a Lithium-Sulfur Battery with High Capacity and Rate Performance. *The Journal of Physical Chemistry C*, 118(4): 1800-1807.
454. Yang, K., Gao, Q., Tan, Y., Tian, W., Zhu, L., and Yang, C. (2015). Microporous Carbon Derived from Apricot Shell as Cathode Material for Lithium-Sulfur Battery. *Microporous and Mesoporous Materials*, 204: 235-241.
455. Yang, K., Zhong, L., Qin, J., Liu, J., Xiao, M., Han, D., et al. (2018). In Situ Laminated Separator Using Nitrogen-Sulfur Codoped Two-Dimensional Carbon Material to Anchor Polysulfides for High-Performance Li-S Batteries. *ACS Applied Nano Materials*, 1(8): 3807-3816.
456. Yang, S., and Zhang, K. (2018). Converting Corncob to Activated Porous Carbon for Supercapacitor Application. *Nanomaterials*, 8(4): 181-191.
457. Yang, W., Yang, W., Feng, J., and Qin, X. (2018). A polypyrrole-Coated Acetylene Black/Sulfur Composite Cathode Material for Lithium-Sulfur Batteries. *Journal of Energy Chemistry*, 27(3): 813-819.
458. Yang, W., Yang, W., Kong, L., Song, A., Qin, X., and Shao, G. (2018). Phosphorus-Doped 3D Hierarchical Porous Carbon for High-Performance Supercapacitors: A Balanced Strategy for Pore Structure and Chemical Composition. *Carbon*, 127(Supplement C): 557-567.
459. Yang, X., Yan, N., Zhou, W., Zhang, H., Li, X., and Zhang, H. (2015). Sulfur Embedded in One-Dimensional French Fries-like Hierarchical Porous Carbon Derived from a Metal-Organic Framework for High Performance Lithium-Sulfur Batteries. *Journal of Materials Chemistry A*, 3(29): 15314-15323.
460. Yang, X., Zhu, W., Cao, G., and Zhao, X. (2015). Preparation of Reduced Carbon-Wrapped Carbon-Sulfur Composite as Cathode Material of Lithium-Sulfur Batteries. *RSC Advances*, 5(114): 93926-93936.

461. Yang, Y., Sun, W., Zhang, J., Yue, X., Wang, Z., and Sun, K. (2016). High Rate and Stable Cycling of Lithium-Sulfur Batteries with Carbon Fiber Cloth Interlayer. *Electrochimica Acta*, 209: 691-699.
462. Yao, H., Zheng, G., Li, W., McDowell, M. T., Seh, Z., Liu, N., et al. (2013). Crab Shells as Sustainable Templates from Nature for Nanostructured Battery Electrodes. *Nano Letters*, 13(7): 3385-3390.
463. Yayuan, L., Dingchang, L., Yan, Y. P., Kai, L., Jin, X., H., D. R., et al. (2017). An Artificial Solid Electrolyte Interphase with High Li-Ion Conductivity, Mechanical Strength, and Flexibility for Stable Lithium Metal Anodes. *Advanced Materials*, 29(10): 1605531-1605539.
464. Yazhou, W., Xiaoxiao, H., Shanqing, Z., and Yanglong, H. (2018). Sulfur Hosts Against the Shuttle Effect. *Small Methods*, 2(6): 1700345-1700368.
465. Ye, X., Ma, J., Hu, Y.-S., Wei, H., and Ye, F. (2016). MWCNT Porous Microspheres with an Efficient 3D Conductive Network for High Performance Lithium-Sulfur Batteries. *Journal of Materials Chemistry A*, 4(3): 775-780.
466. Yong, X., Mingtao, Z., Xun, C., Haobin, F., Hanwu, D., Hang, H., et al. (2017). Hierarchical Porous Carbons Derived from Rice Husk for Supercapacitors with High Activity and High Capacitance Retention Capability. *Chemistry Select*, 2(22): 6438-6445.
467. Yongguang, Z., Jun, R., Daorui, W., Chengwei, Z., Fuxing, Y., Aliya, M., et al. (2018). Sulfur-Infiltrated Three-Dimensionally Ordered Mesoporous Polypyrrole Cathode for High-Performance Lithium-Sulfur Battery. *ChemElectroChem*, 5(12): 1591-1598.
468. Yu, M., Li, R., Tong, Y., Li, Y., Li, C., Hong, J.-D., et al. (2015). A Graphene Wrapped Hair-Derived Carbon/Sulfur Composite for Lithium-Sulfur Batteries. *Journal of Materials Chemistry A*, 3(18): 9609-9615.
469. Yu, M., Yuan, W., Li, C., Hong, J.-D., and Shi, G. (2014). Performance Enhancement of a Graphene-Sulfur Composite as a Lithium-Sulfur Battery Electrode by Coating with an Ultrathin Al₂O₃ Film Via Atomic Layer Deposition. *Journal of Materials Chemistry A*, 2(20): 7360-7366.
470. Yu, W., Wang, H., Liu, S., Mao, N., Liu, X., Shi, J., et al. (2016). N, O-Codoped Hierarchical Porous Carbons Derived from Algae for High-Capacity Supercapacitors and Battery Anodes. *Journal of Materials Chemistry A*, 4(16): 5973-5983.
471. Yu, X., Joseph, J., and Manthiram, A. (2016). Suppression of the Polysulfide-Shuttle Behavior in Li-S Batteries Through the Development

- of a Facile Functional Group on the Polypropylene Separator. *Materials Horizons*, 3(4): 314-319.
472. Yu, X., and Manthiram, A. (2017). Electrode–Electrolyte Interfaces in Lithium–Sulfur Batteries with Liquid or Inorganic Solid Electrolytes. *Accounts of Chemical Research*, 50(11): 2653-2660.
473. Yu, Z., Tetard, L., Zhai, L., and Thomas, J. (2015). Supercapacitor Electrode Materials: Nanostructures from 0 to 3 Dimensions. *Energy & Environmental Science*, 8(3): 702-730.
474. Yuan, G., and Wang, H. (2014). Facile Synthesis and Performance of Polypyrrole-Coated Sulfur Nanocomposite as Cathode Materials for Lithium/Sulfur Batteries. *Journal of Energy Chemistry*, 23(5): 657-661.
475. Yuan, H., Lu, T., Wang, Y., Huang, H., and Chen, Y. (2014). Influence of Pyrolysis Temperature and Holding Time on Properties of Biochar Derived from Medicinal Herb (radix isatidis) Residue and its Effect on Soil CO₂ Emission. *Journal of Analytical and Applied Pyrolysis*, 110(Supplement C): 277-284.
476. Yuan, X., Liu, B., Hou, H., Zeinu, K., He, Y., Yang, X., et al. (2017). Facile Synthesis of Mesoporous Graphene Platelets with In situ Nitrogen and Sulfur Doping for Lithium–Sulfur Batteries. *RSC Advances*, 7(36): 22567-22577.
477. Yuan, X., Wu, L., He, X., Zeinu, K., Huang, L., Zhu, X., et al. (2017). Separator Modified with N,S Co-doped Mesoporous Carbon Using Egg Shell as Template for High Performance Lithium-Sulfur Batteries. *Chemical Engineering Journal*, 320: 178-188.
478. Yunbo, Z., Lixiao, M., Jing, N., Zhichang, X., Long, H., Bin, W., et al. (2015). A Graphene-Oxide-Based Thin Coating on the Separator: An Efficient Barrier Towards High-Stable Lithium–Sulfur Batteries. *2D Materials*, 2(2): 024013-024021.
479. Yunhua, X., Yang, W., Yujie, Z., Karen, G., A., C. K., Bryan, E., et al. (2015). Confined Sulfur in Microporous Carbon Renders Superior Cycling Stability in Li/S Batteries. *Advanced Functional Materials*, 25(27): 4312-4320.
480. Yunpu, Z., Yuqian, D., Dongyuan, Z., F., F. P., T., M. R., and Sheng, D. (2011). Carbon Materials for Chemical Capacitive Energy Storage. *Advanced Materials*, 23(42): 4828-4850.
481. Zeiger, M., Jackel, N., Mochalin, V. N., and Presser, V. (2016). Review: Carbon Onions for Electrochemical Energy Storage. *Journal of Materials Chemistry A*, 4(9): 3172-3196.

482. Zeng, F., Jin, Z., Yuan, K., Liu, S., Cheng, X., Wang, A., et al. (2016). High Performance Lithium–Sulfur Batteries with a Permselective Sulfonated Acetylene Black Modified Separator. *Journal of Materials Chemistry A*, 4(31): 12319-12327.
483. Zeng, P., Huang, L., Zhang, X., Han, Y., and Chen, Y. (2018). Inhibiting Polysulfides Diffusion of Lithium-Sulfur Batteries Using an Acetylene Black-CoS₂ Modified Separator: Mechanism Research and Performance Improvement. *Applied Surface Science*, 427: 242-252.
484. Zeng, P., Huang, L., Zhang, X., Zhang, R., Wu, L., and Chen, Y. (2018). Long-Life and High-Areal-Capacity Lithium-Sulfur Batteries Realized by a HoneyComb-like N, P Dual-Doped Carbon Modified Separator. *Chemical Engineering Journal*, 349: 327-337.
485. Zeng, S.-Z., Zeng, X., Tu, W., Yao, Y., Yu, L., Wu, H., et al. (2017). Facile and Tailored Synthesis of Ultrahigh-Surface-Area Clews of Carbon Nanobelts for High-rate Lithium–Sulfur batteries. *Journal of Materials Chemistry A*, 5(44): 23209-23220.
486. Zhai, P.-Y., Peng, H.-J., Cheng, X.-B., Zhu, L., Huang, J.-Q., Zhu, W., et al. (2017). Scaled-up Fabrication of Porous-Graphene-Modified Separators for High-Capacity Lithium–Sulfur Batteries. *Energy Storage Materials*, 7: 56-63.
487. Zhai, Y., Wan, Y., Cheng, Y., Shi, Y., Zhang, F., Tu, B., et al. (2008). The Influence of Carbon Source on the Wall Structure of Ordered Mesoporous Carbons. *Journal of Porous Materials*, 15(5): 601-611.
488. Zhang, B., Lai, C., Zhou, Z., and Gao, X. P. (2009). Preparation and Electrochemical Properties of Sulfur–Acetylene Black Composites as Cathode Materials. *Electrochimica Acta*, 54(14): 3708-3713.
489. Zhang, B., Qin, X., Li, G. R., and Gao, X. P. (2010). Enhancement of Long Stability of Sulfur Cathode by Encapsulating Sulfur into Micropores of Carbon Spheres. *Energy & Environmental Science*, 3(10): 1531-1537.
490. Zhang, B., Xiao, M., Wang, S., Han, D., Song, S., Chen, G., et al. (2014). Novel Hierarchically Porous Carbon Materials Obtained from Natural Biopolymer as Host Matrixes for Lithium–Sulfur Battery Applications. *ACS Applied Materials & Interfaces*, 6(15): 13174-13182.
491. Zhang, C., Zhu, X., Cao, M., Li, M., Li, N., Lai, L., et al. (2016). Hierarchical Porous Carbon Materials Derived from Sheep Manure for High-Capacity Supercapacitors. *ChemSusChem*, 9(9): 932-937.

492. Zhang, J., Cai, Y., Zhong, Q., Lai, D., and Yao, J. (2015). Porous Nitrogen-Doped Carbon Derived from Silk Fibroin Protein Encapsulating Sulfur as a Superior Cathode Material for High-Performance Lithium-Sulfur Batteries. *Nanoscale*, 7(42): 17791-17797.
493. Zhang, J., Liu, J., and Liu, R. (2015). Effects of Pyrolysis Temperature and Heating Time on Biochar Obtained from the Pyrolysis of Straw and Lignosulfonate. *Bioresource Technology*, 176(Supplement C): 288-291.
494. Zhang, J., Xiang, J., Dong, Z., Liu, Y., Wu, Y., Xu, C., et al. (2014). Biomass Derived Activated Carbon with 3D Connected Architecture for Rechargeable Lithium-Sulfur Batteries. *Electrochimica Acta*, 116: 146-151.
495. Zhang, L., Ji, L., Glans, P.-A., Zhang, Y., Zhu, J., and Guo, J. (2012). Electronic Structure and Chemical Bonding of a Graphene oxide-Sulfur Nanocomposite for use in Superior Performance Lithium-Sulfur Cells. *Physical Chemistry Chemical Physics*, 14(39): 13670-13675.
496. Zhang, L., Wan, F., Wang, X., Cao, H., Dai, X., Niu, Z., et al. (2018). Dual-Functional Graphene Carbon as Polysulfide Trapper for High-Performance Lithium Sulfur Batteries. *ACS Applied Materials & Interfaces*, 10(6): 5594-5602.
497. Zhang, J., Xiang, J., Dong, Z., Liu, Y., Wu, Y., Xu, C., et al. (2014). Biomass Derived Activated Carbon with 3D Connected Architecture for Rechargeable Lithium-Sulfur Batteries. *Electrochimica Acta*, 116: 146-151.
498. Zhang, L., Ji, L., Glans, P.-A., Zhang, Y., Zhu, J., and Guo, J. (2012). Electronic Structure and Chemical Bonding of a Graphene Oxide-Sulfur Nanocomposite for use in Superior Performance Lithium-Sulfur cells. *Physical Chemistry Chemical Physics*, 14(39): 13670-13675.
499. Zhang, L., Wan, F., Wang, X., Cao, H., Dai, X., Niu, Z., et al. (2018). Dual-Functional Graphene Carbon as Polysulfide Trapper for High-Performance Lithium Sulfur Batteries. *ACS Applied Materials & Interfaces*, 10(6): 5594-5602.
500. Zhang, L., Xu, L., Zhang, Y., Zhou, X., Zhang, L., Yasin, A., et al. (2018). Facile Synthesis of Bio-Based Nitrogen- and Oxygen-Doped Porous Carbon Derived from Cotton for Supercapacitors. *RSC Advances*, 8(7): 3869-3877.
501. Zhang, S. (2013). Sulfurized Carbon: A Class of Cathode Materials for High Performance Lithium/Sulfur Batteries. *Frontiers in Energy Research*, 1(10): 1-9.

502. Zhang, S., Ikoma, A., Ueno, K., Chen, Z., Dokko, K., and Watanabe, M. (2015). Protic-Salt-Derived Nitrogen/Sulfur-Codoped Mesoporous Carbon for the Oxygen Reduction Reaction and Supercapacitors. *ChemSusChem*, 8(9): 1608-1617.
503. Zhang, S., Shi, X., Moszyński, D., Tang, T., Chu, P. K., Chen, X., et al. (2018). Hierarchical Porous Carbon Materials from Nanosized Metal-Organic Complex for High-Performance Symmetrical Supercapacitor. *Electrochimica Acta*, 269: 580-589.
504. Zhang, S., Zheng, M., Lin, Z., Li, N., Liu, Y., Zhao, B., et al. (2014). Activated Carbon with Ultrahigh Specific Surface Area Synthesized from Natural Plant Material for Lithium-Sulfur Batteries. *Journal of Materials Chemistry A*, 2(38): 15889-15896.
505. Zhang, S., Zheng, M., Lin, Z., Zang, R., Huang, Q., Xue, H., et al. (2016). Mango stone-Derived Activated Carbon with High Sulfur Loading as a Cathode Material for Lithium-Sulfur Batteries. *RSC Advances*, 6(46): 39918-39925.
506. Zhang, S. S. (2015). Heteroatom-Doped Carbons: Synthesis, Chemistry and Application in Lithium/Sulphur Batteries. *Inorganic Chemistry Frontiers*, 2(12): 1059-1069.
507. Zhang, W., Huang, Y., Chen, X., Wu, H., and Zhang, X. (2017). Shaddock Wadding Created Activated Carbon as High Sulfur Content Encapsulator for Lithium-Sulfur Batteries. *Journal of Alloys and Compounds*, 724: 575-580.
508. Zhang, X., Xie, H., Kim, C. S., Zaghbi, K., Mauger, A., and Julien, C. M. (2017). Advances in Lithium—Sulfur Batteries. *Materials Science and Engineering: R: Reports*, 121: 1-29.
509. Zhang, Y.-Z., Wu, Z.-Z., Pan, G.-L., Liu, S., and Gao, X.-P. (2017). Microporous Carbon Polyhedrons Encapsulated Polyacrylonitrile Nanofibers as Sulfur Immobilizer for Lithium–Sulfur Battery. *ACS Applied Materials & Interfaces*, 9(14): 12436-12444.
510. Zhang, Y.-Z., Zhang, Z., Liu, S., Li, G.-R., and Gao, X.-P. (2018). Free-Standing Porous Carbon Nanofiber/Carbon Nanotube Film as Sulfur Immobilizer with High Areal Capacity for Lithium–Sulfur Battery. *ACS Applied Materials & Interfaces*, 10(10): 8749-8757.
511. Zhang, Y., Bakenov, Z., Zhao, Y., Konarov, A., Doan, T. N. L., Malik, M., et al. (2012). One-Step Synthesis of Branched Sulfur/Polypyrrole Nanocomposite Cathode for Lithium Rechargeable Batteries. *Journal of Power Sources*, 208: 1-8.

512. Zhang, Y., Gao, Z., Song, N., He, J., and Li, X. (2018). Graphene and its Derivatives in Lithium–Sulfur Batteries. *Materials Today Energy*, 9: 319-335.
513. Zhang, Y., Li, K., Huang, J., Wang, Y., Peng, Y., Li, H., et al. (2017). Preparation of Monodispersed Sulfur Nanoparticles-Partly Reduced Graphene Oxide-Polydopamine Composite for Superior Performance Lithium-Sulfur Battery. *Carbon*, 114: 8-14.
514. Zhang, Y., Zhao, Y., and Bakenov, Z. (2014). A Novel Lithium/Sulfur Battery Based on Sulfur/Graphene Nanosheet Composite Cathode and Gel Polymer Electrolyte. *Nanoscale Research Letters*, 9(1): 137-144.
515. Zhang, Y., Zhao, Y., Bakenov, Z., Tuiyebayeva, M., Konarov, A., and Chen, P. (2014). Synthesis of Hierarchical Porous Sulfur/Polypyrrole/Multiwalled Carbon Nanotube Composite Cathode for Lithium Batteries. *Electrochimica Acta*, 143: 49-55.
516. Zhang, Y., Zhao, Y., Konarov, A., Li, Z., and Chen, P. (2015). Effect of Mesoporous Carbon Microtube Prepared by Carbonizing the Poplar Catkin on Sulfur Cathode Performance in Li/S Batteries. *Journal of Alloys and Compounds*, 619: 298-302.
517. Zhang, Y., Zong, X., Liang, Z., Yu, X., Gao, J., Xun, C., et al. (2018). Double-Shelled Hollow Carbon Sphere with Microporous Outer Shell towards High Performance Lithium-Sulfur Battery. *Electrochimica Acta*, 284: 89-97
518. Zhang, Y. Z., Liu, S., Li, G. C., Li, G. R., and Gao, X. P. (2014). Sulfur/Polyacrylonitrile/Carbon Multi-Composites as Cathode Materials for Lithium/Sulfur Battery in the Concentrated Electrolyte. *Journal of Materials Chemistry A*, 2(13): 4652-4659.
519. Zhang, Z., Lai, Y., Zhang, Z., and Li, J. (2015). A Functional Carbon Layer-Coated Separator for High Performance Lithium Sulfur Batteries. *Solid State Ionics*, 278: 166-171.
520. Zhang, Z., Li, Q., Lai, Y., and Li, J. (2014). Confine Sulfur in Polyaniline-Decorated Hollow Carbon Nanofiber Hybrid Nanostructure for Lithium–Sulfur Batteries. *The Journal of Physical Chemistry C*, 118(25): 13369-13376.
521. Zhang, Z., Pfefferle, L., and Haller, G. L. (2014). Comparing Characterization of Functionalized Multi-walled Carbon Nanotubes by Potentiometric Proton Titration, NEXAFS, and XPS. *Chinese Journal of Catalysis*, 35(6): 856-863.

522. Zhang, Z., Wang, G., Lai, Y., Li, J., Zhang, Z., and Chen, W. (2015). Nitrogen-Doped Porous Hollow Carbon Sphere-Decorated Separators for Advanced Lithium–Sulfur Batteries. *Journal of Power Sources*, 300: 157-163.
523. Zhao, C., Liu, L., Zhao, H., Krall, A., Wen, Z., Chen, J., et al. (2014). Sulfur-Infiltrated Porous Carbon Microspheres with Controllable Multi-Modal Pore Size Distribution for High Energy Lithium-Sulfur Batteries. *Nanoscale*, 6(2): 882-888.
524. Zhao, H., Deng, N., Yan, J., Kang, W., Ju, J., Ruan, Y., et al. (2018). A Review on Anode for Lithium-Sulfur Batteries: Progress and Prospects. *Chemical Engineering Journal*, 347: 343-365.
525. Zhao, J., Zhou, G., Yan, K., Xie, J., Li, Y., Liao, L., et al. (2017). Air-Stable and Freestanding Lithium Alloy/Graphene Foil as an Alternative to Lithium Metal Anodes. *Nature Nanotechnology*, 12: 993-1001.
526. Zhao, M.-Q., Zhang, Q., Huang, J.-Q., Tian, G.-L., Nie, J.-Q., Peng, H.-J., et al. (2014). Unstacked Double-Layer Templated Graphene for High-Rate Lithium–Sulphur Batteries. *Nature Communications*, 5: 3410-3418.
527. Zhao, S., Li, C., Wang, W., Zhang, H., Gao, M., Xiong, X., et al. (2013). A Novel Porous Nanocomposite of Sulfur/Carbon Obtained from Fish Scales for Lithium-Sulfur Batteries. *Journal of Materials Chemistry A*, 1(10): 3334-3339.
528. Zhao, X., Kim, J.-K., Ahn, H.-J., Cho, K.-K., and Ahn, J.-H. (2013). A Ternary sulfur/polyaniline/carbon Composite as Cathode Material for Lithium Sulfur Batteries. *Electrochimica Acta*, 109: 145-152.
529. Zhao, Y.-Q., Lu, M., Tao, P.-Y., Zhang, Y.-J., Gong, X.-T., Yang, Z., et al. (2016). Hierarchically Porous and Heteroatom Doped Carbon Derived from Tobacco Rods for Supercapacitors. *Journal of Power Sources*, 307: 391-400.
530. Zhen, M., Wang, J., Wang, X., and Wang, C. (2018). Hierarchical N-Rich Carbon Sponge with Excellent Cycling Performance for Lithium-Sulfur Battery at High Rates. *Chemistry – A European Journal*, 24(22): 5860-5867.
531. Zheng, G., Yang, Y., Cha, J. J., Hong, S. S., and Cui, Y. (2011). Hollow Carbon Nanofiber-Encapsulated Sulfur Cathodes for High Specific Capacity Rechargeable Lithium Batteries. *Nano Letters*, 11(10): 4462-4467.
532. Zheng, M., Hu, Q., Zhang, S., Tang, H., Li, L., and Pang, H. (2017). Macroporous Activated Carbon Derived from Rapeseed Shell for Lithium–Sulfur Batteries. *Applied Sciences*, 7(10): 1036-1047.

533. Zheng, X., Chen, M., Ma, Y., Dong, X., Xi, F., and Liu, J. (2017). Enhanced Electrochemical Performance of Straw-Based Porous Carbon Fibers for Supercapacitor. *Journal of Solid State Electrochemistry*, 21(12): 3449-3458.
534. Zhijiang, C., and Chengwei, H. (2011). Study on the Electrochemical Properties of Zinc/Polyindole Secondary Battery. *Journal of Power Sources*, 196(24): 10731-10736.
535. Zhijiang, C., Xingjuan, S., and Yanan, F. (2013). Electrochemical Properties of Electrospun Polyindole Nanofibers as a Polymer Electrode for Lithium ion Secondary Battery. *Journal of Power Sources*, 227: 53-59.
536. Zhong, C., Deng, Y., Hu, W., Qiao, J., Zhang, L., and Zhang, J. (2015). A Review of Electrolyte Materials and Compositions for Electrochemical Supercapacitors. *Chemical Society Reviews*, 44(21): 7484-7539.
537. Zhou, D., Wang, H., Mao, N., Chen, Y., Zhou, Y., Yin, T., et al. (2017). High Energy Supercapacitors Based on Interconnected Porous Carbon Nanosheets with Ionic Liquid Electrolyte. *Microporous and Mesoporous Materials*, 241: 202-209.
538. Zhou, G., Paek, E., Hwang, G. S., and Manthiram, A. (2015). Long-Life Li/polysulphide Batteries with High Sulphur Loading Enabled by Lightweight Three-Dimensional Nitrogen/Sulphur-Codoped Graphene Sponge. *Nature Communications*, 6: 7760-7771.
539. Zhou, G., Yin, L.-C., Wang, D.-W., Li, L., Pei, S., Gentle, I. R., et al. (2013). Fibrous Hybrid of Graphene and Sulfur Nanocrystals for High-Performance Lithium–Sulfur Batteries. *ACS Nano*, 7(6): 5367-5375.
540. Zhou, J., Guo, Y., Liang, C., Yang, J., Wang, J., and Nuli, Y. (2018). Confining Small Sulfur Molecules in Peanut Shell-Derived Microporous Graphitic Carbon for Advanced Lithium Sulfur Battery. *Electrochimica Acta*, 273: 127-135.
541. Zhou, L., Lin, X., Huang, T., and Yu, A. (2014). Binder-Free Phenyl sulfonated Graphene/Sulfur Electrodes with Excellent Cyclability for Lithium Sulfur Batteries. *Journal of Materials Chemistry A*, 2(14): 5117-5123.
542. Zhou, L., Zong, Y., Liu, Z., and Yu, A. (2016). A polydopamine Coating Ultralight Graphene Matrix as a Highly Effective Polysulfide Absorbent for High-Energy Li-S Batteries. *Renewable Energy*, 96: 333-340.
543. Zhou, T., Cao, Z., Wang, H., Gao, Z., Li, L., Ma, H., et al. (2017). Ultrathin Co-Fe hydroxide Nanosheet Arrays for Improved Oxygen Evolution during Water Splitting. *RSC Advances*, 7(37): 22818-22824.

544. Zhou, W., Chen, H., Yu, Y., Wang, D., Cui, Z., DiSalvo, F. J., et al. (2013). Amylopectin Wrapped Graphene Oxide/Sulfur for Improved Cyclability of Lithium–Sulfur Battery. *ACS Nano*, 7(10): 8801-8808.
545. Zhou, W., Xiao, X., Cai, M., and Yang, L. (2014). Polydopamine-Coated, Nitrogen-Doped, Hollow Carbon–Sulfur Double-Layered Core–Shell Structure for Improving Lithium–Sulfur Batteries. *Nano Letters*, 14(9): 5250-5256.
546. Zhou, W., Yu, Y., Chen, H., DiSalvo, F. J., and Abruña, H. D. (2013). Yolk–Shell Structure of Polyaniline-Coated Sulfur for Lithium–Sulfur Batteries. *Journal of the American Chemical Society*, 135(44): 16736-16743.
547. Zhou, X., Chen, F., and Yang, J. (2015). Core@shell sulfur@polypyrrole Nanoparticles Sandwiched in Graphene Sheets as Cathode for Lithium–Sulfur Batteries. *Journal of Energy Chemistry*, 24(4): 448-455.
548. Zhou, X., Liao, Q., Bai, T., and Yang, J. (2017). Nitrogen-Doped Microporous Carbon from Polyaspartic Acid Bonding Separator for High Performance Lithium-Sulfur Batteries. *Journal of Electroanalytical Chemistry*, 791: 167-174.
549. Zhou, X., Liao, Q., Tang, J., Bai, T., Chen, F., and Yang, J. (2016). A High-Level N-Doped Porous Carbon Nanowire Modified Separator for Long-Life Lithium–Sulfur Batteries. *Journal of Electroanalytical Chemistry*, 768: 55-61.
550. Zhou, X., Wang, P., Zhang, Y., Wang, L., Zhang, L., Zhang, L., et al. (2017). Biomass Based Nitrogen-Doped Structure-Tunable Versatile Porous Carbon Materials. *Journal of Materials Chemistry A*, 5(25): 12958-12968.
551. Zhu, G., Ma, L., Lv, H., Hu, Y., Chen, T., Chen, R., et al. (2017). Pine needle-Derived Microporous Nitrogen-Doped Carbon Frameworks Exhibit High Performances in Electrocatalytic Hydrogen Evolution Reaction and Supercapacitors. *Nanoscale*, 9(3): 1237-1243.
552. Zhu, H., Fu, Y., Jiang, R., Yao, J., Liu, L., Chen, Y., et al. (2013). Preparation, Characterization and Adsorption Properties of Chitosan Modified Magnetic Graphitized Multi-walled Carbon nanotubes for Highly Effective Removal of a Carcinogenic Dye from Aqueous Solution. *Applied Surface Science*, 285: 865-873.
553. Zhu, H., Wang, X., Yang, F., and Yang, X. (2011). Promising Carbons for Supercapacitors Derived from Fungi. *Advanced Materials*, 23(24): 2745-2748.

554. Zhu, J., Ge, Y., Kim, D., Lu, Y., Chen, C., Jiang, M., et al. (2016). A Novel Separator Coated by Carbon for Achieving Exceptional High Performance Lithium-Sulfur Batteries. *Nano Energy*, 20: 176-184.
555. Zhu, P., Zang, J., Zhu, J., Lu, Y., Chen, C., Jiang, M., et al. (2018). Effect of Reduced Graphene Oxide Reduction Degree on the Performance of Polysulfide Rejection in Lithium-Sulfur Batteries. *Carbon*, 126: 594-600.
556. Zhu, S., Wang, Y., Jiang, J., Yan, X., Sun, D., Jin, Y., et al. (2016). Good Low-Temperature Properties of Nitrogen-Enriched Porous Carbon as Sulfur Hosts for High-Performance Li-S Batteries. *ACS Applied Materials & Interfaces*, 8(27): 17253-17259.
557. Zhu, Y., Xu, G., Zhang, X., Wang, S., Li, C., and Wang, G. (2017). Hierarchical Porous Carbon Derived from Soybean Hulls as a Cathode Matrix for Lithium-Sulfur Batteries. *Journal of Alloys and Compounds*, 695: 2246-2552.
558. Zuo, W., Li, R., Zhou, C., Li, Y., Xia, J., and Liu, J. (2017). Battery-Supercapacitor Hybrid Devices: Recent Progress and Future Prospects. *Advanced science*, 4(7): 1600539-1600560.

LIST OF PUBLICATIONS BASED ON THE THESIS

1. C. Reshma., J. Mary Gladis. (2015) Synthesis and Characterisation of Ternary Nanocomposites as Cathode Material for Lithium-Sulphur Batteries. *Materials Science Forum*, 830-83: 604-607.
2. Reshma C., Haritha H., M. Raja, J. Mary Gladis, Arul Manuel Stephan. (2017). Enhanced Cyclability Using Polyindole Modified Cathode Material for Lithium Sulphur battery. *Sustainable Energy & Fuels*, 1: 1774-1781.
3. Reshma C., Haritha H., M. Raja, J. Mary Gladis, A. M. Stephan. (2017). Sulfur-Immobilized Nitrogen and Oxygen Co-Doped Hierarchically Porous Biomass Carbon for Lithium-Sulfur Batteries: Influence of Sulfur Content and Distribution on Its Performance. *ChemistrySelect*, 2: 10484–10495.
4. Reshma C., Haritha H., Mary Gladis J., Effect of *Pyrolysis* Time on the Performance of Heteroatom Doped Carbon as Electrode Material for Symmetric Supercapacitor (*Manuscript submitted*).
5. Reshma C., Haritha H., Mary Gladis J., One Pot Synthesis of Heteroatom Doped Carbon as Electrode Material for Lithium-Sulphur Batteries (*Manuscript under preparation*).
6. Reshma C., Mary Gladis J., Facile Synthesis of tubular Hierarchical Porous Carbon Embedded with Nano Iron oxide as Symmetric Supercapacitor Electrodes and Quadruple Confinement Effect on Polysulphides for High-Performance Lithium-Sulphur Battery Cathodes (*Manuscript under preparation*).
7. Reshma C., Mary Gladis J., Enhanced Electrochemical Kinetics and Reduced Polysulphide Shuttling using Microporous Orange Peel Biochar–Sulphur Composite with Multiwalled Carbon nanotube Coated Separator for Lithium-Sulphur Battery (*Manuscript under preparation*)
8. Reshma C., Mary Gladis J., Effect of Structural Characteristics of the Heteroatom Doped Carbon Electrode material on the Performance of Li-S batteries (*Manuscript under preparation*)
9. Reshma C., Mary Gladis J., Hierarchical Porous Carbon Materials Derived Honeycomb carbon/sulphur composite as high performance cathode material for Lithium – Sulphur Batteries (*Manuscript under preparation*).

Other Publications

1. Haritha H., Reshma C., Mary Gladis J. (2017). Effect of Crystallite Size on the Intercalation Pseudocapacitance of Lithium nickel vanadate in Aqueous electrolyte. *Journal of Solid State Electrochemistry*, 81:1-9.
2. Haritha H., Reshma C., Mary Gladis J. (2018). Micro and Nanocrystalline Inverse Spinel LiCoVO₄ for Intercalation pseudocapacitive Li⁺ Storage with Ultrahigh Energy Density and Long-Term Cycling. *ACS Applied Energy Materials*, 1: 393–401.

PRESENTATIONS IN CONFERENCES/SEMINARS

Oral presentations

1. Reshma C., Mary Gladis J., Hierarchically Porous Carbon-Sulphur Composite as a Cathode Material for Lithium Sulphur Battery in Materials Research Society of India (MRSI) Thiruvananthapuram chapter, jointly organized by MRSI-Thiruvananthapuram Chapter and University of Kerala, Thiruvananthapuram on February 13-15, 2017.
2. Reshma C., Mary Gladis J., Insitu Functionalised Hierarchically Porous Carbon with Iron, Nitrogen and Oxygen for a High-Performance Lithium Sulphur Battery in Indo-US bilateral workshop on nanotechnology for clean energy generation and storage (INDO US Workshop 2018), jointly organized by PSG Institute of Advanced Studies (Coimbatore, India) and SUNY Polytechnic Institute (Albany, New York, USA), Coimbatore on January 10-12, 2018.
3. Reshma C., Mary Gladis J., Quadruple Confinement Effect on Sulphur in Insitu Functionalized Hierarchically Porous Carbon with Silicon, Nitrogen and Oxygen from Honeycomb Nest for a High-Performance Lithium Sulphur Battery in a national level meet of young scientists working in the field of Hydrogen Energy and related Advanced Materials (HEAM Scientist 2018), jointly organized by University of Kerala and ONGC Energy centre, Thiruvananthapuram on March 5-6, 2018.
4. Reshma C., Mary Gladis., Hierarchical Porous Carbon Material Derived from Honeycomb as a Polysulphide Blocking Interlayer for the Enhanced Cycling Stability of Lithium–Sulphur Battery in the International Conference on Materials Science And Technology (ICMST 2018), jointly organized by Indian Institute of Space Science and Technology and MRSI-Thiruvananthapuram Chapter, Thiruvananthapuram on October 10 – 14, 2018.

5. Reshma C., Mary Gladis., Iron, Nitrogen and Oxygen Co-Doped Hierarchically Porous Carbon for Long Cycle Life Lithium Sulphur Battery in International Conference on Chemistry and Physics of Materials (ICCPM 2018), organized by St. Thomas College, Thrissur on December 19–21, 2018 (Best paper award).
6. Reshma C., Mary Gladis., Quadruple Confinement Effect of Intrinsically Functionalized Hierarchically Porous Carbon with Iron, Nitrogen and Oxygen onto sulphur/lithium polysulphides towards High-Performance Lithium-Sulphur Battery in Twelfth International Symposium on Advances in Electrochemical Science and Technology (iSAEST-12), organized by CSIR-Central Electrochemical Research Institute (CSIR-CECRI), Chennai on January 8-10, 2019.
7. Reshma C., Mary Gladis., Multifunctional hierarchically porous carbon as interlayer to mitigate polysulphide shuttle for high performance lithium-sulphur battery in one day Research Scholar Symposium on Materials Science and Engineering, organized by IIM Trivandrum Chapter at CSIR-National Institute for Interdisciplinary Science and Technology (CSIR-NIIST) Trivandrum, April 3, 2019.

Poster presentations

1. Reshma C., Mary Gladis., Developments in Graphene–Sulphur Nanocomposites for Rechargeable Lithium-Sulphur Batteries in International Conference on Advanced Functional Materials (ICAFM 2014), organized by National Institute for Interdisciplinary Science and Technology (CSIR-NIIST) Thiruvananthapuram on February 19-21, 2014.
2. Reshma C., Mary Gladis., Multi-walled Carbon Nanotube-Sulphur Nanocomposite Modified with Conducting Polymer as Cathode Material for Lithium–Sulphur Battery in 7th Bangalore India Nano 2014, organized by Department of IT, BT and S&T, Government of Karnataka in association with Vision Group on Nanotechnology and Jawaharlal Nehru Centre for Advanced Scientific Research (JNCASR) on December 5-6, 2014.
3. Reshma C., Mary Gladis., Synthesis and Characterization of Ternary Nanocomposites as Cathode Material for Lithium-Sulphur Batteries in the International Conference on Advanced Materials and Manufacturing Processes for Strategic Sectors (ICAMPS-2015), Organized by Indian Institute of Metals (Trivandrum Chapter), Thiruvananthapuram on May 13–15, 2015.

4. Reshma C., Mary Gladis., Porous Carbon Derived From Pinecone For Lithium Sulphur battery in the National Conference on Materials Science And Technology (NCMST 2016), organized by Indian Institute of Space Science and Technology, Thiruvananthapuram on July 12–14, 2016.
5. Reshma C., Mary Gladis., Porous Carbon Derived From 4, 4'-Diamino-Diphenyl Sulphone For Supercapacitor Applications in the International Conference of Young Researchers on Advanced Materials (IUMRS-ICYRAM 2016), organized by Indian Institute of Science, Bangalore on December 11-15, 2016.
6. Reshma C., Mary Gladis., Facile Synthesis of Hierarchically Porous Carbon Tubes Inherently Doped with Nitrogen, Oxygen and Iron oxide Nanoparticles as Supercapacitor Electrodes in International Conference on Advanced Materials and Processes (ADMAT 2017), organized by Indian Space Research Organization, Thiruvananthapuram on December 14-16, 2017.
7. Reshma C., Mary Gladis., Heteroatom Doped Porous Carbon Material Modified separator for high performance lithium-sulphur battery in International Conference on Advanced Materials and Manufacturing Processes for Strategic Sectors (ICAMPS-2018), Organized by Indian Institute of Metals (Trivandrum Chapter), Thiruvananthapuram on October 25–27, 2018.

